An Investigation of Plastic Scintillators for Radiation Sensing and Mechanical Applications

A Dissertation Presented for the
Doctor of Philosophy
Degree
The University of Tennessee, Knoxville

Caleb Joseph Redding
May 2021

Copyright © by Caleb Joseph Redding, 2021
All Rights Reserved.

For Andelyn; you are my person.

Acknowledgments

My highest thanks goes to my wife, Andelyn. Without your support on every facet of human need, none of this could have been possible. For your understanding when long hours away were required, for the clarity and encouragement you provided during our many conversations, and for the periods when you did double-duty around our home, no thanks could be enough. You are truly my better half. To my advisor, Jason, thank you for the opportunity and resources to learn and develop as a researcher. Your guidance, both implicit and explicit, has served as an invaluable illuminator to the path of professional conduct, courtesy, and responsibility. I will use these lessons well. Thanks also goes to my committee members for their valuable time, interest, probing questions, and grace during this period. Lastly I would like to thank the members of the RadIdeas research group. Special thanks goes to Cordell Delzer, Michael Moore, Angela Moore, Carl Britt, Zhengzhi Liu, Callie Goetz, Michael Liesenfelt, and Xianfei Wen for all manner of conversation and friendship.

COPYRIGHT DISCLAIMER

Some additional commentary, minor grammatical corrections, redaction, and adaptation of the dissertation author's published journal articles (PJAs) may be transformative of the original work present. Therefore, the PJAs should be referenced directly before citing this work. Embedded PJAs that are part of this submission can be found with their respective DOI links back to the formal publications when.

Chapter 2, is in part a reprint of the material as it appears published in *Nuclear Instruments and Methods in Physics Research Section A*, 2020. *Authors:* C. Redding, A. Hackett, M. Laubach, R. Feng, P. Feng, C. Hurlbut, P. Liaw, and J. Hayward. https://doi.org/10.1016/j.nima.2018.10.126. The dissertation author was the primary investigator and author of this paper.

Chapter 3, in part, is currently being prepared for submission for publication of the material. *Authors:* C.Redding, C. Delzer, and J. Hayward. The dissertation author was the primary investigator and author of this paper.

Chapter 4, in part, is currently being prepared for submission for publication of the material. *Authors:* C.Redding, C. Delzer, H. Yu, T. Chen, Q. Pei, N. Cherepy, and J. Hayward. The dissertation author was the primary investigator and author of this paper.

Section 5.2, is in part a reprint of the material as it appears published in the supporting material for *ACS Applied Nano Materials*, 2021. *Authors:* H. Zhao, H. Yu, C. Redding, Z. Li, T. Chen, Y. Meng, T.J. Hajagos, J.P. Hayward, Q. Pei. https://doi.org/10.1021/acsanm.0c02845. The dissertation author was a co-author on this paper.

Abstract

Plastic scintillators have uses in many fields including defense, high energy physics, health physics, and space applications. In recent years, work has been done to enhance a variety of plastic scintillator properties. These enhancements have largely targeted an increase of the intrinsic gamma efficiency, photopeak efficiency, mechanical robustness, the neutron pulse shape discrimination (PSD) figure of merit, and/or the timing resolution. This body of work seeks to examine these solutions both in a general radiation detection context and in the context of using the plastic scintillator as a frame component of a given detector system; in this work a hypothetical unmanned aerial vehicle (UAV) is used for guiding questions. This examination was accomplished through a series of mechanical properties measurements, a range of simulations using GEANT4 and MCNP, and radiation measurements which serve to validate the simulations as well as further characterize both existing and novel plastic scintillators in select configurations. In particular, basic science studies were conducted to understand, quantify, and/or demonstrate: 1) the mechanical properties of the scintillators and trade-offs which may exist when these are enhanced, 2) the effect on the mechanical properties when adding organometallic molecules to select plastic scintillator matrices, 3) the methods by which moduli measurements made with a dynamic mechanical analyzer may be compared to time-domain moduli measurements, 4) methods to simulate the radiation and optical response of plastic scintillators, including nanocomposites, using Geant4, 5) validation of a Geant4 workspace and aforementioned methods, 6) the simulated scale-up of EJ256 and a 24.5 wt/% ytterbium fluoride/PVT nanocomposite scintillator highlighting emergent trade-offs, 7) a method to deconvolve latent x-ray escape peaks from photopeaks in a gamma spectrum towards determining the energy resolution, 8) a python toolkit for

rapidly simulating a mobile detector system, and 9) the Cramer-Rao lower bound on the timing resolution of EJ232Q in multiple sizes and configurations.

Table of Contents

1 Introduction **1**

1.1 Background . . . 3

1.2 Radiation and Matter . . . 5

1.2.1 Directly Ionizing Radiation . . . 7

1.2.2 Indirectly Ionizing Radiation . . . 13

1.3 Scintillators . . . 25

1.3.1 Inorganic Scintillators . . . 28

1.3.2 Organic Scintillators . . . 32

1.3.3 High-Z Loaded Organic Scintillators . . . 40

1.4 Photomultiplier Tubes . . . 42

1.5 Regarding the Material Properties of Polymers . . . 47

1.6 Original Contributions . . . 50

2 Mechanical and Light Yield Measurements of Select Plastics **52**

2.1 Abstract . . . 52

2.2 Introduction . . . 53

2.3 Materials and Methods . . . 55

2.3.1 Tensile Testing . . . 55

2.3.2 Flexural Testing . . . 59

2.3.3 Light Output Testing . . . 60

2.3.4 Dynamic Mechanical Analysis . . . 63

2.4 Results and Discussion . . . 65

2.4.1 Tensile Testing Results . . . 65

2.4.2 Flexural Testing Results . . . 70
2.4.3 Results of Light Output Testing . . . 72
2.4.4 Dynamic Mechanical Analysis Results . . . 75
2.5 Conclusion . . . 77
2.6 Acknowledgments . . . 79

3 Optical Surface Model Selection in GEANT4 for High Aspect Ratio EJ-200 81

3.1 Abstract . . . 81
3.2 Introduction . . . 82
3.3 Methodology . . . 86
3.3.1 Photomultiplier Tube Calibration . . . 86
3.3.2 Experiments with EJ200 Bars . . . 92
3.3.3 Optical Simulation of EJ200 Bars . . . 99
3.4 Results and Discussion . . . 108
3.4.1 Photomultiplier Tube Calibration . . . 108
3.4.2 Spectrophotometry Results . . . 110
3.4.3 Comparison of Experiments and Simulations . . . 110
3.5 Conclusion . . . 117
3.6 Acknowledgements . . . 117

4 Validation of a GEANT4 Application for Light Transport in High-Z Loaded Plastics 119

4.1 Abstract . . . 119
4.2 Introduction . . . 120
4.3 Methodology . . . 122
4.3.1 Experiments with EJ256 5% Pb . . . 123
4.3.2 Simulation Design . . . 123
4.3.3 Material Scale Up Study . . . 135
4.4 Results and Discussion . . . 135
4.4.1 Validation with EJ256 5% Pb . . . 135

4.4.2 Validation with YbF_3 Nanocomposites . . . 137
4.4.3 Effects of Gradual Scale-Up . . . 144
4.5 Conclusion . . . 155
4.6 Acknowledgments . . . 156

5 Additional Supported Studies **158**
5.1 Abstract . . . 158
5.2 A Method for Deconvolving the x-ray Fluorescence Escape Peak in Gamma Pulse Height Spectra . . . 159
5.2.1 Introduction . . . 159
5.2.2 Photopeak Deconvolution Model . . . 160
5.2.3 Demonstration of Deconvolution Method . . . 163
5.2.4 Conclusion . . . 169
5.3 A Python Program for Rapid Simulation of Mobile Gamma/Neutron Detectors 169
5.3.1 Introduction . . . 169
5.3.2 Program Description . . . 170
5.3.3 Program Demonstration . . . 174
5.3.4 Conclusion . . . 178
5.4 Conclusion of Additional Studies . . . 178

6 Conclusion and Final Remarks **179**
6.1 Dissertation Conclusion . . . 179
6.2 Future Work . . . 181

Bibliography **185**

Appendices **198**
A EJ200 Sample Preparation . . . 199
A.1 Sample Machining . . . 199
A.2 Polishing Procedure . . . 199
B Experimental and Simulated Spectra With EJ200 . . . 202
C Cramer Rao Lower Bound on the Timing Resolution of EJ232Q . . . 211

C.1 Introduction 211
C.2 Methodology 213
C.3 Results 218
C.4 Discussion 218
C.5 Conclusion 242
C.6 Acknowledgments 242

Vita **244**

List of Tables

2.1 Selected materials for mechanical and light output testing. 56
2.2 Mechanical Testing Parameters 58
2.3 Results from Mechanical and Light Output Testing 74

3.1 Material definition for EJ200. 101
3.2 Material definition for optical grease (Polydimethylsiloxane). 101
3.3 Material definition for fused silica. 101
3.4 Sellmeier coefficients for optical dispersion relations. 103
3.5 Optical surface parameters used in GEANT4 simulations. Reflectivity applies to both LUT and *unified* models. 103

4.1 Material definition for EJ256. 128
4.2 Material definitions for YbF_3 nanocomposites. 130

5.1 Description and valuation of fitting parameters. 164
5.2 Material definitions for MCNP simulation of liquid HfO_2 nanocomposite. . . 165
5.3 MCNP Calculated parameters for describing the K-series escape peak. 167
5.4 Final results from fitting algorithm. 168

List of Figures

1.1 Project timeline 2
1.2 UAV concept 4
1.3 Radiation in matter 6
1.4 Bragg curve 9
1.5 Alpha and beta tracks 11
1.6 Photon Reactions and Mass Attenuation Coefficients 15
1.7 Compton scattering 17
1.8 Klein-Nishina Distribution 19
1.9 Neutron Cross Sections for ^{1}H and C 21
1.10 Neutron elastic scattering maximum fractional energy transfer 23
1.11 Creation and collection of scintillation light 26
1.12 Inorganic scintillator band structure 30
1.13 Organic scintillator molecular energy band structure 34
1.14 Jablonski diagram showing singlet and triplet molecular energy states 35
1.15 Absorption and emission for a ternary organic system 38
1.16 Diagram: Linear focused photomultiplier tube 44
1.17 R2059 Photomultiplier tube radiant sensitivity and quantum efficiency . . . 46
1.18 Spring and dashpot models 49

2.1 Conceptual drawing of the UAV concept with a plastic scintillator airframe. 54
2.2 Boxplot of the maximum tensile stress (MPa) of the tested materials shown alongside average PLA and ABS values. 67

2.3 Boxplot of the tensile modulus of elasticity (GPa) of the tested materials shown alongside average PLA and ABS values. 67
2.4 Comparing extensometer strain output with caliper measurements 69
2.5 Boxplot of the maximum flexural stress (MPa) of the tested materials shown alongside average PLA and ABS values. 71
2.6 Boxplot of the flexural modulus of elasticity (GPa) of the tested materials shown alongside average PLA and ABS values. 71
2.7 Locating the Compton edge and Compton edge location for all samples . . . 73
2.8 Measured storage modulus of PVT and PS over frequencies from 0.1 Hz - 10Hz 76
2.9 Aggregated storage modulus values vs. frequency for PVT and PS 78
2.10 Boxplot of the flexural modulus, DMA modulus, and storage modulus measured for PVT and PS 78

3.1 Diagram of the *unified* model implementation of the dielectric-dielectric surface type with the backpainted finish 84
3.2 Diagram of the LUT-LBNL surface model implementation 85
3.3 Block diagram for PMT calibration 88
3.4 Single photoelectron spectrum for the R2059 PMT using the mean of the first 10 samples in data window for baseline subtraction 90
3.5 Single photoelectron spectrum for the R2059 PMT using the location of the maximum bin of the histogrammed 10-point moving average value for baseline subtraction. 90
3.6 Frequency distribution of the MA baseline ADC values 91
3.7 EJ200 samples with teflon, TiO2, or foil reflectors 94
3.8 Block diagram for EJ200 light output study 95
3.9 Fresnel reflection in spectrophotometry experiments 97
3.10 Luminescence spectrum of EJ200 with respect to wavelength 102
3.11 Luminescence spectrum of EJ200 with respect to energy 102
3.12 Refractive indices of simulated optical media with respect to wavelength . . 104
3.13 Refractive indices of simulated optical media with respect to energy 104

3.14 Diagram of the basic detector schema used in the light output simulations . 106
3.15 Photocathode reflectivity, quantum efficiency, and G4 efficiency with respect to energy . . . 106
3.16 ROOT data file structure for EJ200 light output simulation studies 107
3.17 The deconvolved single photoelectron spectrum for the R2059 PMT operated at -2200V. . . . 109
3.18 Frequency distribution of Cs-137 photopeak locations for mapping PMT calibration values to the integrated charge axis . . . 109
3.19 The measured optical transmittance of EJ200 . . . 111
3.20 Optical absorption lengths of EJ200 . . . 111
3.21 Comparison of the experimental and simulated Cs-137 Compton edge location with cylindrical EJ200 and varied optical reflectors . . . 113
3.22 Comparison of the experimental and simulated Cs-137 Compton edge location with rectangular EJ200 and varied optical reflectors . . . 114
3.23 Comparison of the experimental and simulated Cs-137 Compton edge location with hexagonal EJ200 and varied optical reflectors . . . 115

4.1 Diagram of spectrophotometry experiment simulation . . . 125
4.2 Simulated spectrophotometer beam spot . . . 125
4.3 Distribution of initial simulated spectrophotometer photon wavelengths . . . 126
4.4 Simulated reference spectrophotometry transmission distribution vs wavelength 126
4.5 Optical absorption lengths of EJ256 . . . 128
4.6 Luminescence spectrum of EJ256 5% Pb with respect to wavelength . . . 129
4.7 Luminescence spectrum of EJ256 5% Pb with respect to energy . . . 129
4.8 Calculated Rayleigh scattering lengths in YbF_3 nanocomposites . . . 132
4.9 Radioluminescence spectrum of the YbF_3 nanocomposites with respect to wavelength . . . 133
4.10 Radioluminescence spectrum of the YbF_3 nanocomposites with respect to energy 133
4.11 Optical absorption lengths in YbF_3 nanocomposites . . . 134
4.12 Comparison of measured and simulated EJ256 spectrophotometry data . . . 136

4.13 Comparison of measured and simulated Cs-137 spectrum taken with 2x2 inch EJ-256 5 wt/% Pb . . . 138
4.14 Simulated response for a 2x2 inch EJ-256 5 wt/% Pb detector . . . 139
4.15 Comparison of experimental and simulated YbF_3 nanocomposite spectrophotometry data . . . 141
4.16 Comparison of measured and simulated Cs-137 spectra taken with YbF_3 nanocomposites . . . 142
4.17 Simulated spectra using EJ-256 5 wt/% Pb in three different lengths . . . 146
4.18 Changes in the simulated response of EJ256 for different scintillator lengths . 147
4.19 Simulated observables under gradual scale up of EJ256 . . . 148
4.20 Simulated spectra using the 24.5 wt/% YbF_3 nanocomposite in three different lengths . . . 150
4.21 Changes in the simulated response of the 24.5 wt/% YbF_3 nanocomposite for different scintillator lengths . . . 151
4.22 Simulated observables under gradual scale up of the 24.5 wt/% YbF_3 nanocomposite . . . 152
4.23 Simulated Cs-137 spectrum with a scaled up 24.5 wt/% YbF_3 nanocomposite 154
4.24 Simulated response of a scaled up 24.5 wt/% YbF_3 nanocomposite . . . 154

5.1 Simulated pulse height tally and fitted x-ray escape peak . . . 167
5.2 Peak deconvolution results from both experiments . . . 168
5.3 Diagram of an interval in the RadSource class paradigm . . . 171
5.4 Class diagram showing the relationship of the package classes with main . . 175
5.5 Drone measurement points along path and a 2D histogram showing the counts at those points . . . 177
5.6 Gamma counts in the interval for the grid search and the attenuator demonstration . . . 177

A.1 End milling of the EJ200 samples . . . 200
B.1 Aggregation of experimental Cs-137 spectra taken with cylindrical EJ200 and varied optical reflectors . . . 203

B.2 Aggregation of experimental Cs-137 spectra taken with rectangular EJ200 and varied optical reflectors 204
B.3 Aggregation of experimental Cs-137 spectra taken with hexagonal EJ200 and varied optical reflectors 205
B.4 Aggregation of simulated Cs-137 spectra taken with cylindrical EJ200 and varied optical reflectors using the *unified* surface model 206
B.5 Aggregation of simulated Cs-137 spectra taken with rectangular EJ200 and varied optical reflectors using the *unified* surface model 207
B.6 Aggregation of simulated Cs-137 spectra taken with hexagonal EJ200 and varied optical reflectors using the *unified* surface model 208
B.7 Aggregation of simulated Cs-137 spectra taken with cylindrical EJ200 and varied optical reflectors using the LUT-LBNL surface model 209
B.8 Aggregation of simulated Cs-137 spectra taken with rectangular EJ200 and varied optical reflectors using the LUT-LBNL surface model 210
C.1 Comparison of measured and simulated 511 keV gamma spectrum taken with EJ232Q. RESOLUTIONSCALE was set to 2.976 214
C.2 The emulated PMT pulse with and without Gaussian noise 217
C.3 Comparison of the experimental and emulated PMT pulse height spectrum . 217
C.4 Energy window for accepted events and frequency distribution of the pick off time for the 10mm sample under front irradiation 219
C.5 Fit of the time pick off distributions for the 10mm sample under front irradiation 219
C.6 Frequency distributions and covariance matrix of the ordered photon arrival times for the 10mm sample under front irradiation 220
C.7 The calculated CRLB vs. first i arrival times used in its calculation. Data is for the 10mm sample under front irradiation 220
C.8 Energy window for accepted events and frequency distribution of the pick off time for the 10mm sample under side irradiation 221
C.9 Fit of the time pick off distributions for the 10mm sample under side irradiation 221
C.10 Frequency distributions and covariance matrix of the ordered photon arrival times for the 10mm sample under side irradiation 222

C.11 The calculated CRLB vs. first i arrival times used in its calculation. Data is for the 10mm sample under side irradiation 222
C.12 Energy window for accepted events and frequency distribution of the pick off time for the 25mm sample under front irradiation 223
C.13 Fit of the time pick off distributions for the 25mm sample under front irradiation 223
C.14 Frequency distributions and covariance matrix of the ordered photon arrival times for the 25mm sample under front irradiation 224
C.15 The calculated CRLB vs. first i arrival times used in its calculation. Data is for the 25mm sample under front irradiation 224
C.16 Energy window for accepted events and frequency distribution of the pick off time for the 25mm sample under side irradiation 225
C.17 Fit of the time pick off distributions for the 25mm sample under side irradiation 225
C.18 Frequency distributions and covariance matrix of the ordered photon arrival times for the 25mm sample under side irradiation 226
C.19 The calculated CRLB vs. first i arrival times used in its calculation. Data is for the 25mm sample under side irradiation 226
C.20 Energy window for accepted events and frequency distribution of the pick off time for the 50mm sample under front irradiation 227
C.21 Fit of the time pick off distributions for the 50mm sample under front irradiation 227
C.22 Frequency distributions and covariance matrix of the ordered photon arrival times for the 50mm sample under front irradiation 228
C.23 The calculated CRLB vs. first i arrival times used in its calculation. Data is for the 50mm sample under front irradiation 228
C.24 Energy window for accepted events and frequency distribution of the pick off time for the 50mm sample under side irradiation 229
C.25 Fit of the time pick off distributions for the 50mm sample under side irradiation 229
C.26 Frequency distributions and covariance matrix of the ordered photon arrival times for the 50mm sample under side irradiation 230
C.27 The calculated CRLB vs. first i arrival times used in its calculation. Data is for the 50mm sample under side irradiation 230

C.28 Energy window for accepted events and frequency distribution of the pick off time for the 75mm sample under front irradiation 231
C.29 Fit of the time pick off distributions for the 75mm sample under front irradiation 231
C.30 Frequency distributions and covariance matrix of the ordered photon arrival times for the 75mm sample under front irradiation 232
C.31 The calculated CRLB vs. first i arrival times used in its calculation. Data is for the 75mm sample under front irradiation 232
C.32 Energy window for accepted events and frequency distribution of the pick off time for the 75mm sample under side irradiation 233
C.33 Fit of the time pick off distributions for the 75mm sample under side irradiation 233
C.34 Frequency distributions and covariance matrix of the ordered photon arrival times for the 75mm sample under side irradiation 234
C.35 The calculated CRLB vs. first i arrival times used in its calculation. Data is for the 75mm sample under side irradiation 234
C.36 Energy window for accepted events and frequency distribution of the pick off time for the 100mm sample under front irradiation 235
C.37 Fit of the time pick off distributions for the 100mm sample under front irradiation 235
C.38 Frequency distributions and covariance matrix of the ordered photon arrival times for the 100mm sample under front irradiation 236
C.39 The calculated CRLB vs. first i arrival times used in its calculation. Data is for the 100mm sample under front irradiation 236
C.40 Energy window for accepted events and frequency distribution of the pick off time for the 100mm sample under side irradiation 237
C.41 Fit of the time pick off distributions for the 100mm sample under side irradiation 237
C.42 Frequency distributions and covariance matrix of the ordered photon arrival times for the 100mm sample under side irradiation 238
C.43 The calculated CRLB vs. first i arrival times used in its calculation. Data is for the 100mm sample under side irradiation 238

C.44 The calculated CRLB vs. scintillator length for front and side modes of irradiation 239
C.45 The FWHM of the frequency distribution of the pick off times using the emulated PMT pulse and CFD fraction of 0.3 239

Chapter 1

Introduction

The body of research contained in this document is meant to serve as a response to the Defense Threat Reduction Agency's call for Fundamental Research to Counter Weapons of Mass Destruction (C-WMD). It is specifically intended that this research support DTRA's Basic and Applied Sciences Department (J9-BA) by targeting **Thrust Area 1:** "Science of WMD Sensing and Recognition" and **Topic G3:** "Robust Organic Scintillators and Algorithms to Advance Autonomous Radionuclide (RN) Search". Due to the multitude of subtopics which may fall into this primary topic, a collaboration consisting of three departments from two universities has been assembled. The development and basic characterization of the new plastic scintillators has been carried out by Professor Qibing Pei's group within the Materials Science and Engineering Department at the University of California, Los Angeles. Further characterization and performance predictions of these new materials, in addition to some materials which are commercially available, has been performed by Professor Jason Hayward's group within the Nuclear Engineering Department at the University of Tennessee, Knoxville. The development and testing of various algorithms useful for autonomous RN search has been advanced by Professor Hairong Qi's group within the Electrical Engineering and Computer Science Department at the University of Tennessee, Knoxville. The general tasks and associated timelines are outlined in Figure 1.1.

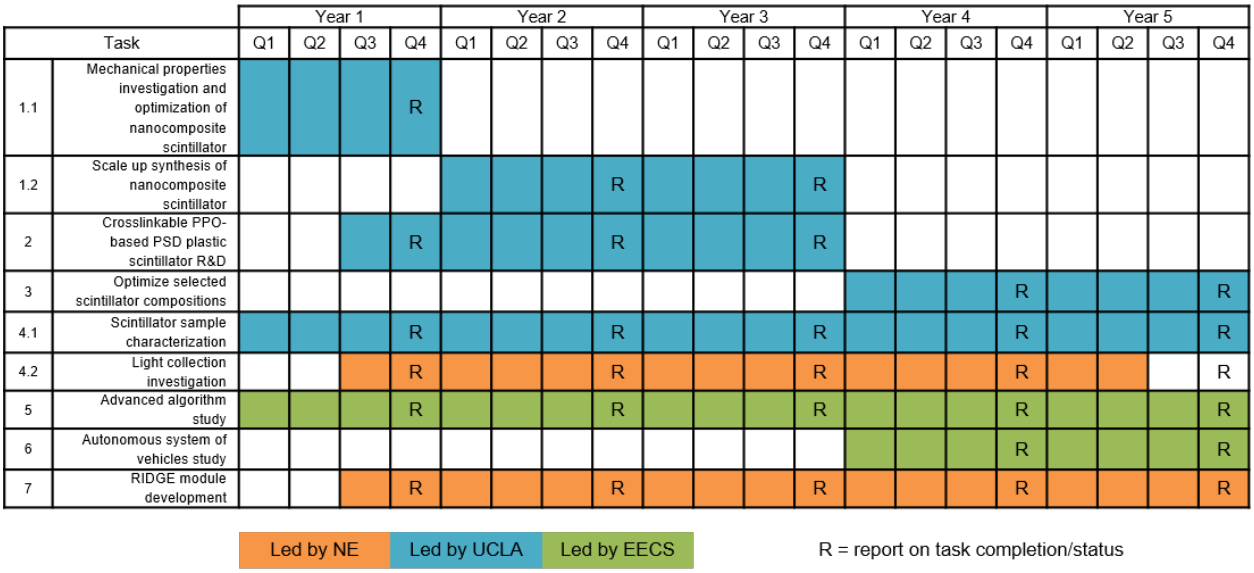


Figure 1.1: Timeline of task completion. Year 1 begins January, 2018. Years 4 and 5 are option years which did not receive funding.

1.1 Background

For conceptual and illustrative purposes, consider that the mobile platform utilized for the autonomous RN search is a moderately sized quadrotor drone (UAV) in an "X" configuration. In recent years, it has been demonstrated that moderately sized UAVs can be operated by algorithms which allow them to race in an indoor environment and even avoid obstacles [1, 2]. In many cases though, the algorithms used for autonomous racing drones utilize an ad hoc approach in which they search for a particular "checkpoint" or "goal" that is built as part of the racing stage or as part of the UAV's patrol path [3]. In general indoor applications, these "checkpoints" will not be present to assist with path planning. Other more general approaches to machine vision and path planning have been reported on in the literature. Some examples rely on assisted mapping of the environment as in [4], while others are completely autonomous, generating both a map of the environment and a flight path [5–7]. However, due to the computational requirements for data processing, both [5] and [6] send data to be processed to an off-board CPU. In [7], wireless connections are completely avoided by implementing an RGB-D camera used in conjunction with a 1.86-GHz Core Duo processor and 4-GB of RAM. These added onboard sensing and computational requirements though, can have an undesirable effect on the flight time due to added taxation on the system power reserves.

In anticipation of limited UAV power resources when performing autonomous indoor RN searches, the air frame of the UAV may be replaced with plastic scintillator thus removing the need to carry an additional radiation detector while simultaneously increasing the UAV's sensitivity to radiation. This concept is illustrated in Figure 1.2.

The idea of using UAVs to detect radioisotopes is not a new idea. As early as 2011, the initial development phase of a UAV for indoor RN detection is highlighted in [8]. In the described design, the drone must be provided a path and uses a vision-based localization algorithm to estimate its position which is then used as the feedback mechanism for staying on the desired path. The radiation detection equipment consisted of a small CZT crystal and a modified GAMPIX [9] gamma camera. This paper did not report on the performance of the system as a whole, but only on the individual components. Of particular note is that

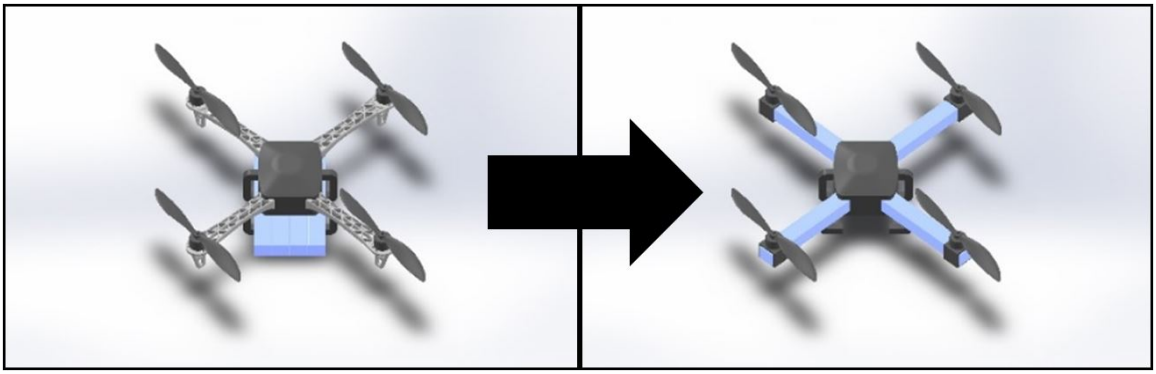


Figure 1.2: UAV concept of replacing the standard air frame with scintillating material (blue) [16].

this system is the only UAV radiation detection system reported in the literature with an indoor application design basis. Other standard UAV systems have been designed for use in large outdoor areas such as those in [10–13] while some others are based on an unmanned helicopter airframe which can carry much larger payloads [14, 15].

Even though the use of UAV's for radiation detection applications is not a new idea, this work does include some conceptualizations and related newly-discovered understandings which may be helpful in aiding and furthering such an endeavor. Some of the new ideas and accomplishments related to this work include: (1) integrating radiation-sensitive material as a part of the UAV airframe or other mobile/stationary platforms (2) designing algorithms to allow for fully onboard autonomous radiation search in an indoor environment (3) creating new scintillating materials which may be suitable for integration into a UAV and (4) characterizing these new materials such that others may understand the potential benefits and drawbacks associated with utilizing these materials for a given detector system design. The primary focus of the work contained herein, though, lies in item (4). The goal of the subsequent sections is to develop an understanding of the underlying physics and mechanisms of radiation detection with scintillating materials in addition to the mechanical properties of plastics as they relate to plastic scintillators.

1.2 Radiation and Matter

Radiation, for the purposes of this manuscript, arises from an atom or through nuclear processes and can be broken down into two distinct categories: **directly ionizing** radiation and **indirectly ionizing** radiation. Directly ionizing radiation generally describes charged particles such as betas (electrons & positrons), muons, or heavy charged particles like alphas, protons, or nuclei from fission fragments which ionize matter directly via Coulombic interactions. On the other hand, indirectly ionizing radiation generally describes neutral particles such as photons, neutrons, or neutral pions, which ionize matter via charged particle secondaries. In either case, when radiation interacts with matter it may deposit some or all of its energy into the host material as depicted in Figure 1.3. Radiation detectors operate on

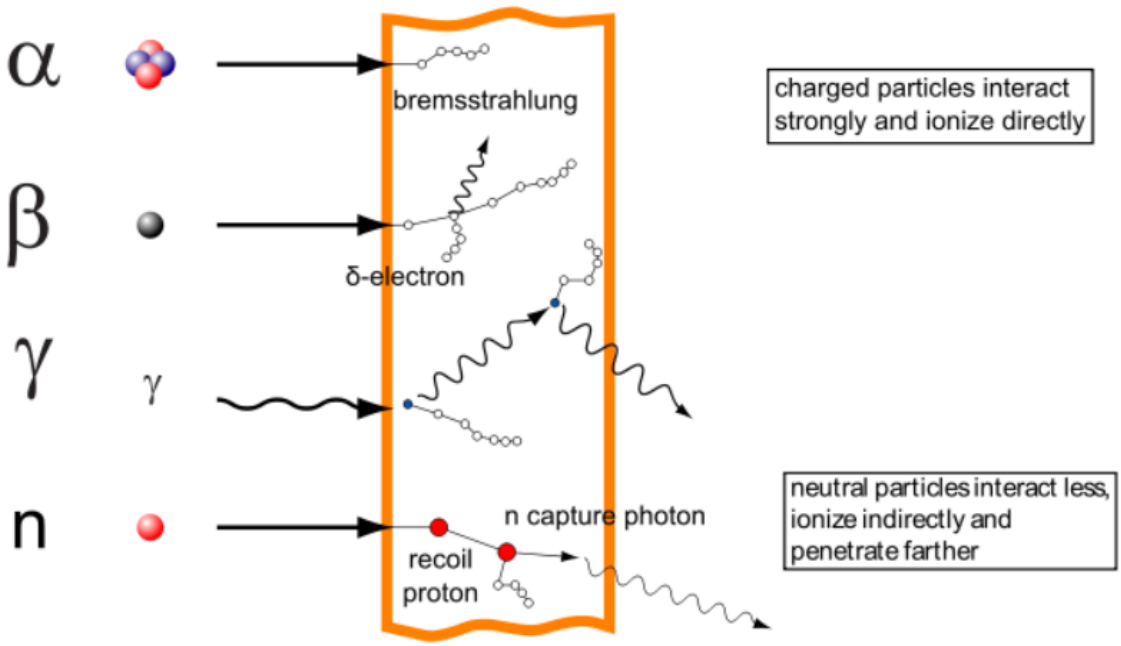


Figure 1.3: A limited depiction of various types of radiation interacting with matter. Graphic modified by the author. Used in accordance with the Creative Commons License. [17]

the premise that in the right environment or material, this deposited energy can be detected via various energy transfer and amplification mechanisms.

1.2.1 Directly Ionizing Radiation

Some forms of radiation ionize the constituents of the target material directly through Coulombic interactions with the electrons contained within the electron shells surrounding the nuclei of the target material. Since the target atoms are generally ionized via Coulombic forces, it follows that directly ionizing radiation must contain some electrical charge. This stipulation is what generally limits directly ionizing radiation to Beta particles (electrons and positrons), alpha particles (physically identical to a Helium nucleus), muons, protons, deuterons, tritons, and other heavy charged particles. Since the Coulomb interaction has no limitation on its range, directly ionizing radiation interacts with all the nearby electrons in the target material concurrently and continuously. As the radiation particle interacts with the orbital electrons, energy is imparted to the electrons. If only a little energy is provided, the electron may only be raised into an excited state. However, if enough energy is imparted, an amount known as the ionization potential, then the electron may become completely unbound and thereby leave behind an ionized atom.

Due to the fact that beta particles (electrons and positrons) behave quite differently in matter than the much larger (more than 1,000 X's) alpha particles, protons, and other nuclei, which together are classified as **heavy charged particles**, a different subsection will be dedicated to each of these types of radiation. Do note that the following review is not meant to be exhaustive on this subject but merely present the material and concepts needed to understand the "whys" behind most of the decisions made to guide the direction of this body of research. For a more complete review and references to articles which present significantly more depth on the subject, the curious and interested reader should see [18, 19].

Heavy Charged Particles

Heavy charged particles are generally considered to be any energetic and charged radiation which has a mass of 1 a.m.u. or greater [18]. It should be noted that some references refer to

a charged particle with a mass larger than an electron (or positron) as being a heavy charged particle [19], but since we are not giving any consideration to the interaction of traditional "mesons" such as muons (which are now classified as leptons in the standard model), either definition will work well in an operational sense for this manuscript.

The energy lost by heavy charged particles as they travel through matter can be described mathematically by the Bethe formula which was first derived by H.A. Bethe in [20]. The classical expression for the energy loss is provided in Equation 1.1 as shown in [18].

$$-\frac{\mathrm{d}E}{\mathrm{d}x} = \frac{4\pi k_0^2 e^4 z^2}{m_e v^2} NB \tag{1.1}$$

where

$$B \equiv Z\left[\ln\frac{2m_e v^2}{I} - \ln\left(1-\beta^2\right) - \beta^2\right] \tag{1.2}$$

In these equations, v and z are the velocity and charge of the primary particle, β is the ratio of the particle's velocity to the speed of light $\left(\frac{v}{c}\right)$, e and m_e are the unit charge and rest mass of an electron, k_0 is the Coulomb constant $(8.99 \times 10^9 N \cdot m^2 \cdot C^{-2})$, while N and Z are the number density and atomic number of the target atoms, and finally I is the average ionization potential of the target material. Upon examination of the Bethe formula, it is clear that the energy lost by the incident radiation per unit path length increases with the charge of the particle, and the atomic number and number density of the target material while it decreases with the speed of the particle and the average ionization potential of the target material. For a given heavy charged particle incident upon a given target material, all values are constant except for the speed of the particle. As the particle slows down the energy lost per unit path length increases, this leads to formation of what is known as the Bragg peak in the stopping power curve and is illustrated in 1.4. This behavior leads to the majority of the deposited energy, or dose, from a heavy charged particle to be located near its stopping point at the Bragg peak.

Other characteristics of note for heavy charged particles are energy straggling and range straggling. Both of these features arise from the stochastic nature of the interactions with the target material on an atomic level. The end result is that if a parallel beam of monoenergetic

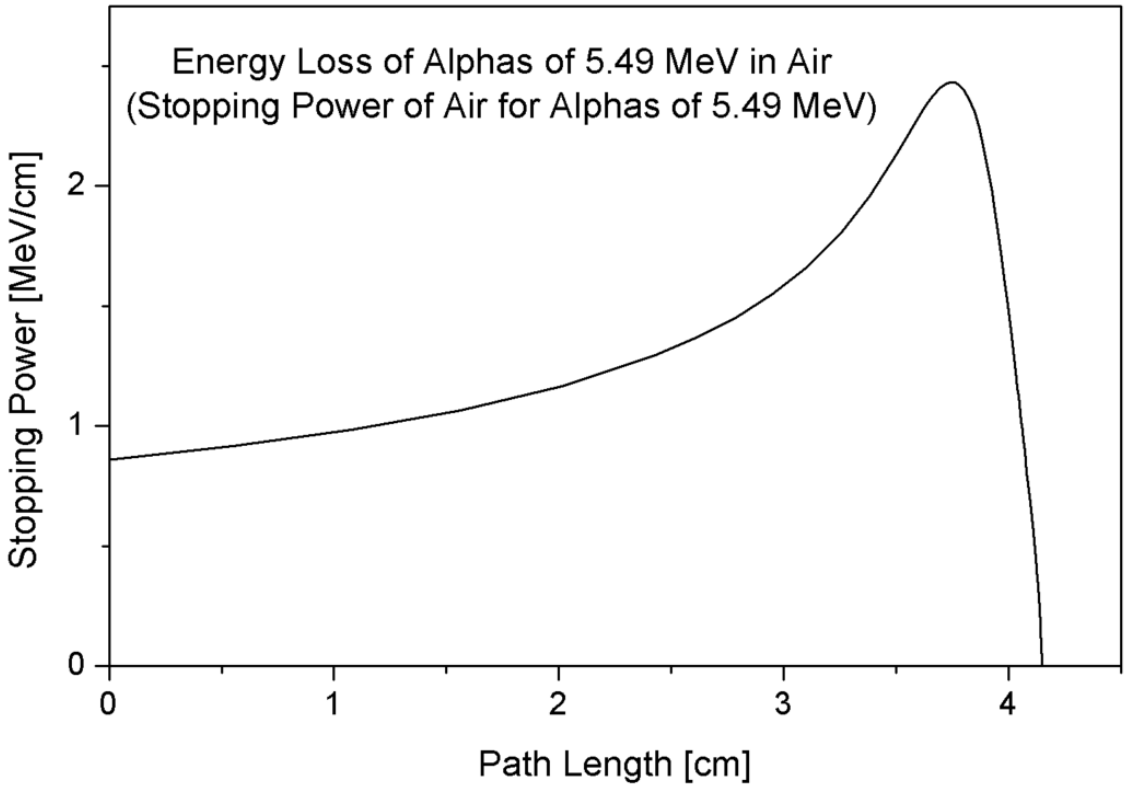


Figure 1.4: Energy loss curve for a heavy charged particle illustrating the Bragg peak.

heavy charged particles is passed through a slab of target material, the outgoing beam will no longer be monoenergetic, but will instead contain particles with a distribution of energies. Transforming this idea to the quantity of range, it follows that if a parallel beam of monoenergetic particles enter into a target and stop at some distance, R, all particles will not stop at the same R but will stop following a distribution about the mean value of R.

Beta Particles

Beta particles consist of electrons (β^-) and positrons (β^+) which are emitted from the nucleus of an atom via weak nuclear force processes. In terms of kinematics within a material, they behave identically to electrons from other sources. Compared to heavy charged particles, beta particles move quite erratically inside a material as demonstrated in Figure 1.5b. Because of this, the average range of an ensemble of beta particles is greater than the average penetration depth. There is no analytical equation for the range and penetration depth of betas in a target material, though some empirical formulas do exist. Because of this, these quantities are best modeled with a Monte Carlo approach, perhaps with codes such as MCNP or GEANT4.

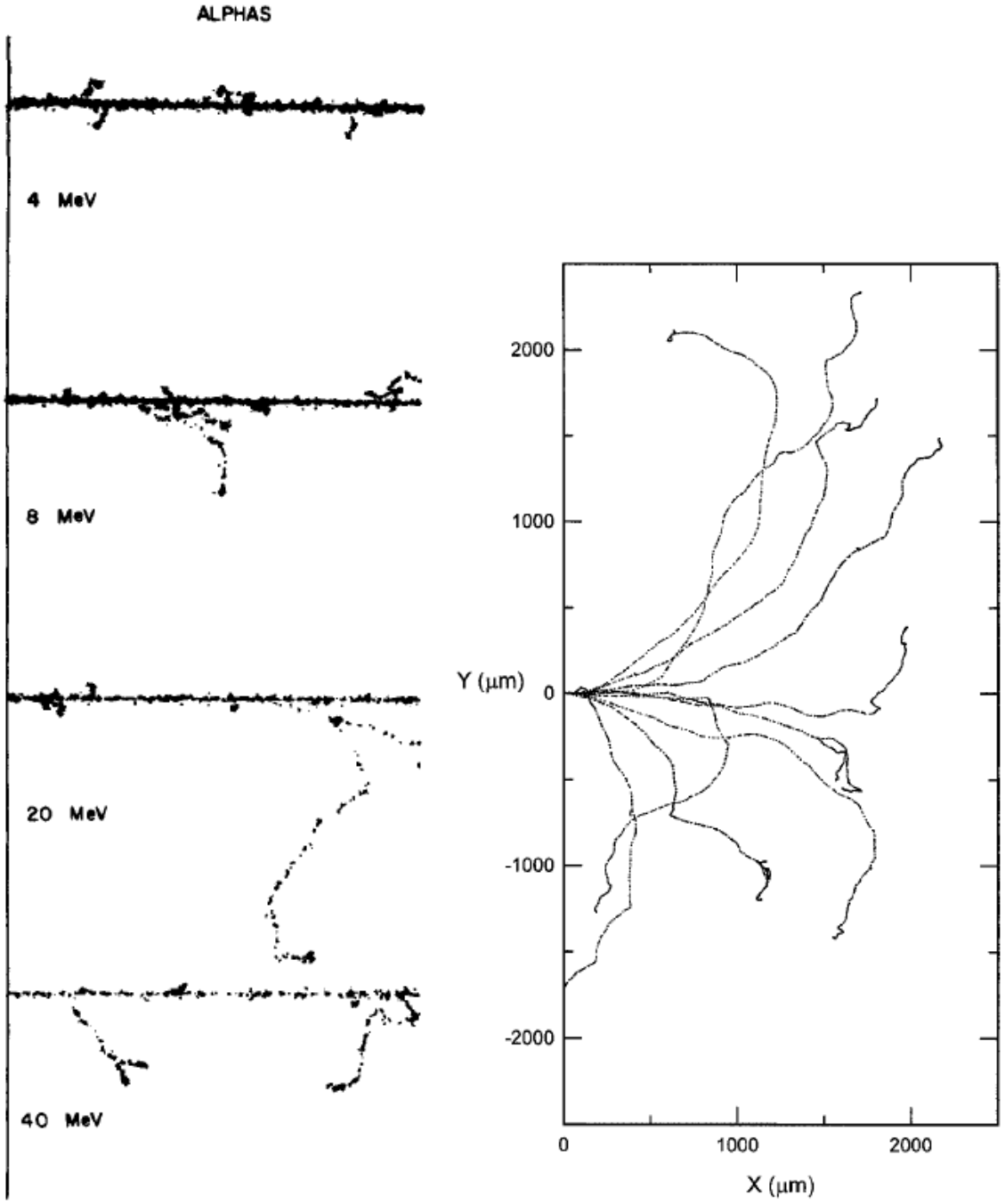
Energy loss from betas occurs through two distinct mechanisms. Much like heavy charged particles, betas can lose energy through Coulombic interactions which result in ionization or excitation of the atoms in the target material; this is referred to as **collisional energy loss**. The second energy loss mechanism occurs when the beta particle abruptly changes direction which produces bremsstrahlung radiation (high energy photons); this is referred to as **radiative energy loss**. This results in a two-term equation for the total stopping power which is shown in Equation 1.3.

$$\left(-\frac{\mathrm{d}E}{\mathrm{d}x}\right)^{\pm}_{tot} = \left(-\frac{\mathrm{d}E}{\mathrm{d}x}\right)^{\pm}_{col} + \left(-\frac{\mathrm{d}E}{\mathrm{d}x}\right)^{\pm}_{rad} \tag{1.3}$$

where

$$\left(-\frac{\mathrm{d}E}{\mathrm{d}x}\right)^{\pm}_{col} = \frac{4\pi k_0^2 e^4}{m_e v^2} ZN \left[\ln \frac{m_e c^2 \tau \sqrt{\tau+2}}{\sqrt{2}I} + F^{\pm}(\beta)\right] \tag{1.4}$$

and the approximate relationship to the radiative energy loss for electrons is:



(a) **(b)**

Figure 1.5: **(a)** Calculated track segments ($0.7\mu m$) of alpha particles in water, tracks are straight with spurious delta rays (secondary electrons). **(b)** Calculated tracks (projected into the X–Y plane of the figure) of ten $740 - keV$ electrons entering a water slab normally from the left at the origin. One electron is seen to be scattered back out of the slab. [19]

$$\left(-\frac{\mathrm{d}E}{\mathrm{d}x}\right)^{-}_{rad} = \frac{ZE}{800}\left(-\frac{\mathrm{d}E}{\mathrm{d}x}\right)^{-}_{col} \tag{1.5}$$

The correction formulas for electrons and positrons needed for a full description of Equation 1.4 are shown in Equations 1.6 and 1.7.

$$F^{-}(\beta) = \frac{1-\beta^2}{2}\left[1 + \frac{\tau^2}{8} - (2\tau+1)\ln 2\right] \tag{1.6}$$

$$F^{+}(\beta) = \ln 2 - \frac{\beta^2}{24}\left[23 + \frac{14}{\tau+2} + \frac{10}{(\tau+2)^2} + \frac{4}{(\tau+2)^3}\right] \tag{1.7}$$

The parameters in the above equations are identical to those in Equations 1.1 and 1.2 with the exception of the addition of τ which is a quantifier of the kinetic energy of the beta particle expressed as the ratio of the beta's kinetic energy to the beta's rest energy $\left(\frac{T}{m_e c^2}\right)$.

One final quantity of importance relating to beta particles is the radiation yield. Unlike Equation 1.5 which expresses the instantaneous radiative stopping power as it relates to the instantaneous collisional stopping power, the radiation yield is the fraction of the total initial energy which goes to radiative losses by the time the beta particle comes to rest. This amount is given approximately for β^- particles in Equation 1.8.

$$Y \cong \frac{6\times 10^{-4} ZT}{1 + 6\times 10^{-4} ZT} \tag{1.8}$$

Where T is the kinetic energy of the electron, which is expressed as $T = E - m_e c^2$. In most cases, it is desirable to avoid production of bremsstrahlung since high energy photons may have quite a significant penetration depth. Analysis of the equation shows that if one is to reduce bremsstrahlung production from high energy betas, use of a low-Z material would be ideal until the beta is brought to a sufficiently low energy at which point higher-Z materials may be used. In some cases, such as in the production of x-rays for imaging or experimental purposes, bremsstrahlung is intentionally produced by shooting a high-Z target (usually tungsten) with high energy electrons.

1.2.2 Indirectly Ionizing Radiation

Indirectly ionizing radiation consists of neutral particles and as such it does not ionize atoms directly through Coulombic interactions. Instead, the ionization only occurs after the neutral particle interacts via electromagnetic or nuclear processes and then produces a charged secondary particle as a result of this interaction. The charged secondary particle then behaves identically to those mentioned in Subsection 1.2.1, causing ionization and excitation of the target material's atoms. Since indirectly ionizing radiation is uncharged, it may penetrate quite far into matter before an interaction occurs. This is distinctly different from directly ionizing radiation which is always interacting with the material around it and losing energy along every infinitesimal step. Because of this, energy loss equations like those presented in Equations 1.1 and 1.3 are not a possibility for indirectly ionizing radiation. Instead, the computations of quantities like energy loss, energy transfer, interaction lengths, and reaction rates are all done probabilistically and are rooted in a quantity referred to as a **cross section**.

Cross sections can be categorized as either microscopic or macroscopic. A microscopic cross section is used to describe the cross section of a single atom and is usually given in **barns**, (1 barn = $10^{-24} cm^2$). This quantity can be used to derive a macroscopic cross section which is used to describe an entire material given the atomic constituents and density. The macroscopic cross section, also called the attenuation coefficient, is usually provided in units of cm^{-1}. The inverse of the macroscopic cross section is the average distance a particle must travel before it has a $1/e$ probability of undergoing the particular interaction described by the cross section within the host material, this distance is referred to as the interaction length. The subject of cross sections is enormous as the cross section varies with the types and energies of the particles involved as well as the reaction mechanism/type; the total possible number of combinations of these values is nearly limitless. The following sections will examine interactions by particle type, namely photons (x-rays and gammas) and neutrons.

Photons

For the purposes of this section, photons include electromagnetic wavelets which originate from electrodynamic processes (x-rays and bremsstrahlung) and nuclear processes (gammas). While the origins of x-rays, bremsstrahlung, and gammas differ, their physical nature after birth is identical. Photons may interact with matter on an electronic basis via scattering (coherent and incoherent) or absorption (photoelectric effect) and if the photon energy is high enough, nuclear interactions are also possible (photo-fission and pair-production) as shown in Figure 1.6a. Each of these reaction types involve distinctly different processes and underlying physical mechanisms. As a result the a priori and post interaction states of the photon and any resulting secondaries are also different.

The attenuation coefficient for photons is also energy dependent as demonstrated in Figure 1.6b. It should be noted that the ordinate axis is given as the mass attenuation coefficient, which neglects the material density. However, the general characteristics illustrated in the figure hold true for most materials.

Photoelectric Interaction

In the photoelectric interaction, the incoming photon is absorbed by an atom and an electron is ejected. The direction of the emitted electron is generally along the axis of the photon's electric field. Whereas the energy of the ejected electron is determined by the energy of the photon and the work function of the material involved; this relationship is shown in Equation 1.9 where T_{max} is the maximum energy of the ejected electron and φ is the work function of the material. In general the work function is only a few $(1-8)$ electron-volts .

$$T_{max} = h\nu - \varphi \tag{1.9}$$

The Photoelectric Effect is the dominant interaction for materials with a high effective Z and/or for photons in the lower energy regime ($< 500keV$). The mass attenuation coefficient for the photoelectric effect follows the trend shown in Equation 1.10. In this equation the value $h\nu$ is the energy of the incoming photon, Z_{eff} is the effective atomic number of the material, while n and m are both constants that range in value from $(3-5)$ [21]. It is for this reason that it is often said the probability for the photoelectric effect to occur goes as

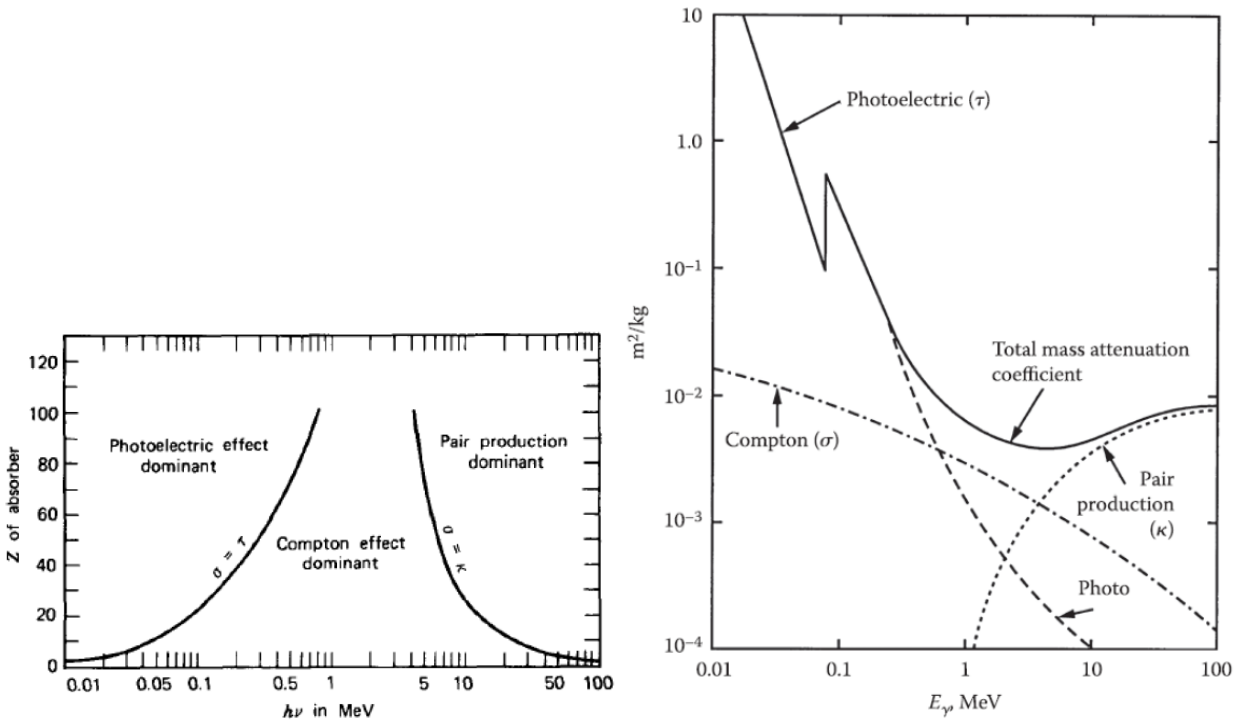


Figure 1.6: **(a)** The relative importance of the three primary photon interactions in a material given the photon energy and Z of the material. **(b)** Mass attenuation coefficients for Lead. [21]

Z^4, which is substantial as a doubling of the Z will result in a 16-times higher probability of photoelectric effect occurrence.

$$\frac{\mu}{\rho} \propto \frac{Z_{eff}^n}{(h\nu)^m} \tag{1.10}$$

Compton Scattering

Compton scattering is the mechanism for the incoherent scattering of a photon off of an atomic electron. The result of this interaction is a change in direction and reduced energy of the photon and a freed electron as shown in Figure 1.7.

Referencing the variables in Figure 1.7, the equations which describe Compton scattering are given in Equations 1.11, 1.12, and 1.13.

$$T_e = h\nu - h\nu' \tag{1.11}$$

$$h\nu' = \frac{h\nu}{1 + \alpha\,(1 - \cos\theta)} \tag{1.12}$$

$$T_e = \alpha \frac{h\nu\,(1 - \cos\theta)}{1 + \alpha\,(1 - \cos\theta)} \tag{1.13}$$

where

$$\alpha = \frac{h\nu}{m_e c^2} \tag{1.14}$$

The maximum scattered electron energy as a function of θ, which corresponds to the minimum scattered photon energy, occurs when the photon undergoes backscattering. At this point, $\theta = \pi$ and the minimum scattered photon energy is given by Equation 1.15 while the maximum scattered electron energy is shown in Equation 1.16.

$$h\nu_{min} = \frac{h\nu}{1 + 2\alpha} \tag{1.15}$$

$$T_{e,max} = \frac{2\alpha h\nu}{1 + 2\alpha} \tag{1.16}$$

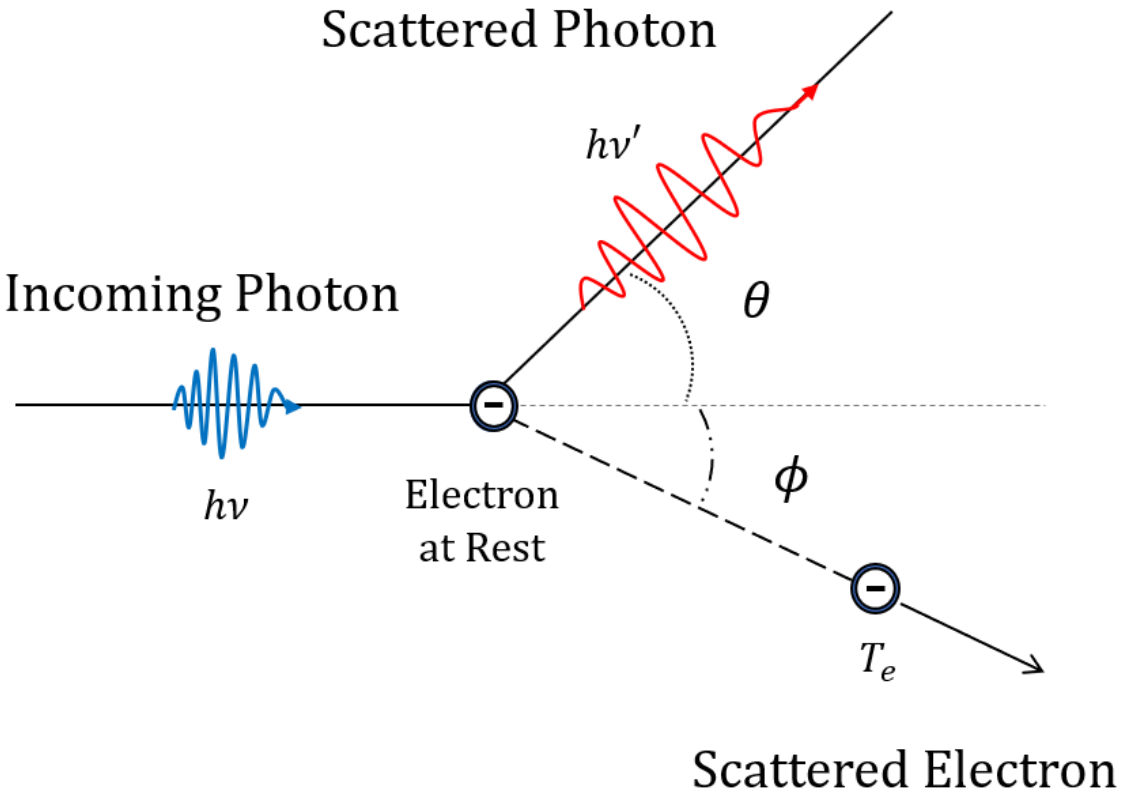


Figure 1.7: Diagram illustrating Compton scattering.

The microscopic scattering cross section for a photon on an electron can be found by integrating the Klein-Nishina formula for the differential scattering cross section [22] which is shown in Equation 1.17.

$$\frac{\mathrm{d}\sigma_{KN}}{\mathrm{d}\Omega} = \frac{1}{2} r_e^2 \left(\frac{\nu'}{\nu}\right)^2 \left[\frac{\nu'}{\nu} + \frac{\nu}{\nu'} - \sin^2\theta\right] \tag{1.17}$$

Where $r_e = 2.8179 \times 10^{-15} m$ is the classical electron radius, which when squared gives $r_e^2 = 7.94 \times 10^{-30} m^2 = 79.4 mBarns$. Substituting Equation 1.12 for ν' into 1.17 and integrating with respect to θ yields the total microscopic scattering cross section which is shown in Equation 1.18. Prior to integration, the differential cross section can be plotted as a function of θ and incoming photon energy ν. This is illustrated in Figure 1.8.

$$\sigma_{KN} = 2\pi r_e^2 \left\{\frac{1+\alpha}{\alpha^2}\left[\frac{2(1+\alpha)}{1+2\alpha} - \frac{1}{\alpha}\ln(1+2\alpha)\right] + \frac{1}{2\alpha}\ln(1+2\alpha) - \frac{1+3\alpha}{(1+2\alpha)^2}\right\} \tag{1.18}$$

The Compton scattering reaction probability increases directly and proportionally with the electron density of the material. Therefore, the mass attenuation coefficient for the Compton interaction increases with the effective-Z of the material, or $\left(\frac{\mu}{\rho}\right)_{compton} \propto Z_{eff}$.

Pair Production and Photonuclear Interactions

At higher photon energies ($> 1.022 MeV$), interactions with atomic nuclei become possible. One of the more common interactions is pair production in which case the photon interacts with the electric field of the nucleus or an orbital electron and is then transformed into a β^- and a β^+ particle. At minimum 1.022 MeV of energy, the mass of the produced particles, is required for this interaction to occur. Any photon energy above this threshold is shared as kinetic energy between the electron and positron. If a photon has sufficient energy to overcome the binding energy of a nucleon or to provide the Q energy for a certain reaction channel (usually several MeV), photonuclear reactions then become possible. In these reactions, the photon interacts directly with the nucleus resulting in the emission of one or more nucleons, gammas, and in some cases photofission can occur.

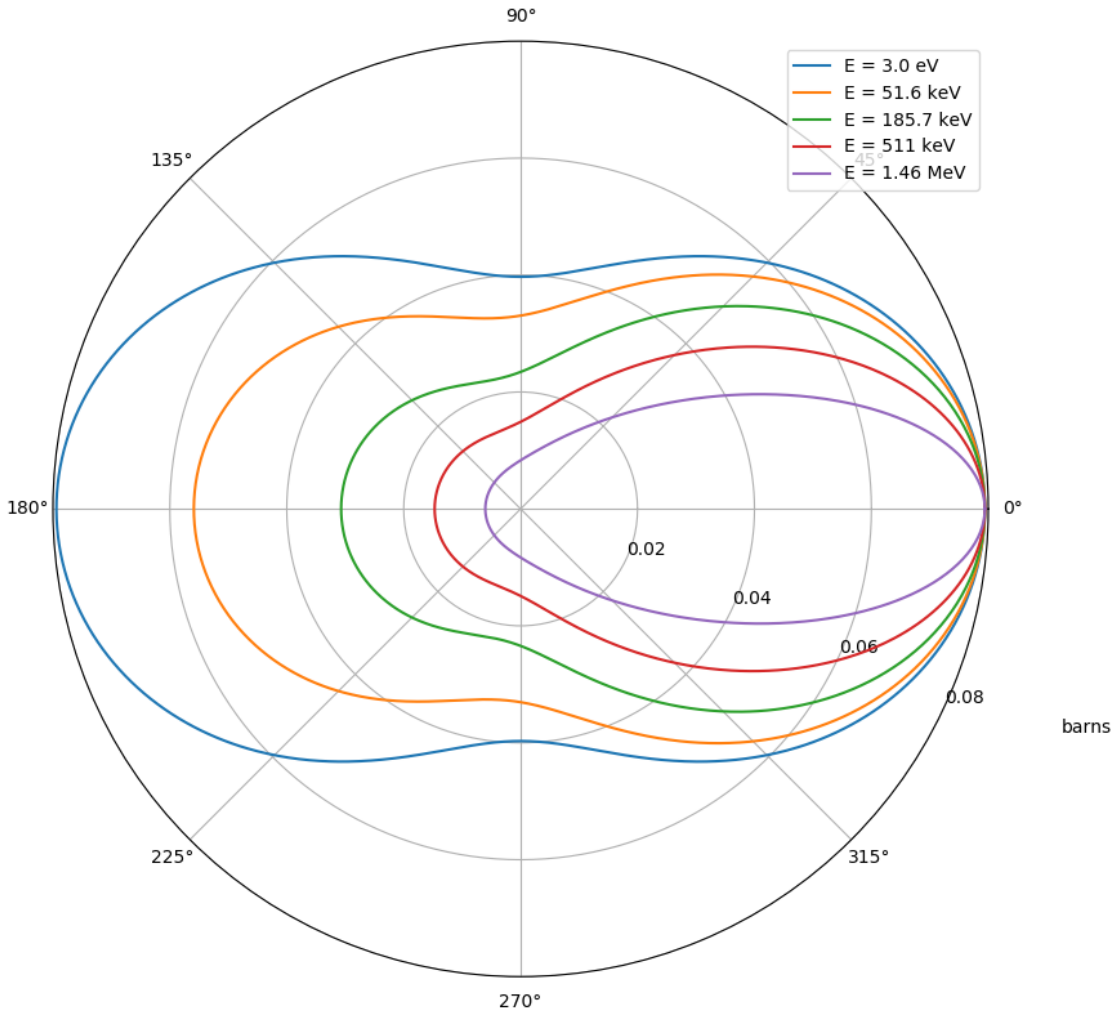


Figure 1.8: Differential scattering cross sections derived from the Klein-Nishina formula for a range of incident photon energies.

Neutrons

Neutrons are neutrally charged nucleons and are typically bound to a nucleus. They can be ejected from nuclei through a plethora of processes such as spontaneous fission in sources like ^{252}Cf, alpha mediated reactions which produce neutrons via the $X(\alpha, n)Y$ reaction in sources such as $AmLi$, $AmBe$, or $PuBe$, fusion reactions such as that produced in $D-T$ neutron generators, and finally photon induced reactions like the (γ, n) reaction produced by bombarding ^{9}Be, or other materials, with high energy bremsstrahlung. When external to a nucleus (and other perturbations) the neutron has a mean lifetime of $881.5s$ after which it decays into a proton (via β^- decay), picks up a free electron, and becomes hydrogen.

The transport of neutrons through material is somewhat similar to photons in that since neutrons are not charged, they do not constantly interact with the material via Coulombic interactions. As a result, neutrons may penetrate quite far into a material without interacting. Also, in similar fashion to photons, the portion of an ensemble of neutrons which have not undergone an interaction while passing through a material decreases exponentially with distance at a rate governed by the neutron cross section of the material.

The total neutron cross section is strongly energy and material dependent as illustrated in Figure 1.9. In general the total neutron cross section is the sum of the cross sections for the three primary neutron reaction types: elastic scattering, inelastic scattering, and absorption.

Elastic Scattering

In elastic scattering, the kinetic energy of the neutron is preserved and shared between the target nucleus and the scattered neutron. This type of interaction is largely responsible for moderating the neutron from higher energies of several MeV to thermal energies of 0.025 eV in nuclear reactors. The reaction may be well described by basic kinematics as shown in Equation 1.19 where $T^{'}$ is the kinetic energy of the outgoing neutron.

$$T^{'} = T\left[\frac{\cos\theta + \sqrt{A^2 - \sin^2\theta}}{A+1}\right]^2 \tag{1.19}$$

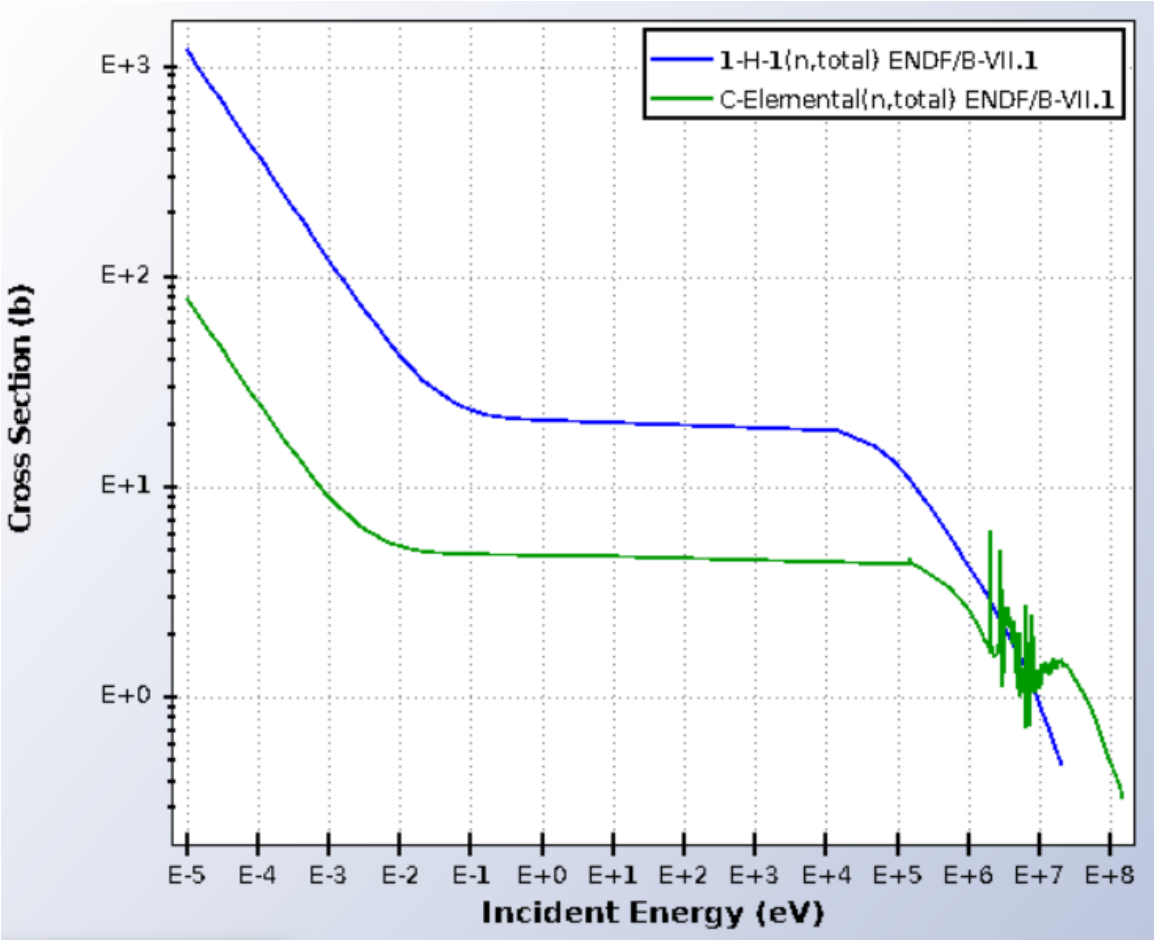


Figure 1.9: Total neutron cross sections for ^{1}H and elemental C. Source: nndc.bnl.gov

The maximum energy transference occurs at $\theta = \pi$ at which point Equation 1.19 reduces to Equation 1.20 and the maximum fraction of energy transferred to the target nucleus is shown in Equation 1.21.

$$T'_{min} = T\left[\frac{A-1}{A+1}\right]^2 \tag{1.20}$$

$$\alpha_{max} = \frac{T - T'_{min}}{T} = 1 - \left[\frac{A-1}{A+1}\right]^2 \tag{1.21}$$

Equation 1.21 is plotted in Figure 1.10. From the figure, it is apparent that for $A = 1$ the neutron may transfer 100% of its energy to the target nucleus. This is why ^{1}H is so effective at moderating neutrons. The maximum energy transfer decreases quite rapidly, dropping below 10% for nuclei with $A = 38$.

The elastic scattering reaction is of particular importance to the detection of fast neutrons, $T > 1MeV$. To detect these neutrons, the reaction should occur in a detector which is sensitive to charged particles. When the scatter occurs, the resulting recoil nucleus often gains enough kinetic energy to become ionized. At this point, the ionized recoil nucleus behaves as a heavy charged particle creating tertiary electrons which may then contribute to a detectable signal either by being collected directly by electronics or by creating light in a scintillator detector which may then be converted into an electronic signal via photodetectors.

Inelastic Scattering

In an inelastic scattering reaction, the neutron-target system momentum is conserved but the kinetic energy is not. At the atomic scale, the neutron is absorbed briefly by the nucleus and then a neutron (usually a different neutron) is emitted from the nucleus with a lower kinetic energy. The nucleus is left in an excited state and then deexcites, usually through the emission of a gamma, though other deexcitation modes are possible. Inelastic scatter reactions usually occur on larger nuclei since there is a larger number of excited nuclear states available to allow the interaction to occur. It is for this reason that materials such as steel and lead which have large A and high density are utilized in spallation neutron facilities to slow very fast neutrons, $T > 20MeV$, down to fast levels such that concrete,

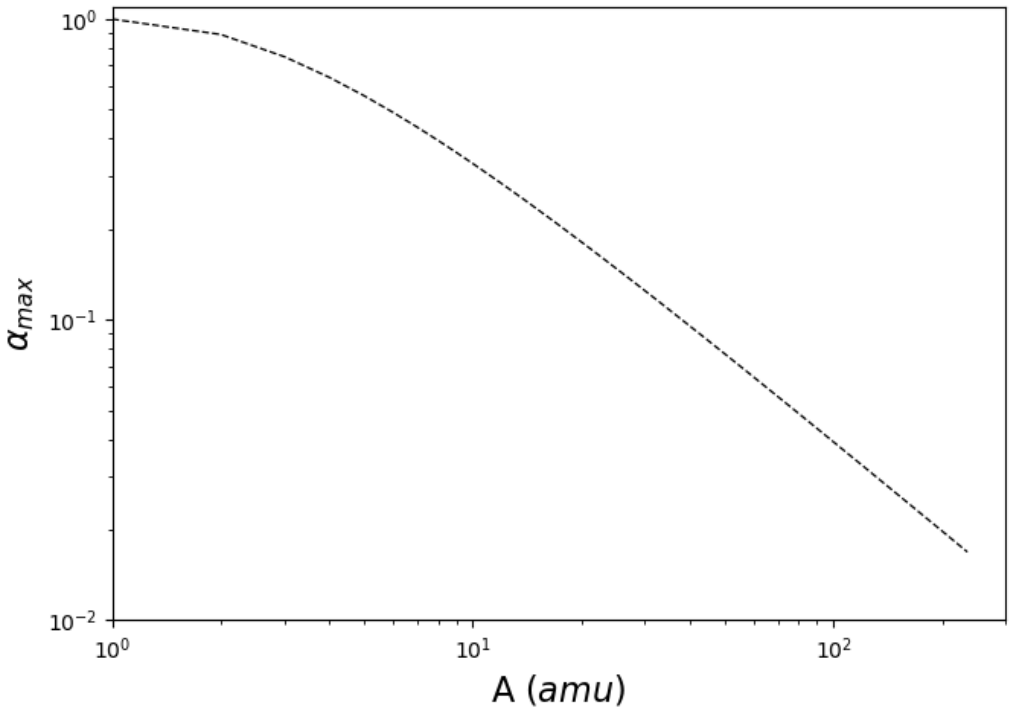


Figure 1.10: The maximum fraction, α_{max}, of energy transferred from the neutron to the target nucleus during an elastic scatter event as a function of the target's atomic mass number.

which is hydrogenous, may slow the neutrons further to near thermal levels at which point they are absorbed.

Neutron Absorption

Neutron absorption, or neutron capture, is responsible for a whole host of various post-absorption phenomena. In general, these can be grouped into three categories: radiative capture (n, γ), particle emission (n, b), and fission (n, f). Radiative capture generally occurs on medium to large nuclei at neutron energies below $500keV$. Some exceptions to this do occur, most notably is the ${}^{1}\mathrm{H}\,(n, \gamma)^{2}\mathrm{H}$ which results in a prominent $2.2MeV$ gamma; a common feature in light water reactors and spallation neutron sources moderated by water and/or liquid hydrogen. Radiative capture is useful for nuclear spectroscopy as the gammas emitted from radiative capture are characteristic of the target material being identical in energy to the levels of the nucleus. Particle emission reactions normally occur at energies above $500keV$. But as always, exceptions do exist. One such exception is the ${}^{6}\mathrm{Li}\,(n, \mathrm{t})^{4}\mathrm{He}$ reaction which has a huge cross section of nearly a thousand barns at thermal neutron energies. The most common particles which may be emitted are protons, deuterons, tritons, and alphas; occasionally neutrons may be emitted alongside an alpha particle. Fission occurs at low neutron energies, generally thermal energies, and on very large nuclei such as ${}^{235}\mathrm{U}$ and ${}^{239}\mathrm{Pu}$. This is not to say that fission does not happen at fast neutron energies, indeed it does. In most cases though the fission cross section is larger, sometimes by a factor of a couple-hundred, for thermal neutrons as compared to fast neutrons. Once a fission occurs, more neutrons are produced in conjunction with large fission fragments and prompt gammas. The average number of neutrons produced during a fission event depends on the material and even on the energy of the neutron causing the fission, with fast neutrons generating more fission neutrons than thermal neutrons. The energy of the fission neutrons varies according to the Watt Distribution with the average energy ranging between $1-3MeV$ and the maximum energy being near $10MeV$ depending on the fissile material. The fission fragments are two large nuclei, usually containing between 80 and 160 nucleons, these behave as heavy charged particles in the host material and come to rest quite quickly. Lastly, the emission of prompt gammas from a fission event is often used to indicate the start of a fission event. There are also delayed gammas which result from the deexcitation of the fission fragment nuclei.

1.3 Scintillators

Scintillators are a class of materials which emit visible light when energy from radiation is deposited within the scintillator volume. In general, scintillators are classified as either organic or inorganic; indicating whether the material is primarily made up of hydrocarbons or not, respectively. Each of these classes of scintillators has vastly different operation mechanisms and general characteristics. Even so, there is also considerable variance in certain properties within these two classes which reinforce the notion that each scintillating material must be understood on an individual basis within the context of its larger classification.While some types of inorganic scintillators and their properties are referenced in this document, the primary focus of this section will be on organic scintillators and some of their derivatives which are of research interest. Particular focus is given to plastic scintillators, the history of high-Z loaded plastics, and nanocomposite plastics which are more recent.

Because of their unique light emitting properties, scintillating materials are primarily used for the detection and characterization of radiation. However, the amount of light emitted from a single scintillation event is low, generally ranging from several hundred to many tens of thousands of photons, and requires a sensitive transduction mechanism such as a photomultiplier tube or avalanche photodiode to create a measurable signal. A general schematic outlining this process is provided in Figure 1.11.

It is important to keep in mind, that in either case of organic or inorganic scintillators, the production of scintillation light is due to the electronic structure of material. As electron secondaries produced by the impinging radiation travel through the material, they excite bound electrons into higher energy states. For inorganic scintillators, the available energy states are a property of the crystal lattice. However, within most organic scintillators the electron energy levels are determined by the molecular energy states of the constituent organic molecules. Once electrons are raised into an excited energy state, they then preferentially deexcite. The deexcitation process may lead to the production of a photon, but not always. It may also be possible for electrons to lower their energy levels by instead transferring energy to vibrational states of the lattice or molecule, thereby contributing to phonon (heat) production.

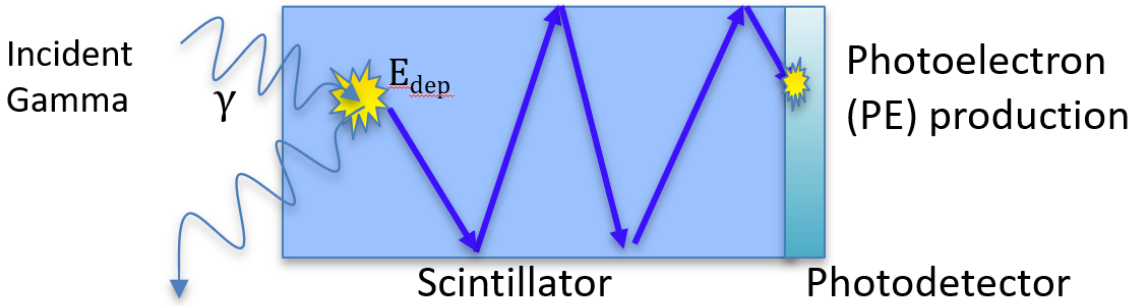


Figure 1.11: The creation and collection of scintillation light. The light is converted into an electrical signal and amplified via a transducer. This signal is then typically processed to be utilized for deducing a quantity of interest relating to the incident radiation.

In general, a scintillator with ideal properties would:

1. Be bright: generally, brighter scintillators have better energy resolution and pulse shape discrimination performance when applicable.

2. Be fast, consistently: faster scintillators can reduce the occurrence of pulse pileup thereby increasing their application in high count rate environments. Scintillators with 'consistent' timing properties are those which have good timing resolution. Better timing resolution generally leads to better performance in applications requiring time-of-flight (TOF) data.

3. Emit light with an intensity proportional to the amount of energy deposited in the scintillator.

4. Emit light with wavelengths that are well-matched to commonly available photon transducers.

5. Be dense and have high effective Z: scintillators which are more dense have an increased intrinsic efficiency; higher effective Z values will lead to increased probability of photoelectric interactions.

6. Have no self-absorption of the scintillation photons: this item reinforces the first.

7. Be robust against damage from radiation, heat, environmental, and mechanical stresses.

8. Be cheap and easy to produce at scale.

9. Be able to discriminate between different types of interacting radiation.

As is true with most things, there is no scintillator (yet) which meets all of the requirements above perfectly. Trade-offs must be made in such a way that the chosen material best meets the application needs.

1.3.1 Inorganic Scintillators

Consider a range of radiation detection applications. In medical fields one may find such applications in x-ray radiography, computed tomography (CT), and positron emission tomography (PET). In industry these applications may range from oil well logging to x-ray radiography of products for quality control purposes. In defense applications radiation detectors may be used for treaty verification, portal monitoring, the search, interdiction, and render safe of special nuclear material, imaging for source localization, and of course x-ray radiography and walk-through pedestrian portals at airports. Inorganic scintillators find a home in all of these uses and many more.

In order to understand why this is the case, it helps to start at what constitutes an inorganic scintillator. For the purposes here, an inorganic scintillator is any *crystalline* material composed primarily of elements exclusive of hydrogen and carbon. Typically these have densities comparable to many naturally occurring minerals and generally falls in the range of $3\,g/cc$ to $10\,g/cc$. An example of an untypical low density inorganic is Li_3YCl_6:Ce^{3+} with a density of $2.45\,g/cc$ [23] while a typical example of a high density inorganic is $CdWO_4$ [24]. Another feature of inorganic scintillators is that they are commonly found with high-Z constituents which is beneficial for increasing the overall sensitivity to gammas and also heightening the probability of full energy deposition via the photoelectric effect which was presented in Section 1.2.2.

In all scintillators, the origin of the energy used to create the scintillation photons comes from the lost energy of charged particles slowing down in the scintillator material. These charged particles may be the direct incident radiation, for example from an alpha emitter or an ion beam. However, in most common circumstances, the incident radiation is either a gamma or neutron and the charged particle is secondary. This secondary charged particle may be an electron as the result of a photoelectric or Compton interaction, it may be a proton from a knock-on interaction between a neutron and hydrogen nucleus, or it may be from neutrons being absorbed by a constituent of the detector material resulting in ionized atom fragments traversing the scintillator. As these charged particles traverse the scintillator volume, they cause 'delta showers' which is simply a tertiary electron being kicked out of a

bound state. As the secondary and higher order particles are slowing down they are ionizing the atoms and molecules. The excited electrons are then able to deexcite. If the conditions are right, scintillation photons may be produced.

The scintillation process of inorganic scintillators is dependent on the lattice structure of the material, specifically the resulting electron energy band structure. The electronic theory of crystalline and polycrystalline materials is often described using energy band diagrams and associated terminology. Three energy band features are of importance for this discussion: one is the valence band of the crystal which describes the uppermost energy level occupied by an electron in a non-excited state, another feature is the conduction band, and in semiconductors there is a region between the valence band and the conduction band referred to as the band gap. When ionization occurs in an inorganic scintillator, the electron is pushed up into the conduction band leaving behind an energy vacancy referred to as a hole. In most instances, the electron and hole are weakly bound via the Coulombic interaction and form a quasiparticle referred to as an exciton. Scintillation light is created when the electron and hole recombine. What is typical in a pure crystal, something difficult to achieve in practice, is that the energy levels of the conduction band and the valence band result in a large band gap ($> 4\,eV$). For reasons outside the scope of this introduction, when the band gap is this large a direct recombination may be inefficient at producing scintillation light. Even when scintillation light is produced, the energy of the resulting photon will likely be above that which most photon detectors are sensitive to.

To get around this issue, a dopant is added in very low concentrations during the crystal growing process. If chosen well, this dopant may act as an *activator* because it allows for more efficient, and sometimes more expedient, conversion of electron-hole pairs into scintillation light. A typical activator has energy bands which lie within the band gap energy range of the pure (intrinsic) crystal. This allows the electron and hole to occupy once forbidden energy states and makes recombination more likely. Since the gap energy between the activator ground state and excited state is less than the band gap of the intrinsic crystal, the photon emitted during deexcitation on the activator site will be of a lower energy than one produced in an equivalent intrinsic crystal. This can have the desired effect of producing photons which

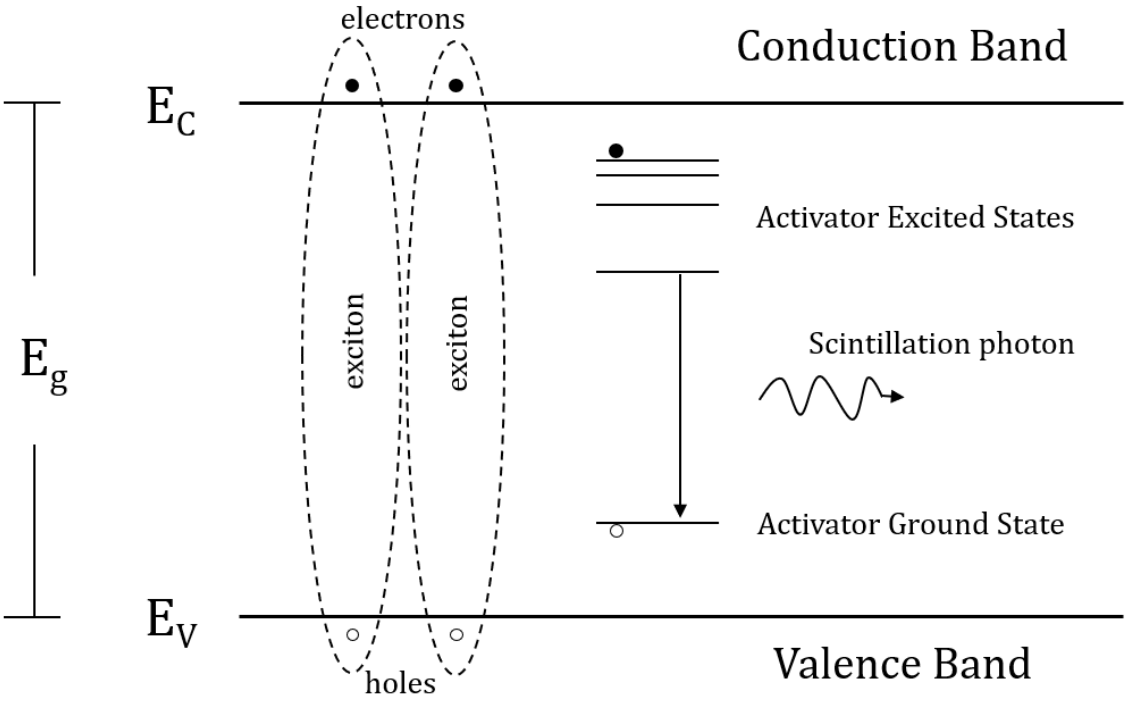


Figure 1.12: The creation of scintillation light in an activated inorganic scintillator.

are more likely to be detected by the photon detector. The scintillation process is outlined for such a crystal in Figure 1.12.

Some of the most prolific inorganic scintillators are in a group known as the metal-halides. As the name suggests, these materials are made up of a metal generally from Group 1A or 2A paired with a halogenic element from Group 7A. Some typical activators for metal-halide scintillators are Ce^{3+}, Tl^{+}, and Eu^{2+}. As far as the author is able to discern, the earliest reported metal-halide scintillator crystal developed out of the study and application of phosphors. (Note: Phosphor here is a somewhat vague term.) This early crystal is the very common NaI scintillator and was reported in 1948 alongside the acknowledgment of scintillation in a crystal of KI:Tl^{+} which was produced in 1938 [25]. NaI:Tl^{+} scintillators are usually cited as having a light yield of 38 photons/keV of energy deposited and an energy resolution of around 7% at $662\,keV$ though the best reported energy resolution is 5.6% at $662keV$ [26–28]. The principle decay time of NaI:Tl^{+} is $230\,ns$. Of note is that sodium iodide is quite hygroscopic and will deteriorate quickly in typical room atmospheres. These crystals, and other hygroscopic scintillators must be hermetically sealed to protect them from the environment.

Other inorganic scintillators of note are:

1. CsI activated with either Tl^{+} or Na^{+}.

2. SrI or KSrI activated with Eu^{2+}: these are some of the brightest scintillators and have the highest energy resolutions for larger volume detectors.

3. LSO and LYSO which have decay times of $40\,ns$ or less and have a high density of $> 7\,g/cc$ making them great candidates for PET/TOF-PET applications.

4. BGO which has the highest intrinsic photoelectric efficiency of any inorganic scintillator due to its high density ($7.13\,g/cc$), and the high effective Z imparted by bismuth ($Z = 83$).

5. YAP:Ce^{3+} is quite fast with a principle component decay time of $27\,ns$ and boasting a light yield of around 20 photons per keV of energy deposited. It is quite a robust material but is lower in density than LYSO, coming in at around $5.35\,g/cc$.

6. CLYC:Ce^{3+} is useful because of its ability to detect and discern (via pulse shape discrimination) both thermal neutrons and gammas if $^{6}_{3}$Li enriched lithium is used. CLYC can also be useful for detecting and discerning fast neutrons due to $^{35}_{17}$Cl having a small yet appreciable $n(^{35}_{17}Cl,^{35}_{16}S)p$ reaction cross section for $1-10\,MeV$ neutrons [29, 30].

In general, inorganic scintillators are considered to be bright, be good for gamma spectroscopy due to high-Z components, have high density, and the potential for good energy resolution, have slow fall times, be prone to damage, and be costly to produce (some much more than others). Of course, there are exceptions to nearly all of these.

1.3.2 Organic Scintillators

Organic scintillators are primarily made up of hydrocarbonic compounds. Typically they are thought of as a solution containing a solvent, such as toluene or styrene, and one or several solutes, such as 2,5-diphenyloxazole (PPO) and/or 1,4-bis[2-(5-phenyloxazolyl)]-benzene (POPOP) [31]. The resulting solution may remain liquid or may be polymerized via curing and become a plastic. The scintillation mechanism in most organic scintillators relies on the electron energy band structure of the constituent molecules, as shown in Figure 1.13 which is in contrast to inorganic scintillators whose scintillation mechanism is dependent on the crystalline nature of the material and resulting electron energy band structure. An example of how scintillation light is created in an organic scintillator may go as follows: incident radiation interacts with the material and initiates molecular energy transitions into excited states. As the molecule begins to de-excite, energy may be emitted as a photon which may then be detected by a PMT. As was the case with inorganics, not all deposited energy is converted into scintillation photons. No small portion of the deposited energy contributes to molecular rotational and vibrational energy transitions. The efficiency of the photo-conversion process is referred to as the *quantum yield* and is generally denoted with the symbol, Φ; this is not to be confused with the *quantum efficiency* of photomultipliers.

One interesting fact is that some of the most commonly used fast neutron detectors are organic scintillators. The reason for this is because many organics exhibit varied decay

times for particles with differing ionization densities, or ionization per unit path length. The ionization density is closely related to the energy loss equations: Equation 1.1 for heavy charged particles and the collisional part of Equation 1.3 for electrons. The ionization density is much greater for heavy charged particles, especially those that are near the end of their track. This feature of varied decay times for particles with different ionization densities was first reported by G.T. Wright in 1956 [32]. The work done to show that this property could be utilized to distinguish between different ionizing particles, protons and electrons, was reported two years later using a mixed gamma/neutron PoBe source [33]. The exact origin of this behavior is quite complex and dependent on the molecular components of the scintillator. The most commonly recited and accepted explanation which is used more as a teaching tool than a 'universal explanation' describes the scintillation decay times to be based on two underlying molecular energy state structures; one structure containing the singlet states the others containing the triplet states as shown with the Jablonski diagram in Figure 1.14. As an aside, singlet states contain paired electrons (one spin up and one spin down); when such a system is placed in a magnetic field, the electronic energy levels remain unitary. On the other hand, triplet states contain unpaired electrons (both are spin up or both are spin down) and when this system is placed in a magnetic field the energy levels split into three levels (-1, 0 , +1) giving origin to the name "triplet state". When radiation excites a molecular electron into an excited singlet state, de-excitation into the ground state occurs rapidly giving rise to the prompt component of the scintillation pulse. The longer decay time component derives from the excitation of an electron into a singlet state whose vibrational and/or rotational substate wavefunction overlaps with one of the vibrational and/or rotation substates within the triplet excited state. This overlap in the wavefunction can lead to intersystem crossing by which the electron transfers to a triplet state (Franck-Condon Principle). De-excitation of the first triplet state to the ground state is unfavorable due to varying spin multiplicity. As such, the characteristic time for direct triplet de-excitation, can range from milliseconds to seconds and is considered phosphorescence. Instead, the often cited preferred mechanism for triplet state de-excitation is through the triplet-triplet annihilation process, $T_1 + T_1 \rightarrow S_0 + S_1 + phonons$. This interaction has a characteristic time which varies from material to material, though is usually on the order of 10s of nanoseconds. More information regarding

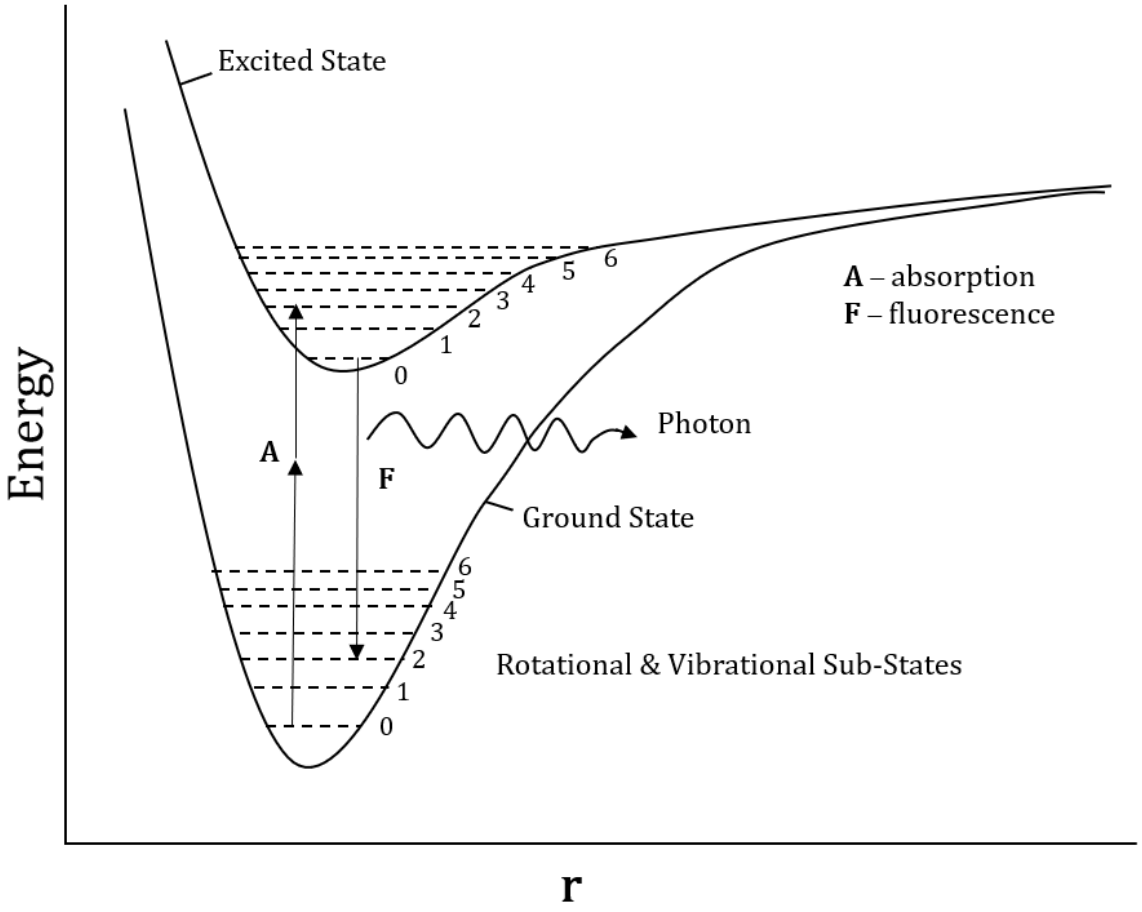


Figure 1.13: The creation of scintillation light in an organic scintillator.

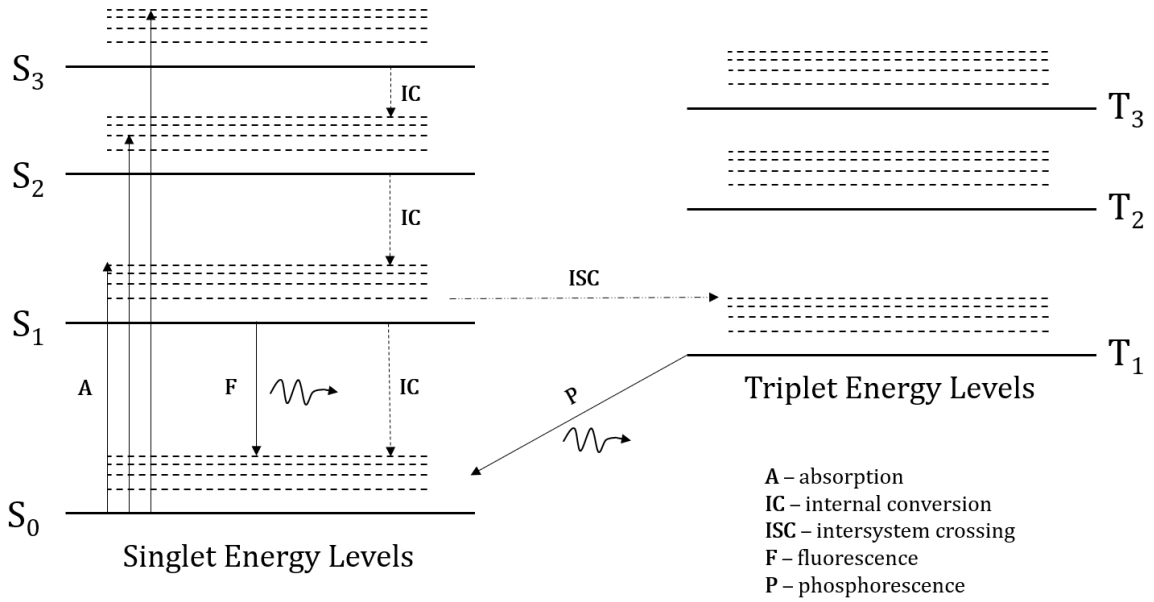


Figure 1.14: Electrons may be excited into higher energy states, each with their own sub-levels which relate to spin-orbital angular momentum, and molecular vibrational/rotational states. If there is overlap in the singlet and triplet vibrational energy state wavefunctions, the electron may change into a triplet state configuration. When compared to singlet state de-excitation, complete de-excitation of the triplet state occurs over a longer time period leading to phosphorescence.

organic scintillator development, photophysics, and photochemistry may be found in [31, 34–38].

Oftentimes the energy deposited in a pure organic solvent, such as xylene or toluene, does not convert into scintillation light at a very useful wavelength; instead a dye, also called a fluor, must be added. The molecules of the fluor facilitate the detection of scintillation light via wavelength shifting. Since the fluor component is generally a small part of the overall material, typically a few percent or less, the majority of the initial excitation occurs on the solvent molecules. In the case of plastics, this is normally referred to as the base matrix or base matrix molecule(s). The excited molecule of the solvent then transfers the excitation energy to a fluor molecule. This transfer may happen radiatively through the emission and absorption of a photon or non-radiatively via either Förster resonance energy transfer (FRET) or Dexter energy transfer [39, 40]. Dexter energy transfer, or electron transfer, relies on slightly overlapping wavefunctions between neighboring molecules which permits an excited electron to jump from one molecule to another. Due to the overlapping wavefunction requirement, the Dexter mechanism is classified as a close range interaction and operates at typical distances of less than 10Å. FRET on the other hand works due to the coupled oscillation of two nearby electric dipoles and has a range of up to 100Ådepending on the donor-acceptor pair. Once the energy is transferred to the fluor, fluorescence may occur and a photon with less energy (generally) than was initially transferred to the dye molecule is emitted. In many instances, one example with PPO being the primary fluor, the emitted wavelength of light is still too short (355nm) to be efficiently detected by the photodetector which is usually more sensitive to longer wavelengths of light. As an example, typical bialkali photomultipliers have peak sensitivity to 420nm wavelength light while many silicon photomultipliers have peak sensitivity near 500nm. To solve this problem, another fluor may be added to absorb the emission of the initial/primary fluor and re-emit light of a longer wavelength. A typical secondary fluor to use in combination with PPO is POPOP, though many potential combinations exist. An example of the absorption/emission wavelengths for a common ternary organic system is shown in Figure 1.15 and highlights the importance of overlap in the emission wavelengths of the solvent/primary fluor with the absorption wavelengths of the primary fluor/secondary fluor respectively. The final goal is

that the emission of the secondary fluor is well matched to the sensitivity of the photon detector. More information on this topic in the context of plastic scintillator design may be found in [41].

One property of both inorganic and organic scintillators which should be mentioned is the non-proportionality of the response to energy deposited; when referring to the 'response' what is meant is the number of scintillation photons produced. Before doing this though it is worth pointing out, due to the confusion that it often causes, the nuances between the terms *non-linearity* and *non-proportionality*. Strictly speaking, a response is proportional to the deposited energy if it may be fully described by Equation 1.22, while a response is linear if it may be described by Equation 1.23. In these equations R is the total absolute light output response, LY is the light yield per unit energy deposited, and E_{dep} is the total energy deposited. Based on this definition, the following logic applies:

1. All proportional responses are linear responses (with $C = 0$).
2. All non-linear responses are non-proportional responses.
3. A non-proportional response may still be linear (with $C \neq 0$).
4. A linear response may not be necessarily be proportional.

$$R(E_{dep}) = \text{LY} \cdot E_{dep} \tag{1.22}$$

$$R(E_{dep}) = \text{LY} \cdot E_{dep} + C \tag{1.23}$$

In the case of scintillators, the two words are often interchanged without much regard for the nuances between them. What is most often meant, though, is a response which is both non-linear and non-proportional, meaning there is some curvature present in the response over part or all of the deposited energy range. It is known that the response is different for varying kinds of charged particles depositing energy in scintillators and that the response is dependent on the ionization density along the path of the charged particle. In general, less scintillation light per unit energy is produced in path segments where the ionization density

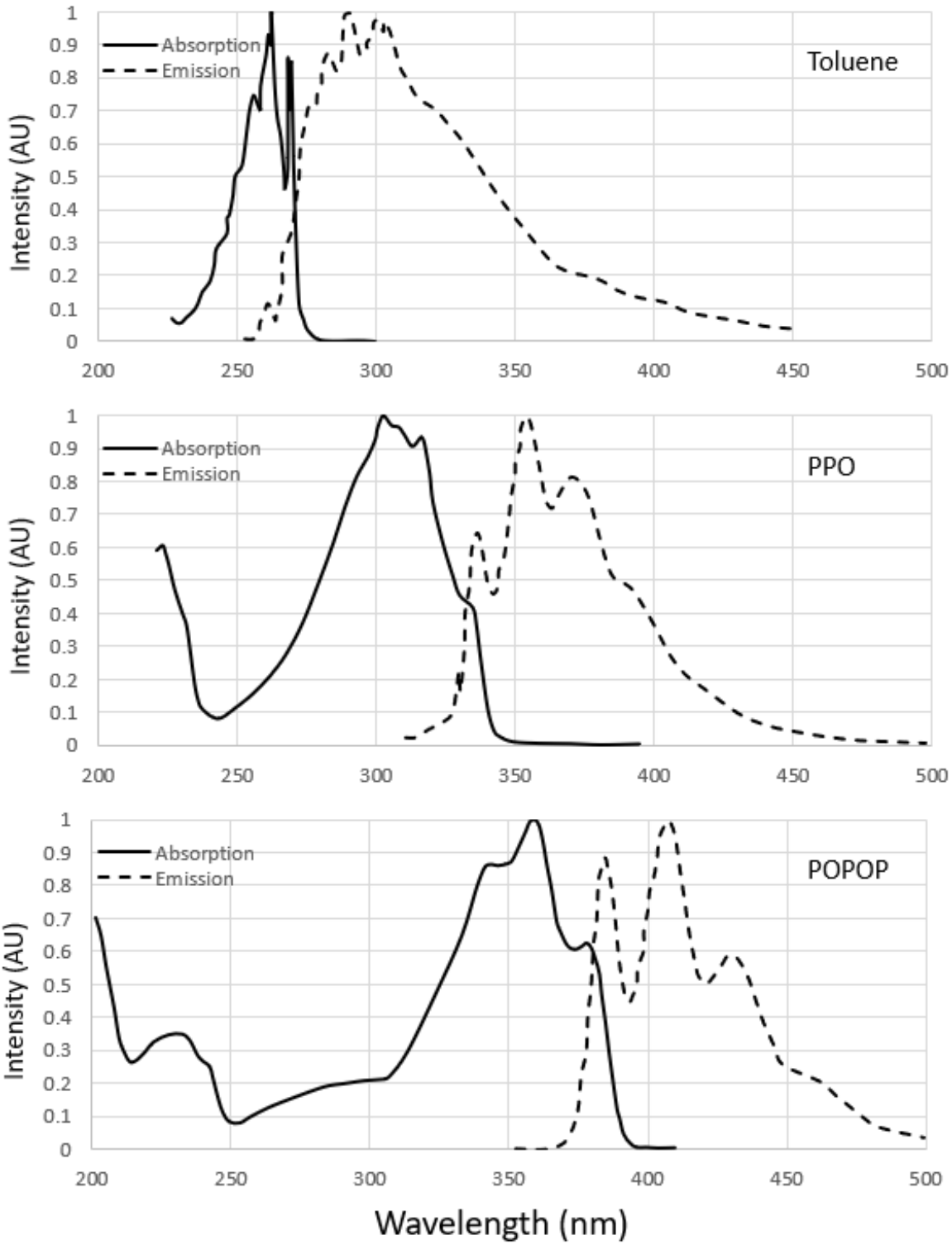


Figure 1.15: Absorption and emission spectra of toluene (top), PPO (middle), and POPOP (bottom). Photons (real or virtual) emitted by an excited toluene molecule may be absorbed by PPO, re-emitted at a longer wavelength, followed by secondary absorption by POPOP then remission at a wavelength suitable to many photon detectors. Data from PhotochemCAD database, original works for these data are currently not known to the author [46].

is higher. A full understanding of this phenomenon has still not been obtained, even so there are ways that it may be described for the purposes of scintillator response modeling [42]. Most commonly used, in codes like GEANT4 for example, is the single parameter Birk's formula shown in Equation 1.24 where $\mathrm{d}L/\mathrm{d}x$ is the fluorescence energy emitted per unit path length, $\mathrm{d}E/\mathrm{d}x$ is the energy deposited in the scintillator per unit path length, S is the normal scintillation efficiency, and kB is normally referred to as Birk's parameter which is different for each material [43, 44]. A second empirical formula, very similar to Birk's formula was presented in 1969 by Craun and Smith, which saw marginal improvements in performance [45]. Craun's formula is sometimes referred to as a 2-parameter Birk's formula because the only difference between the two is the addition of a second term in the denominator of Equation 1.24 which is equivalent to the square of the preceding term multiplied by a constant.

$$\frac{\mathrm{d}L}{\mathrm{d}x} = \frac{S\frac{\mathrm{d}E}{\mathrm{d}x}}{1 + kB\frac{\mathrm{d}E}{\mathrm{d}x}} \tag{1.24}$$

Just as was done for inorganic scintillators, it is now time to mention some typical properties of organic scintillators as they pertain to radiation sensing; this in addition to some interesting one-offs. Due to being primarily made up of hydrogen and carbon, the effective Z for typical organic scintillators is low and results in virtually no photoelectric effect; the primary mode of gamma interaction is Compton scattering. Compared to inorganic scintillators, organics are considerably less dense, with most being between $1\,g/cc$ and $2\,g/cc$. Organic scintillators are typically renowned for being very fast, with typical principal decay times on the order of several nanoseconds or less. There are a subset of organic scintillators which are known to be useful for discriminating different types of ionizing radiation through the application of pulse shape discrimination (PSD) techniques. Historically many of the best organic scintillators for PSD have been liquid, which typically carries the drawback of being flammable and/or highly toxic. Recently, however, plastics have been developed which outperform liquid scintillators for fast neutron PSD applications, though the commercialization of this formulation remains to be seen [47]. The best performing organic scintillator for fast neutron PSD has been and remains the organic crystal,

stilbene. Another type of organic crystal, anthracene, has previously been regarded as the brightest organic scintillator ($16.5\,photons/keV$) and is often used as a reference for reporting organic scintillator brightness (e.g 60 % anthracene). However, the recent discovery of triplet harvesting via the use of an iridium-complex fluor, has produced organic scintillators with light yields in excess of $30\,photons/keV$ which is nearly comparable to NaI [48]!

1.3.3 High-Z Loaded Organic Scintillators

One of the primary undertones of this work is the furthering of the basic scientific understanding of high-Z loaded plastic scintillators. Much has been done over the last half-century to increase the effective Z number in organic scintillators by utilizing methods of loading heavy metals such as lead, tin, mercury, and bismuth into the polymer base matrix by introducing organometallic compounds [34, 49–55]. Several reported factors have negatively affected the performance of high-Z organics loaded with organometallics. Light output quenching due to the so called 'heavy atom effect' is a constant and recurring theme, as is increased optical photon absorption of scintillation light. Another reported feature was that in many cases the photopeak was not as prominent as had been hoped for given the increase in effective Z. Organic scintillators loaded with high-Z components in this way have found their place on the commercial front as exhibited by the lead loaded plastic, EJ-256, from Eljen which is meant to boost sensitivity to gammas with energy less than $100\,keV$. Recent advances with bismuth loading into polyvinyl carbazole (PVK), and now PVT, have been demonstrated with the brightest of these utilizing the aforementioned iridium-complex fluor [56–60].

An additional subset of high-Z loaded organics is the class of nanocomposite scintillators. This group of materials utilizes high-Z nanoparticles, usually with diameters of less than $10\,nm$, as the vessel for decreasing the gamma attenuation length. Nanocomposites with hafnium oxide nanoparticles have been demonstrated to have a resolution of 8% at $662\,keV$ and light output that is 75% of EJ-212 with a $16.5\,wt/\%$ nanoparticle loading [61]. Another material using ytterbium fluoride nanoparticles reports 9% resolution at $662\,keV$ with a light output $\sim$ 68% of EJ-212 with a $24.5\,wt/\%$ nanoparticle loading [62, 63]. Another type of interesting nanocomposite utilizes small semiconductor materials known as quantum

dots (QDs). A particular feature of QDs is that they have a tuneable band gap which is a function of particle size and shape. Smaller QDs have larger band gaps and emit more in the blue and UV region, while larger QDs have smaller band gaps and emit more into the red end of the color spectrum. This tunability, in theory, allows one to tailor an emission wavelength that is a veritable match to the photosensor sensitivity. However, QDs are very efficient emitters with a small Stokes shift which results in significant self absorption of the light emitted. A demonstrated way around this, following previous themes, is to add a fluor which shifts the wavelength of the light emitted by the QD to a longer wavelength which is not easily absorbed by the QD. This has the consequence, though, of paralyzing ones ability to tune the emission wavelength to the photosensor, instead one must tune the QD emission to the absorption of the wavelength-shifting fluor with the resulting emission wavelength being a set property of the fluor. The demonstrated nanocomposite of this type utilizes $Cd_xZn_{1-x}S$/ZnS core-shell QDs combined with a 4,7-bis2'-9',9'-bis[(2"-ethylhexyl)fluorenyl]-2,1,3-benzothiadiazole (FBtF) fluor. This composition has resulted in a reported energy resolution of 9.8% at $662\,keV$ and light output that is 93% of EJ-212 with a $38.1\,wt/\%$ QD loading [64]. Care must be taken in the synthesis of QD nanocomposites, and any nanocomposites, to avoid a bad choice in NP band gap and also avoid aggregation of the NPs which can produce unusable materials [65].

Due to the fact that nanocomposites have small inclusions of materials which differ from the host material, the emitted light may scatter off of these inclusions due to the different electric permittivity and refractive indices. Many papers discussing nanocomposites iterate that Rayleigh scattering is a significant contributor to the observed reduction in optical transmittance with the flux of non-scattered light being described by Equation 1.25. This equation and/or equivalent descriptions of Rayleigh scattering in nanocomposites is found in [61, 63, 66, 67] with [67] containing an error/typo in the equation.

$$I = I_0 \exp\left\{-\frac{32\phi_p x \pi^4 r^3 n_m^4}{\lambda^4}\left[\frac{(n_p/n_m)^2 - 1}{(n_p/n_m)^2 + 2}\right]^2\right\} \tag{1.25}$$

In the preceding equation, ϕ_p is the nanoparticle packing fraction, x is the distance traveled by the photon, r is the radius of the nanoparticle, n_m is the index of refraction of the matrix, and n_p is the index of refraction of the nanoparticle.

Other articles reference a second equation, Equation 1.26, describing the interaction length of Rayleigh scattering in nanocomposites; with one reference seeming to acknowledge both instances even though they result in different outcomes [61, 62]. The variables in Equation 1.26 are identical to those in Equation 1.25 except that it is believed λ refers to the wavelength of light in the matrix as opposed to the vacuum wavelength as in Equation 1.25.

$$I = I_0 \exp\left[-\frac{3\phi_p x r^3}{4\lambda^4}\left(\frac{n_p}{n_m} - 1\right)\right] \tag{1.26}$$

Equation 1.26 may be most recently traced to an article by Walter Caseri published in 2000 [68], then to an article by Bruce Novak published in 1993 [69], to a 1982 textbook on ceramics [70]. I was unable to acquire the text during this phase of my research due to the closure of the campus library in the early phases of the SARS-CoV-2 pandemic; a digital copy was unavailable. At any rate, Walter Caseri published a later work on the topic utilizing Equation 1.25 [71]. Like his first, this work was a review article covering nanocomposites and cited a dissertation for the credit of Equation 1.25 [72]. Access to the dissertation was blocked due to its being a locked reference. Due to the change exhibited by Walter, and since Equation 1.26 breaks when $n_m \geq n_p$, it is assumed, for this work, that Equation 1.25 is the established and accepted equation for describing the non-scattered incident photon flux upon a nanocomposite slab. This does not assume that the equation is correct; this work does take some steps in determining the trustworthiness of Equation 1.25 and establishing the use-cases where it is best thought to apply; this and more is described more fully in Chapter 4.

1.4 Photomultiplier Tubes

Photomultiplier tubes, and photosensors in general, are important to understand in the context of scintillation detectors because these devices are ultimately responsible for

producing the usable electronic signal which is later processed and mapped into information structures useful for discerning properties of the incident radiation. Any scintillator response measured through a PMT will inevitably be muddied by the response of the PMT itself. A typical PMT is an electronic device with a photocathode at one end, an anode at the opposite end, and a series of electron multiplication stages called dynodes between the photocathode and the anode. This is illustrated in 1.16. The typical transmission mode photocathode is a thin film semiconductor composed of at least one low work-function metal, typically an alkali metal. In a direct broad-beam geometry, the probability of an incoming photon to produce a photoelectron on the photocathode is wavelength dependent and is referred to as the quantum efficiency. The quantum efficiency is not measured directly, but is inferred from measurements of the photocathode radiant sensitivity which is defined as the photo-current off of the photocathode divided by the incoming radiant flux and has units of (A/W). The relationship between the quantum efficiency and the radiant sensitivity is given in Equation 1.27 where $QE(\lambda)$ is the quantum efficiency as a function of wavelength, λ, which is in nanometers and $S_R(\lambda)$ is the radiant sensitivity as a function of wavelength. It is important that radioluminescence spectrum of the scintillator is sufficiently matched to the peak quantum efficiency of the PMT.

$$QE(\lambda) = \frac{1239.84\, nm\, WA^{-1}}{\lambda} S_R(\lambda) \tag{1.27}$$

Other PMT properties which are important, and usually declared by PMT manufacturers are (1) the PMT gain, a multiplication factor indicating how many electrons will be in the output pulse for a single photoelectron, (2) the spectral response range, (3) the PMT pulse rise time, (4) the transit time, the time it takes for the photoelectron to cascade through the dynode stages and be collected at the anode, (5) the transit time spread, this is related to the standard deviation of the transit time and is usually given as full width at half maximum (FWHM), (6) and the dark current, which is descriptive of the amount of noise one may expect from thermionic emission off of the photocathode and dynodes, and the leakage current.

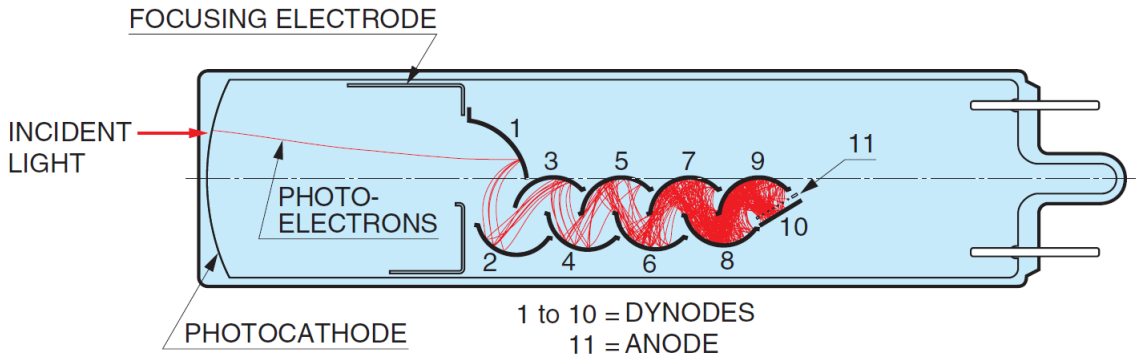


Figure 1.16: A linear focused PMT which is the same type as the R2059. Shown is the creation of a photoelectron on the photocathode which is then transported to the dynode stages and multiplied into a measurable pulse. For the R2059, a single photoelectron is typically multiplied to the amount of 2.0×10^7 according to the manufacturer. [73]

The primary PMT used for the experiments represented in this work is the R2059 Hamamatsu PMT. This is a 2-inch (51 mm) PMT with the photocathode area covering a diameter of 46 mm. The photocathode material is labeled as bialkali and could either be RbCsSb (green enhanced) or KCsSb (more blue-sensitive)[73, 74]. Though it is important to note that the blue extent of the sensitive range is more of a property of the PMT window material than the photocathode. For the R2059 PMT, the window material is composed of fused quartz (aka silica glass), which has an absorption edge at around 180 nm. PMTs with fused quartz windows (as opposed to borosilicate) degrade more quickly over time due to atmospheric helium permeating through the window. However, the fused quartz window is needed for applications where shorter wavelengths of light, between 200 nm and 300 nm, need to be detected. The quantum efficiency and radiant sensitivity of the R2059 PMT is shown in Figure 1.17. Typical gain for the R2059 is 2×10^7, but is highly dependent on the applied voltage. The rise time of the R2059 is 1.3 ns, resulting in a PMT fall time of approximately 3.9 ns since the fall time is about a factor of 3 more than the rise time, per the manufacturer.

The expected collected charge at the anode for a given scintillation pulse may be estimated by using Equation 1.28, where E_{dep} is the energy deposited in the scintillator by the incident radiation, LY is the absolute scintillation light yield per unit energy, LCE is the light collection efficiency, QE is the photocathode quantum efficiency appropriately weighted by the scintillator radioluminescence spectrum, G is the PMT gain, and e is the unit charge: $1.662 \times 10^{-19} C$.

$$Q = E_{dep} \cdot LY \cdot LCE \cdot QE \cdot G \cdot e \tag{1.28}$$

One may also use this information to make estimates of the peak current and voltage for a given output pulse when consideration is given to the fall times of the scintillator and PMT. For example, the peak voltage from a 1 MeV energy deposition in plastic EJ-200 with a decay time of 2.1 ns and light yield of 10 photons/keV will produce a peak voltage that is approximately 28 times higher than the peak voltage produced from 1 MeV deposited in NaI(Tl) with a higher light yield of 38 photons/keV but longer decay time of 230 ns. These

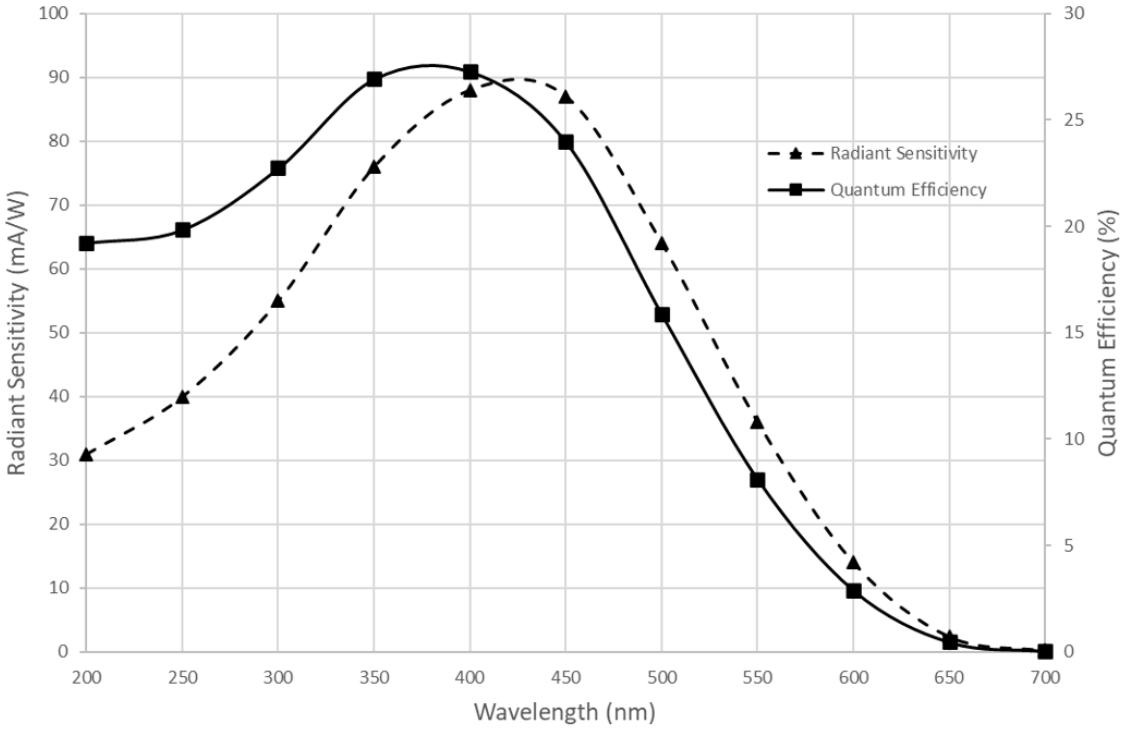


Figure 1.17: The radiant sensitivity and quantum efficiency of the Hamamatsu R2059 PMT. These are properties of the combined PMT window and PMT photocathode system. The peak sensitivity reported by the manufacturer is at 420nm, which is difficult to discern on this plot due to the artificial nature of the splines and the sparse data points.

are important considerations when designing an experiment which may have components of limited dynamic range; for example the CAEN DT5742b digitizer which has a 1V peak-peak dynamic range or the CAEN DT5720 digitizer which has a 2V peak-peak dynamic range.

Other more general properties of PMTs are the various instabilities which are observed over the course of a few minutes, to hours, to many years. Short term instabilities include PMT gain drift, and variances due to atmospheric conditions such as temperature/humidity. In the long term, degradation to the photocathode, dynodes, or dielectric materials used to construct the PMT may lead to large changes in the gain and/or dark current, some of which may render the PMT unusable [73].

1.5 Regarding the Material Properties of Polymers

As this body of work focuses on plastic scintillators, specifically those which may be mechanically robust, high-Z loaded, loaded with high concentrations of PPO, or are otherwise novel, the completeness of the introduction would be lacking without a summary intro to the topic of polymer viscoelasticity and the modes of material property measurement which are relevant to this research. For a more complete understanding of these topics, the author would like to refer the reader to [75–80].

As the name implies, viscoelastic materials are a set of materials which exhibit both viscous and elastic components in their mechanical behavior. The viscous properties are those which impart to the material a "fluid-like" behavior and are typically responsible for phenomena such as a loss of restorative energy when placed under a stress, susceptibility to creep, or the display of memory effects which cause specimens having undergone a particular strain history to have different stress responses when compared to specimens with a differing strain history. The elastic properties are those which are typical to ideal solids such as the ability of the material to store energy under deformation and then return all this energy when the material is returning to its initial zero-strain state. These two different components are often conceptualized using spring and dashpot models as shown in Figure 1.18. In this figure, springs represent elastic behavior and serve to provide restorative forces to bring the spring to equilibrium. The force applied by the spring is proportional to the displacement

of the spring and points in the direction of the spring equilibrium position. The spring proportionality constant, k, is multiplied with the displacement (as in Hooke's Law) to determine the magnitude of the force. Dashpots, on the other hand, represent the viscous components of the material and are essentially dampeners. Their function is to oppose whatever motion is occuring by an amount proportional to the velocity of local system.

A proper interpretation of Figure 1.18 should bring the reader to conclude that under constant stress, σ, the Maxwell model will be continuously extended while the Kelvin-Voigt model will only extend to the point where the stress force is equal to $k \times displacement$. When the stress is removed, the Maxwell model will not be able to return to its initial configuration, however the Kelvin-Voigt model will eventually return to its initial configuration thanks to the restorative force of the spring. If instead a constant strain, ϵ, is applied, the Maxwell model will begin to relax until the stress is completely dissipated while the Kelvin-Voigt model will relax somewhat initially until the stress is equivalent to $k \times displacement$. If the constant strain mechanism is removed after each system has reached its asymptotic stress, the Maxwell model will remain unchanged in its extended position while the Kelvin-Voigt model will slowly return to its initial state. Further analysis should lead the inquisitive reader to suppose interesting dynamic behaviors of these systems exist. This supposition would be true, however it is not the intent of the author to examine all possible phenomena these system models may present as this phenomena has been studied extensively in physics (classical mechanics) and in mechanical engineering.

Since this study focuses on plastic scintillators that are at least as robust as EJ200 (polyvinyl toluene), and since PVT based plastic scintillators have been utilized for decades under normal conditions without observational evidence of the more fluid-like behaviors, such as significant creep or flow, it is believed by the author that the relevant materials may be best expressed by the Kelvin-Voigt solid model. The mechanical properties most relevant to this study are those which may typically apply to designing a macroscopic system using a material of this type. Some of these are the elastic (Young's) or tensile modulus, the flexural modulus, tensile and flexural strength, and the dynamic modulus which may be broken down into the components of storage and loss moduli.

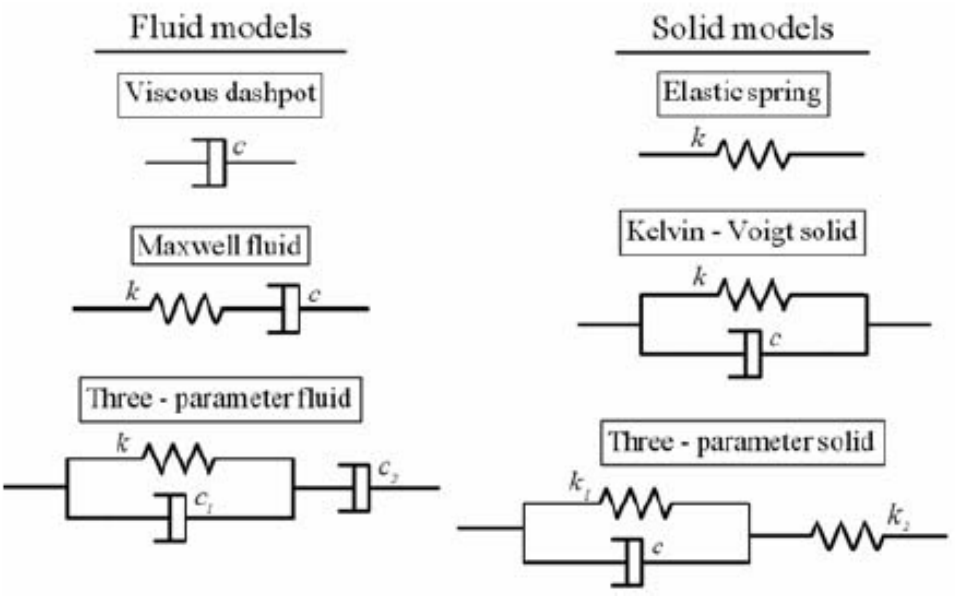


Figure 1.18: Common spring and dashpot models to communicate the rheological behavior of viscoelastic materials. The variable k is the spring constant and represents the elastic modulus of the material, the variable c is the dampening constant and represents the viscosity of the material [81].

In reference to mechanical properties, a modulus is simply a measure of how much a material resists deformation. (This is not in reference to the permanent 'plastic deformation' but instead refers to any displacement of the relative points in the solid from their preferred position when in equilibrium). There are many different types of moduli depending on the mode of deformation (e.g. tensile, bulk, shear, flexural). For each of these, larger values of the modulus indicates a required higher degree of difficulty to achieve a given level of strain; or that more work/energy is required to deform the material in that mode as compared to a material with a smaller modulus. The strength is simply a reference to the maximum pressure sustained before a material breaks, ruptures, or becomes permanently deformed through plastic deformation.

1.6 Original Contributions

The following is a list of original contributions contained in this work.

1. Measurements of the tensile strength and modulus of nine types of plastic scintillators.
2. Measurements of the flexural strength and modulus of nine types of plastic scintillators.
3. Measurements of the relative light collection of twelve types of plastic scintillators.
4. Measurements of the dynamic mechanical response in the frequency domain of two plastic scintillators and the comparison to time domain measurements.
5. The creation of a GEANT4 application for the study of light collection in scintillators coupled to a PMT.
6. The validation of the GEANT4 application using gamma spectra measurements from EJ-200 and EJ-256 coupled to a calibrated PMT.
7. The demonstration that the current understanding of light scattering/absorption mechanisms in YbF_3 nanocomposite scintillators is incomplete. This was accomplished using a combination of simulations and calculations.

8. The demonstration of the performance of a scaled up YbF_3 nanocomposite scintillator utilizing the current set of assumptions.

9. The simulation and measurement of gamma spectra using EJ-200 in multiple aspect ratios with varied optical surface reflectors. Measurements were completed using a calibrated PMT for the purpose of choosing optical surface models in GEANT4.

10. The calculation of the Cramer-Rao Lower Bound (CRLB) of the timing resolution for TOF-PET measurements using EJ-232Q.

11. The development and demonstration of a method for deconvolving latent x-ray escape peak features from the photopeak in gamma spectra.

12. The development and demonstration of a source injection tool for a mobile radiation detection test bed.

Chapter 2

Mechanical and Light Yield Measurements of Select Plastics

The following chapter generally outlines the work as it appears in the author's PJA [16]. Since publishing the aforementioned PJA, additional materials have been characterized within the same analysis framework described in the original article. These materials are EJ-290, EJ-270, EJ-276, and EJ-200NF. Furthermore, additional sections have been added to show results for dynamic mechanical analysis measurements of the EJ-200 scintillator which were formulated with both toluene and styrene solvents.

2.1 Abstract

In order to design structures, such as unmanned vehicle structures, out of plastic scintillator, e.g., for radionuclide searches, suitable materials must either be identified or developed. In searches utilizing unmanned vehicles, the absence of an additional detector attached to the vehicle body as a payload could enable the vehicle to travel faster, carry a longer lived battery, or carry other auxiliary equipment which may be useful for search and/or response. To this end, four mechanical characteristics of selected organic scintillators manufactured by Eljen technologies, Sandia Livermore, and Lawrence Livermore National Lab have been measured. Specifically, tensile and flexural tests have been performed to ASTM specifications on organic scintillators with polyvinyl toluene (PVT), polystyrene (PS), or crosslinked versions of these

bases. In addition to these mechanical tests, light output testing was performed in order to quantify whether crosslinking or adding organometallic complexes affects light output in the particular scintillator compositions we measured. We found that the tested plastic scintillators have strengths that are comparable to common structural plastics. We also show that chemically modifying the polymer base can show improvements in the mechanical properties without being overly detrimental to the scintillator light output.

2.2 Introduction

Solid organic scintillators find common use as radiation detectors for national defense and homeland security applications due to their low cost and reliability. Common forms include polyvinyl toluene (PVT) and polystyrene (PS). Important advances in the last decade have included successes in high Z loading in solid organic scintillators [55, 58, 62], fabrication of solid organic scintillators with good pulse shape discrimination characteristics [82–85], and methods advances allowing for improved spectroscopy with large solid organic scintillators [86]. Mechanically robust, solid organic scintillators may be particularly useful in applications where it is desirable for the detector material to also function as a mechanical component of an apparatus which may be used for the detection of special nuclear material (SNM) or other radionuclides. An example of such an application is utilizing the detector material as part of the frame of a vehicle for unmanned SNM searches.

One focus of this study is to determine whether solid organic scintillators could be used as a structural material, for example, as an airframe for a lightweight unmanned aerial vehicle (UAV). Due to the limited payload capacity of lightweight UAVs, on-board SNM detectors should not significantly add to the weight of the UAV. One potential solution to this problem is to utilize the detector material as the primary component of the UAV airframe, as shown in Figure 2.1. In this situation, the detectors are integrated as part of the UAV body and account for a significant portion of the vehicle's overall weight and mechanical integrity. An additional focus of this study is to report on the effect of polymer crosslinking on scintillator strength and light output. Since it is expected that crosslinking may improve the mechanical robustness of the scintillator, it is important to understand

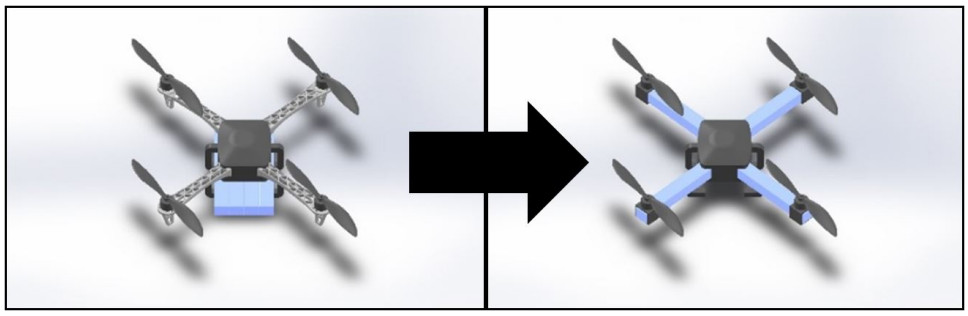


Figure 2.1: Illustration of UAV structural modification to include organic scintillator (shown in blue) as part of the vehicle body instead of adding a dedicated detector to the vehicle payload.

what, if any, trade-offs exist and to what degree they affect the detector performance. Since light yield is directly related to energy resolution, pulse shape discrimination performance, and other performance properties, it is an important property to understand as changes are made to the polymer matrix.

2.3 Materials and Methods

A large variety of materials are potential candidates to serve the dual purpose role of vehicle frame (or other structural plastic) and radiation detector. The material selection for this study is provided in Table 2.1. All materials were fabricated by Eljen Technologies, with the exception of the PD-02-55.02 materials which were fabricated by Patrick Feng's group at Sandia National Lab Livermore. The materials selected for this study were chosen with the intent to probe existing material candidates which are either commercially available or are not yet fully commercialized but are in the late stages of development. In order to study the effect of crosslinking the polymer base, the commercially available materials were requested to be manufactured with and without crosslinking of the base. The crosslinked samples are tagged with "XL" in the label. In addition to crosslinking, two standard bases were also compared while using the same fluors as exhibited by the EJ-200 vs. EJ-200PS which have PVT and PS bases respectively. An additional variable whose effect was examined is the addition of tin-containing organometallic complexes to the PD-02-55.02 scintillator. This material is tested with and without 5 wt% tin.

2.3.1 Tensile Testing

The tensile test samples were machined from a bulk sheet or boule of material into large type IV and/or small type V dog-bone shapes. The dimensions of these sample types are fully defined in the ASTM test standard D638 [87] which also served as the primary basis for the experimental guidelines. The measurements were performed using an MTS 810 servo-hydraulic load frame equipped with an MTS 647 hydraulic wedge system and controlled by the MTS Multi-Purpose Testware software. The tensile strain was recorded by the software using data generated by the MTS 634.31E-24 extensometer which was set to a gauge length

Table 2.1: Selected materials for mechanical and light output testing.

Material	Description
EJ-200	Standard PVT based plastic from Eljen
EJ-200PS	Polystyrene based version of EJ200 from Eljen
EJ-200PSXL	Polystyrene based scintillator with added crosslinker from Eljen
EJ-299-33	PSD plastic from Eljen
EJ-299-33XL	PSD plastic with crosslinker from Eljen
EJ-270	Li-6 loaded plastic from Eljen
PD-02-55.02	Plastic from Sandia (P. Feng)
PD-02-55.02(Sn)	Plastic from Sandia with 5 wt/% tin loading (P. Feng)
N555V	Plastic developed at LLNL and produced by Eljen with 5% each of PPO, PMMA, and DVB in a PVT matrix
EJ-290	Plastic formulated using Eljen's proprietary casting resin cured and machined at Eljen
EJ-276	PSD plastic which has been formulated to replace EJ-299-33
EJ-200NF	Advanced EJ-200 formulation to address the fogging issue in portal monitors

of 12.5 mm. The rate of separation of the crosshead is provided in Table 2.2 along with other experimental parameters such as the data sampling rate, nominal cross-sectional area of the narrow section of the sample, and whether or not the nominal or measured cross-sectional area was used for calculating the stress on the sample. A small pre-load force (18N) was applied to all samples in order to remove slack in the system prior to recording data.

Using the strain and applied force data, stress vs. strain curves were then constructed. From this data the maximum tensile stress and the tensile modulus of each sample were determined. The tensile stress is defined as the applied force divided by the cross-sectional area of the narrow portion of the sample. This is shown in Equation 2.1, where P is the load/applied force, and $\langle a \rangle$ is the average cross sectional area of the neck of the dog bone sample from measuring at the top, middle, and bottom of the neck. The tensile strain is defined here as the elongation within the extensometer, Δl, divided by the extensometer gauge length, l_g, as shown in Equation 2.2. In order to find the maximum tensile stress, the stress vs. strain data was first smoothed using a centered moving average containing 21 data samples. The number of data samples in the moving average was chosen to minimize the mean square error (from adding too many data points) and to also minimize the oscillatory effect in the mean square error which is observed from adding in additional data points for inclusion in the mean calculation (a result of having too few data points). The maximum value in the stress data was then found and recorded for each sample. The tensile modulus is defined as the slope of the stress vs. strain curve. The modulus of each material sample was calculated using a minimum of 400 non-smoothed data samples taken from the Hookean (proportional) region of the stress vs. strain curves and determining the line-slope by using the least squares methodology.

$$\sigma_t = \frac{P}{\langle a \rangle} \tag{2.1}$$

$$\epsilon_t = \frac{\Delta l}{l_g} \tag{2.2}$$

Table 2.2: Mechanical Testing Parameters

Test Material	Tensile Test Parameters					Flexural Test Parameters					
	Sample Type	N Samples	Measured or nominal dimensions	Crosshead Rate (mm/min)	Sampling Rate (Hz)	Sample Type	N Samples	Measured or nominal dimensions	Support Span (mm)	Crosshead Rate (mm/min)	Sampling Rate (Hz)
PD-02-55.02	V	5	Meas.	0.3	50	Sm.	5	Meas.	52	1.387	50
PD-02-55.02 (Sn)	V	6	Meas.	0.3	50	Sm.	7	Meas.	52	1.387	50
EJ200	V	5	Meas.	0.3	50	Sm.	5	Meas.	52	1.387	50
EJ200-PS	V	5	Meas.	0.3	50	Sm.	5	Meas.	52	1.387	50
EJ200	IV	5	Nom.	1.5	100	Lg.	5	Nom.	100.3	0.256	100
EJ200-PS	IV	5	Nom.	1.5	100	Lg.	5	Nom.	100.3	0.256	100
EJ200-PSXL	IV	5	Nom.	1.5	100	Lg.	5	Nom.	100.3	0.256	100
EJ299-33	IV	5	Nom.	0.75	50	Lg.	4	Meas.	101	0.675	50
EJ299-33-XL	IV	5	Nom.	1.5	100	Lg.	5	Nom.	100.3	0.254	100
N555V	-	-	-	-	-	Lg.	4	Meas.	101	0.675	50
EJ270	V	5	Meas.	0.3	50	Sm.	5	Meas.	52	13.87	50
EJ290	V	5	Meas.	0.3	50	Sm.	5	Meas.	52	1.387	50
EJ276	V	5	Meas.	0.3	50	Sm.	6	Meas.	52	13.87	50
EJ200NF	V	5	Meas.	0.3	50	Sm.	6	Meas.	52	1.387	50

The tensile samples of EJ-270, EJ-290, EJ-276, and EJ-200NF were measured using an Instron ElectroPuls^{TM}All-Electric Dynamic Test Instrument outfitted with Screw Side-Action Grips to affix the small ASTM type V dogbone samples. The strain on these samples was measured using an Epsilon 3442-005M-020-ST extensometer. Data was collected using Instron's BLUEHILL^{TM}experimental control and data collection suite. The gauge length of the Epsilon extensometer is 5 mm. Even so, the instructions indicated that a gauge length of 10 mm should be entered into the BLUEHILL^{TM}software. Since the origin of this instruction was not clear to the author, the 5 mm gauge length of the extensometer was entered instead. Initially observations indicated that the % strain provided by the extensometer were incorrect because the % strain recorded by the software exceeded what would have been possible based on the crosshead position (a separately measured data point). To address this, the extensometer was tested against a caliper. The extensometer was attached across the caliper opening, as the caliper was opened the extensometer reading was recorded. This was completed for multiple trials, and it was determined that the gauge length entered into the software should have in fact been 10 mm. To account for this, the moduli calculated in post was ultimately multiplied by a factor of two. This has no effect on the measured tensile strength. The testing with the extensometer and caliper is shown in the results.

2.3.2 Flexural Testing

In a manner similar to the tensile test samples, the samples for the flexural tests were also machined from large sheets or castings of bulk material into one of two sample sizes. The large samples were machined to have nominal dimensions of 127 x 25.4 x 25.4 mm (length x width x depth) while the small samples were machined to nominal dimensions of 65 x 12.7 x 3.2 mm. The testing procedures utilized for this portion of the study were derived from the ASTM standard for flexural testing, D790 [88]. The physical setup of the measurement equipment is nearly identical to the setup used for the tensile tests with two caveats: 1) the hydraulic grips are used to hold the upper and lower components of the flexural testing apparatus instead of the sample directly and 2) there is no need for use of an extensometer as the position of the loading nose is controlled directly by the system software. The flexural

testing apparatus consists of a lower component that has two points of contact separated by a variable span, L. The upper component of the apparatus has a single point of contact, the loading nose, which applies the load to the sample midway between the support span of the lower component. The radius of all contact points on the flexural testing apparatus is 5 mm. Prior to running the test, a small preload of 18N was applied to the sample. The complete list of experimental parameters used is outlined in Table 2.2 alongside the tensile test parameters. It should be noted, that ASTM standard D790 requires the support span be 16± 1 times longer than the depth and that the ends of the sample have an overhang of 10% of the support span extruding beyond the lower supports. The small samples can meet this requirement whilst the large samples maintain a span-to-depth ratio of approximately 4:1. The effects of this are discussed more in the results section.

The MTS software provides data for the applied force and the loading nose displacement. This must be converted into flexural stress and flexural strain according to Equations 2.3 and 2.4, respectively.

$$\sigma_f = \frac{3PL}{2bd^2} \tag{2.3}$$

$$\epsilon_f = \frac{6Dd}{L^2} \tag{2.4}$$

In these equations, P is the load, L is the span between the supports, b is the sample width, d is the sample depth, and D is the midspan deflection which is identical to the recorded vertical position of the loading nose. After the stress vs. strain curves are built, the maximum flexural stress and the flexural modulus of elasticity are found for each sample in an identical manner as outlined in the tensile test section.

2.3.3 Light Output Testing

The samples used for light output testing were taken from the ends of the mechanical testing samples after breaking since the material experiences little to no mechanical stress at the ends of the sample during the mechanical testing procedure. The samples were cut into a rectangular prism with nominal dimensions of 12 x 12 x 3 mm. The samples were then

incrementally polished on all sides with polishing pads up to a grit size of P2000 which has an average abrasive particulate size of 10.3 μm. The samples were then visually inspected for fracturing, as fractures in these materials are highly visible due to Fresnel reflection at the fracture boundary. No fracturing was evident under visual inspection.

The 12 x 12 mm side of the sample was mounted to a Hamamatsu R2059 PMT using Visilox V-788 optical coupling compound. The maximum quantum efficiency of the R2059 PMT in the blue spectrum matches well with the peak emission of EJ200. The sample was then covered with seven layers of white Teflon tape and sealed using four layers of black electrical tape. The PMT was operated at a bias of -1550V. The anode signal was split and sent to the trigger channel and standard channel of a CAEN DT5742b digitizer configured to acquire 1024 data samples per event at a sampling rate of 5 GS/s. A 1μCi Cs-137 source was placed 15 mm from the outer face of the scintillator sample. With the source present, the PMT was allowed to stabilize for 40 minutes on the first sample of each measurement day while same-day subsequent measurements allowed 10 minutes of stabilization time. The waveforms were utilized in post processing to calculate the pulse height spectrum with integrated charge as the abscissa.

To calculate the integrated charge, the current was found via Ohm's Law and integrated. The signal voltage was determined by distributing the 1V dynamic range across the 2^{12} ADC channels (0.244 mV/ADC channel) and the digitizer input impedance is 50 Ω. The signal baseline was determined by averaging the first 10% of samples (102 samples) for each event and then the waveform was transformed via a standard baseline correction. The integration window was set to begin 15 ns before the signal peak and end 75 ns after the signal peak which is sufficient for the typical rise/and fall times of the measured pulses, which are approximately 3ns and 20ns respectively. The waveform was integrated using trapezoidal integration and the resulting integral value was placed into a histogram structure containing 800 bins ranging from 0 - 150 pC. The histogram structure was transformed from having bin edges to having a bin value on the charge axis which is the average of the bin edges. This allowed the data to be smoothed and differentiated using a Savitsky-Golay filter [89]. The filter parameters for smoothing included using a window size of 31 bins with a second order filter. To differentiate the data, the same filter parameters were used on the smoothed data

but with the additional filter parameter of 1st order derivative. The inflection point in the spectral neighborhood of the Compton edge was used as the location of the real Compton edge energy of 478 keV. This occurs at the minimum of the calculated derivative and the process is better demonstrated in Section 2.4.3.

Since the light output measurements occurred on four separate days, the EJ200 sample was measured at the beginning of each measurement day to calculate a daily correction factor to adjust for any environmental effects and/or systematic effects in the measurement system. This factor was calculated as follows:

$$cf_n = \frac{CE_0}{CE_n} \tag{2.5}$$

where CE_0 is the Compton edge location on the charge axis for the very first EJ200 light output measurement and CE_n is the Compton edge location for the EJ200 light output measurement taken at the beginning of the nth measurement day. This correction factor was multiplied into the value of the Compton edge for all samples measured on the identical n^{th} measurement day. It should be noted that the correction factor had values of 1.002, 1.002, and 1.012, which indicates that the systematic error introduced approximately 1-1.5 % error to these measurements; the intent is that this error has been reduced by utilizing the correction factor. Regardless though, the error cannot be reduced below the 0.2 % level due to the data binning structure. After the Compton edge is located on the integrated charge axis, the value is normalized to that of the PVT-based EJ200. For reference, EJ200 has a light output of 10,000 photons per MeVee according to the manufacturer [90].

The final four samples: EJ270, EJ290, EJ276, and EJ200NF were measured in the same way as above except the digitizer used to acquire the data was a CAEN DT5720 250-MHz 4-channel desktop digitizer. The signal was not split to separate trigger and DAQ channels as was done when using the DT5742b digitizer as this was not needed since the 5720 digitizer could trigger off of each individual channel. As was done before, the relative Compton edge positions were found to determine the relative light output.

2.3.4 Dynamic Mechanical Analysis

As mentioned in Chapter 1, a large part of the collaboration working under the DTRA grant funding this work is based at UCLA with the goal of developing and characterizing new, mechanically robust, high-z or high wt/% concentration PPO loaded plastic scintillators. As part of the characterization effort, the UCLA team utilizes a dynamic mechanical analyzer (DMA) to determine storage and loss moduli, $E'\&E''$, as a function of temperature in order to determine the glass transition temperature, T_g, of the new samples.

There is interest within the collaboration to understand if and how the moduli measured with the DMA can be compared to the moduli measured utilizing the ASTM standards. To gain an understanding of this query, five additional samples each of EJ-200 and EJ-200PS with nominal dimensions of $65 \times 12.75 \times 3.25 - mm$ were tested on the TA Instruments Q800 DMA housed at the Polymer Characterization Laboratory (PCL) within the Joint Institute for Advanced Materials (JIAM) building at the University of Tennessee. In order to maintain similar span to depth ratios (16:1) as used in the D790 tests, a three point bending kit with a fixture having a 50 mm span was acquired from TA Instruments. It is believed, due to the results of flexural testing, that the span to depth ratio has a significant factor on the outcome of flexural modulus and strength measurements. It is likely that this has to do with the strain regime for which Equations 2.3 and 2.4 are valid. It is believed that smaller samples, than required by ASTM standards, with similar 16:1 span to depth ratios may still produce measured values which are comparable to those larger samples as specified by ASTM. However, this is not examined in this work.

To complete the DMA testing, an isothermal frequency sweep was performed from 0.1Hz to 10Hz on a logarithmic scale at $25\,^{\circ}C$. Measurements were taken at 20 frequencies in total. All sample dimensions were measured before DMA testing to the nearest 1/100th of a millimeter and were input into the DMA software for internal modulus calculations to be performed. The storage and loss modulus for each frequency were saved to an individual data file for each sample.

Consideration was given to a method by which frequency domain measurements are transformed to time domain via an integral transform as shown in Equation 2.6, where $E(t)$

is the relaxation modulus, $E'(\omega)$ is the storage modulus, and ω is the DMA oscillation frequency. This method was demonstrated recently in [91].

$$E(t) = \frac{2}{\pi} \int_0^\infty \frac{E'(\omega)}{\omega} \sin(\omega t)\, \mathrm{d}\omega \tag{2.6}$$

Solutions to Equation 2.6 require measuring E', $\forall\, \omega \in (0, \infty)$; this creates the so called 'master curve' of storage modulus vs. frequency at a reference temperature. The direct measurement of this is not only impractical, but impossible to achieve in practice. This may be rectified, though, through the use of the time-temperature superposition (TTS) principle and the application of the Williams-Landel-Ferry equation as shown in 2.7, where a_T is the ratio of the materials' relaxation time at a temperature,T, to the relaxation time at a reference temperature, T_0, (a_T is also referred to as the frequency shift factor); the values of C_1 and C_2 are empirical fitting constants [92].

$$\log_{10}(a_T) = \frac{-C_1 (T - T_0)}{C_2 + (T - T_0)} \tag{2.7}$$

The general gist of the TTS principle says that a storage modulus measured over a range of frequencies, (ω_1, ω_2) at a given temperature, T, may be shifted horizontally (and/or vertically) to obtain the storage modulus over a different range of frequencies at a different temperature. Instead of measuring over frequencies from $(0, \infty)$, one may measure the storage modulus over a given range of frequencies, (e.g. 0.1 Hz - 100 Hz), at many temperatures. If the master curve at $T = 25\,^\circ C$ is to be generated, then measurements taken above $25\,^\circ C$ would correspond to lower frequencies (since the viscous flow becomes more predominant, as would be the case in lower frequency/longer time measurements), and measurements taken below $25\,^\circ C$ would correspond to higher frequencies. After measurements at a sufficient number of temperatures have been obtained, a single master curve may be generated in a sufficiently well described manner that it may be fit to a smooth sigmoid type function which is able to be integrated (even if only numerically). This type of function is shown in Equation 2.8 [91].

$$E'(\omega) = a \tanh[b(\ln \omega + c)] + d \tag{2.8}$$

Once the relaxation modulus, $E(t)$, is found, stress and strain curves may be built where the stress is defined by Equation 2.9 and the strain is defined by Equation 2.10 where $\dot{\epsilon}$ is the strain rate used in the time domain experiment and t' is a dummy variable for integration.

$$\sigma(t) = \dot{\epsilon} \int_0^t E(t')\mathrm{d}t' \tag{2.9}$$

$$\epsilon(t) = \dot{\epsilon}t \tag{2.10}$$

Of course, once a stress-strain curve is built, the time domain modulus for that particular mode of deformation may be found. Ideally the modulus derived from the DMA experiment would agree with the modulus found using time domain methods. Nevertheless, this approach was not utilized due to uncertainties surrounding the assumptions made when applying the TTS principle, see [93]. Particularly, uncertainty exists as to if these assumptions allow the TTS principle to be valid for PVT and PS scintillators in addition to the nanocomposites and high wt/% PPO samples fabricated by UCLA; after all, this method is only useful to our collaboration if it can be used for these materials. Another aspect to consider, is that as many samples would be required as the number of temperatures which are being tested. This would have the result of increasing the burden on the fabrication team.

2.4 Results and Discussion

In order to have a meaningful picture of the mechanical testing data, the relevant values for two common structural plastics, acrylonitrile butadiene styrene (ABS) plastic and polylactic acid (PLA) based plastic are also provided. These values come from Matweb in the categories of *Overview of material for ABS, sheet* [94] and *Overview of materials for Polylactic Acid (PLA) Biopolymer* [95].

2.4.1 Tensile Testing Results

The results of the tensile tests are shown in Figures 2.2 and 2.3. There is good agreement within the bounds of statistical uncertainty across the two different sample types (type IV

and type V) in the two cases where the same material was used: EJ200 and EJ200-PS. This is due to the fact that the cross sectional area used to calculate the stress and the applied stressing force are parallel to each other. This makes calculating the stress, which is a pressure (force per unit area), a rather straightforward operation, even for the two different sample sizes. Aside from assessing that the materials across sample types can be directly compared, it is also apparent that while three of the materials are stronger than the average ABS plastic, none are stronger than the average PLA plastic. On the other hand, all the materials are stiffer (have a higher tensile modulus) than the average ABS plastic whilst four of the tested materials are stiffer than even the average PLA plastic. In general, this appears to indicate that plastic scintillators tend to be slightly more brittle than the common structural ABS and PLA plastics.

When identifying the effects of modifications to a particular plastic base (e.g., crosslinking EJ200-PS) several things stand out. The first thing that stands out (and has been previously known) is that the polymer base matters; the PVT based EJ200 is not quite as strong or stiff as the PS-based counterpart. Additionally, it is apparent with these results that crosslinking as implemented has a larger effect on some base/fluor mixtures than others. For instance, a significant increase in the strength and stiffness of EJ299-33 can be observed in its crosslinked counterpart EJ299-33-XL, but this effect is not as dramatic when one compares the results from EJ200-PS to EJ200PS-XL. This could be due perhaps to the particular choice in the crosslinking molecule for EJ200-PS or due to an upper limit on the added strength which can be provided by crosslinking molecules in reference to the initial strength of the base. Furthermore, it appears that by doping in organometallic complexes, at least as implemented in the 5 wt/% tin loaded sample, a very small or perhaps negligible decrease in strength and stiffness results.

In regards to the materials which were tested at a later date using the Instron Dynamic Test Instrument, (i.e. EJ270, EJ290, EJ276, and EJ200NF), the summary results are as follows. Lithium loaded EJ270 is the weakest of these four materials under tensile deformation with a strength of 21.9 MPa, which is only marginally stronger than the weakest measured material, EJ299-33. The strength of both EJ290 and EJ276 are quite comparable to one another, both are weaker than both the PVT and PS based EJ200. The tensile

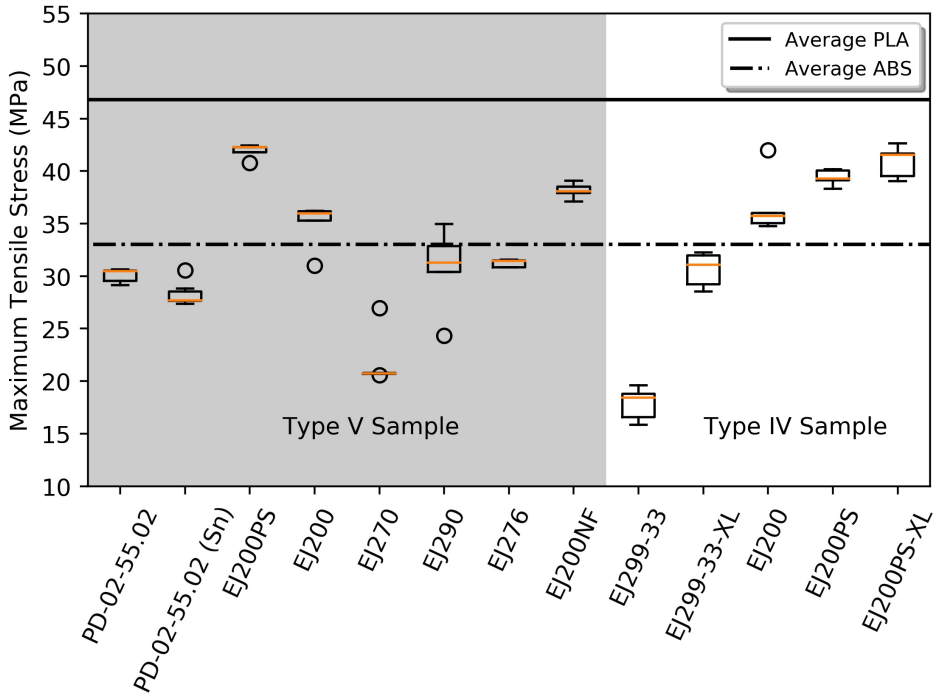


Figure 2.2: Boxplot of the maximum tensile stress (MPa) of the tested materials shown alongside average PLA and ABS values.

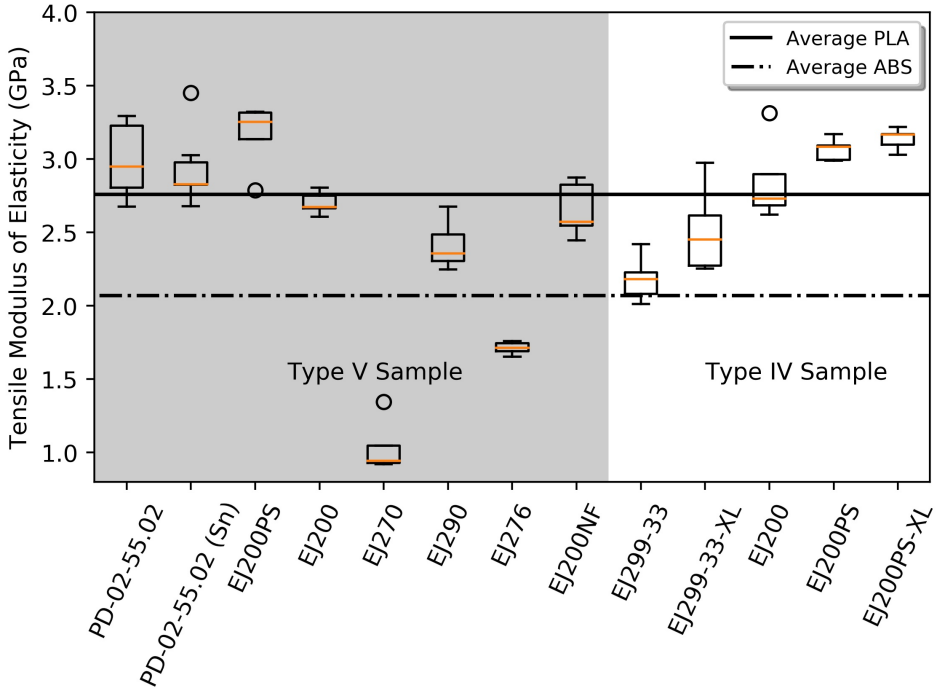


Figure 2.3: Boxplot of the tensile modulus of elasticity (GPa) of the tested materials shown alongside average PLA and ABS values.

strength of EJ-200NF comes in at 38.1 MPa which is right between the strength of the PVT and PS based EJ-200. EJ-270 was not only quite weak, but also has the lowest recorded tensile modulus by a significant margin. The modulus for EJ290 is less than both EJ200 and EJ200PS, coming in at a level comparable to EJ299-33-XL. EJ276 has the second lowest recorded tensile modulus, coming in even lower than the EJ299-33 and 33-XL counterparts. This makes EJ276 as strong as EJ299-33-XL, but more 'stretchy', indicating that it is less brittle than EJ299-33-XL. Lastly, the modulus for EJ200NF is most comparable to EJ200. This ultimately means that EJ200NF is marginally stronger than EJ200 but with comparable moduli. The end result is that EJ200NF is marginally less brittle than EJ200. This is an interesting result given some thoughts that have been provided on the kinetics of fogging in plastics [96].

The final result for tensile testing rests not in the results for the materials, but in the acknowledgment that an error was made during data collection and corrected in post processing. This applies only to the modulus measurements for those final four materials measured on the Instron apparatus. Since the extensometer had a 5 mm gauge length, the amount for the gauge length entered into the software was 5 mm even though passed-down instructions said it should be 10 mm. Upon processing the data and seeing really low modulus values, an experiment was conducted using the extensometer and a caliper. The extensometer was affixed to the caliper in such a way as to measure the gap in the caliper jaws. The reading of the caliper was recorded as the abscissa while the strain was recorded as the ordinate. The results of four trials are shown in Figure 2.4 along with linear least-squares fits and corresponding equations. The slope of these lines average to near 0.4 mm/mm/mm (strain/caliper). Referencing back to Equation 2.2, and multiplying by the extensometer gauge length of 5 mm yields a slope of 2 mm/mm (extensometer measure/caliper measure), indicating that the extensometer readings were two times higher than they should have been. Since the modulus is inversely proportional to the strain, this required multiplying the modulus values by a factor of two in order to bring them into compliance with reality. This would also yield the same result as using a value of 10 mm for the gauge length in the software while utilizing 5 mm as the extensometer gauge length to convert from strain to Δl values.

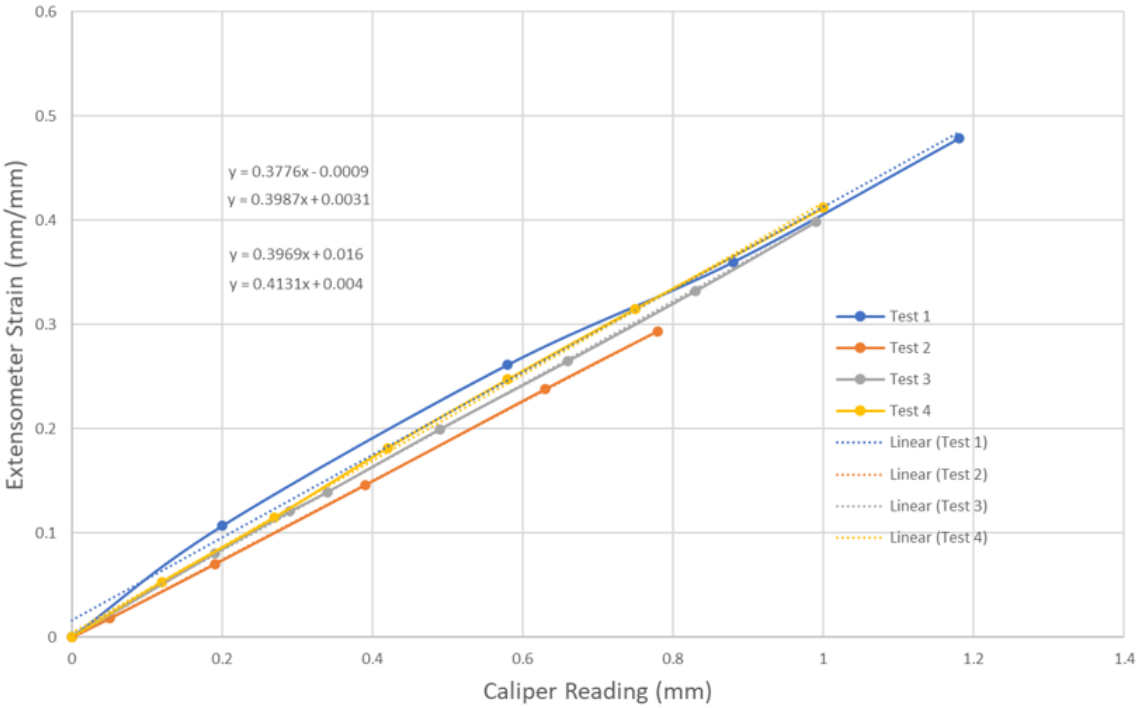


Figure 2.4: A plot showing four trials, and linear fits, using the extensometer affixed to the caliper to determine what the proper software gauge length should be. For these trials, the gauge length was set to 5 mm. The results of these trials show that the gauge length should have been 10 mm.

2.4.2 Flexural Testing Results

The results for the flexural tests are highlighted in Figures 2.5 and 2.6. Unlike in the case of the tensile testing, the results generated from the large and small flexural samples of the same material do not agree. The stress calculation is not so straightforward since the force and resisting cross sectional area are perpendicular to each other. Because of this, Equations 2.3 and 2.4 from ASTM D790 are likely based on a set of assumptions which only make them valid in the regime where the span to depth ratio of the sample is approximately 16:1 (i.e. in the flexural mode of strain as opposed to the shear mode of strain). This is where it is believed that the discrepancy originates between the results from the large and small flexural test specimens of the same material. Despite this fact, it is observed in the figures that the difference in the measured means of maximum flexural stress between the two baseline materials (EJ200 and EJ200PS) within the small and large size classes is statistically identical, having a value of 11±6 MPa for the small samples and 9.1±1.7 MPa for the large sample sizes. This may imply that the results from the large samples can easily be mapped to the same scale of comparison as the small samples by adding a baseline shift of 14±4 MPa to their maximum flexural stress values.

This type of direct mapping does not appear to be applicable in the case of the flexural modulus. Instead, a qualitative reasoning can be used by comparing other materials of the same size to the EJ200 and EJ200PS values within both size classes. For example, in Figure 2.6 it is apparent that PD-02-55.02 has a somewhat smaller flexural modulus than EJ200 when comparing within the small sample class. This means, then, that within the large sample class it can be expected that PD-02-05.22 is also somewhat less than EJ200 which further implies that PD-02-05.22 is not as stiff as N555V, EJ200PS, and EJ200PS-XL.

Using the means of comparison given above, the flexural testing results, and the conclusions which can be drawn from them, are quite similar to the results and conclusions provided by the tensile tests. Perhaps the primary exception to this is that the flexural modulus of the tested materials does not appear to exceed the flexural modulus of PLA plastic to the same level as observed with the tensile modulus.

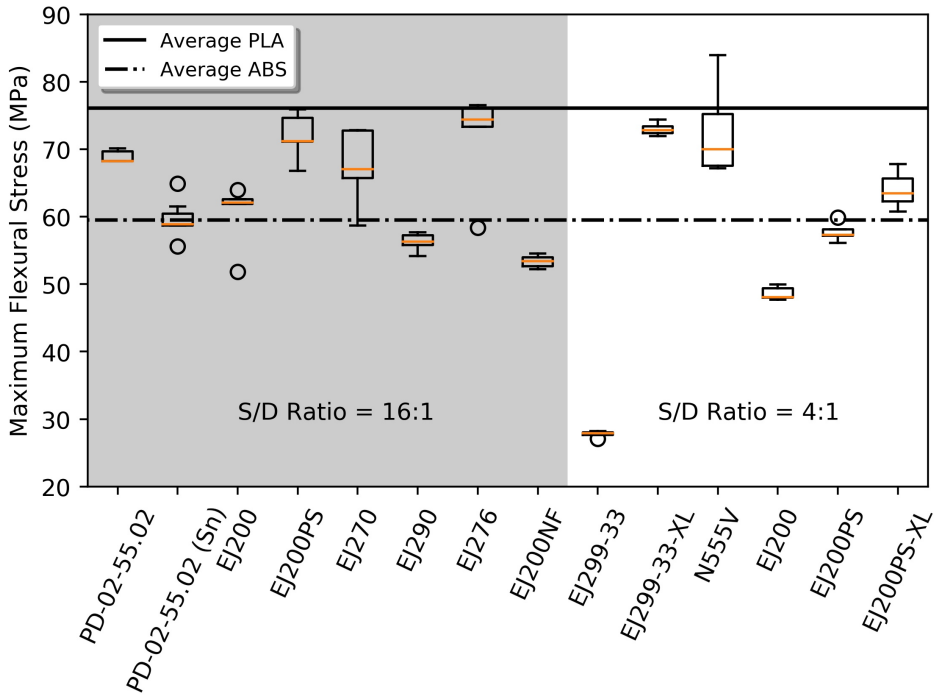


Figure 2.5: Boxplot of the maximum flexural stress (MPa) of the tested materials shown alongside average PLA and ABS values.

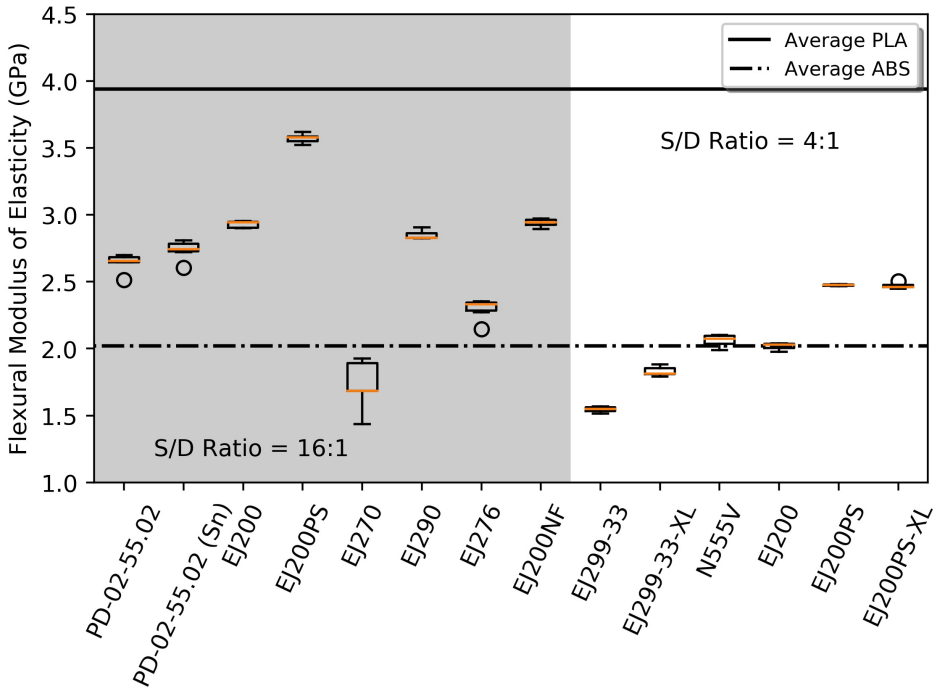


Figure 2.6: Boxplot of the flexural modulus of elasticity (GPa) of the tested materials shown alongside average PLA and ABS values.

Now some mention should be given to the last material additions to the bank of flexural tests, again these are EJ270, EJ290, EJ276, and EJ200NF. Some interesting behaviors are seen here in that the relative flexural moduli and strength do not track with each other as they do in the tensile tests. In fact, they are inverted. The relative flexural moduli track well with the relative tensile moduli, but the relative values for the maximum flexural stress are inverted compared to the relative values of the maximum tensile stress for these samples. This seems to indicate some type of anisotropy in the mechanical response of these materials.

2.4.3 Results of Light Output Testing

Figure 2.7 illustrates how the Compton edge energy is determined from the integrated charge spectrum using the inflection point methodology. All numerical light output values are reported in Table 2.3 as being relative to EJ200. As indicated by Figure 2.7 and Table 2.3, most light output values are relatively close to each other with the most collected charge coming from EJ200 and the least coming from EJ270. The results indicate that EJ270 has a light output that is 47% of EJ200, which agrees quite well with the 4,800 photons/MeVee found in the literature [97]. In regards to the effects of crosslinking molecules being added to a particular system, there is no noticeable effect on the light output of EJ200PS vs. EJ200PS-XL and only a minimal effect on EJ299-33 vs. EJ299-33-XL. The addition of Sn to PD-02-05.22 appears to have a negligible effect on the light output with a light output 82% of EJ200 vs. 83% in the Sn loaded case, these indicate no difference given the margin of error $\pm$ 1%.

The difference in error margins for EJ270, EJ290, EJ276, and EJ200NF light output measurements stems from uncertainties related to the now aged EJ200 reference sample and the disparities seen for EJ290 and EJ276 as compared to the manufacturer stated values. For EJ290, Eljen states a light yield of 90% EJ200, vs. our measured 84%. In the case of EJ276, Eljen states a light yield of 86% EJ200, vs. our measured 91%. It is possible, perhaps, that the difference could come from different radioluminescence (RL) spectra and therefore differing PMT sensitivities. However, the available RL spectra indicate nearly identical features with a primary emission peak near 425 nm and a low intensity secondary emission peak near 460 nm, all superimposed on a slight decay of intensity from the peak at

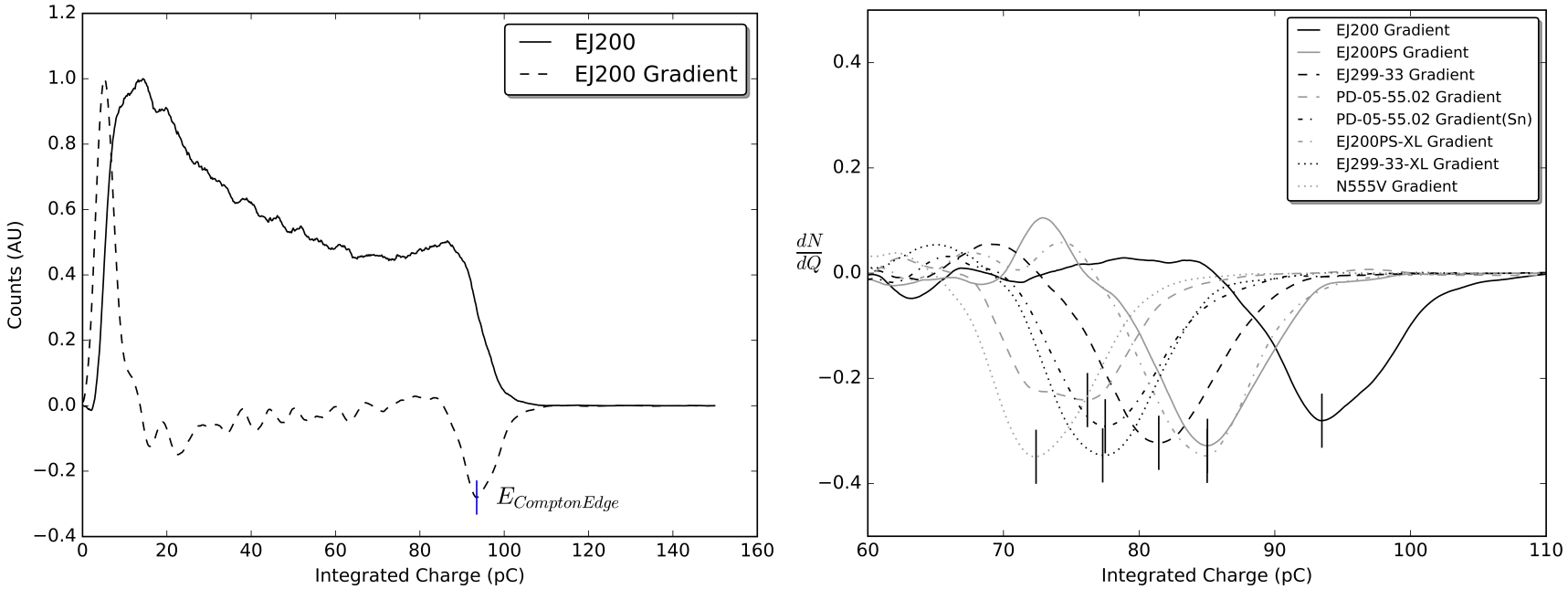


Figure 2.7: **(a)** Demonstration of locating the Compton edge on the Cs-137 spectrum using the inflection point found by the derivative. **(b)** Location of the Cs-137 inflection points for all investigated materials.

Table 2.3: Results from Mechanical and Light Output Testing

Test Material	Tensile Testing Results			Flexural Testing Results			Relative Light Output @ 478 keV, ± 0.01
	Sample Type	Tensile Strength (MPa)	Tensile Modulus (GPa)	Sample Type	Flexural Strength (MPa)	Flexural Modulus (GPa)	
PD-02-55.02	V	30.1±0.6	2.99±0.24	Sm.	68.9±0.9	2.64±0.07	0.82
PD-02-55.02 (Sn)	V	28.3±1.1	2.94±0.25	Sm.	59.7±2.9	2.74±0.07	0.83
EJ200	V	34.9±2.0	2.70±0.07	Sm.	60±5	2.930±0.026	1.00
EJ200-PS	V	41.9±0.6	3.16±0.20	Sm.	72±4	3.57±0.04	0.91
EJ200	IV	36.7±2.7	2.85±0.27	Lg.	48.6±1.0	2.017±0.026	1.00
EJ200-PS	IV	39.4±0.7	3.07±0.07	Lg.	57.7±1.4	2.474±0.008	0.91
EJ200-PSXL	IV	40.9±1.4	3.14±0.07	Lg.	64.0±2.8	2.470±0.022	0.91
EJ299-33	IV	17.9±1.4	2.18±0.14	Lg.	27.8±0.5	1.545±0.023	0.87
EJ299-33-XL	IV	30.6±1.5	2.51±0.27	Lg.	73.0±0.9	1.83±0.04	0.83
N555V	-	-	-	Lg.	73±8	2.06±0.05	0.77
EJ270	V	21.9±2.8	1.04±0.18	Sm.	67±6	1.72±0.20	0.47±0.08
EJ290	V	31±4	2.41±0.17	Sm.	56.2±1.4	2.85±0.03	0.84±0.08
EJ276	V	31.2±0.4	1.7±0.8	Sm.	72±7	2.30±0.08	0.91±0.08
EJ200NF	V	38.1±0.7	2.7±0.4	Sm.	53.4±0.9	2.94±0.03	0.87±0.08

425 nm to around 10% of maximum at 500 nm. However, there is a very slight green-shift, ∼5 nm, for the EJ290 sample.

2.4.4 Dynamic Mechanical Analysis Results

The results for the frequency sweep DMA tests are shown in Figures 2.8 and 2.9. These figures show the value of the storage modulus vs. frequency for each sample and for each material, where the data point indicates the mean value of the modulus and the error bar is plus and minus one standard deviation from the mean. These data indicate that higher frequencies result in higher moduli, which is not too surprising as the molecules have less and less time to relax and thus reduce the stress required to achieve 1% strain. Also, for all frequencies, PS based EJ200 has a higher storage modulus than PVT based EJ200, which is consistent with the data from the D790 testing procedure.

The ultimate goal of the DMA measurements is to show how well they may compare to tests carried out using the ASTM standard, D790. To do this, it is important to set controls for everything as closely as possible. Several controls have already been accounted for, though one more remains. At this point in the analysis the DMA modulus has been measured at multiple frequencies. The last step to getting a comparable value, then, will be to choose the frequency which has a corresponding strain rate as close as achievable to the strain rates used in the D790 experiments. The ASTM D790 standard requires a strain rate of 1%/min for Procedure A and a 10%/min strain rate for procedure B. For the small EJ200 PVT and PS materials, procedure A was used. This corresponds to the crosshead rate of 1.387 mm/min. The lowest frequency in the DMA test was 0.1 Hz. At this frequency, the oscillation drove the sample from the equilibrium position to 1% strain once every ten seconds. This means that the time to go from 0% strain to 1% strain is 5 s. The *average* strain rate for the 0.1 Hz oscillation frequency, then, is 12%/min. This is quite close to the procedure B strain rate, but is approximately a factor of 10 larger than the procedure A strain rate. In order to achieve the average 1%/min strain rate on the DMA, a frequency of 0.0083 Hz should be used. However, this is below the 0.01 Hz operating limit of the DMA. Furthermore, testing at that low of a frequency drives up the experiment run time (by a factor of 10) which would be impractical for this test bank, which took ∼1 week to complete

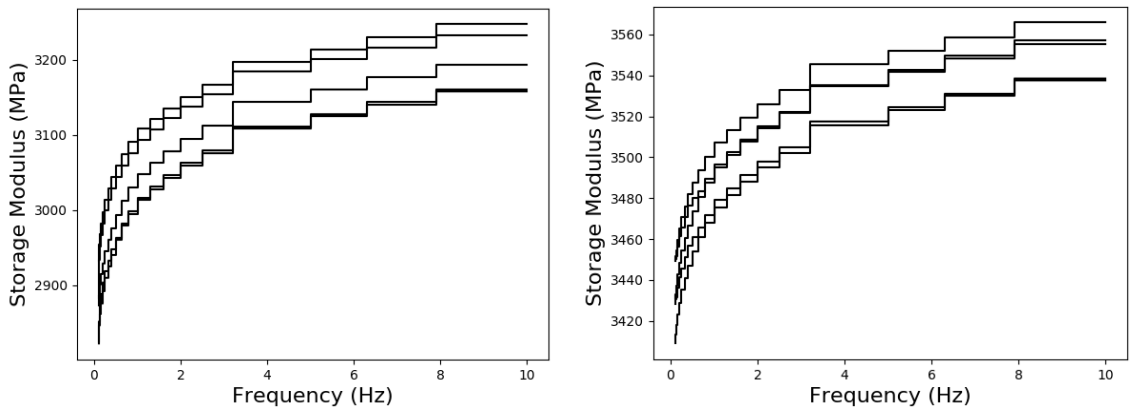


Figure 2.8: The DMA measured storage modulus in an isothermal frequency sweep test from 0.1 Hz to 10 Hz at $25\,^{\circ}C$. **(a)** Results for PVT samples. **(b)** Results for PS samples.

by itself. At any rate, this leaves no choice but to use the values of the modulus taken at the frequency of 0.1 Hz. A comparison of the D790 flexural module, DMA modulus (sum of the loss and storage modulus in quadrature), and storage modulus is provided in Figure 2.10.

The percent difference between the D790 flexural modulus and the DMA modulus at 0.1 Hz was calculated according to Equation 2.11, which is the standard equation for the percent difference with the standard treatment for propagation of error.

$$\Delta(\%) = 100 \times \left[\frac{E_{DMA} - E_{D790}}{E_{D790}} \pm \left(\left(\frac{1}{E_{D790}} \right)^2 \sigma_{DMA}^2 + \left(\frac{E_{DMA}}{E_{D790}^2} \right)^2 \sigma_{D790}^2 \right)^{\frac{1}{2}} \right] \tag{2.11}$$

The results show that the DMA modulus is $2.2 \pm 1.8\,\%$ lower for EJ200 and $3.9 \pm 1.1\,\%$ lower for EJ200PS than the flexural modulus measured using the D790 procedure A. As a reference, the ASTM D790 procedure indicates that standard between-lab differences in the measured flexural modulus for a plastic normally range between 4% and 16% for any given material [88]. For these materials, then, the DMA modulus at 0.1 Hz and the flexural modulus from using ASTM D790 are in agreement. Though this will likely not apply to all viscoelastics, and likely works well for these material due to the very low loss modulus (inferred from Figure 2.10) at this temperature and strain rate/frequency. In the case of smaller samples, such as those that may be synthesized by UCLA, it may still be possible to use this approach so long as the span to depth ratio remains approximately 16:1. For a bar shaped sample, that can be supported on a 10 mm span, this would require a depth (or sample thickness) of 0.625 mm. However, this approach and assumption would still need to be verified.

2.5 Conclusion

We have made measurements on a variety of plastic scintillating materials to gather data that may help one 1) determine whether these scintillating materials are suitable as structural materials for particular applications and 2) better understand the expected effects of chemical modifications, such as crosslinking or doping organometallic complexes into the polymer

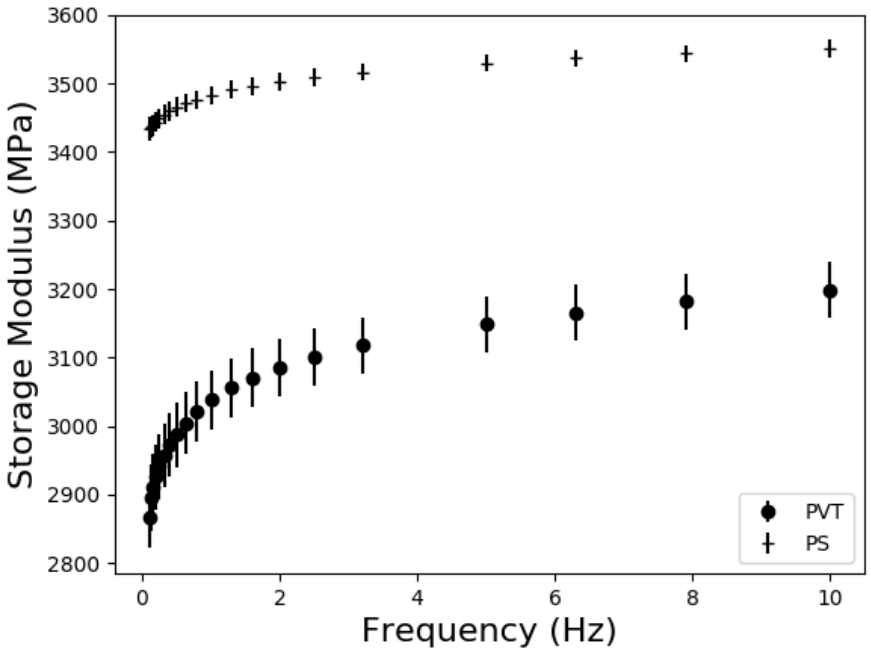


Figure 2.9: Average storage modulus values vs. frequency for PVT and PS. Error bars are ± one standard deviation.

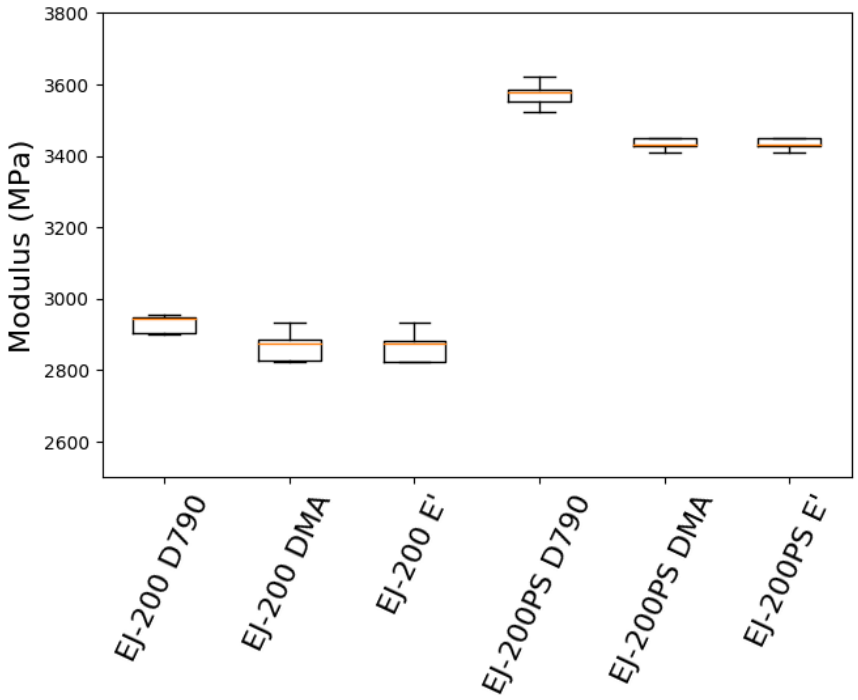


Figure 2.10: Boxplot of the flexural modulus (D790), DMA modulus, and storage modulus of PVT and PS based plastic scintillator. The box outlines the 2^{nd} and 3^{rd} quartiles, the whiskers bound the lower edge of the 1^{st} quartile and upper edge of the 4^{th} quartile. Outliers are marked with a circle.

matrix, on the mechanical and radiation detection properties. Crosslinking the matrix can significantly improve the mechanical strength and this has been demonstrated to have a most significant effect when the polymer has been quite loaded with fluors, as in the case of EJ299-33, to the point that it becomes soft. However, the effect of crosslinking on the mechanical properties of an organic scintillator is not always observed to be so significant. Either by properties of the base material, crosslink selection, or combination of the two, a gain in mechanical strength is not always observed, as in the case of crosslinking EJ200PS. The effect of crosslinking on light output appears to be minimal with only a 5% loss observed by crosslinking EJ299-33 and no loss observed by crosslinking EJ299PS. Doping Sn based organometallic complexes into PD-02-55.02 did cause a decrease in the mechanical strength of this material, but it also appears to have slightly increased the light output. The sample with the lowest light output was determined to be EJ270, which also happens to have poor mechanical robustness.

These findings further indicate that the mechanical strength of most of the tested organic scintillators is comparable to and in some cases greater than that of ABS plastic, though not necessarily as strong as the more robust PLA plastic. Further still, it has been shown that chemical methods can effectively be utilized to enhance mechanical properties of the material without having a significant impact on the light output of the scintillator, which is important for radiation detection and identification purposes. The key to advancing these materials further, then, remains in the realm of organic and polymer chemistry.

Lastly, comparisons between the DMA modulus (from three point bending) and the measured flexural modulus utilizing the ASTM D790 procedure have been shown to be comparable to each other for EJ200 formulated with both PVT and PS bases.

2.6 Acknowledgments

This material is based on work supported in part by the Defense Threat Reduction Agency under grant number HDTRA 1-18-1-005, in part by the Department of Energy National Nuclear Security Administration through the Nuclear Science and Security Consortium under

Award Number DE-NA-0003180, and in part by BAE Systems Contract No. W911NF-08-2-0004.

Chapter 3

Optical Surface Model Selection in GEANT4 for High Aspect Ratio EJ-200

At the time of submitting this dissertation, the following chapter was concurrently being prepared for submission for publication as one of the authors PJAs. The co-authors of this to-be-submitted PJA are: C. Delzer, and J. Hayward.

3.1 Abstract

The optical response of scintillators is directly coupled to many of the performance characteristics of these materials. As such, it is important for the designers of scintillation detectors to adequately be able to predict the detector response for a given configuration prior to constructing the final detector assembly. This process is usually carried out by utilizing codes for optical transport modeling such as Zemax or GEANT4. Despite significant advances in modeling of the optical surfaces in the 1980's-2000's, many of the prepackaged optical surface models in GEANT4 are not well understood by many users of the code and its derivatives (such as GATE). With parameterized models containing up to 9 parameters, or look-up-table models derived from measurements on select scintillator materials, choosing an appropriate model is not very straightforward. In response to this, and in an effort

to understand which model performs better in a practical application, experiments are performed on polished EJ-200 samples with aspect ratios of 2:1, 8:1, and 16:1 using a calibrated photomultiplier tube. Three cross-sectional area types are investigated along with three surface reflectors: Teflon, aluminum foil, or titanium dioxide paint. The experimental results are compared to the model result for both the *unified* and LUT (LBNL) models with reasonably selected parameters. Early results show that the *unified* model performs better in absolute terms when compared to the LUT model for the chosen parameters.

3.2 Introduction

Plastic scintillators have been in use as radiation detectors for many decades due to their low price per unit volume and ability to be readily manufactured in a variety of shapes and sizes. Some of the shape and size combinations useful for a variety of applications result in high aspect ratio geometries. Modeling the combined radiation and optical response of these geometries is informative in design applications but comes with a host of difficulties and assumptions which are not very well understood in relation to the performance prediction capability of real-world scintillators. One of the significant assumptions concerns the choice of the optical surface model. The importance of the optical surface model should not be understated, especially for high aspect ratio configurations, which, by their geometry alone, force more surface interactions to occur.

Many surface models exist in GEANT4 including *glisur*, *unified*, LUT (LBNL), DAVIS (LUT), and now dichroic [43]. There is a lot of overlap between the *glisur* and *unified* models, with *unified* being the most flexible and therefore the selected parameterized model [98]. The LUT and DAVIS models are both in the form of lookup tables with LUT having the broadest count of surface selection options and therefore the selected look up table model [99, 100]. The assumptions within the *unified* model are: 1) the reflectors are either purely specular or purely Lambertian (denoted by 'PolishedxPainted' or 'GroundxPainted'), 2) the probability of reflection off of the reflector has no angular dependence, 3) the surface roughness of the scintillator may be described by microfacets whose surface normal deviates from the average surface normal according to a Gaussian with a standard deviation equal to the parameter

sigma_alpha, 4) if reflection occurs off the microfacet, it is either specular, specular lobe, back scatter, or Lambertian, according to user-set probabilities. A cartoon illustrating the *unified* model is shown in Figure 3.1. Aside from the non-physicality of some of these assumptions, there is uncertainty regarding what the appropriate values for these parameters should be for a given system. Additionally, surface scattering profiles do exist in real life which are not well described by any combination of the four scattering types [99, 101, 102].

The LUT model, on the other hand, is based on relative light intensity measurements with a laser impinging a hemisphere of BGO with a selected reflector on the flat side and an arch of photodiodes that would sweep over the surface of the hemisphere. The 35 photodiodes themselves subtend 5° in ϕ and the arch supporting this array goes from -90° to 90° in 4° steps for θ. The laser would sweep over 2° to 82° in 4° steps in θ while remaining at $\phi = 90°$. Uncertainties related to these measurements were not quantified, but measurements which would have error greater than 1° were avoided and not reported. Because of this, it is believed that the angular uncertainties were kept below 1°; the uncertainties in the relative reflectivity were not discussed or are they known. Assumptions related to using the LUT model are: 1) that the light scattering kernel internal to a BGO crystal is comparable to that of other crystals/materials, and 2) the probability of reflection has no angular dependence. A cartoon of the LUT model is provided in Figure 3.2. The need to specify reflectivity for LUT models is not indicated in the GEANT4 documentation, but, upon examining the code, it is clear that reflectivity must be specified by the user; otherwise, no surface absorption will occur. If the photon is reflected, then it reflects into an angle selected from a probability distribution which varies given the incident angle. Ultimately, one is again faced with a breakdown in physicality, but one is spared the problem of 'guessing' very many unknown parameters. In the LUT model, total internal reflection cannot be fully taken into account since the reflectivity is not dependent on the incident angle.

The purpose of this work is to investigate which of these models perform the best, given a set of parameters, in the context of high aspect ratio EJ-200, which is of interest in applications including fast neutron block detectors, the single volume scatter camera, and structural components that may be used, for example, in unmanned vehicles. This improved understanding can lead to improved detector performance predictions.

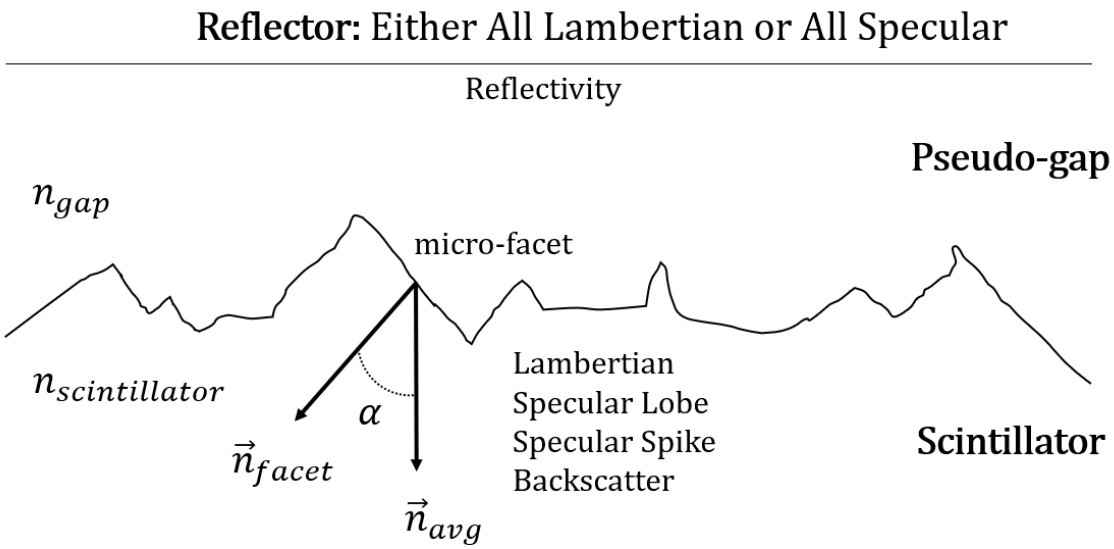


Figure 3.1: Diagram of the *unified* model implementation of the dielectric-dielectric surface type with the backpainted finish. When a photon encounters the surface, the first completed operation is the determinination of the angle α based on a Gaussian with the mean direction corresponding to n_{avg}, and standard deviation of sigma_alpha. Then, it is determined if the photon reflects by using Snell's Law, if it reflects, it does so according to the probabilites set by SPECULARSPIKECONSTANT, SPECULARLOBECONSTANT, BACKSCATTERCONSTANT, with the Lambertian constant being free to bring the sum of the four constants to 1. If the photon instead continues to the reflector it then reflects according to the probability set by REFLECTIVITY. If it reflects off of the reflector, it will only be pure Lambertian for groundXpainted finishes or pure specular for polishedXpainted finishes.

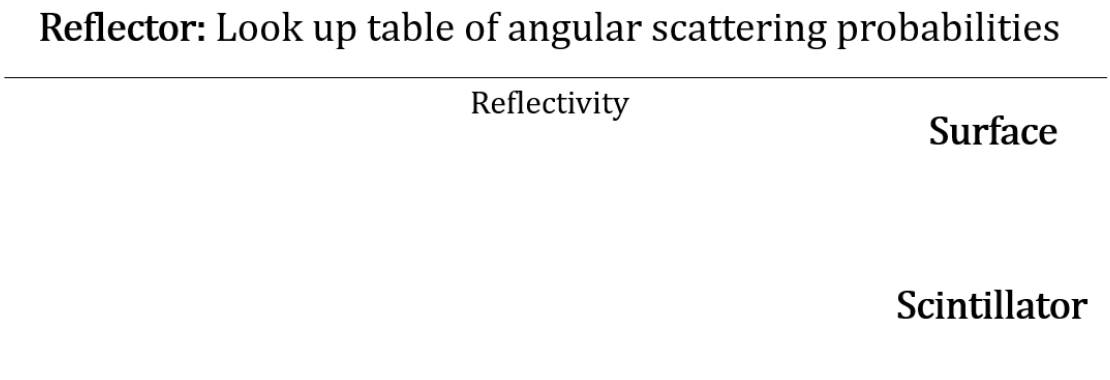


Figure 3.2: Diagram of the LUT-LBNL surface model implementation. The model only provides a scattering kernel. First the program determines if the photon reflects or not, according to REFLECTIVITY. If it does reflect then it does so according to the distribution provided by the LUT.

3.3 Methodology

Our methodology consists of comparing experimental measurements using EJ-200 coupled to a calibrated photomultiplier tube, with GEANT4 simulations which simulate the radiation interaction, scintillation light production, light transport, and photoelectron production on the photocathode.

3.3.1 Photomultiplier Tube Calibration

The photomultiplier tube used for all experiments in this study is the Hamamatsu R2059 general purpose PMT. Characteristics of this PMT were described in the introductory section on PMTs, Section 1.4. The topic of absolute PMT calibration is one that is often avoided in the field of radiation detection. In fact, the vast majority of articles which characterize scintillators utilize reference samples or fail to fully describe the method by which the utilized PMT is calibrated. In the view of the author, there is nothing wrong with the use of reference samples, as their use is often expedient and allows speedy, publishable results. Of course it should be a critical point that the reference sample be well characterized and understood as sample-sample variances are often reported for most materials and manufacturer stated values are only an expectation of the response one should receive. None the less, PMT calibration, especially in the age of desktop digitizers is not widely discussed, so a feeble attempt at that will be done here.

First and foremost, the general method used to calibrate the PMT is found in E.H. Bellamy's 1994 paper [103]. However, some critical differences exist. In the Bellamy paper, a CAMAC based LeCroy QDC was used for measuring the output of the PMT. In this experiment, a CAEN DT5720 250-MHz flash-ADC based digitizer is used. Initially, an attempt to use the 5-GHz CAEN DT5742b was made, but over the course of many months, and utilizing many tricks to process the data, no usable data came to fruition. The reason why was not well understood for quite some time, but now it seems that this failure with the DT5742b stems from a very unstable voltage baseline. This was also observed with the PSI DRS Evaluation Board which utilizes the same domino ring sampling technology that is used in the CAEN DT5742b digitizer. It is important to understand, for those who would

try and use these DRS based digitizers for PMT calibration, that they were designed for *timing* experiments and not for measurements where the voltage noise is required to be both uniform and stable over the entire data acquisition window. Another difference between this and the Bellamy paper is in the use of a light source. In the Bellamy paper a synthetic light source is used, but in this experiment the PMT is kept in a dark box which is given a slight breach to the outer room. The PMT response was monitored on an oscilloscope until noticeable random pulses appeared in the 5 mV - 20 mV range.

The PMT was calibrated at -2200V in order to produce a signal that would separate from the noise pedestal. The PMT readout was sent to CH1 of a CAEN DT5720 digitizer. In order to build the pedestal, a requirement of the method, events without any pulse need to be acquired. In order to achieve this, a trigger signal from a waveform generator was sent to CH0 of the same digitizer. The digitizer was then configured to acquire CH1 data anytime CH0 received a trigger. A block diagram for the setup is shown in Figure 3.3.

Raw waveforms from CH1 were captured and stored in ROOT files [104]. A total of 340,000 events were captured. The length of the data window was set to 1 μs, but only a fraction of this was used. Once collected, the waveforms need be converted from ADC number Vs. time to the integrated charge corresponding to the pulse area of the event. The general procedure for post-processing the waveforms is as follows: (1) find the ADC baseline value and subtract this from the total waveform, (2) correct for polarity so the resulting pulse is positively oriented, (3) convert from ADC channel to voltage, here the voltage dynamic range is 2V and the ADC is 12-bits in length, (4) integrate the area of interest, trapezoidal integration was used here, this is not to be confused with the *trapezoidal filter*, (5) divide by the integration time and the 50 Ω resistance over which the pulse was measured to arrive at the value for the integrated charge. The data window used here was statically placed from 60 ns to 350 ns. This 290 ns window was positioned so that the trigger pulse was occurring at the front third of the data window. However, given the random nature of the pulse arrival from the PMT, the window placement is not all too important.

Usually, it is sufficient to use the first 10-20 data points for determining the baseline. However, when this was done, the expected pedestal and photoelectron spectrum were significantly smeared together as shown in Figure 3.4. A new approach for determining

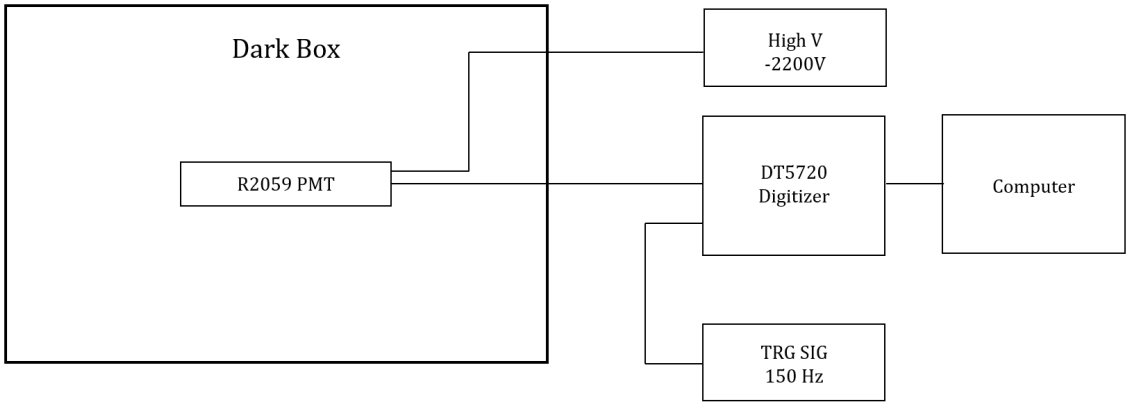


Figure 3.3: Block diagram for the PMT calibration setup. The dark box was very slightly opened to allow in enough light for the measurement.

the baseline ADC channel number involves using a 10-point moving average (MA) as defined by Equation 3.1 where k is the number of points in the MA, i is the index for which the MA is being calculated, and j is the index of the waveform contributing to the MA calculation. The frequency distribution of all the $\langle a \rangle_i$ values is found and the most frequent one is utilized as the MCA baseline value. An example of this frequency distribution for one captured waveform is shown in Figure 3.6. The benefits of using this approach in this situation are highlighted in Figure 3.5. A drawback is that it takes considerably more time to process the waveforms.

$$\langle a \rangle_i = \frac{1}{k} \sum_{j=i}^{i+k-1} a_j \tag{3.1}$$

After the waveforms are processed and the SPE spectrum is generated, the deconvolution approach outlined in [103] is used to fit the data and find the amount of integrated charge belonging to a single photoelectron when the PMT is at -2200V. The deconvolution model is based on a statistical model which is congruent to PMT physics in a general sense. The model used in this work is described by Equations 3.2 - 3.7, and depends on 7 free parameters. The pedestal is defined by Q_0 and σ_0, w and α describe discrete background processes in the PMT, and the real SPE signal is described using Q_1 and σ_1 for the location and spread of the first photoelectron response in the spectrum, and μ describes the expectation value for the number of photoelectrons in a given data window.

$$S_{real}(x) = \sum_{n=0}^{\infty} \frac{\mu^n \mathrm{e}^{-\mu}}{n!} \times \left[(1-w)\, G_n(x - Q_0) + w I_{G_n \otimes E}(x - Q_0) \right] \tag{3.2}$$

$$I_{G_n \otimes E}(x - Q_0) = \frac{\alpha}{2} \exp\left[-\alpha \left(x - Q_n - \alpha \sigma_n^2 \right) \right] \times M \tag{3.3}$$

$$M = \left[\mathrm{erf}\left(\frac{|Q_0 - Q_n - \alpha\sigma_n^2|}{\sigma_n \sqrt{2}} \right) + \mathrm{sign}\left(x - Q_n - \alpha\sigma_n^2 \right) \times \mathrm{erf}\left(\frac{|x - Q_n - \alpha\sigma_n^2|}{\sigma_n \sqrt{2}} \right) \right] \tag{3.4}$$

$$Q_n = Q_0 + nQ_1 \tag{3.5}$$

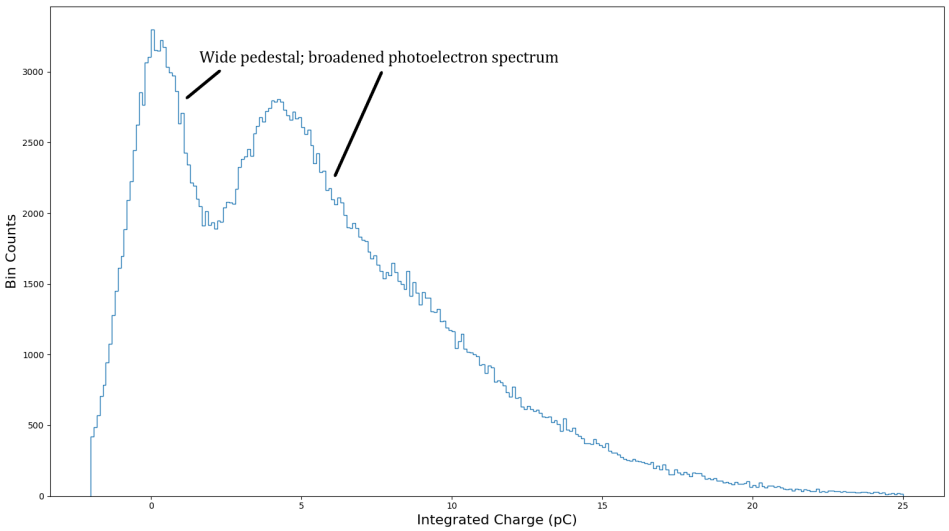


Figure 3.4: Single photoelectron spectrum for the R2059 PMT using the mean of the first 10 samples in data window for baseline subtraction. Notice the broadened pedestal and photoelectron spectrum features.

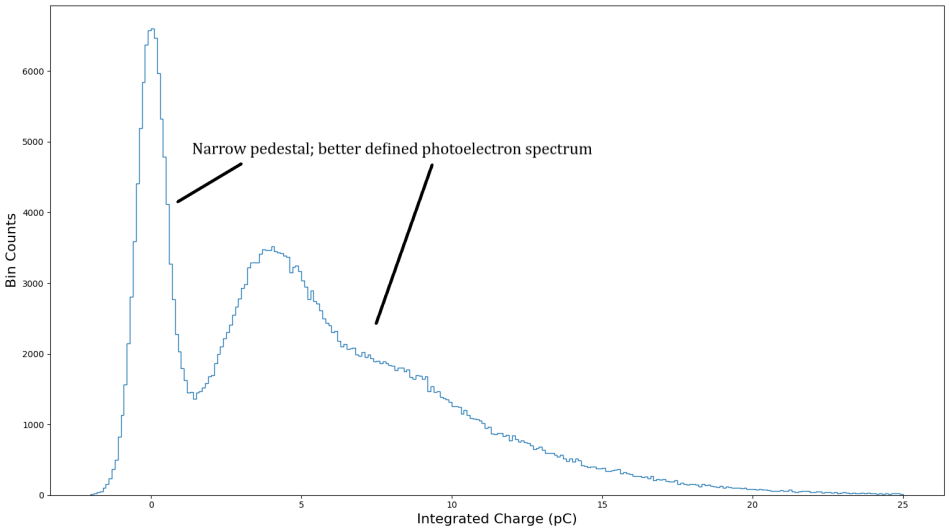


Figure 3.5: Single photoelectron spectrum for the R2059 PMT using the location of the maximum bin of the histogrammed 10-point moving average value for baseline subtraction. Notice the better defined pedestal and photoelectron spectrum features.

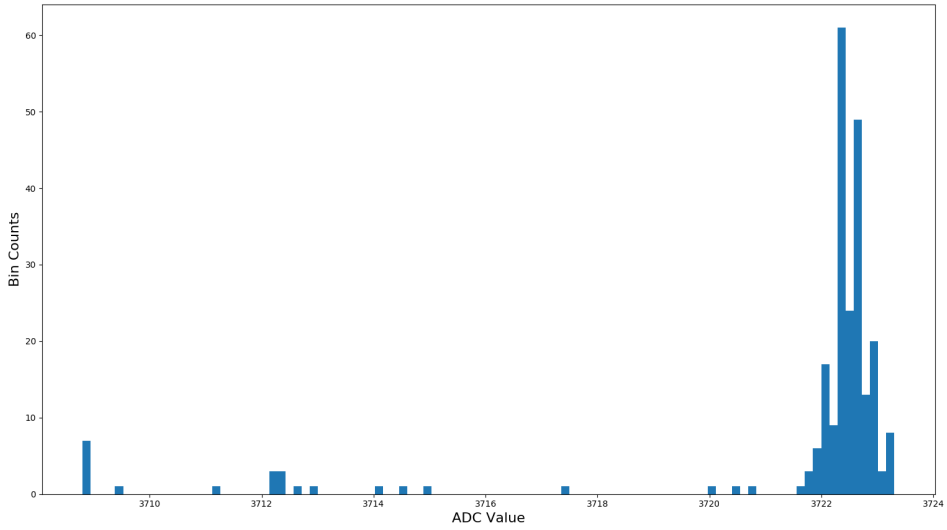


Figure 3.6: Frequency distribution of the MA baseline ADC values using 10 data points in the MA window. The most frequent value is used as the true baseline for building the SPE spectrum.

$$\sigma_n = \sqrt{\sigma_0^2 + n\sigma_1^2} \tag{3.6}$$

$$G_n\left(x - Q_0\right) = \frac{1}{\sigma_n\sqrt{2\pi}} \exp\left(-\frac{\left(x - Q_n\right)^2}{2\sigma_n^2}\right) \tag{3.7}$$

After completing the calibration measurement, a spectrum was taken using a 1x1 inch NaI scintillator with a Cs-137 source. The NaI scintillator was mounted to the PMT using Visilox V-788 optical coupling compound. Black electrical tape was used to secure the scintillator to the PMT. To be comparable to the calibration data, the PMT was still at operated at a bias of -2200V. The waveforms were processed in post using the standard baseline subtraction method with 15 samples. The integration was setup to begin 60 ns before the pulse peak location and end 2.5 μs after the pulse peak. With the SPE calibration and NaI/Cs-137 662 keV photopeak location on the same scale, it may be known how many photoelectrons correspond to the 662 keV peak. This information may then be used to calibrate the PMT at lower biases using the same NaI crystal and Cs-137 source.

3.3.2 Experiments with EJ200 Bars

Two different types of experiments were performed with EJ200. The first one described examined how the light output of the scintillator varies with the scintillator aspect ratio, the type of optical reflector used, the geometry of the scintillator, and whether the radiation source was in front of the scintillator or to the side of the scintillator. The second experiment was a simple spectrophotometry experiment to help provide simulation inputs for the absorption length of EJ200.

Light Output Study

EJ200 scintillators with aspect ratios of 2:1, 8:1, and 16:1 are investigated with circular, square, and hexagonal cross-sectional shapes; reflectors of Teflon tape, aluminum foil, or titanium dioxide (TiO2) paint are used. The samples initially came from Eljen in 17 inch lengths and 1 inch cross sectional dimensions. The samples were machined to the requisite

lengths in the Nuclear Engineering machine shop using the band saw and the knee-mill which gave an excellent finished look to the milled surface. The samples are shown in Figure 3.7. After milling, the samples were polished on all sides incrementally up to the ultra-fine abrasive level of 2500P. Some small scratches did remain; these likely came from rogue (larger than expected) abrasive particles on the rougher abrasive papers used early in the process. After hand polishing, the scintillators were mechanically polished using TC6 and then PBC polishing compounds on a flannel buffing wheel.

The radiation source was Cs-137 with a nominal activity of $1\mu Ci$ and was 16 months old at the time of the experiment. The source was placed in front-irradiation or side-irradiation configurations for each geometry-surface combination. The front-irradiation measurements had the source placed 10 cm from the face of the scintillator. The side-irradiation geometry nominally had the source placed 10 cm from the axis of the scintillator at the mid-length. A block diagram of the setup is presented in Figure 3.8. Due to the configuration of the optics table upon which the experiment was performed, the side-on distances were not always, or exactly, 10 cm. The distance was measured with a caliper and recorded to be used with the description of the source location in the simulation.

A brief description of the surface reflectors is as follows: the teflon is a minimum of 4-layers of Teflon tape, the foil is a single layer of Reynolds aluminum foil (the shiny side), and the TiO_2 is many coats of Glidden GL9000 flat interior white paint, a sufficient number of coats was used so that exterior light was not significantly entering the scintillator. After applying the surface treatment, the samples were wrapped in 2 layers of black electrical tape and then mounted to the PMT using Visilox V-788 optical coupling compound and electrical tape to secure the samples.

For these measurements, the PMT was operated at a bias of -1700V. In order to carry over the PMT calibration data at -2200V, the NaI scintillator was used with the Cs-137 source and the photopeak location was found. This was done at the beginning of every measurement day using a 10 minute measurement, and only after the PMT had been allowed to stabilize for 40 minutes. The photopeak location (in pC) was recorded and used in post processing, with the calibration data, to build the 'photoelectron' axis in the EJ200 measurements. Once the intermediate calibration measurement had been taken, measurements would commence using

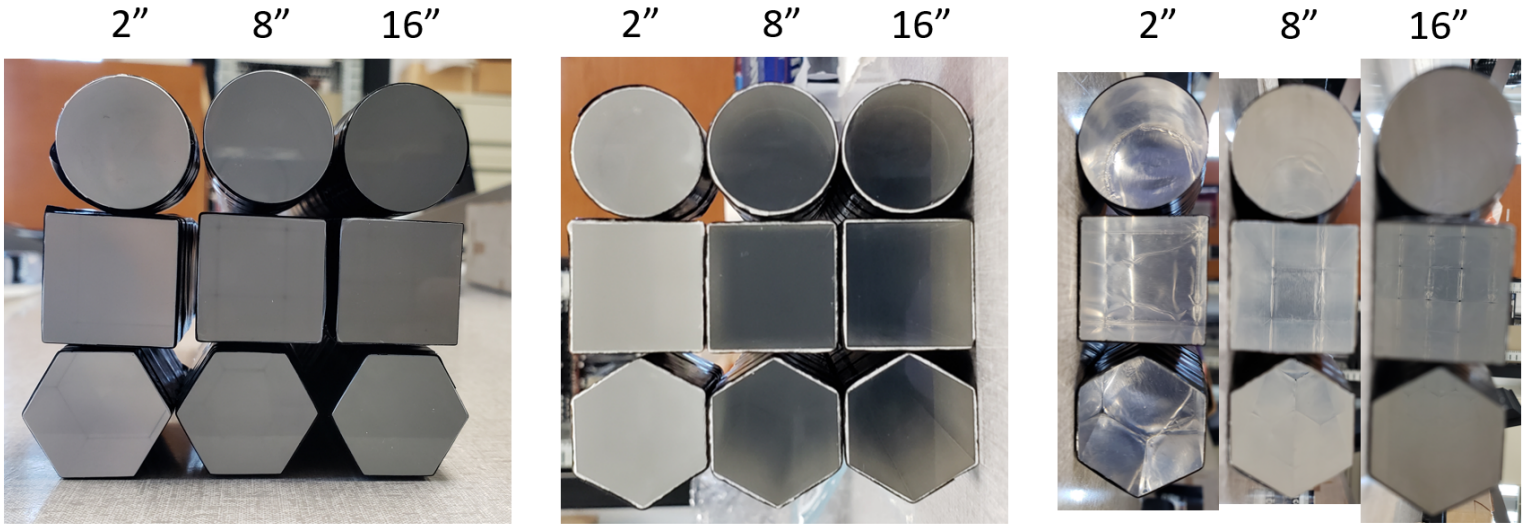


Figure 3.7: EJ200 samples with teflon, TiO2, or foil reflectors (left to right). The lengths are 2 inches, 8 inches, or 16 inches. The cylindrical sample has a diameter of 1 inch, the rectangular sample has a 1x1 inch square cross section, and the hexagonal samples measure 1 inch across between any of the 3 sets of parallel edges.

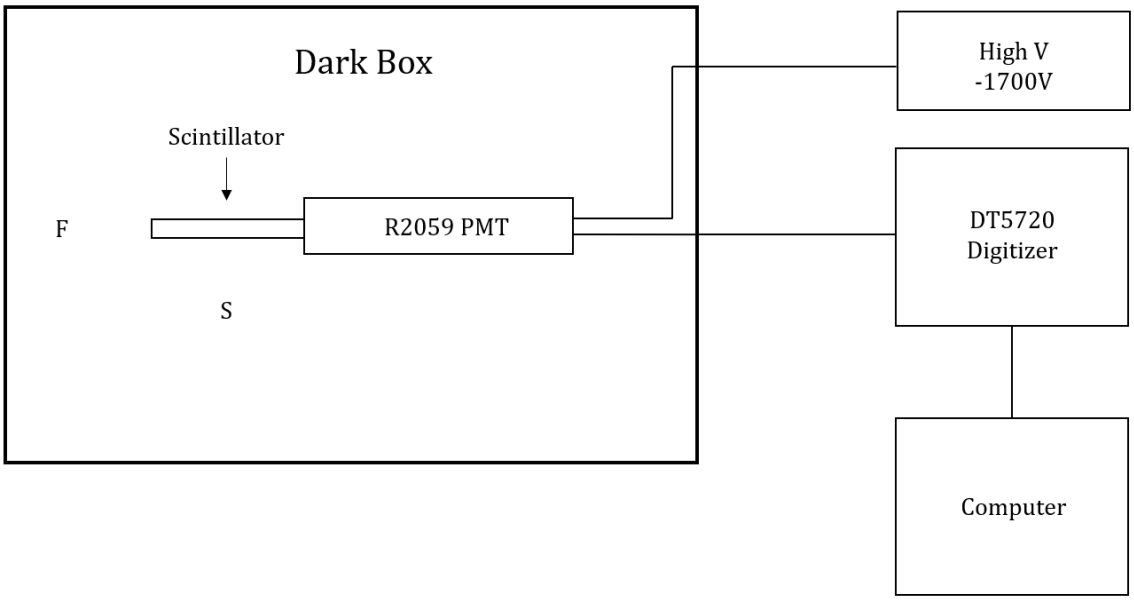


Figure 3.8: Block diagram for EJ200 light output study. The source was placed at either location 'F' for the front irradiation measurement or location 'S' for the side irradiation measurement.

the EJ200 samples. Each sample-surface combination was used for three measurements, Cs-137 in front irradiation, Cs-137 in side-irradiation, and a background measurement. Each measurement lasted 30 minutes.

In post processing, the waveforms were brought to baseline using a standard 15 point average and subtraction. The first 15 points were utilized for this purpose. The pulse integration window began 60 ns before the peak and 500 ns after the peak. The resulting integrated charge values were mapped to single photoelectron values and then histogrammed using a bin width of 2 photoelectrons. A bank of all the resulting histograms was stored in a single ROOT file for further comparison with simulated data.

Spectrophotometry Study

In order to simulate the EJ200 samples, it was desired to measure the optical absorption length as a function of the wavelength. This was done using the 6 inch rectangular bar which was machined, but not utilized in the Light Output study. The bar was placed on end in a Varian Cary 5000 UV-Vis-NIR spectrophotometer. The reference sample was air. The thickness of the sample, through which light traversed, was 2.549 cm. The % Transmission was measured from 200-800 nm.

In converting the % Transmission data into absorption lengths requires that Fresnel reflection be accounted for in the conversion process. Fresenel reflection occurs at the boundary of two dielectric media with different refractive indices, and may even occur when the photon is incident perfectly normal to the surface. Figure 3.9 shows how this applies in the spectrophotometry experiment.

The probability of reflection of a directly incident electromagnetic plane wave at the boundary of two different dielectric media with refractive indices n_1 and n_2 may be calculated according to Equation 3.8. Now consider the case where the light is incident on a slab of thickness, l, the probability of the optical photon being absorbed while traversing that slab only once is given by Equation 3.9.

$$R = \left(\frac{n_1 - n_2}{n_1 + n_2} \right)^2 \tag{3.8}$$

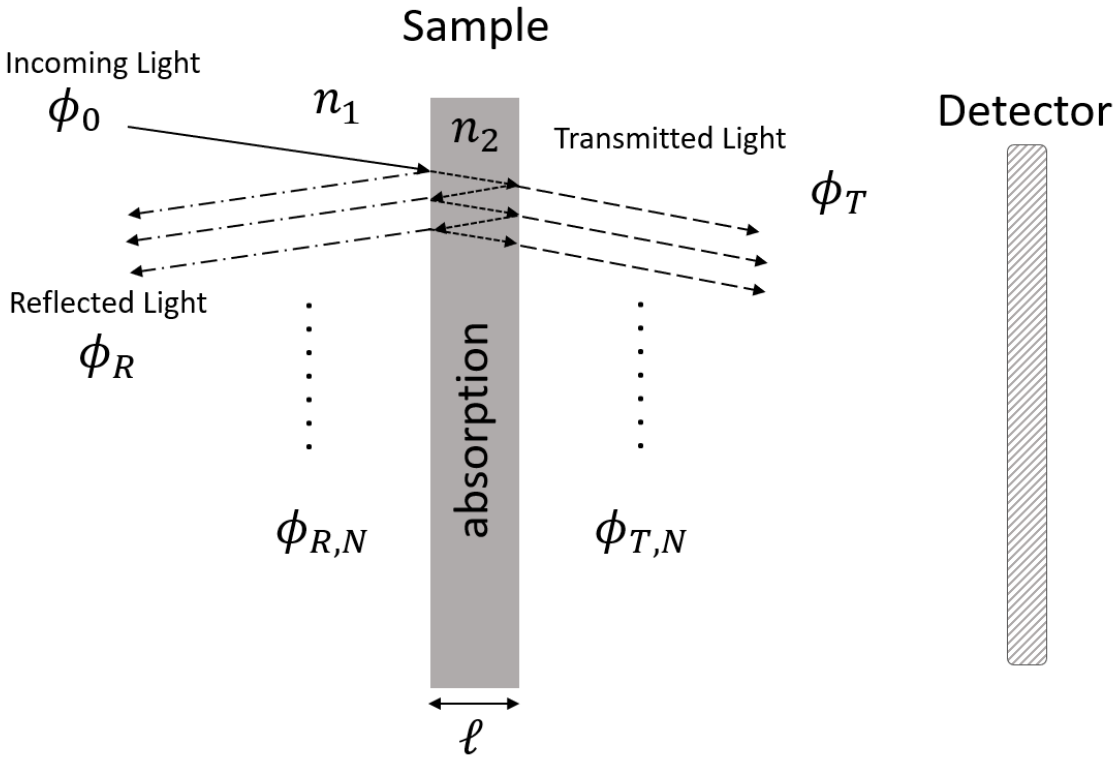


Figure 3.9: Fresnel reflection in spectrophotometry experiments. The significance of the reflected light increases as the difference between n_1 and n_2 increases. An approximate optical transmission length may be found after correcting for this reflection loss.

$$A = 1 - \exp\left(-\mu l\right) \tag{3.9}$$

Referring back to Figure 3.9, it is clear that incident light, ϕ_0, first encounters the surface of the sample; at this point it may be reflected with probability, R, or continue. The amount of light which continues may be expressed as: $\phi_0(1-R)$. This light may then pass through the sample, but some will be absorbed along the way, the portion of initial light which is not absorbed (nor reflected by the first boundary) may be expressed by: $\phi_0(1-R)(1-A)$. Now, again, the initial beam of light encounters a border and may be reflected with a probability of R. The light which continues is given by multiplying the previous expression by $(1-R)$, this gives the total of the initial light which was transmitted on the first pass, $\phi_{T,1}$, which is fully expressed in Equation 3.10. Circling back to the light which was reflected at the second boundary, this will pass through the sample again and may be reflected back towards the detector by the first boundary. Again it passes through the sample and arrives back at the second boundary where it may be reflected or transmitted. The total light transmitted to the detector from the second pass is expressed in Equation 3.11. Clearly, this is becoming a geometric series, and the total light which is transmitted through to the detector may be defined by Equation 3.12.

$$\phi_{T,1} = \phi_0 \left(1-R\right)\left(1-A\right)\left(1-R\right) = \phi_0 \left(1-R\right)^2\left(1-A\right) \tag{3.10}$$

$$\phi_{T,2} = \phi_0 \left(1-R\right)^2\left(1-A\right)^3 R^2 = \phi_{T,1} R^2 \left(1-A\right)^2 \tag{3.11}$$

$$\phi_T = \phi_{T,1} \sum_{i=0}^{\infty} \left(R^2\left(1-A\right)^2\right)^i = \frac{\phi_0\left(1-R\right)^2\left(1-A\right)}{1-R^2\left(1-A\right)^2} \tag{3.12}$$

Using Equations 3.12, 3.9, and remembering that the fractional transmission, T, is ϕ_T/ϕ_0, using a little bit of algebra yields the optical absorption length, shown in Equation 3.13. The positive form of the quadratic solution is the one which should be used for our physical purposes here.

$$absLength = \frac{1}{\mu} = -\frac{l}{\ln\left[\frac{-(1-R)^2 \pm \sqrt{(1-R)^4 + 4T^2R^2}}{2TR^2}\right]} \tag{3.13}$$

Finally, using Equation 3.13 with the optical transmission data, and using a constant 1.58 as the refractive index for EJ200 and using 1 for air, the absorption lengths of EJ200 were calculated and then used in the simulation of EJ200.

3.3.3 Optical Simulation of EJ200 Bars

GEANT4-10.04.p02 was used to simulate the same experiments which were physically performed. Two banks of simulations, 54 simulations in each bank, were completed; the only change between the two is the surface model used to describe the optical reflectors which was discussed in the introduction. Successfully simulating any material in a radiation transport context requires a good definition of the material properties which affect the outcome. The successful simulation of EJ200 is no exception. The general material definition for EJ200 is provided in Table 3.1, along with the material definitions for the optical grease and fused silica which are shown in Tables 3.2 and 3.3 respectively. The luminescence spectrum of EJ200 was digitized from the Eljen website and is provided in Figures 3.10 and 3.11 vs. wavelength and energy [90]. The Birks quenching coefficient, kB, was set to 0.126 mm/MeV, see Equation 1.24. The optical values with respect to energy are shown because this is the way they must be provided to GEANT4, they are provided with respect to the wavelength because this is most often how they are communicated in the scintillator material characterization discipline. The optical absorption data for EJ200 originates from our own transmission measurements on these samples and is presented in the results section for these measurements. For optical grease the absorption was assumed to be zero, and for fused silica the absorption length was set to 9.49 cm. The refractive index was determined by fitting the dispersion relation to refractive index data for PVT found in [105], which presents the needed coefficients to find the wavelength dependent refractive index, an offset of K was made so that the refractive index would be 1.58 at 633 nm. The refractive index data for the optical grease and fused silica originated from [106, 107]. The Sellmeier equation as shown in Equation 3.14 was used

with the coefficients shown in Table 3.4 to derive the refractive index data. The plots of the refractive indices vs. wavelength and energy are shown in Figures 3.12 and 3.13.

$$n(\lambda) = \left(1 + \frac{B_1\lambda^2}{\lambda^2 - C_1^2} + \frac{B_2\lambda^2}{\lambda^2 - C_2^2} + \frac{B_3\lambda^2}{\lambda^2 - C_3^2}\right)^{\frac{1}{2}} + K \tag{3.14}$$

Surface parameters for the *unified* model implementation come from the literature, as does the value for the reflectance of the reflectors for use with the LUTs [99, 101, 102]. The definitions of the various optical surfaces which were used in the simulation are presented in Table 3.5. It it important to note, due to a lack of clarity in the literature and GEANT4 manual, the surface roughness parameter, sigma_alpha, should be presented to GEANT4 in units of radians. The value used in our simulation corresponds to 1.3°, which was presented in literature as a value to be used for polished surfaces. The parameter, SPECULARLOBECONSTANT was set to 1, indicating that all scatters off of the scintillator-gap interface will follow a specular lobe distribution with respect to the facet normal.

An estimation of the optics of the photocathode was also included in the model. This, too, seems to be a point which is frequently overlooked, though it has been called out on a couple occasions [74, 108, 109]. The primary point to understand from these as it applies to our simulation is that once a photon traveling through the silica window reaches the photocathode, a few things can happen: (1) the photon may reflect back towards the scintillator, (2) the photon may be absorbed by the photocathode, or (3) the photon may be transmitted through the photocathode. The first process, reflection off of the photocathode, potentially allows the photon to interact with the photocathode again at a later point in the photon lifetime. The second process, absorption on the photocathode, is what allows for photoelectron production, though there is some photo-conversion efficiency which comes into play here as not every absorbed photon will generate a photoelectron. The third process, transmission through the photocathode, may occur and the photon then is able to interact with the internal structure of the PMT. This may cause electron emissions on one of the dynode stages, the photon may reflect back off of the internals and re-interact with the photocathode, or it may be absorbed by one of the internal components and cause no effect to the measured signal. The probability of each of these occurrences in reality is a complicated

Table 3.1: Material definition for EJ200.

EJ200	
Density (g/cc)	1.023
Light Yield (photons/keV)	10
Num. Hydrogen	10
Num. Carbon	9

Table 3.2: Material definition for optical grease (Polydimethylsiloxane).

Optical Grease	
Density (g/cc)	1.06
Abs. Length (cm)	Inf
Ref. Index	1.458
Num. Hydrogen	6
Num. Carbon	2
Num. Oxygen	1
Num. Silicon	1

Table 3.3: Material definition for fused silica.

Fused Silica	
Density (g/cc)	2.203
Abs. Length (cm)	9.49
Num. Oxygen	2
Num. Silicon	1

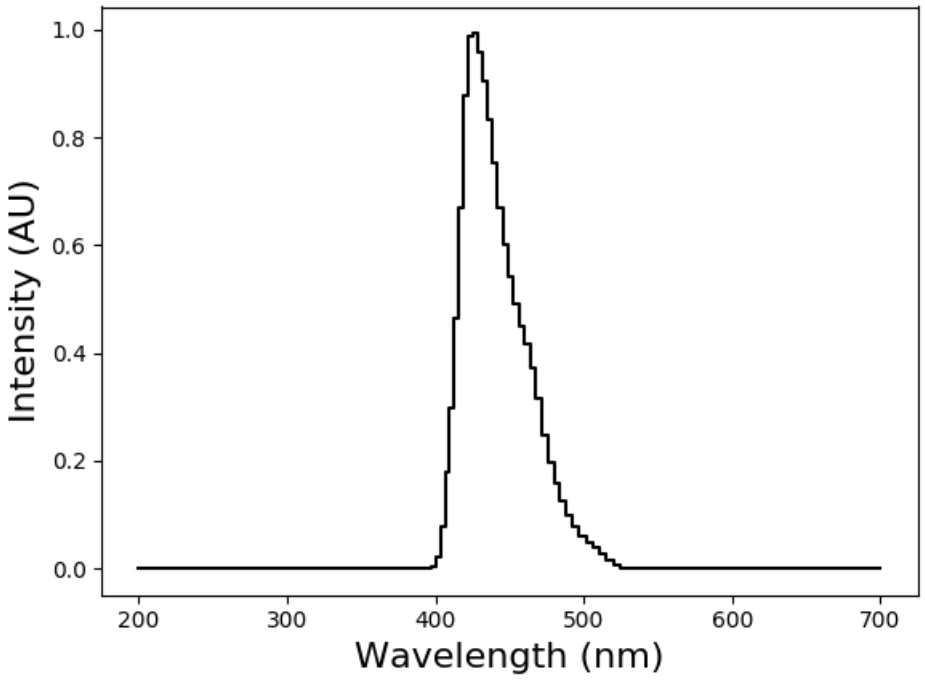


Figure 3.10: Luminescence spectrum of EJ200 with respect to wavelength. [90]

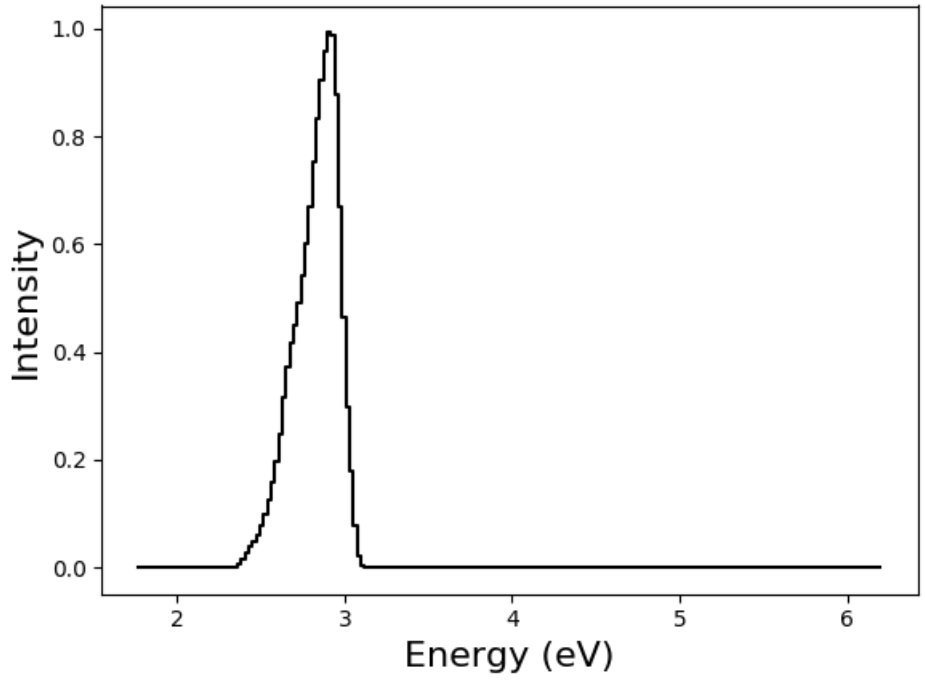


Figure 3.11: Luminescence spectrum of EJ200 with respect to energy.

Table 3.4: Sellmeier coefficients for optical dispersion relations.

Material	Sellmeier Coefficients						K
	B1	B3	B3	C1 μm	C2 μm	C3 μm	
EJ200 (PVT)	0.986138	0.533576	1.914173	0.063439	0.192713	16.69461	-0.027
Fused Silica	0.696166	0.407943	0.897479	0.068404	0.116241	9.896161	0
Optical Grease	1.0057	0	0	0.114965	0	0	0

Table 3.5: Optical surface parameters used in GEANT4 simulations. Reflectivity applies to both LUT and *unified* models.

Surface	Reflectivity	LUT Model	*unified* Model	sigma_alpha	nGap
Teflon	0.99	polishedteflonair	groundbackpainted	0.022689	1
Foil	0.787	polishedvm2000air	polishedbackpainted	0.022689	1
TiO2	0.951	polishedtioair	groundbackpainted	0.022689	1.61

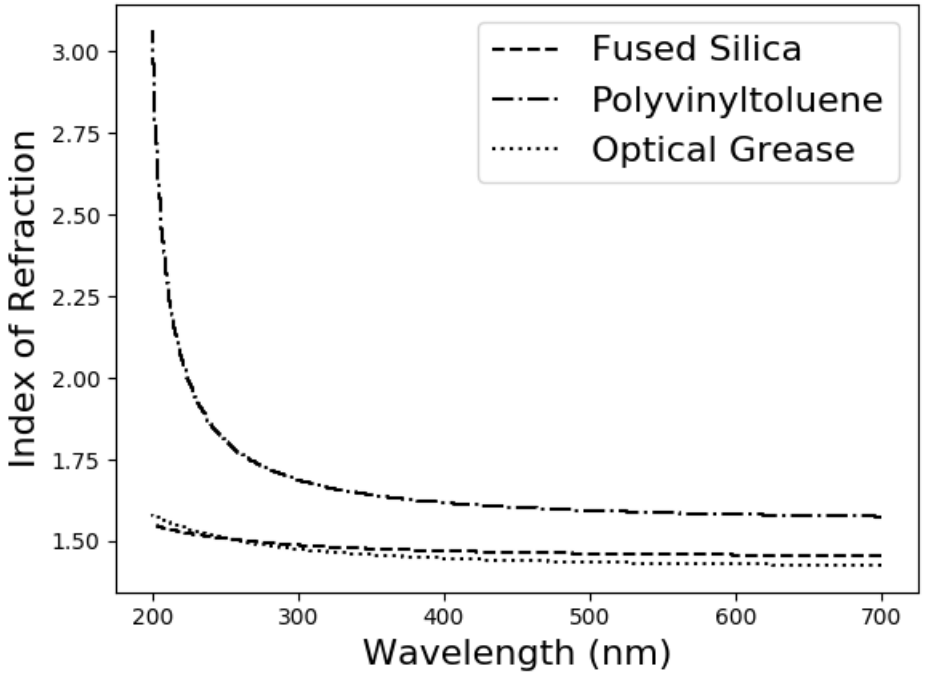


Figure 3.12: Refractive indices of simulated optical media with respect to wavelength.

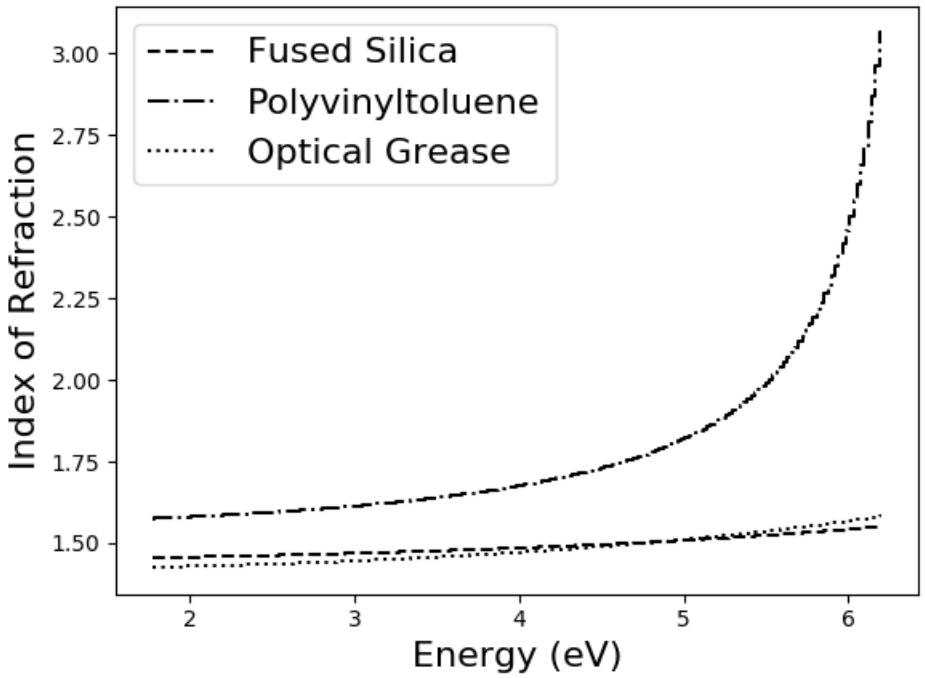


Figure 3.13: Refractive indices of simulated optical media with respect to energy.

function dependent on many inputs, including the wavelength, polarization, and incident angle of the photon on the photocathode surface.

The model of the photocathode used in this work relies on two inputs and the method presented in [109]. The first input is the value of photocathode reflectance, or reflectivity, as a function of photon wavelength, R_p. The reflectance was for a Hamamatsu R2083 PMT and was measured at 8° incidence as found in Figure 4 of [109]. The R2083 is a bialkali PMT with a borosilicate window and spectral response code 400K, this matches the sensitivity response of the R2059 PMT for wavelengths above 350nm which is sufficient for our purposes. The second input is the *external* quantum efficiency (QE), this is the manufacturer reported QE. The externally measured QE is not the same as the QE of the photocathode, because, as described before, a fraction of the incident light is removed due to Fresnel reflection at the air-window boundary. This means that the incident light on the photocathode is less than the incident light on the PMT window, resulting in a higher *internal*, or photocathode, QE than what is reported at the 'quantum efficiency' by the manufacturer. With these two values in hand, the internal QE may be calculated using Equations 3.15 and 3.16 where R is the probability of reflection off of the PMT window as given by Equation 3.8 using $n_1 = 1$, for air and $n_2 = 1.5$ for the PMT window.

$$QE_{in} = \frac{QE_{ex}}{1 - R_m} \tag{3.15}$$

$$R_m = R + \frac{(1 - R)^2 R_p}{1 - R_p R} \tag{3.16}$$

Now we are nearly there. In GEANT4, the functional part of the photocathode is described as the *optical surface* between the PMT window and the volume in the simulation representing the photocathode (essentially a dummy volume), see Figure 3.14. This surface is defined as dielectric_metal in the *glisur* model paradigm using the polished surface finish. With the model, the photon is either reflected or absorbed according to the probabilities set by REFLECTIVITY, *if it is absorbed*, then it can be detected (status set to 'detect') according to the probability of photoconversion set by the GEANT4 surface parameter, EFFICIENCY. The relationship between them is quite simple: $QE_{in} =$

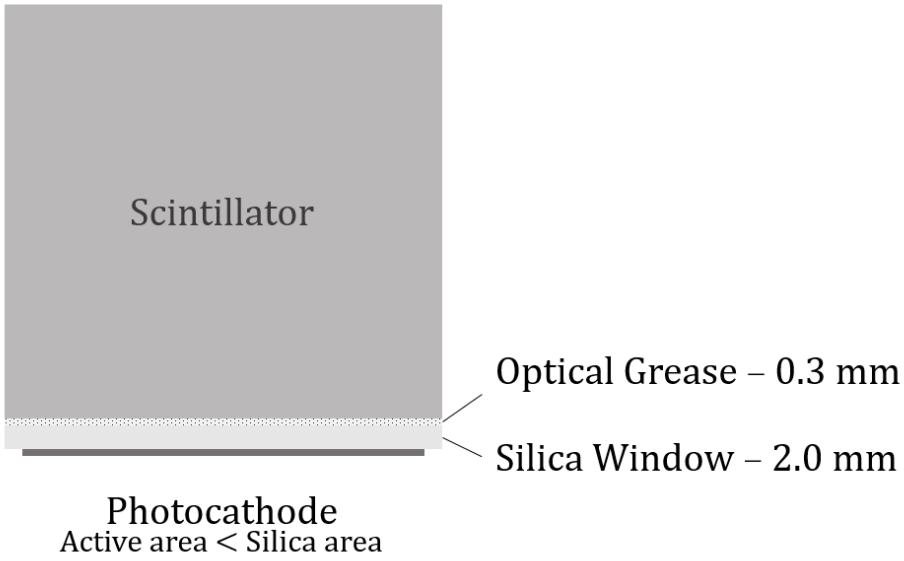


Figure 3.14: Diagram of the basic detector schema used in the light output simulations. The photocathode has a diameter of 46 mm while the PMT window diameter is 50.8 mm. The scintillator shapes and dimensions are variable per the user selection.

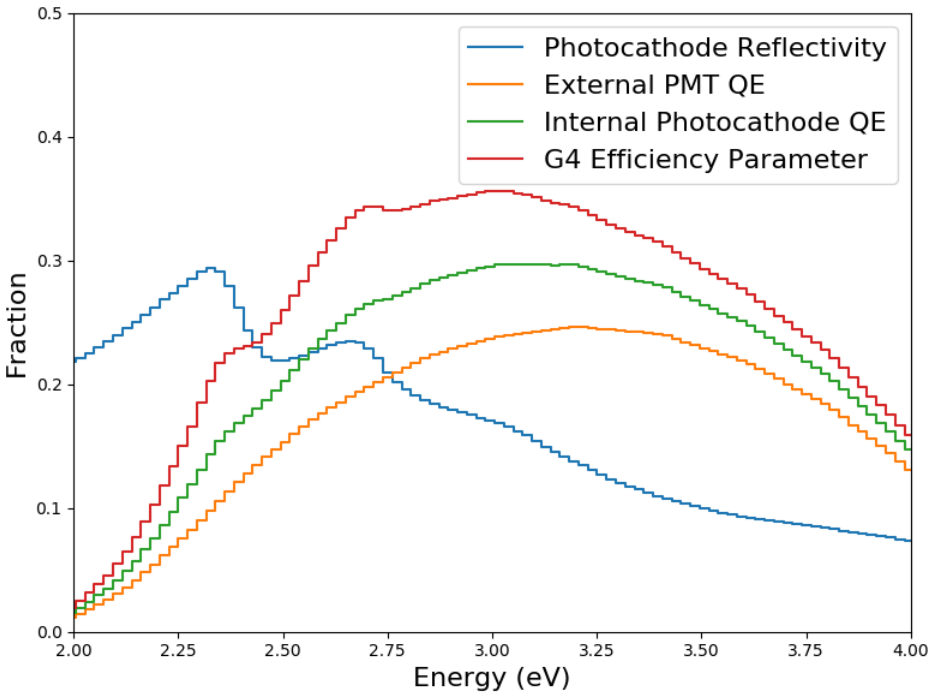


Figure 3.15: Photocathode reflectivity, quantum efficiency (internal and external), and G4 efficiency with respect to energy.

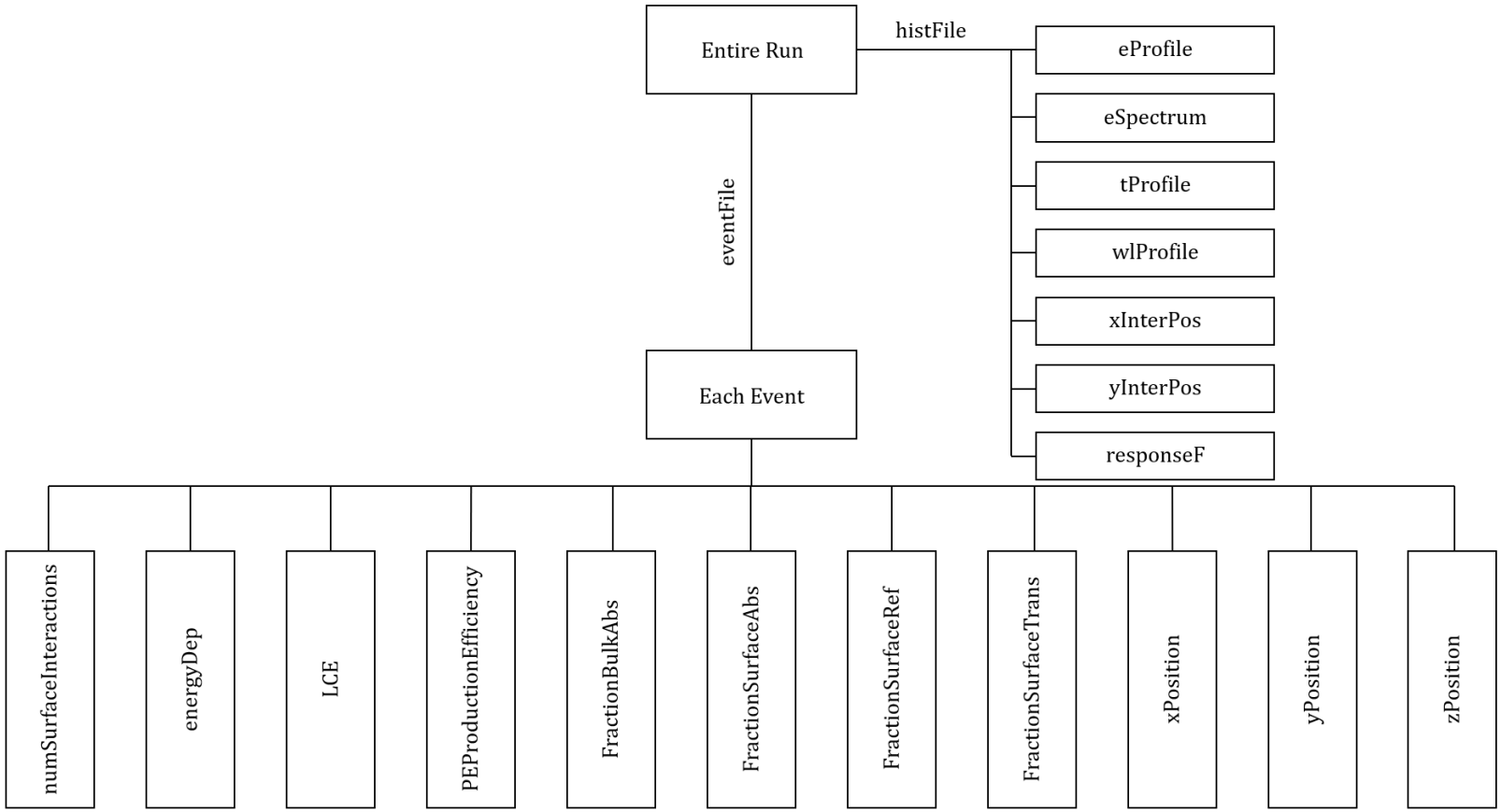


Figure 3.16: ROOT data file structure for EJ200 light output simulation studies.

$(1 - REFLECTIVITY) \times EFFICIENCY$. The values used for these parameters are shown in Figure 3.15.

As a final note, the physics list registered G4EmStandardPhysics_option4() to handle electromagnetic processes (the most detailed handling of these physics processes) and the standard G4OpticalPhysics() option for optical photon transport and processes, the Cerenkov process for optical photon creation was disabled. All data was stored in ROOT files for post processing. The structure of these files for this batch of simulations is shown in Figure 3.16. The simulations were designed to collect a very significant amount of information related to a range of potential performance indicators. Unfortunately, the only analysis which has been performed with this data up to this point involves comparing Compton edge locations for the purpose of model validation and surface model selection.

3.4 Results and Discussion

3.4.1 Photomultiplier Tube Calibration

The results of the PMT calibration experiment are shown in Figure 3.17, which also shows the result of the deconvolution fitting. The values of the fitted parameters are $Q_0 = -0.0377 \pm 0.0023\,pC$, $\sigma_0 = 0.5191 \pm 0.0023\,pC$, $Q_1 = 3.668 \pm 0.011\,pC$, $\sigma_1 = 1.465 \pm 0.012\,pC$, $w = 0. \pm 8,000$, $\alpha = 0. \pm 8,000$, and $\mu = 1.402 \pm 0.010$. The values of w and α indicate that the solver had a difficult time fitting PMT background processes. Despite this, the results which are essential to the calibration, Q_0 and Q_1 appear reasonable and are congruent with what is presented in the Bellamy paper.

Immediately following the collection of the calibration data, a Cs-137 spectrum was measured with the 1x1 inch NaI crystal mounted to the PMT. The bias was set to the same voltage as used in the calibration experiment, -2200V. The resulting photopeak location occurred at $Q_{pp-2200} = 10,952 \pm 5\,pC$. This means that one may expect the Cs-137 photopeak to be representative of 2985 ± 9 photoelectrons when the 1x1 inch NaI crystal is coupled to the R2059 PMT. The photopeak location at the start of each measurement day was found, and recorded in order to convert the integrated charge axis to photoelectrons. The frequency

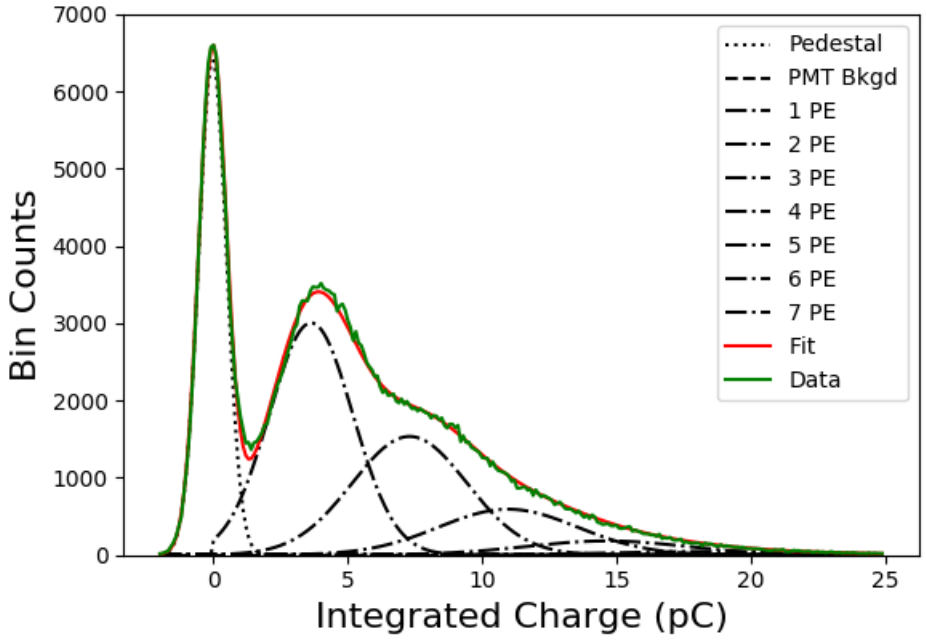


Figure 3.17: The deconvolved single photoelectron spectrum for the R2059 PMT operated at -2200V.

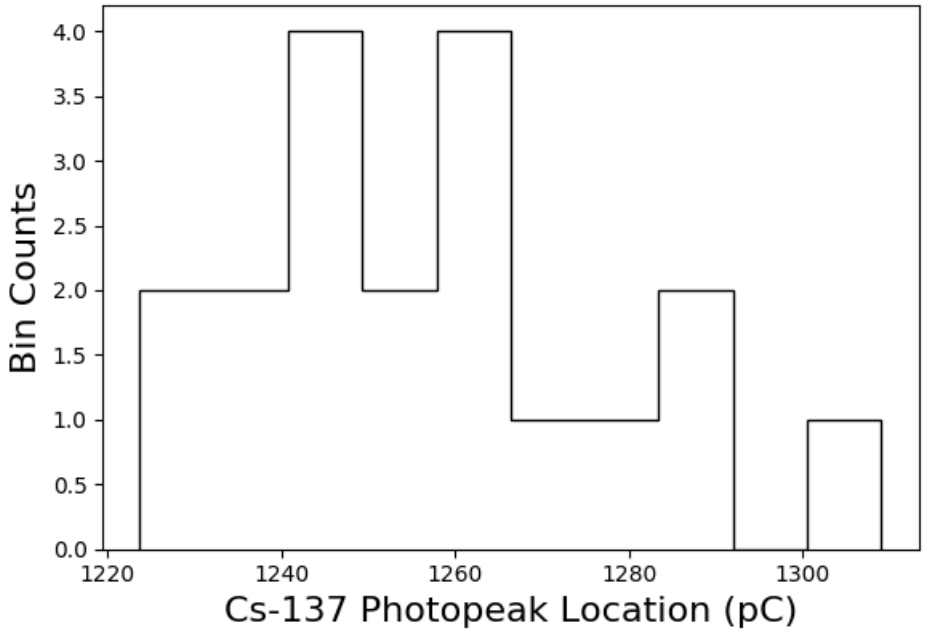


Figure 3.18: Frequency distribution of Cs-137 photopeak locations for mapping PMT calibration values to the integrated charge axis. The PMT bias for these data was set to -1700V.

distribution of the photopeak locations is shown in Figure 3.18. The average value of the Cs-137 peak location, when the PMT was at -1700V, is 1258 pC with a standard deviation of 21 pC.

3.4.2 Spectrophotometry Results

The result of the spectrophotometry measurement on the EJ200 sample is shown in Figure 3.19. The calculated optical absorption lengths, following the method presented in Subsection 3.3.2, are presented in Figure 3.20. The optical absorption length at the peak RL emission, 425 nm or 2.9 eV, is 68 cm. This is a good deal different than the 380 cm reported by Eljen. Even when using the variable refractive index (n=1.60636 at 425 nm) instead of the constant 1.58, the absorption length comes to 82.5 cm. This does indicate that correcting and solving for the absorption length for high values of % transmission, in the asymptotic region, is quite sensitive to the refractive index. Certainly, a more sensitive method for determining the optical absorption lengths would be of value here. Nevertheless, this is the approach which used and it could be argued that for samples with dimensions much less than the absorption length, this difference is not too appreciable.

3.4.3 Comparison of Experiments and Simulations

The background subtracted experimental spectra for the EJ200 experiments are contained in Appendix B.

Comparing the experimental and simulated results involves locating the Compton edge and comparing the number of corresponding photoelectrons. This is shown in Figures 3.21, 3.22, and 3.23. The hexagonal shape simulations for the LUT model crashed, so are not presentable. The cause of the crash seems to link to a null pointer. Indications are that something in the geometry has gone awry, particularly when combined with the LUT model. The Compton edge was located using the inflection point, in the same manner as was done in Subsection 2.4.3. For the longest samples, with the foil or TiO_2 reflectors, the amount of collected light was so low that the inflection point was not well determined using the SG filter due to so few data points leading up to the decline of the Compton continuum. For

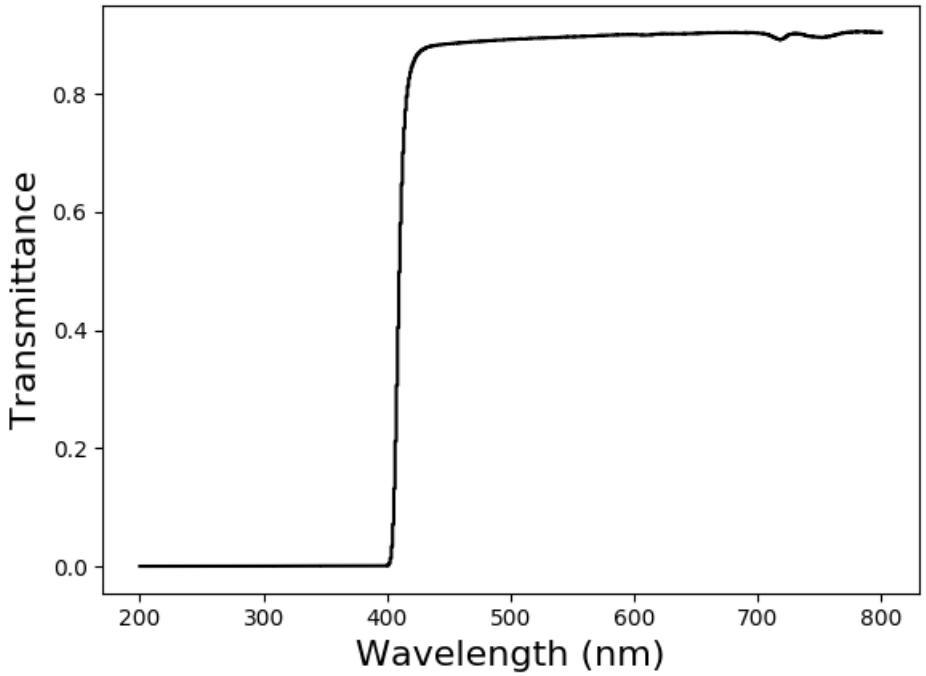


Figure 3.19: The measured optical transmittance of EJ200. The sample thickness was 2.549 cm. A strong absorption edge is evident at 400 nm. The transmittance at the peak RL emission wavelength is 0.86896.

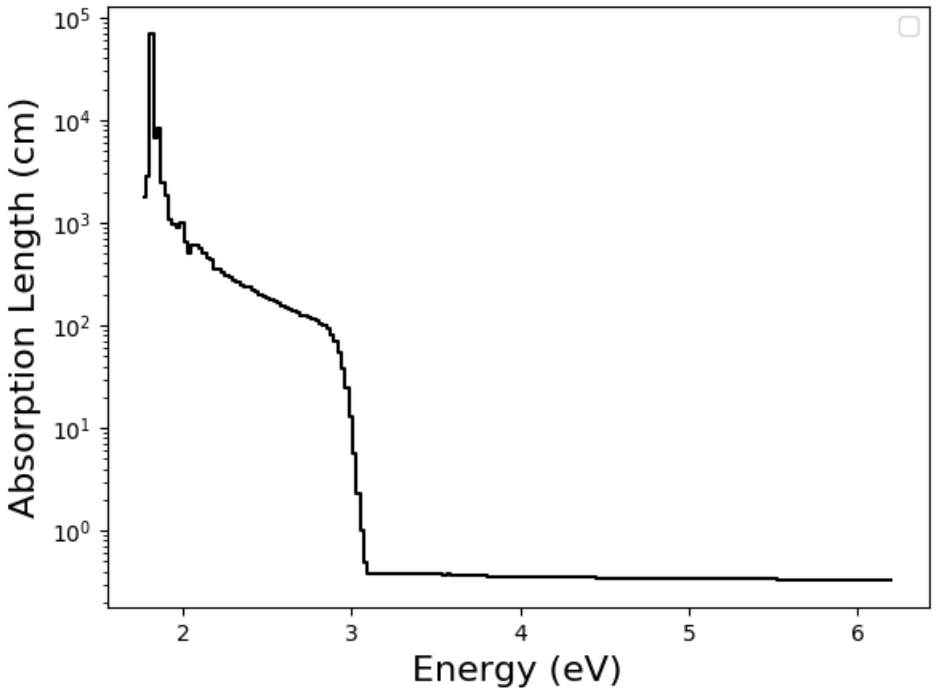


Figure 3.20: The optical absorption lengths of EJ200 calculated using the Fresnel correction and a constant refractive index of 1.58 for EJ200.

these, 0.8 of the Compton maximum was used as the CE location, if this feature was not discernible, then 0.8 of the Compton 'shoulder' was used, otherwise, 0.8 of the peak value was used. For these instances, the light output was very low, resulting in only a few tens of photoelectrons at the declared CE location.

Comparing the results of the Compton edge locations indicates a few things. The first of these is how difficult of a problem this is to adequately address. Difficulty aside, the universal model wins in 6 instances and the LUT model wins in 5 instances with a tie in one instance. The six instances with the hexagonal geometry are not counted since the LUT model dropped out. The foil surface always goes to the *unified* model. The teflon surface is predominantly best described by the LUT model, though this is only by a very small margin. In general, both models result in an under prediction of the light output for the teflon wrapped surface. This could be due to using a lower light yield than is real in the sample (i.e. the absolute light yield), or perhaps due to the PMT sensitivity being too low. If this is the case, the results would have to be reinterpreted across the board. Lastly, the TiO_2 surface goes to the *unified* model in the cylindrical geometry and the LUT model in the rectangular geometry. In both of these cases, the winning model best agrees at the 2 inch length, followed by both models disagreeing by near equal amounts in the opposite direction for the 8 and 16 inch lengths. With regards to the macroscopic shapes and surface model performance, the *unified* model performs best for the cylinder, 4 wins and a tie, and the LUT model performs best for the rectangle with 4 wins. The *unified* model performance in the rectangular shape tracks nearly identically to its performance in the case of the hexagonal shape. While nothing can be definitively said about how it competes with the LUT model in this case, it does lead one to wonder which wins since the hexagon is geometrically between the rectangle/square and the circle.

Some general trends observed in the experimental and simulated data sets indicate that light output for the teflon wrapping is highest, followed by foil, and then by TiO_2. Additionally, the higher aspect ratio scintillators have reduced light output across all reflectors and scintillator shapes. In the case of these experiments, the reason for this may be two-fold:

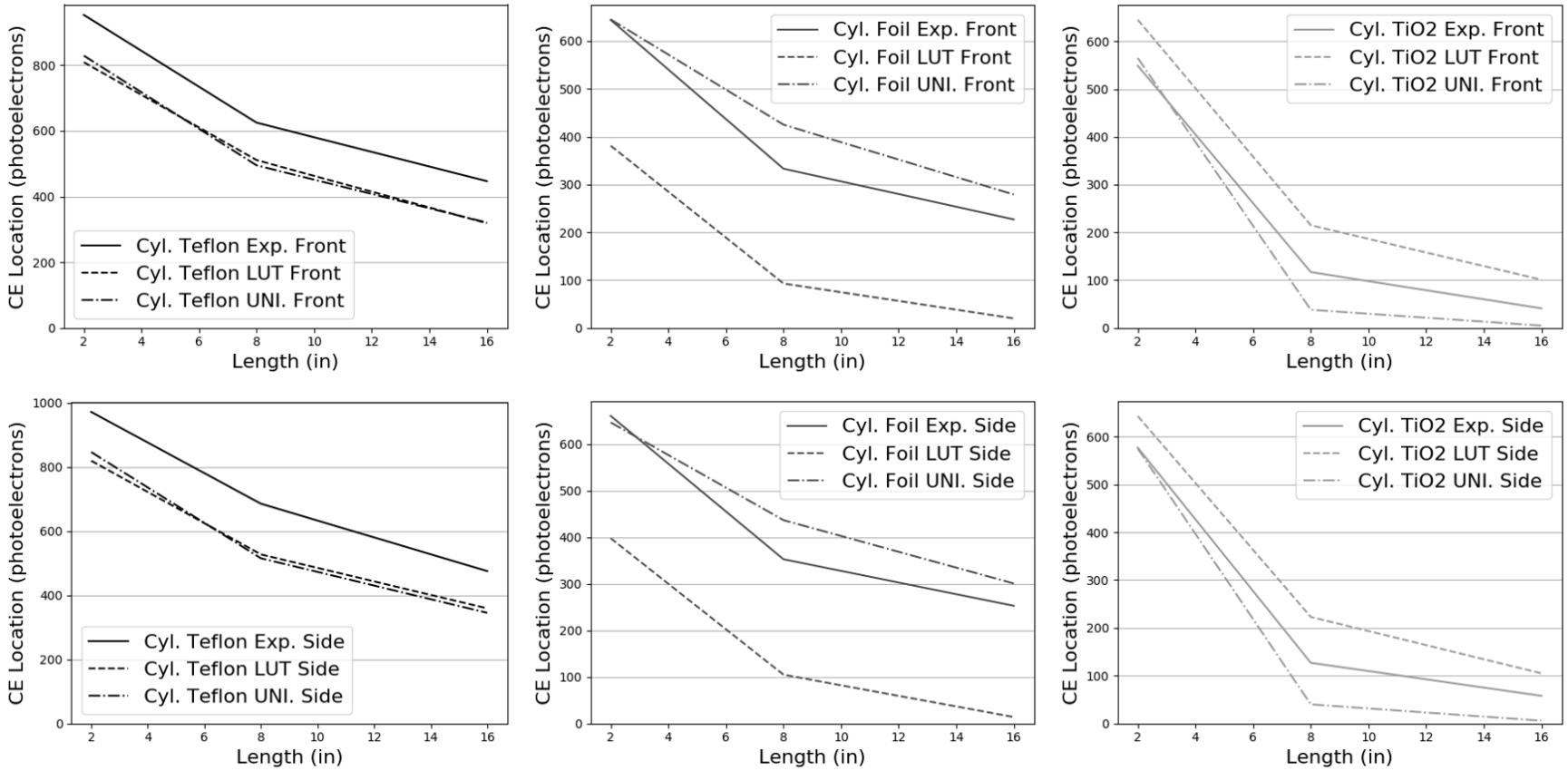


Figure 3.21: Comparison of the experimental and simulated Cs-137 Compton edge location with cylindrical EJ200 and varied optical reflectors. Teflon is used in the left column, foil in the center column, and TiO_2 in the right column. Data in the top row are from front irradiation; the bottom row represents side irradiation.

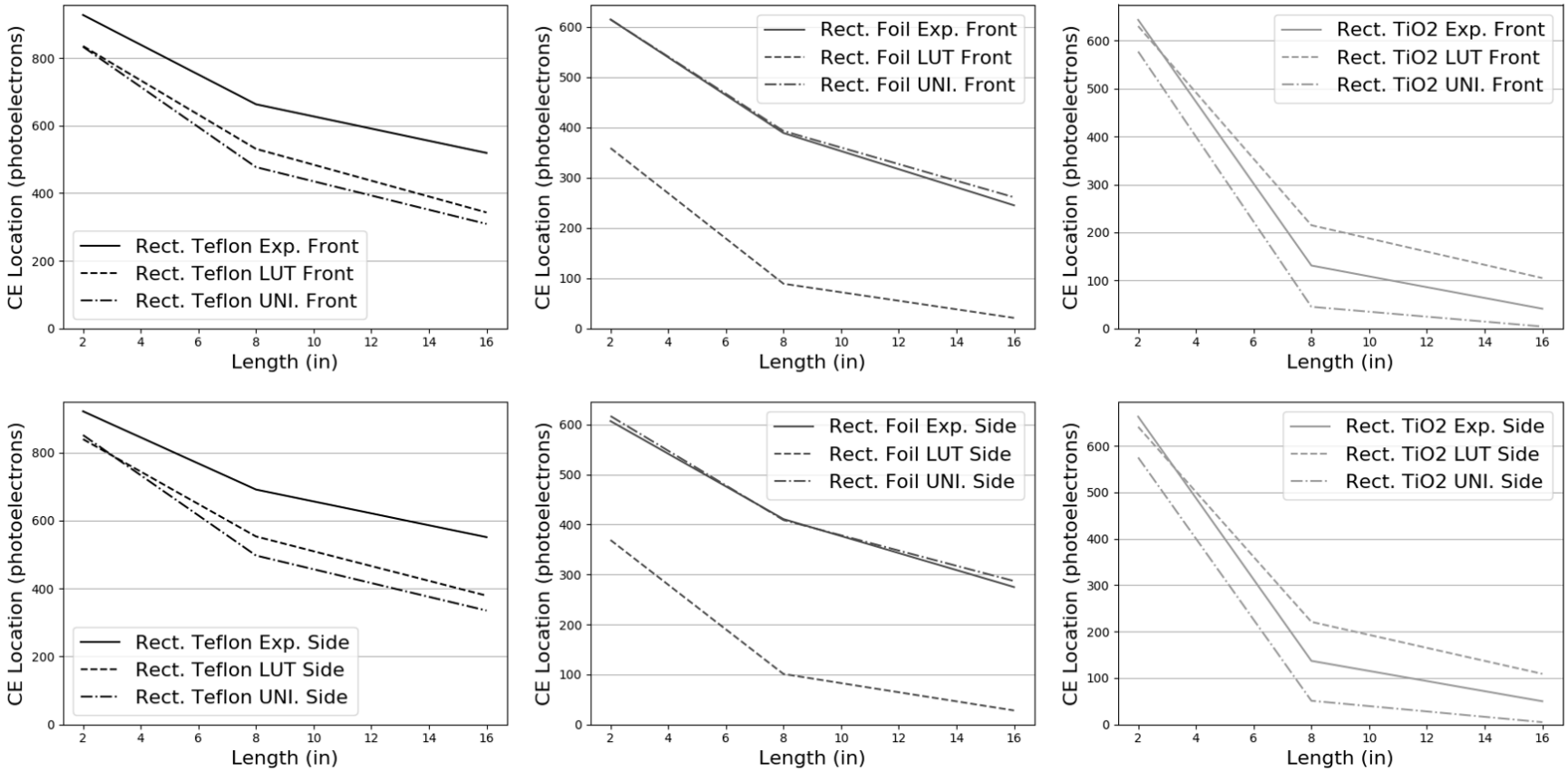


Figure 3.22: Comparison of the experimental and simulated Cs-137 Compton edge location with rectangular EJ200 and varied optical reflectors. Teflon is used in the left column, foil in the center column, and TiO_2 in the right column. Data in the top row are from front irradiation; the bottom row represents side irradiation.

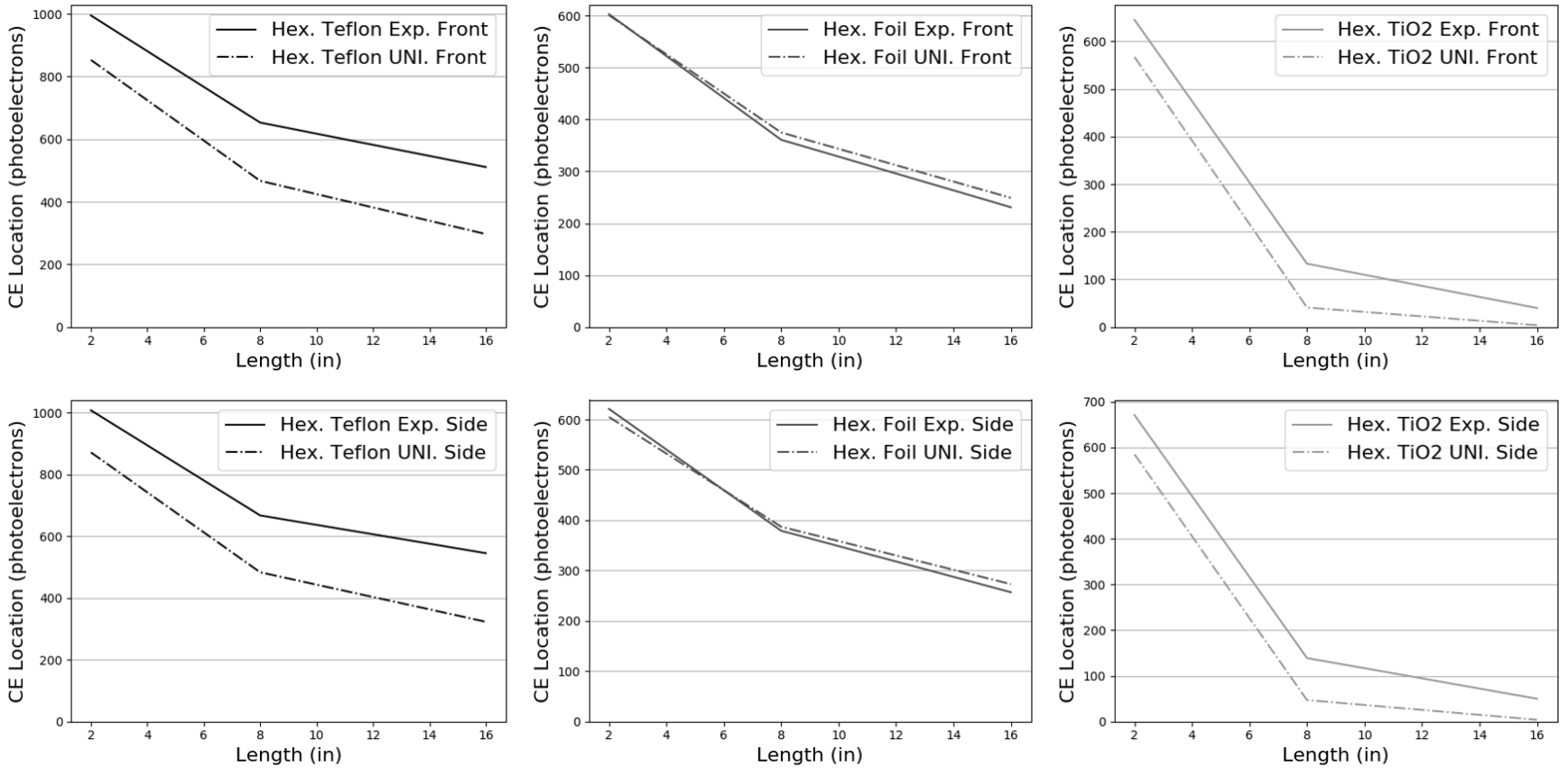


Figure 3.23: Comparison of the experimental and simulated Cs-137 Compton edge location with hexagonal EJ200 and varied optical reflectors. Teflon is used in the left column, foil in the center column, and TiO_2 in the right column. Data in the top row are from front irradiation; the bottom row represents side irradiation. The LUT model simulations did not complete for the hexagonal configuration.

1. Higher aspect ratios force more optical photon interactions to occur on the surface, the probability of the photon being absorbed follows a power relation with the number of surface interactions in the exponent (i.e. $A = 1 - R^n$), even in the case of teflon where $R = 0.99$, if the photon interacts with the reflector 15 times it has a 14% chance of being absorbed. In the case of foil or TiO_2 ($R = 0.787 or 0.951$), this is increased further to 97% and 53% respectively. Of course the reason why the foil reflectors show higher performance compared to TiO_2, though, is due to the air gap present for foil but not for the TiO_2 reflector. This air gap allows total internal reflection to occur, and is also present in the teflon use case.

2. Not only are higher aspect ratios used in this experiments, but so are larger scintillators. This results in a longer optical path which will lead to increased bulk absorption.

Ultimately, these two light-loss mechanisms result in the decreased light output observed for longer/higher aspect ratio scintillators. The simulation data currently exists so that these to competing loss mechanisms may be compared. Cursory inspection of this simulated data for the cylinder using *unified* models and front irradiation show that:

1. The average teflon surface absorption probability is 0.055, 0.083, and 0.091 for 2, 8, and 16 inch samples respectively

2. The average bulk absorption probability when using the teflon reflector is 0.359, 0.575, and 0.689 for 2, 8, and 16 inch samples respectively

3. The average foil surface absorption probability is 0.35, 0.390, and 0.404 for 2, 8, and 16 inch samples respectively

4. The average bulk absorption probability when using the foil reflector is 0.215, 0.331, and 0.411 for 2, 8, and 16 inch samples respectively

5. The average TiO_2 surface absorption probability is 0.326, 0.566, and 0.596 for 2, 8, and 16 inch samples respectively

6. The average bulk absorption probability when using the TiO_2 reflector is 0.229, 0.381, and 0.399 for 2, 8, and 16 inch samples respectively

This indicates that bulk absorption is the primary loss mechanism when using the teflon reflector. There is quasi-parity for both the surface and bulk absorption mechanisms when using the foil reflector. Use of the TiO_2 reflector results in more absorptions occurring on the surface as opposed to the inside the scintillator volume.

3.5 Conclusion

The results of this work show, that for the selected parameters, the *unified* model outperforms the LUT model in cylindrical geometries and the LUT model performs better for the rectangular shapes. While the LUT model did better for teflon+cylinder, it did so by only a small margin; much smaller than the total error of both models in this case. Given the small difference in objective performance for the two models in the cylinder+teflon configuration, and the consideration that the simulation time using the *unified* model is much shorter than when using the LUT model, it would likely be advantageous to use the *unified* model for all cylindrical scintillators.

The simulation results also provide some additional understanding related to the competing light loss mechanisms. For teflon-wrapped surfaces the model shows the majority of the light loss coming from bulk optical absorption. For foil wrapped surfaces, surface and bulk absorption are comparable. Since TiO_2 treated surfaces have no air gap, the dominant mode of light loss is derived from surface absorption. Even though the EJ200 optical absorption lengths used for this may be called into question, it is likely that these generalities will hold.

3.6 Acknowledgements

The author would like to thank Cordell Delzer and the Scintillation Materials Research Center for the use of the spectrophotometer and data collection for measurements on the EJ200 sample using the same. Additional thanks goes to Michael Liesenfelt for his efforts to configure the knee mill in the Nuclear Engineering Department's machine shop for facing the ends of the scintillator samples.

This material is based on work supported in part by the Defense Threat Reduction Agency under grant number HDTRA 1-18-1-005 and in part by the Department of Energy National Nuclear Security Administration through the Nuclear Science and Security Consortium under Award Number(s) DE-NA0003180 and/or DE-NA0000979.

Disclaimer: "This report was prepared as an account of work sponsored by an agency of the United States Government. Neither the United States Government nor any agency thereof, nor any of their employees, makes any warranty, express or implied, or assumes any legal liability or responsibility for the accuracy, completeness, or usefulness of any information, apparatus, product, or process disclosed, or represents that its use would not infringe privately owned rights. Reference herein to any specific commercial product, process, or service by trade name, trademark, manufacturer, or otherwise does not necessarily constitute or imply its endorsement, recommendation, or favoring by the United States Government or any agency thereof. The views and opinions of authors expressed herein do not necessarily state or reflect those of the United States Government or any agency thereof."

Chapter 4

Validation of a GEANT4 Application for Light Transport in High-Z Loaded Plastics

At the time of submitting this dissertation, the following chapter was concurrently being prepared for submission for publication as one of the authors PJAs. The co-authors of this to-be-submitted PJA are: C. Delzer, H. Yu, T. Chen, Q. Pei, N. Cherepy, and J. Hayward.

4.1 Abstract

As new scintillators are constantly under development for radiation detection, often starting in small volumes, it is important to understand and demonstrate how well and to what extent our current modeling tools may be utilized for predicting the expected performance of these materials when scaled up appropriately for radiation sensing applications. While many novel scintillators may be characterized experimentally and be readily modeled by Monte Carlo simulations such as GEANT4, the applicability of this method to some novel materials is not always so clear. This work examines recently developed, potentially promising high-Z loaded plastic scintillators and the extent to which they may be modeled by GEANT4. In particular, we report on the validation of simulations of plastics loaded with lead organometallic complexes and nanocomposites consisting of ytterbium fluoride nanoparticles. Additionally,

since these materials may currently be limited in scalability, performance predictions of incrementally scaled-up samples are performed. These predictions focus on examining the relationships between the photopeak position and resolution, optical absorption, variance in the photoelectron production efficiency (which is closely linked to the variance in the light collection efficiency), and the probability of fluorescence x-ray escape.

4.2 Introduction

The *primary focus* of this chapter is on demonstrating and validating the application of GEANT4 to the scenario of high-Z loaded plastic scintillators. Attention is given to both organometallic and nanocomposite high-Z loading frameworks. Much of what would be considered introductory for this chapter has already been presented in the dissertation introduction; specifically in Subsection 1.3.3. Contained in that section, is a description of the current state of high-Z loaded organic scintillators. The section ended on the discussion of Rayleigh scattering in nanocomposites and the current equation used to describe the interaction lengths of that process in this subset of materials. It is here that the introductory discussion will continue as the work in this chapter brings this issue to the forefront.

To have it available in this present discussion, the equation is shown below:

$$I = I_0 \exp\left\{ -\frac{32\phi_p x \pi^4 r^3 n_m^4}{\lambda^4} \left[\frac{(n_p/n_m)^2 - 1}{(n_p/n_m)^2 + 2} \right]^2 \right\} \tag{4.1}$$

where ϕ_p is the nanoparticle packing fraction (volume fraction), x is the distance traveled by the photon, r is the radius of the nanoparticle, n_m is the index of refraction of the matrix, and n_p is the index of refraction of the nanoparticle. This equation and/or equivalent descriptions of Rayleigh scattering in nanocomposites is found in recent papers on nanocomposite scintillators [61, 63, 66, 67]. From these, the equation traces back to two references [71, 110]. Reference [71] hits a dead end at an inaccessible thesis [72], and reference [110] has an apparent mis-reference for the equation credit to [111] which contains no equation and instead discusses how to increase refractive indices in hybrid materials using a sol-gel process. It is believed that maybe [110] intended to reference the book [112].

During this same dive into the literature, an article from outside the reference tree presented itself which discusses light loss mechanisms in nanocomposite waveguides [113]. This article presents an equation for the scattering efficiency factor, Q_{sca}, for optical photons on small spheres as shown in Equation 4.2. The reference for this equation was to the van de Hulst text [114] where it may be found in Section 6.31.

$$Q_{sca} = \frac{8}{3}x^4 \left(\frac{m^2-1}{m^2+2}\right)^2 \tag{4.2}$$

Section 2.4 of the van de Hulst text defines the scattering efficiency factor as the ratio of the microscopic scattering cross section, σ_{sca}, to the geometric cross section of the scatterer, σ_{geo}. The text further defines x as the particle size parameter which is given by:

$$x = \frac{2\pi r}{\lambda_m} \tag{4.3}$$

where λ_m refers to the wavelength of the light in the medium (as opposed to the vacuum wavelength). Using these relationships and Equation 4.2, the microscopic scattering cross section may be defined by:

$$\sigma_{sca} = \sigma_{geo}Q_{sca} = \pi r^2 \times \frac{8}{3}\left(\frac{2\pi r}{\lambda_m}\right)^4 \left(\frac{m^2-1}{m^2+2}\right)^2 = \frac{128}{3}\frac{\pi^5 r^6}{\lambda_m^4}\left(\frac{m^2-1}{m^2+2}\right)^2 \tag{4.4}$$

The scattering attenuation coefficient is simply defined as:

$$\mu_{sca} = N\sigma_{sca} \tag{4.5}$$

where N is the number density of the nanoparticles. The volume fraction of the nanoparticles in the scintillator, ϕ_p, may be related to the number density by expressing the volume of nanoparticles in a unit volume of the composite:

$$\phi_p = \frac{V_{np}}{V_{nc}} = \frac{(N \times 1cc)\frac{4}{3}\pi r^3}{1cc} \tag{4.6}$$

Rearranging for N gives:

$$N = \frac{3\phi_p}{4\pi r^3} \tag{4.7}$$

Substituting Equations 4.4 and 4.7 into 4.5 gives:

$$\mu_{sca} = \frac{3\phi_p}{4\pi r^3}\frac{128}{3}\frac{\pi^5 r^6}{\lambda_m^4}\left(\frac{m^2-1}{m^2+2}\right)^2 = \frac{32\phi_p\pi^4 r^3}{\lambda_m^4}\left(\frac{m^2-1}{m^2+2}\right)^2 \tag{4.8}$$

Further, using the definitions of $\lambda_m = \lambda/n_m$ and $m = n_p/n_m$, we arrive at:

$$\mu_{sca} = \frac{32\phi_p\pi^4 r^3 n_m^4}{\lambda^4}\left[\frac{(n_p/n_m)^2-1}{(n_p/n_m)^2+2}\right]^2 \tag{4.9}$$

This is clearly identical to the scattering coefficient present in Equation 4.1. At this point, it is evident that the equation used to describe the Rayleigh scattering length in nanocomposites stems from Rayleigh's theory [115] and was exposited in the van de Hulst text [114]. As such, it is bound to the terms and conditions of the context for which it was derived.

This final point is the crux of this discussion. Section 6.31 of the van de Hulst text applies when the size parameter, Equation 4.3, is much less than 1, making the Born approximation valid, and when the particle is spherical and optically 'soft'. A particle is considered optically soft when $|m-1| \ll 1$. In the case of YbF_3/PVT nanocomposites [62, 63], the nanoparticles have a diameter of approximately 5 nm, and $m = 1.52/1.55 = 0.981$ using the values for the refractive indices in [62]. The nanoparticles are assumed to be spherical. The evaluation of these gives, for 420 nm light, $x = 0.037 \ll 1$ and $|m-1| = 0.019 \ll 1$; and therefore this seems to indicate that Equation 4.1 applies to this system. At this point, everything seems like it should work. There are, however, some overlooked technicalities which possibly rear their ugly head. This will be delved into in Section 4.4.

4.3 Methodology

Our methodology, ultimately, consists of comparing experimental results with simulated results. Experimental results are garnered through our own experiments in the case of lead loaded EJ256, while *all* experimental results for the YbF_3 nanocomposite are obtained from the literature in [62]. The result of using two different sources for the experimental information leads to EJ256 being quantified on an absolute scale while the

energy/photoelectron data for the nanocomposites is compared on an arbitrary scale. The simulation for both of these materials handles all the physics processes involved in radiation transport and optical photon transport through the scintillator to the PMT photocathode.

4.3.1 Experiments with EJ256 5% Pb

The experiments performed on EJ256 were identical to a subset of the experiments performed on the EJ200 bars as described in Subsection 3.3.2. Light output studies were performed using the calibrated R2059 PMT operated at -1700V. A 2x2 inch cylindrical sample of EJ256 with 5% lead loading was obtained after being machined and mechanically polished by Agile Engineering. This sample was wrapped with four layers of Teflon tape and coupled to the R2059 PMT using Visilox V-788 optical coupling compound. A background measurement was taken for 30 minutes followed by front irradiation of the sample using a Cs-137 source placed 10 cm on-axis from the detector face. This data allows the EJ256 sample to be compared to the simulation both in terms of light output and the count rate for a given light output.

Just as was done for the EJ200 scintillator, a transmission measurement was performed on the EJ256 sample. The cylinder was placed on its side, and stabilized, in a Varian Cary 5000 UV-Vis-NIR spectrophotometer. The reference sample was air. The thickness of the sample, through which light traversed, was 5.076 cm. The optical transmission was measured from 200-800 nm. The results of this measurement were converted into optical absorption lengths using the method presented in Subsection 3.3.2 and then used as inputs for the simulation.

4.3.2 Simulation Design

The simulations of the radioactive source injection using Cs-137 were also very similar in design to those presented in Chapter 3. GEANT4-10.04.p02 was used to perform the simulations utilizing the G4EmStandardPhysics_Option4() and standard G4OpticalPhysics() in the physics list. The optical surface model used for these simulations is the *unified* model with the parameters for Teflon shown in Table 3.5. The refractive indices used for both

EJ256 and all versions of the nanocomposite were the same as those used for EJ200 as defined by Equation 3.14 using the parameters found in Table 3.4. The descriptions of the optical grease, silica PMT window, and photocathode were also identical to those presented in Chapter 3.

Spectrophotometry Simulations

In order to validate the optical absorption lengths, the effect of optical absorption was directly simulated by emulating a spectrophotometry experiment. A diagram of this is shown in Figure 4.1. The size of the simulated beam spot on the sample was based on the manual specifications and is shown in Figure 4.2. The simulated experiment utilizes a focused-beam light source uniformly distributed in wavelengths from 200 nm - 700 nm as shown in Figure 4.3. The detector was similar to the one used in the simulations with the radiation source except that the window was borosilicate and no reflection is assumed to occur off of the photocathode. All simulated spectrophotometry experiments were normalized using a reference run with no sample, (i.e. only air), between the light source and the detector. The result of this reference run is the transmission through air and the photo detector window and it is provided in Figure 4.4.

The sample and photodetector are axially aligned and separated by 20 cm. All optical surfaces are described using the *unified* model with the surface type of dielectric_dielectric and a polished finish. In regards to the wavelength frequency distribution of the initial photons, Figure 4.3, the strange oscillatory behavior observed in the longer wavelengths is most like attributed to artifacts arising when attempting to define a uniform wavelength distribution in energy space. Since wavelength and energy are inversely related, equispaced energy points are no longer equally spaced in wavelength; this gives rise to the every increasing period of the amplitude with respect to the wavelength. Furthermore, the sawtooth pattern arises because of the interpolation between adjacent energy bins and how this maps over to wavelength. At any rate, these small artifacts are of no concern because they are accounted for when the sample transmission data is normalized using the reference transmission run; essentially this behavior cancels itself out.

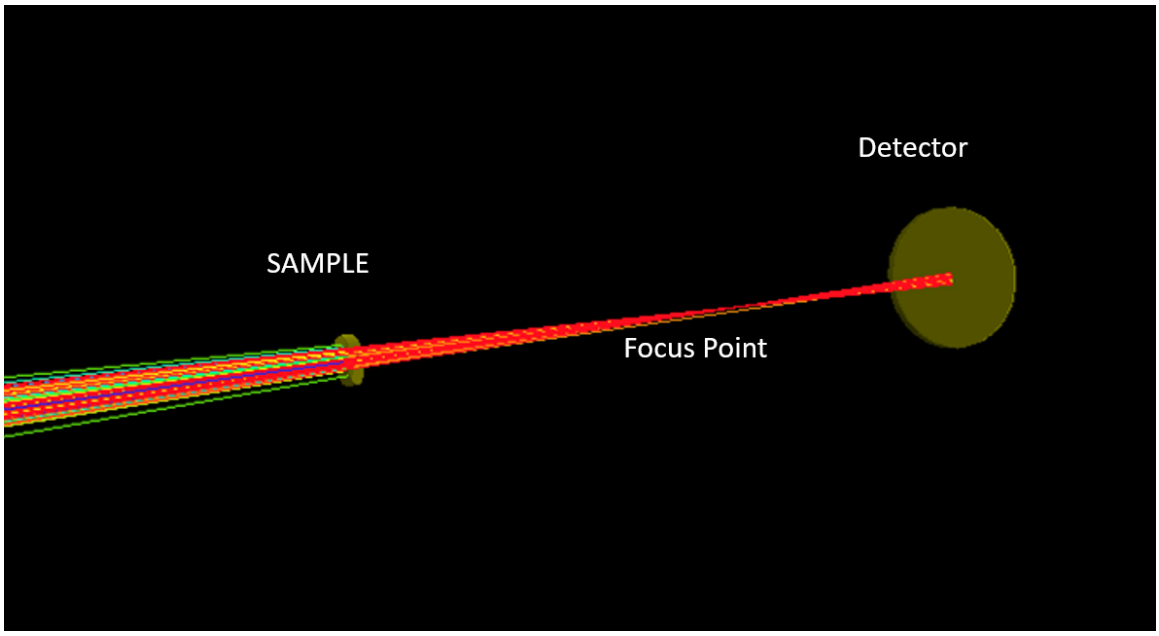


Figure 4.1: Diagram of spectrophotometry experiment simulation. A reference run, without a sample, was used to normalize against and remove the effects of the detector material.

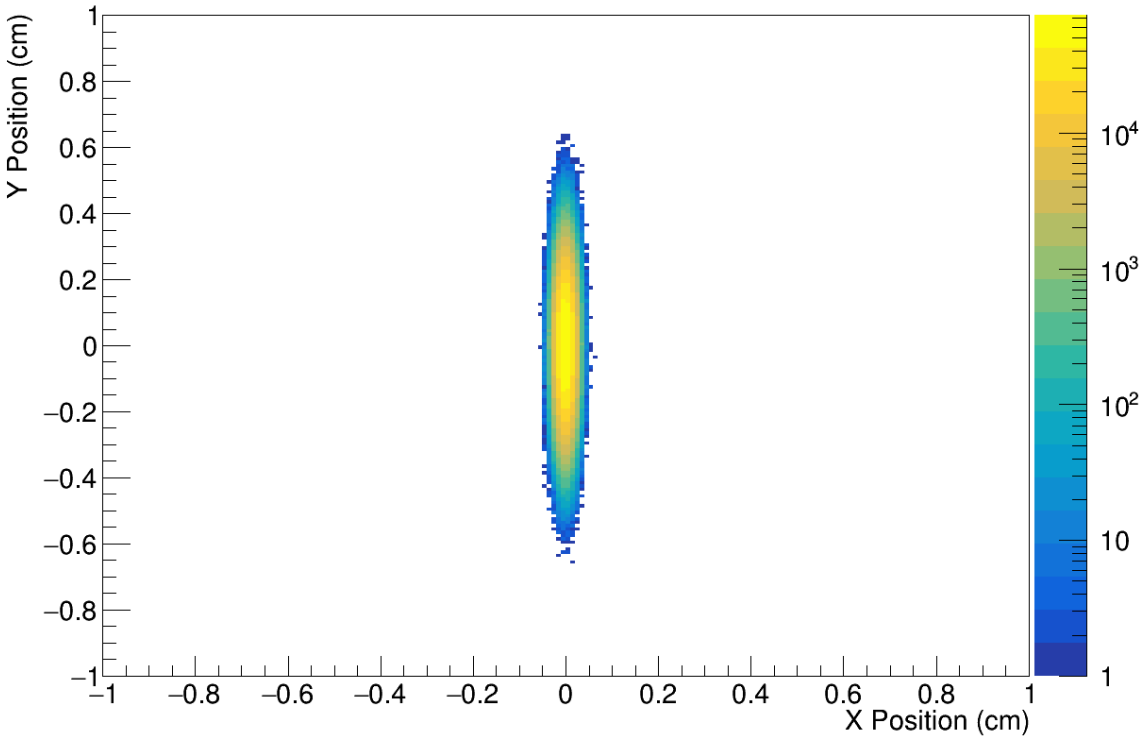


Figure 4.2: Simulated spectrophotometer beam spot. The most intense area is approximately 1x0.2 cm, congruent with the manual specifications.

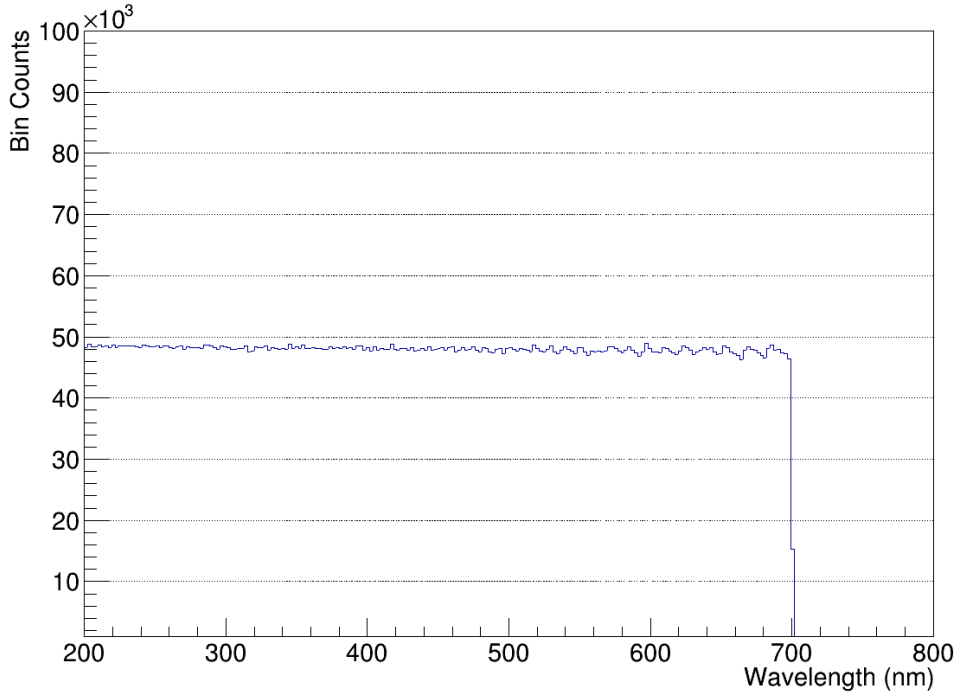


Figure 4.3: Distribution of initial simulated spectrophotometer photon wavelengths. The target distribution was uniform.

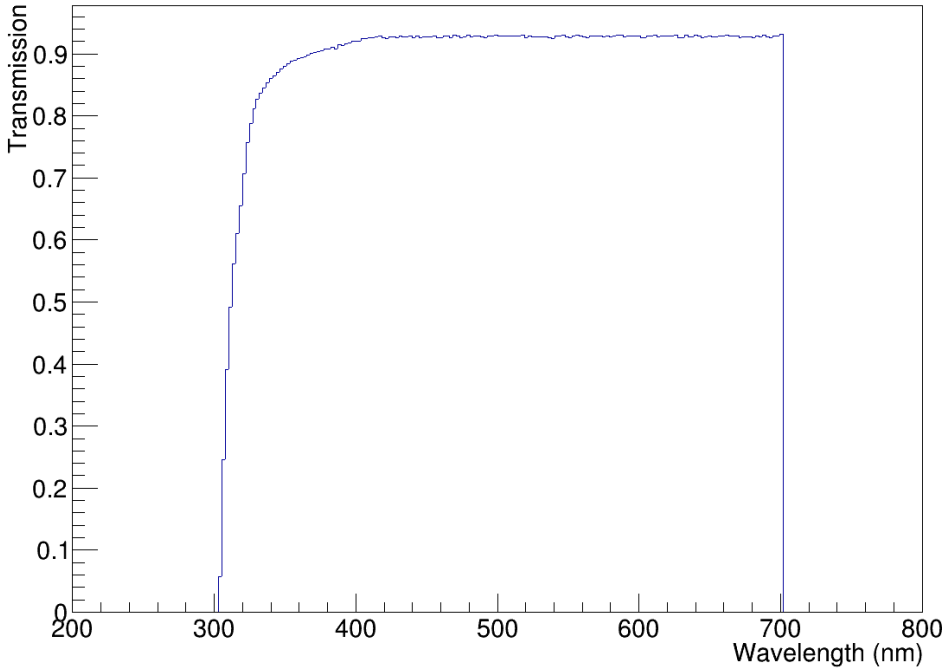


Figure 4.4: Simulated reference transmission distribution vs wavelength. This is used to normalize into the sample transmission data.

Simulating EJ256 5% Pb

The material composition and density for EJ256 were stated by the manufacturer and are provided in Table 4.1. The optical absorption lengths were found by using our own transmission data and correcting for Fresnel reflection at the sample interfaces. The resulting values of the optical absorption lengths are shown in Figure 4.5. Lastly, the scintillation light was produced according to the emission spectrum provided by the manufacturer which is shown with respect to both wavelength and energy in Figures 4.6 and 4.7.

Simulating YbF3 Nanocomposites

The material composition and density for the various nanocomposite formulations are approximate and were derived from procedural data found in [62] and the raw material data came from Sigma-Aldrich. All parts of the recipe components were considered. For example, a base recipe may state 58.9 w/w% YbF_3 nanoparticles, 1 w/w% POPOP, 2 w/w% PBD, 2 w/w% DVB, and 1 w/w% DTTMC. These were then further broken down into other real or implied components. For example, 58.9 w/w% YbF_3 nanoparticles implies 8.65 w/w% of the BMEP ligand (since the ligand makes up 12.8% of the nanoparticle plus ligand complex). The other components were also broken down into their sub-components: the DVB was 80% pure, with EVB making up the other 20%, the POPOP was a 50% concentration in a VT solution, and DTTMC was 75% pure with VT assumed to make up the other 25%. Using this approach, the atom mass fractions were estimated for each nanocomposite sample. The sample density was also estimated using the contribution to the total sample density from the major components: the PVT, with a density of 1.023 g/cc, the YbF_3 nanoparticles with a density of 8.17 g/cc, and the BMEP ligands with a density of 1.28 g/cc. The primary assumption is that the density and atom fractions of the components do not change upon mixing and curing of the samples. The resulting material properties for all the nanocomposite samples are shown in Table 4.2.

The remaining nanocomposite properties to be defined are the optical absorption lengths, Rayleigh scattering lengths, and the radioluminescence spectrum. The Rayleigh scattering lengths were determined using Equation 4.1 with the refractive index of the matrix at 417

Table 4.1: Material definition for EJ256.

EJ256	
Density (g/cc)	1.081
Light Yield (photons/keV)	5.2
Hydrogen, f_m	0.08199
Carbon, f_m	0.86801
Lead, f_m	0.05

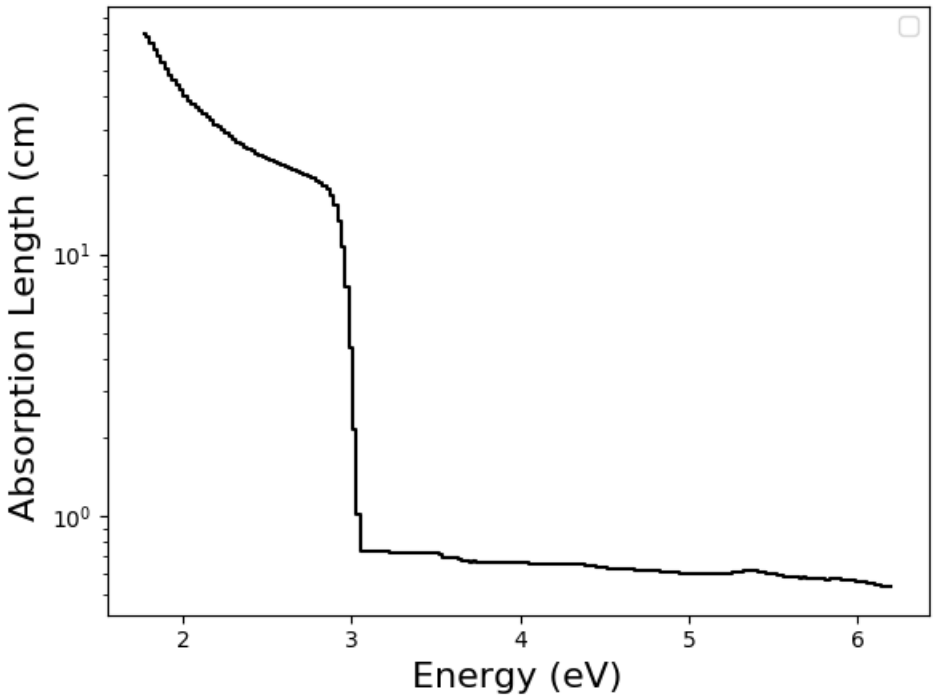


Figure 4.5: The optical absorption lengths of EJ256 calculated using transmission data and the Fresnel correction with a constant refractive index of 1.58.

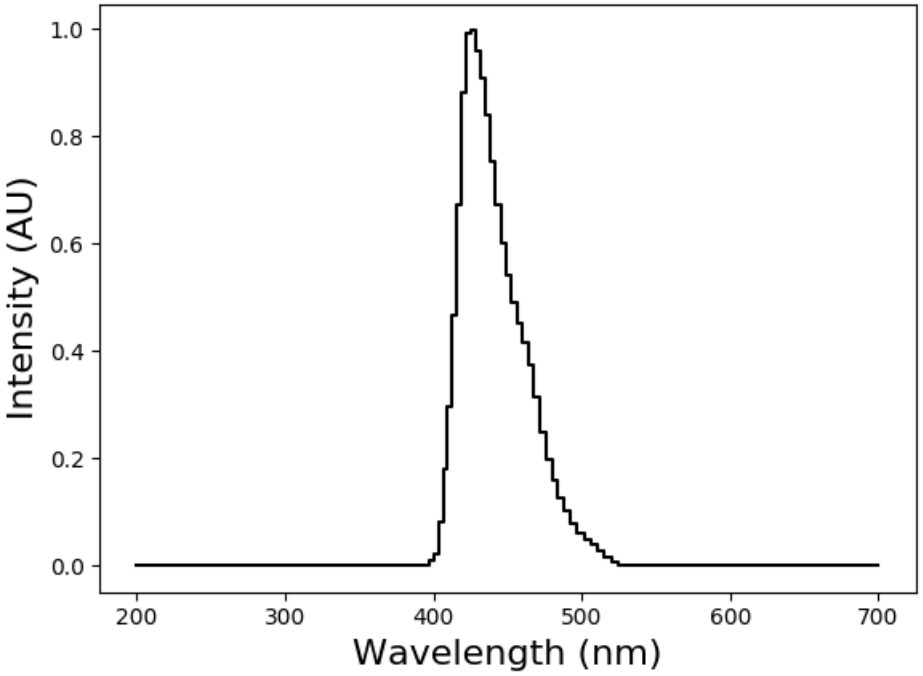


Figure 4.6: Luminescence spectrum of EJ256 5% Pb with respect to wavelength [90].

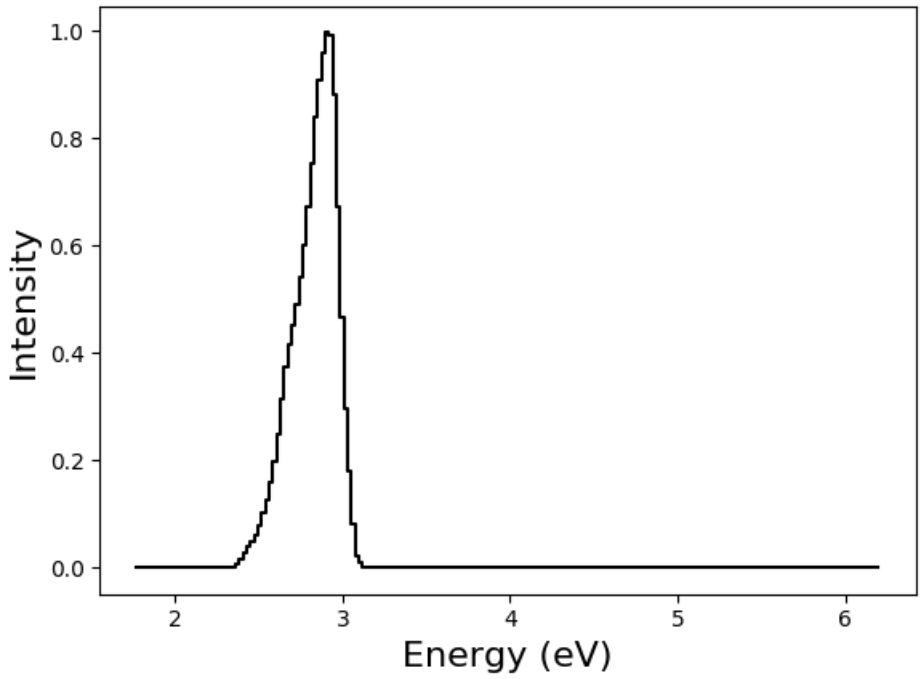


Figure 4.7: Luminescence spectrum of EJ256 5% Pb with respect to energy.

Table 4.2: Material definitions for YbF_3 nanocomposites.

Sample	Light Output (photons/keV)	Matrix + Ligand Density (g/cc)	Sample Density (g/cc)	Nanoparticle Volume Fraction, (%)	Element Mass Fractions, f_m (%)						
					H	C	N	O	F	P	Yb
0 wt/%	9.5	1.023	1.023	0	8.497	91.114	0.297	0.091	0	0	0
24.5 wt/%	6.5	1.033	1.314	3.941	6.314	67.019	0.297	1.519	6.071	0.346	18.433
35.9 wt/%	5.19	1.04	1.515	6.656	5.299	55.807	0.297	2.184	8.896	0.507	27.01
45.8 wt/%	3.75	1.049	1.746	9.789	4.416	46.07	0.297	2.762	11.35	0.646	34.459
58.9 wt/%	2.44	1.068	2.189	15.779	3.249	33.186	0.297	3.526	14.596	0.831	44.315

nm, the peak emission wavelength, given as $n_m = 1.6121$ and the refractive index of the nanoparticle at 417 nm as $n_p = 1.5717$ found using the Cauchy parameters for YbF_3 in [116]. The nanoparticle radius was 2.5 nm, and the volume fractions of the nanoparticles are provided in Table 4.2 after being calculated according to Equation 4.10, which was derived from first principle relations. In that equation, f_V is the volume fraction of the nanoparticles, f_W is the nanoparticle mass fraction, δ_{np} is the nanoparticle density, and δ_m is the density of the matrix + ligands. The resulting Rayleigh scattering lengths are shown in Figure 4.8, where the 'Equation 1' data set is referring to Equation 4.1, and the 'Equation 2' data is referring to the abandoned Equation 1.26. These are shown together to emphasize the enormous difference between the two equations.

$$f_V = \left(1 + \frac{\delta_{np}}{\delta_m}\frac{1 - f_W}{f_W}\right)^{-1} \tag{4.10}$$

The radioluminescence data for the nanocomposites was taken from the literature in [62]. This is shown against photon wavelength and energy in Figures 4.9 and 4.10, respectively. The peak RL wavelength is approximately 417 nm, with a smaller secondary peak around 450 nm, and finally tailing to 520 nm, where the intensity terminates. In energy space, the RL peak occurs at around 2.97 eV.

The optical absorption lengths were determined from the transmission data presented in [62] after being corrected for Fresnel reflection according to our prescribed method. The resulting absorption lengths are shown in Figure 4.11. The effect of Rayleigh scattering was not adjusted for in this correction since the calculated Rayleigh scattering lengths are quite long, many hundreds of centimeters, and the sample thickness in the transmission measurement was only 2 mm. The assumption herein, then, is that Rayleigh scattering did not contribute to light losses in the reported optical transmission measurements. Examining the optical absorption data at just under 3eV, the location of the RL peak, the sample with no nanoparticle loading has an absorption length of around 3 cm, while all samples with nanoparticles have an absorption length of around 1 cm. Of particular note is that the 0 wt/% sample, has an absorption length that is smaller than that of EJ200 by a factor of more than an order of magnitude; the reason for this is not very clear.

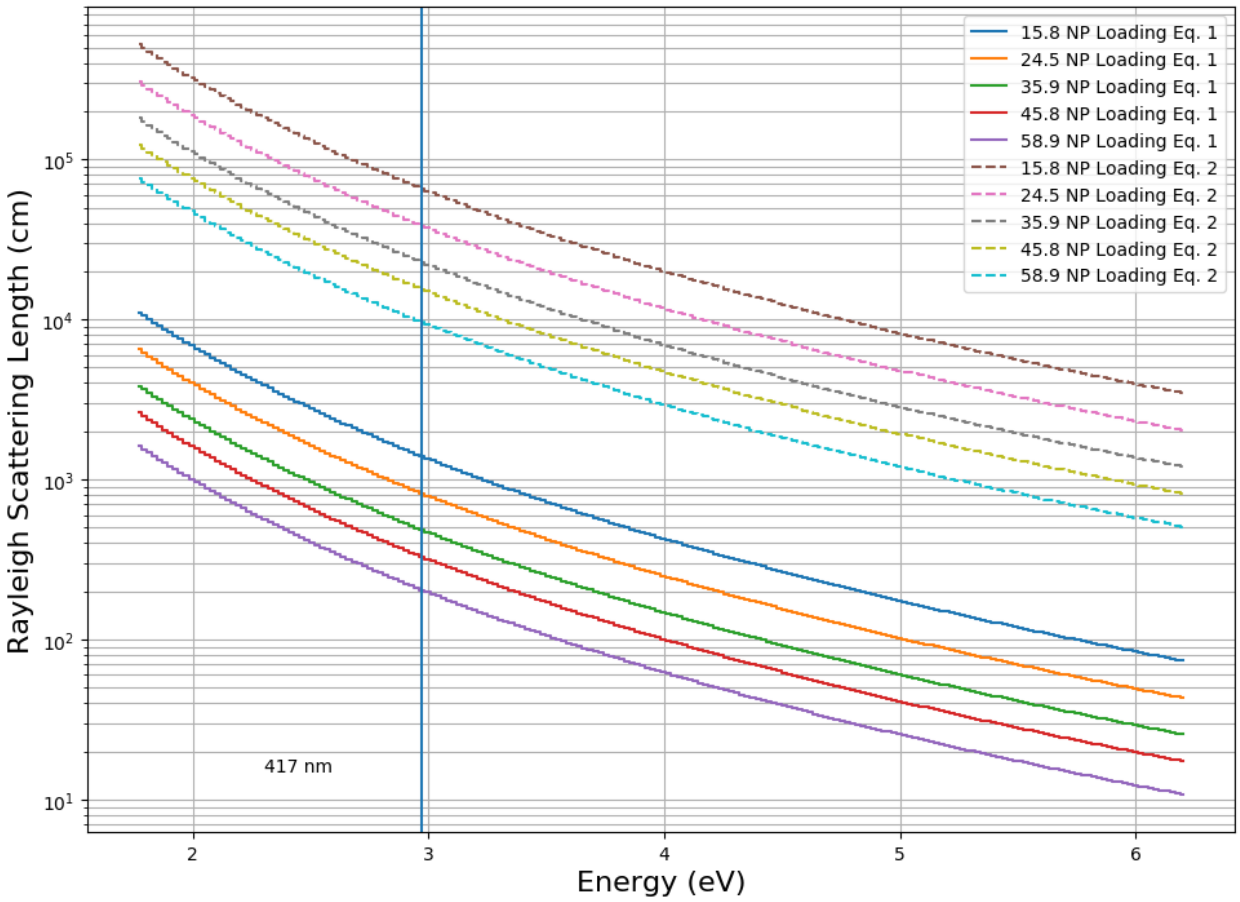


Figure 4.8: Calculated Rayleigh scattering lengths in YbF_3 nanocomposites. Eq1 refers to lengths using the relation in Equation 4.1, while Eq2 refers to the lenghts from the relation given in Equation 1.26. The refractive indices used for the matrix and nanoparticles are taken at a wavelength of 417 nm, the maximum radioluminescence wavelength.

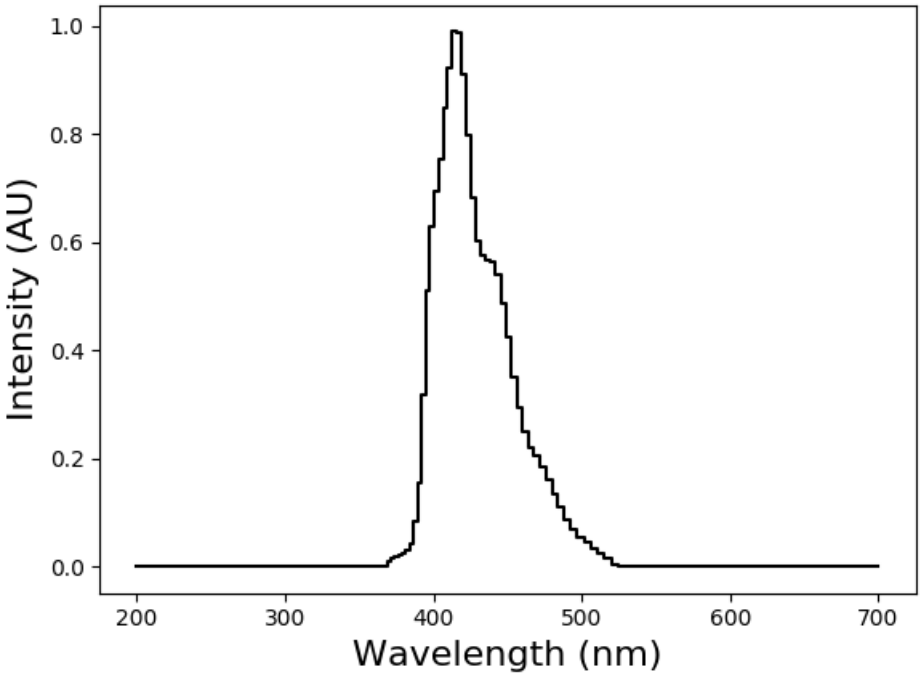


Figure 4.9: Radioluminescence spectrum of the YbF_3 nanocomposites with respect to wavelength [62].

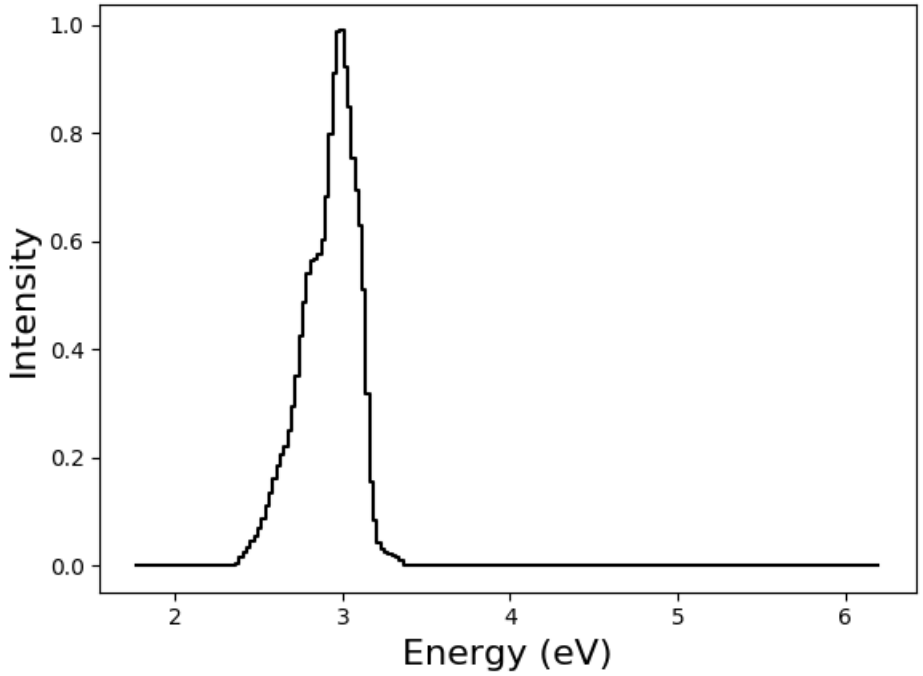


Figure 4.10: Radioluminescence spectrum of the YbF_3 nanocomposites with respect to energy.

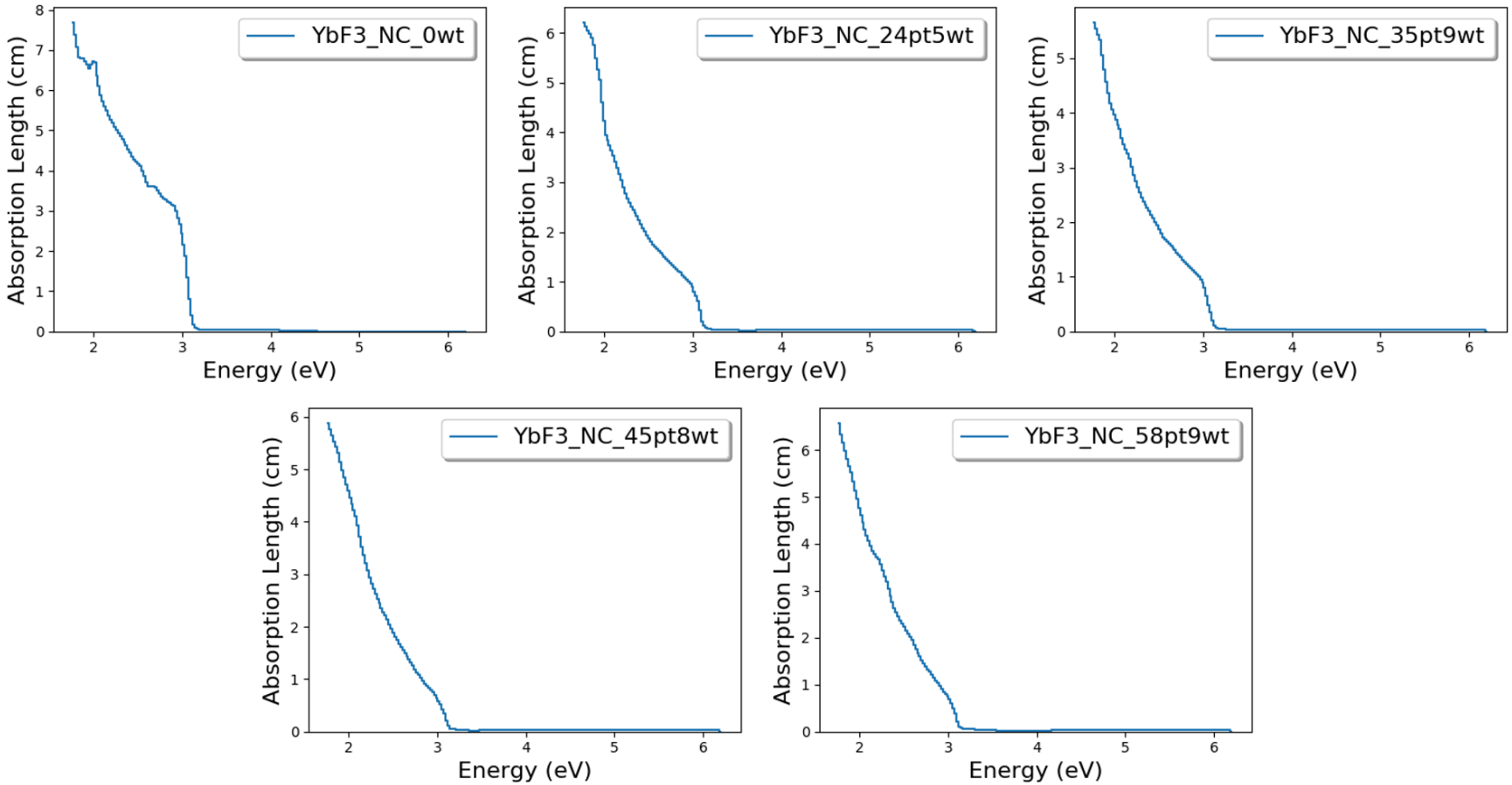


Figure 4.11: Optical absorption lengths in YbF_3 nanocomposites. The transmission data was from [62] and was corrected for Fresnel reflections during the absorption length calculation.

The simulated source was Cs-137, the same as that used in the reference for bench marking. In the simulation, the source was placed 2 cm from the face of the samples. The rest of the simulation geometry is identical to that described in Chapter 3.

4.3.3 Material Scale Up Study

Using the previously defined materials, simulations were performed to show the effects of gradually scaling up EJ256 and the 24.5 wt/% YbF_3 nanocomposite. The 24.5 wt/% composition was chosen because it had the highest reported energy resolution in [62]. The EJ256 material was simulated in right-circular cylinder (RCC) geometry with a diameter of 10 mm and lengths from 2 mm - 50 mm in increments of 2 mm. The YbF_3 nanocomposite was also simulated in RCC geometry having a 10 mm diameter and varying in length from 1 mm - 10 mm in 1 mm step sizes and from 10 mm - 50 mm in 2 mm increments. The simulated source was Cs-137 which was placed 2 cm from the face of the scintillator. The source was placed on axis with the scintillator and its particles were uniformly emitted within a cone having a half-angle of 15 degrees and which shared the scintillator axis. All runs were completed with 10^6 source particles. An exception to these is the simulation of the 2x2 inch nanocomposite where the source was placed 10 cm in front of the scintillator and the cone half-angle was 14.3 degrees.

4.4 Results and Discussion

4.4.1 Validation with EJ256 5% Pb

The results for the simulated and experimental spectrophotometry measurement on EJ256 are shown in Figure 4.12. The simulated and experimental result agree with each other exceedingly well across all represented wavelengths. The results show the absorption edge to be located at approximately 410 nm. The transmission then steadily increases from 450 nm to 700 nm. This is consistent with the slight orange hue which was apparent when examining these samples.

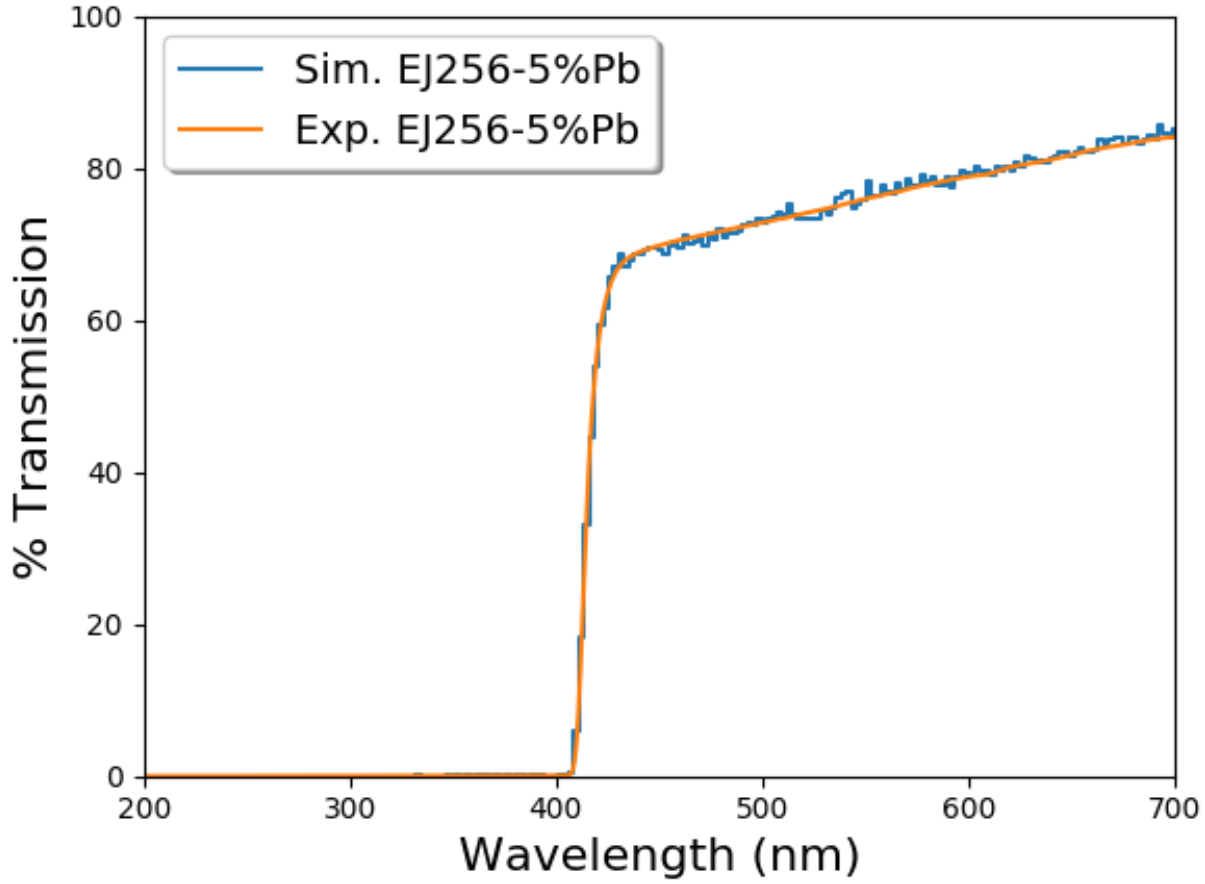


Figure 4.12: Comparison of measured and simulated EJ256 spectrophotometry data. The experiment and simulation agree very well, one with the other.

The measured and simulated Cs-137 spectrum are shown in Figure 4.13. Both the bin count rate and the number of photoelectrons are comparable absolutes in this data set. The extent to which these agree is quite astonishing to the author. The simulation does under-predict the Compton edge location by about 10% which is similar to the under-predictions seen when using the simulated Teflon surfaces in Chapter 3. The simulated and experimental bin count rates related to the Compton maximum and the Compton minimum match nearly exactly. Despite the loading of Pb into the plastic, there is no evident photopeak in either the simulated or experimental spectra.

The reason for the lack of a noticeable photopeak is explained by examining Figure 4.14. This figure contains the frequency distribution of the number of photoelectrons produced for a given amount of energy deposited in the scintillator. Viewing this in terms of vertical slices, one may infer the detector response for any given deposited energy. It is clear from projecting to the deposited energy axis that photoelectric interactions and fluorescence x–ray escapes did occur, but these peaks are lost in the photoelectron spectrum because the variance in the number of photoelectrons produced for a given amount of deposited energy is so large. For example, depositing 400 keV of energy may produce 100 photoelectrons on the low end of the distribution, but it may also produce 250 photoelectrons on the upper end of the distribution. Looking at this in terms of photoelectrons, it is possible to have 200 photoelectrons produced from 320 keV of energy deposited, but it is also possible to receive that same number of photoelectrons from the photopeak at 662 keV.

According to the simulation, the primary mode of optical photon loss for the 2x2 inch EJ256 sample is through bulk optical absorption. This results in an expected loss of 68.56% of light for any given scintillation event. Absorptions on the optical surface, however, account for 1.13% of lost light for a typical event.

4.4.2 Validation with YbF_3 Nanocomposites

The simulated and experimental spectrophotometry results with each of the nanocomposite formulations are shown in Figure 4.15. As was the case with EJ256, there is excellent agreement between the experimental and simulated values for the transmission across all wavelengths presented. There is a strong absorption edge at around 400 nm for all samples.

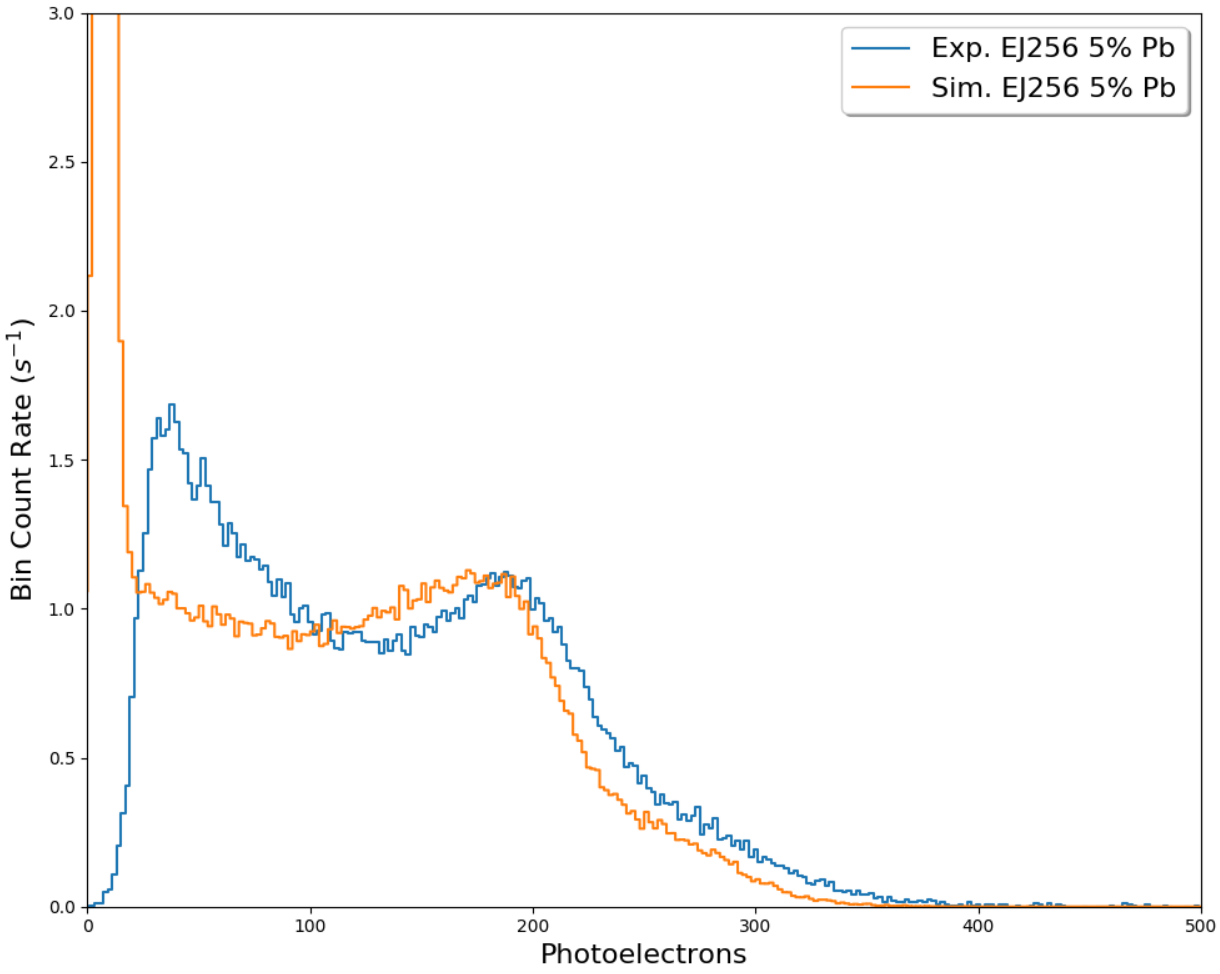


Figure 4.13: Comparison of measured and simulated Cs-137 spectrum taken with 2x2 inch EJ-256 5 wt/% Pb. This is an absolute comparison in both the number of photoelectrons and the bin count rate. The bin width is two photoelectrons.

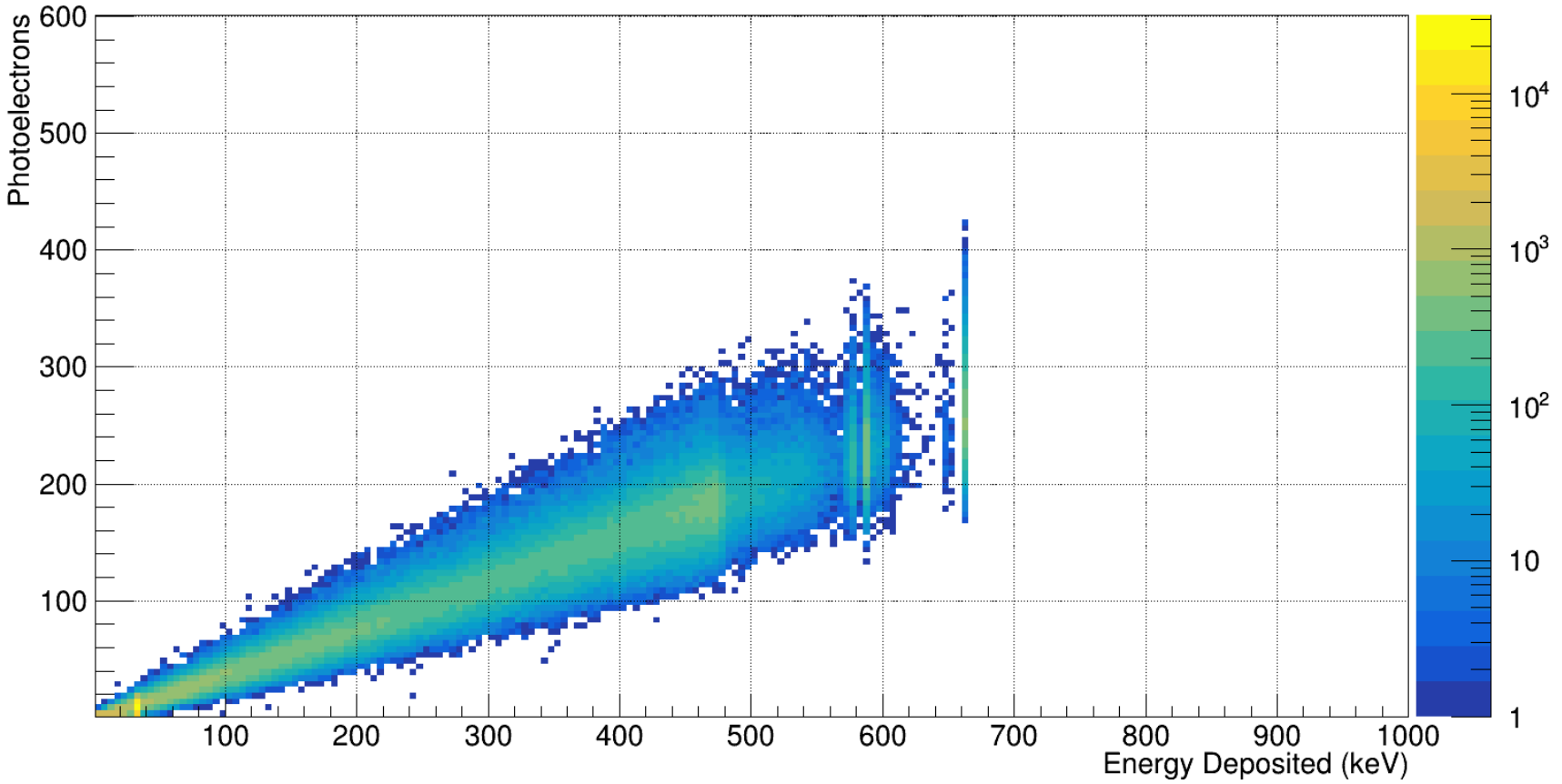


Figure 4.14: Simulated response of a 2x2 EJ-256 5 wt/% Pb detector when using a Cs-137 source. Notice the presence of the photopeak (662 keV) and x-ray escape peaks (just below 600 keV). These peaks are not observed in the energy (photoelectron) spectrum because of the large variance in the number of photoelectrons produced for a given energy deposited in the scintillator. The color scale refers to the counts per pixel.

The sample with 0 wt/% loading has a sharp corner transitioning from the transmission regime to the absorption edge while the samples with nanoparticles have a steady decrease and soft corner in when making the transition from the transmissible range of wavelengths to those wavelengths which are absorbed.

The experimental and simulated Cs-137 spectra taken with different wt/% loading nanocomposites are shown in Figure 4.16. The experimental x and y values are arbitrary, but consistent such that $AU_x = \alpha \times Ch_{MCA}$ and $AU_y = \beta \times N_{bin}$. Values for α and β were chosen so that the photopeaks and Compton maxima for the loaded samples have the best overall agreement. This resulted in a value for α of 0.34 and a value for β of 0.63. Again, these same scaling factors were used for all experimental data. Also important, is that the experiments were stated to occur over the same length of time.

Comparing the results in Figure 4.16 reveals photopeaks in all of the nanocomposites. The simulated and experimental photopeak locations agree quite well with each other. The match is nearly identical for the 24.5 and 35.9 wt/% samples. For the 45.8 wt/% sample the simulated photopeak and Compton edge locations deviate very slightly from the experimental values coming in just below what is reported by the experiment. The 58.9 wt/% YbF_3 sample agrees quite well in location, but not as well in the height of the Compton maximum or the width of the photopeak. The experimental data was screen digitized using the apparent mean of the bin counts, so the added real bin count variance may change that appearance somewhat. At any rate, the last comparison discussed here is with the 0 wt/% sample. Using the same arbitrary scaling as was used for the nanocomposites, the location of the Compton edge does not agree very well at all, certainly not as well as the agreement seen in the other samples.

The reason for this is not very well understood, but there are a couple theories. The first is that the description of the Rayleigh scattering length is incorrect. Suppose that there is a strong Rayleigh scattering component; if this were the case then it would be possible that the measured reduction in the optical transmission for the nanocomposites may simply be due to photons scattering out of the spectrophotometer beam path as opposed to being absorbed. This would have the effect of inducing a longer absorption length and a shorter Rayleigh scattering length. This would allow the photons to further traverse the sample, albeit in

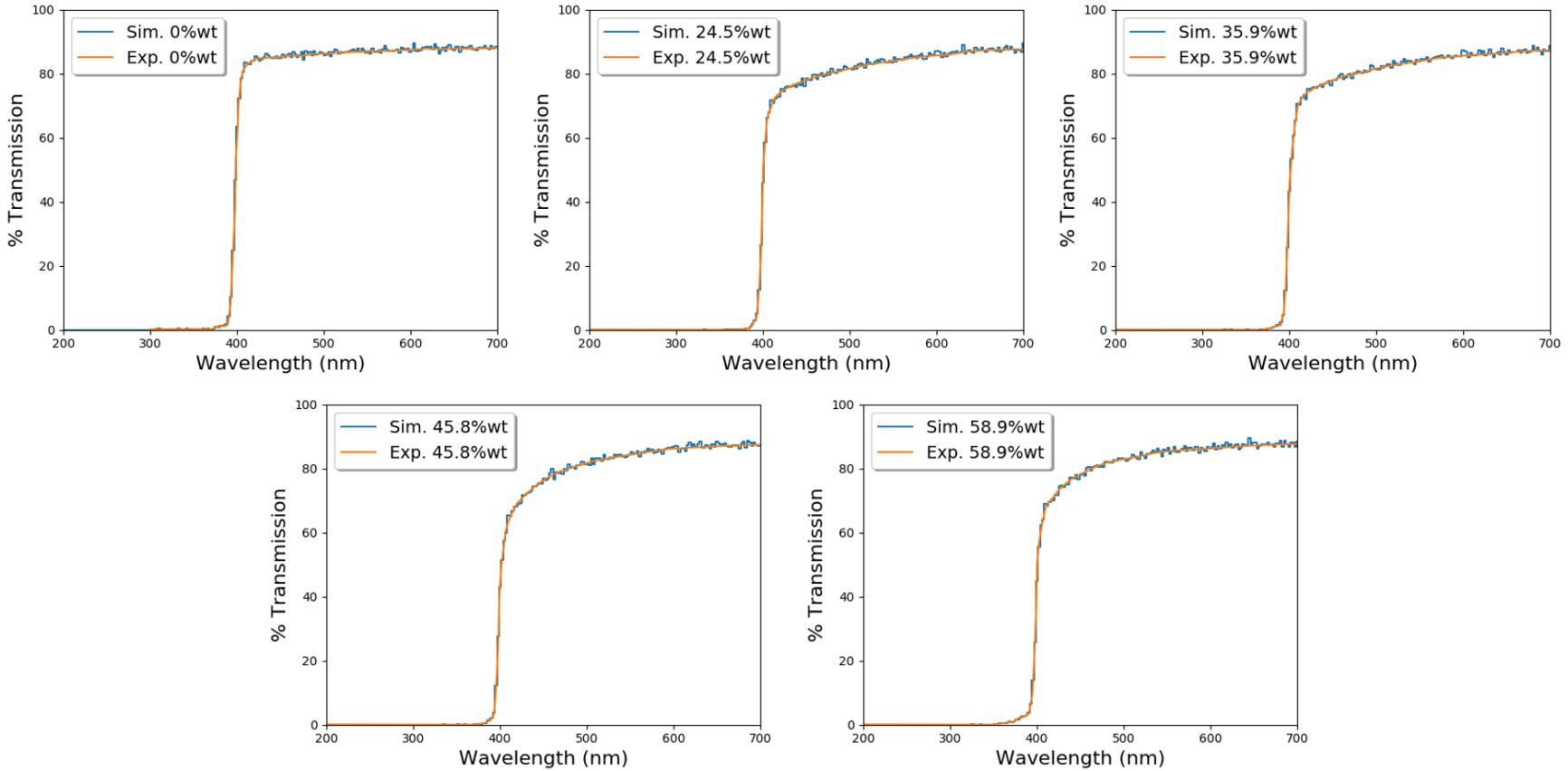


Figure 4.15: Comparison of measured and simulated YbF_3 nanocomposite spectrophotometry data for the range of YbF_3 wt/% loading. The samples were 2 mm thick. The simulated data matches very well to the experimental data from [62].

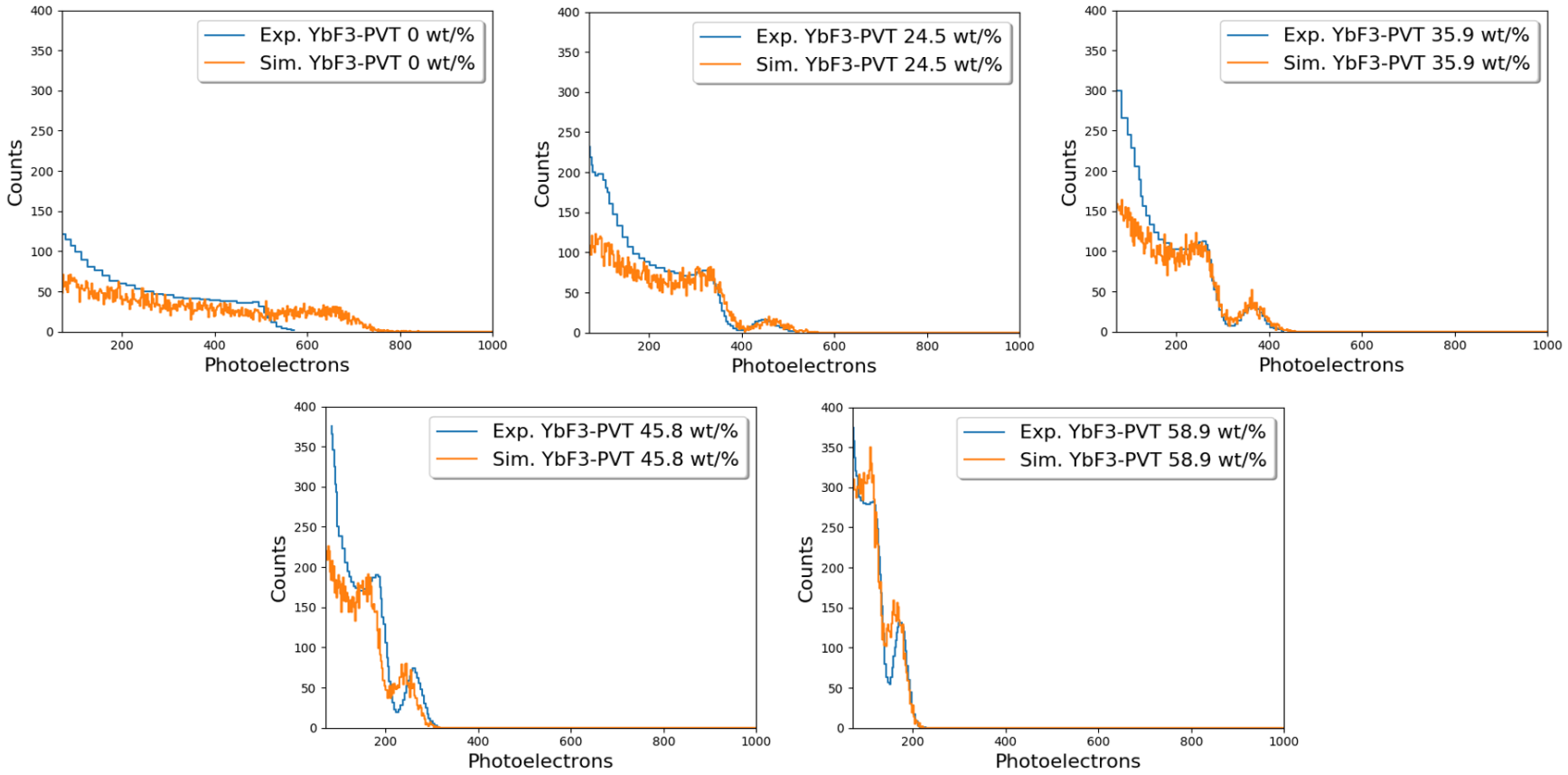


Figure 4.16: Comparison of measured and simulated Cs-137 spectra taken with YbF_3 nanocomposites. The x and y axis is arbitrary, but the same, for the experimental data. These data were multiplied by 0.34 and 0.63 for x and y values, respectively. The experimental data is from [62].

a more chaotic fashion, and perhaps increase the simulated number of photoelectrons in only the nanocomposite samples. There is evidence that perhaps the stated relation for the Rayleigh scattering lengths in these nanocomposites is in error; this brings the conversation from Subsection 1.3.3 and Section 4.2 full circle. The issue arises in the context for which the van De Hulst text applies. The text states that its application is limited to scenarios where the scatterers are located far from each other in the perspective of the photon, (i.e. a couple of wavelengths). This is clearly not the case when looking at TEM images of YbF_3 nanocomposites in a secondary reference [63]. The nanoparticle spacing may be further quantified by using Equation 4.11, where $\langle R_v \rangle$ is the average nearest neighbor distance, r_p is the nanoparticle radius, ϕ_p is the volume fraction of the nanoparticles, and $\Gamma\left(\frac{4}{3}, 8\phi_p\right)$ is the incomplete gamma function [117].

$$\langle R_v \rangle = \frac{r_p e^{8\phi_p}}{\phi_p^{1/3}} \Gamma\left(\frac{4}{3}, 8\phi_p\right) \tag{4.11}$$

Using the above formula with a nanoparticle radius of 2.5 nm, the average nearest neighbor distance (center to center) for the 24.5 wt/% nanocomposite is 7.63 nm, and is 5.97 nm for the 58.9 wt/% nanocomposite. This is significantly less than the wavelength of light which is 417 nm for the maximum RL emission (259 nm in the composite). So now, it is clear, that the equation used to describe the Rayleigh scattering length was not intended to be used in this particular situation. Further experiments on these materials need to be performed in order to know how well this equation works, or if some other method of describing the scattering of light in these materials should be used.

An additional potential explanation for the disagreement when switching from the non-loaded sample to the nanocomposites may be that the optical absorption length and Rayleigh scattering description is correct, but the real, absolute, light yield may be higher than reported. This is because the light yield is based on relative Compton edge locations and is corrected using the external PMT quantum efficiency. There is no correction performed for light lost in the scintillator.

Of course, either one of these or a combination of both may explain the observed disagreement. Though it is believed that the effect is tied to the absorption since this

is distinctly different between the loaded and unloaded samples, with the loaded samples having similar absorption lengths. Either way, further experimentation must be done to know these with any certainty.

4.4.3 Effects of Gradual Scale-Up

Several different event observables are presented in order to better illustrate and explain the observed effects of scaling up these high-Z loaded scintillators. These will be explained here. It is first important to understand that only information from events which produce at least one photoelectron on the photocathode is used. In particularly lossy media, this means some events which do occur and produce light within the scintillator may not contribute to the observables.

The first observable to be mentioned is presented in the figures as 'Fraction Absorbed'. This is referring to the *expected* fraction of optical photons which undergo bulk optical absorption for any given recorded event. This does not include losses due to surface absorption or absorption in the optical grease or silica window. The next observable is provided in the plot legends as the 'Photoelectron Efficiency'. This is a somewhat vague term which would be more clearly stated as the 'Photoelectron Production Efficiency' (it was not stated this way in the plots due to space limitations). This efficiency is defined as the *expected* fraction of optical photons produced in any given scintillation event which will go on to eventually produce a photoelectron on the photocathode. It is essentially a combination of the optical transport efficiency and the internal PMT quantum efficiency.

The next reported observable is shown in the figure legends simply as P_k. This refers to the probability of a photoelectric event producing a fluorescence x-ray which then goes on to escape the material. It was calculated by taking the number of counts in the slice of 'Energy Deposited' corresponding to the x-ray escape peak and dividing this by the sum of counts in the slices corresponding to the x-ray escape peak and the photopeak.

Additionally reported are the spreads of the photoelectron efficiency and the photopeak. These are provided as percent full-width at half-maximum (FWHM). The photopeak spread is found by taking the slice of 'Energy Deposited' corresponding to the photopeak and projecting to the photoelectron axis. The FWHM of the resulting frequency distribution is

found and then divided by the mean of this distribution which is separately reported as the 'Photopeak Location'. Note: Even though the photopeak location is reported, this does not mean the photopeak is visible in the energy spectra (photoelectron spectra).

Results with EJ256

The simulated results from the gradual scale up of EJ256 are contained in the following few pages. Figure 4.17 contains the simulated spectra from three lengths of the simulated scintillator: 2 mm, 24 mm, and 50 mm. Figure 4.18 contains the response matrix for lengths of 2 mm, 10 mm, 24 mm, and 50 mm. While Figure 4.19 contains the observables of the fraction of photons absorbed, the photoelectron production efficiency, P_k, the spread of both the photoelectron production efficiency and the photopeak, as well as the photopeak location. All of these are reported with respect to scintillator length.

Upon examining Figure 4.17, a photopeak presents in the 2 mm sample at the location of approximately 800 photoelectrons while the more prominent x-ray escape is present at around 700 photoelectrons. These peaks are no longer present in the 24 mm and 50 mm samples although an apparent shoulder is visible beyond the standard Compton shoulder. Additionally, the longer samples present with a reduction in light output as indicated by the leftward shift in the Compton maximum which is located around 550 photoelectrons for the 2 mm sample and 200 photoelectrons for the 50 mm sample.

A similar story is told by the data in Figure 4.18. Longer lengths result in a decreased number of photoelectrons produced for equivalent energy deposited. This is in addition to an increased vertical spread of the 2D distribution which further indicates an increase in the energy resolution. Figure 4.19 ties these things together by revealing that the longer lengths result in a marked increase of the expected fraction of absorbed photons. At 2 mm this is less than 20% while the simulation of the 50 mm sample shows more than 60% of the light produced in a given event will be lost to bulk absorption. Furthermore, the overall photoelectron production efficiency decreases with length while the spread of this quantity and of the photopeak increases. This is all tied to the reduction of the photon signal and the resulting diminished counting statistics.

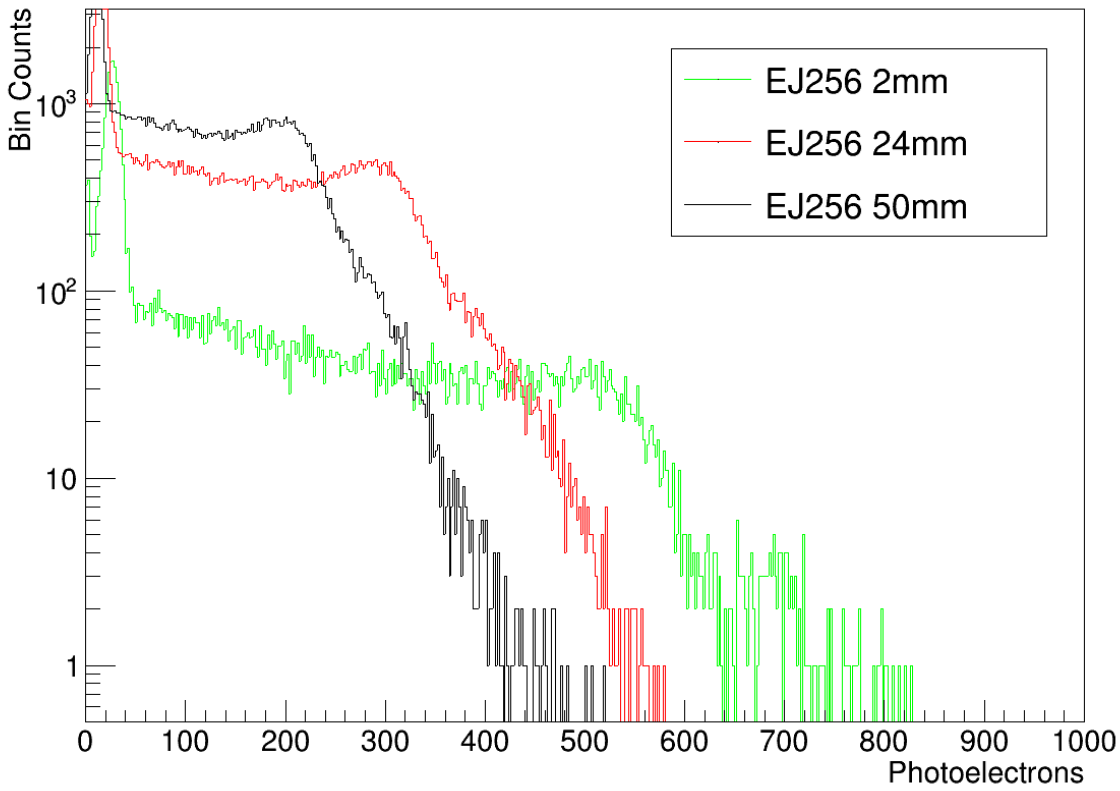


Figure 4.17: Simulated spectra using EJ-256 5 wt/% Pb in three different lengths. The diameter is 10 mm.

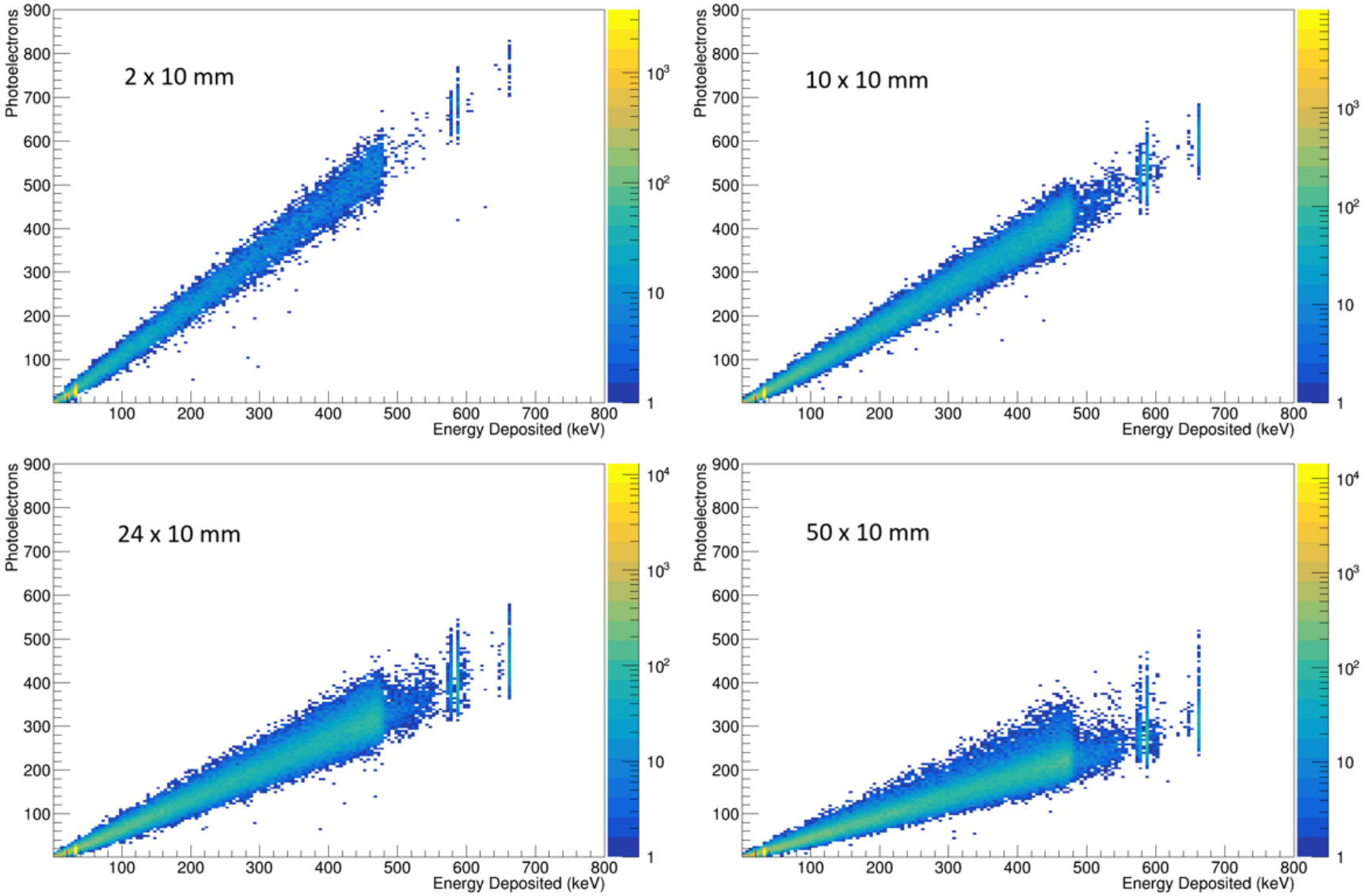
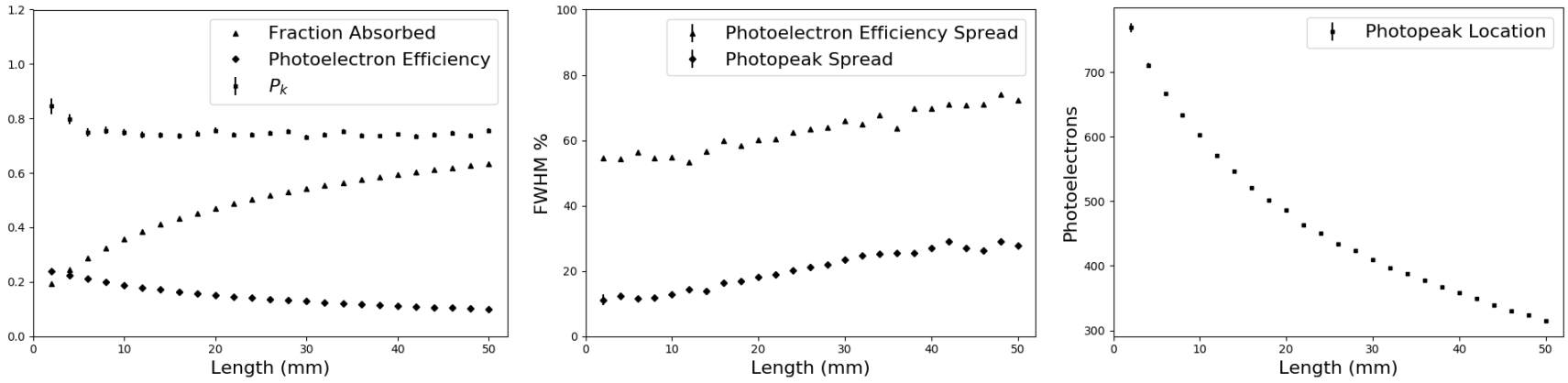


Figure 4.18: Changes in the simulated response of EJ256 for different scintillator lengths. The color scale refers to the counts per pixel.



(a) **(b)** **(c)**

Figure 4.19: Simulated observables under gradual scale up of EJ256. **(a)** The fraction of photons absorbed, photoelectron production efficiency, and the x-ray escape probability, P_K, all with respect to the length of the scintillator. The diameter is 10 mm. **(b)** The spread of the photoelectron efficiency and photopeak. **(c)** The 662 keV photopeak location with respect to length.

Lastly, examining the value of P_k in Figure 4.19a indicates that a steady state is reached at 6 mm and lengths longer than this do not further reduce the probability of x-ray escape. This is because the cylinder only has a diameter of 10 mm and once the length exceeds the radius, x-ray escape out of the sides will become more dominant than escape out of the PMT-end of the detector. Even in the scenario where both the radius and length are increased together, eventually escape out of the source-facing surface will dominate, meaning no configuration will completely eliminate x-ray escape, only minimize it. When considered in conjunction with the light losses, there is little benefit in exceeding the 6 mm length for 10 mm diameter scintillators. However, in situations where only count data is needed, longer scintillators can be advantageous as a significant increase in the intrinsic efficiency was noted, though not reported on. Lastly, it should be noted that since the two x-ray escape peaks are quite separated from each other, this can act as an additional 'smearing' factor.

Results with the 24.5 wt/% YbF_3 nanocomposite

The simulated results from the gradual scale up of the 24.5 wt/% YbF_3 nanocomposite are contained in the following few pages. Figure 4.20 shows the simulated spectra taken with scintillators having lengths of 1 mm, 5 mm, and 10 mm. While Figure 4.21 contains the response for simulated samples in lengths of 1 mm, 2 mm, 4 mm, and 10 mm. Finally Figure 4.22 contains the already discussed simulated observables.

Examining Figure 4.20 that a photopeak is present for the 1 mm sample and it was previously shown in Figure 4.16 that the 2 mm sample retains a photopeak. However, by the time a length of 5 mm is reached, the photopeak is no longer separated from the Compton edge, although a marked shoulder (noted by the concavity), is still apparent. The responses shown in Figure 4.21 indicate a drastic fall-off in the light output with small increases in the length; this is in addition to considerable vertical spread indicating an increasing energy resolution.

Figure 4.22a indicates a drastic amount of optical absorption which increases quite quickly with scintillator length. Around 51% of the light is absorbed in the 1 mm sample and 93% is absorbed in 20 mm long sample. Data was not presented for the longer lengths because they did not add much value to this discussion as the trends had already stabilized at the

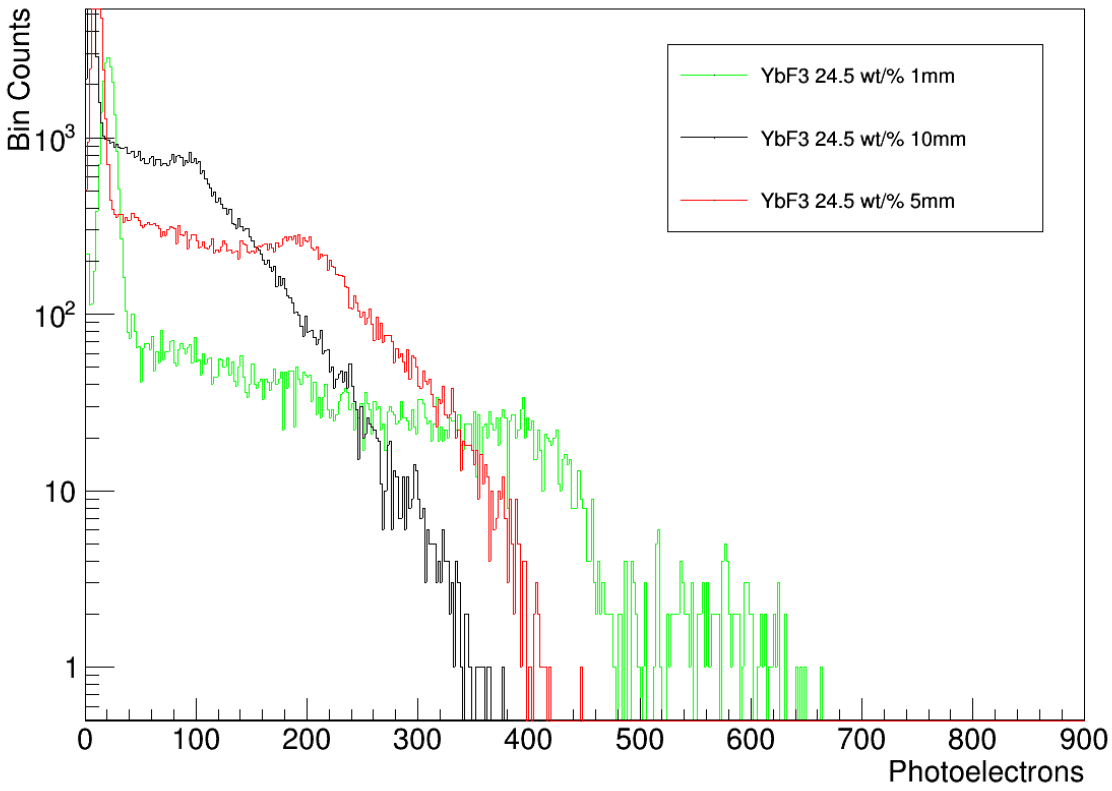


Figure 4.20: Simulated spectra using the 24.5 wt/% YbF_3 nanocomposite in three different lengths. The diameter is 10 mm.

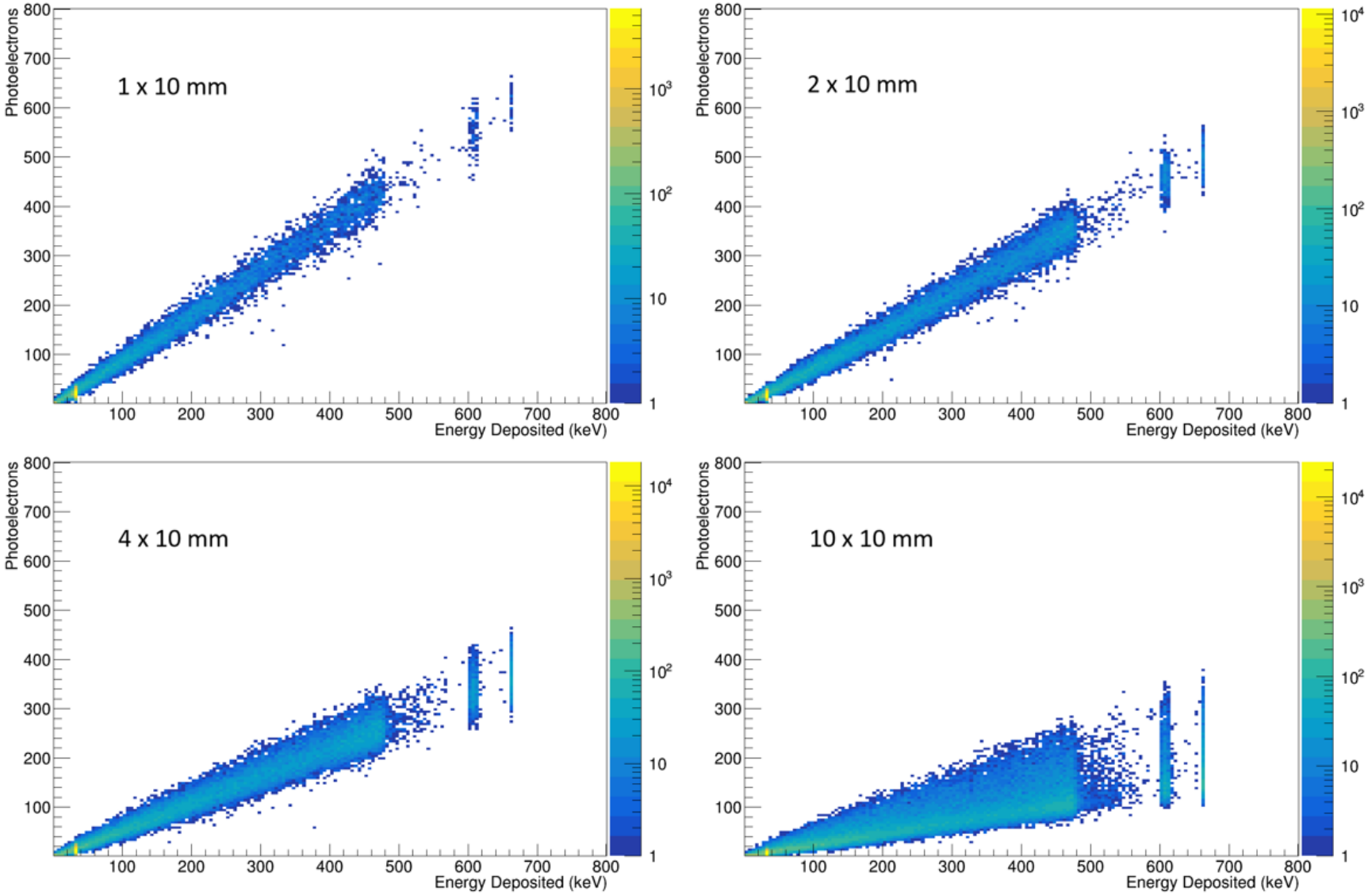
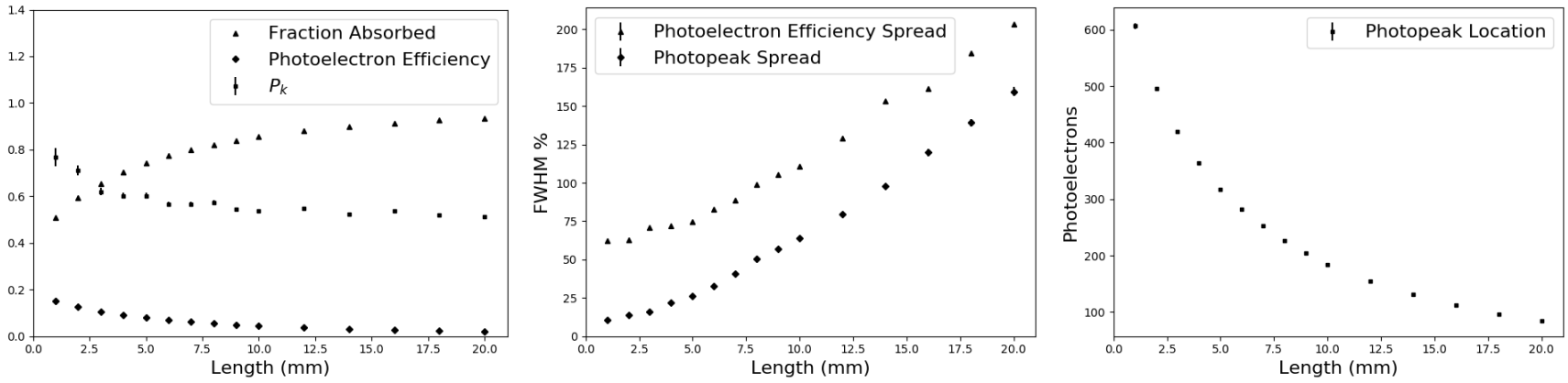


Figure 4.21: Changes in the simulated response of the 24.5 wt/% YbF_3 nanocomposite for different scintillator lengths. The color scale refers to the counts per pixel.



(a) **(b)** **(c)**

Figure 4.22: Simulated observables under gradual scale up of the 24.5 wt/% YbF_3 nanocomposite. **(a)** The fraction of photons absorbed, photoelectron production efficiency, and the x-ray escape probability, P_K, all with respect to the length of the scintillator. The diameter is 10 mm. **(b)** The spread of the photoelectron efficiency and photopeak. **(c)** The 662 keV photopeak location with respect to length.

point indicating most light is lost. At any rate, the photoelectron production efficiency, not surprisingly, decreases to almost zero for the longer samples. This, again, is due to the fact that most photons are absorbed and therefore are not able to contribute to photoelectron production. Figure 4.22b indicates that both the photopeak spread and the photoelectron production efficiency spread increase significantly with length. This is due to the resulting large variance in the light collection efficiency, as this is what is changing with length since the internal QE of the PMT is fixed. The FWHM exceeds the 100% mark because of heavy tails in the distributions which, in this case, lead to values of the standard deviation times 2.355 to exceed the mean value of these underlying distributions. The data presented in Figure 4.22 is congruent with what should be expected with significant light loss with increasing length. This figure shows that the mean number of photoelectrons produced from a full energy distribution is slightly above 600 for 1 mm thickness and 84 for the 20 mm thickness. Given the results of the simulation, the recommended thickness of a 10 mm diameter RCC detector of this material should not exceed 3 mm, at which point the x-ray escape probability has decreased from 78% to 62% (this never falls below 50% for the 10 mm diameter cylinder), and the photopeak % FWHM has changed from 10.8% to 16.2%. The photopeak resolution continually degrades over increasing lengths.

The earlier discussion regarding the validation for the nanocomposites indicated that uncorrected light loss may have led to incorrect values for the light yield. The results of the incremental scale up support this assertion. In the simulation of the 2 mm thick sample, the same reported thickness used in the light output experiment, 60% of the light is absorbed indicating that the true light yield may be as high as 16.3 photons/keV. This could be verified by experimenting with a thinner sample, such as the simulated 1 mm sample, and seeing if the measured light yield increases. If the optical absorption is correct, simulations suggest that an increase of 23% to 8.0 photons/keV from 6.5 photons/keV may be observed.

The results of scaling up the 24.5 wt/% nanoparticle sample to a size of 2x2 inches are shown in Figures 4.23 and 4.24. Not surprisingly, there is no photopeak evident in the spectrum which extends to an output of only 275 photoelectrons compared to the 12 mm thick sample whose spectrum extended to 450 photoelectrons. Again, there is a huge variance in the number of photoelectrons produced for a given amount of energy deposited

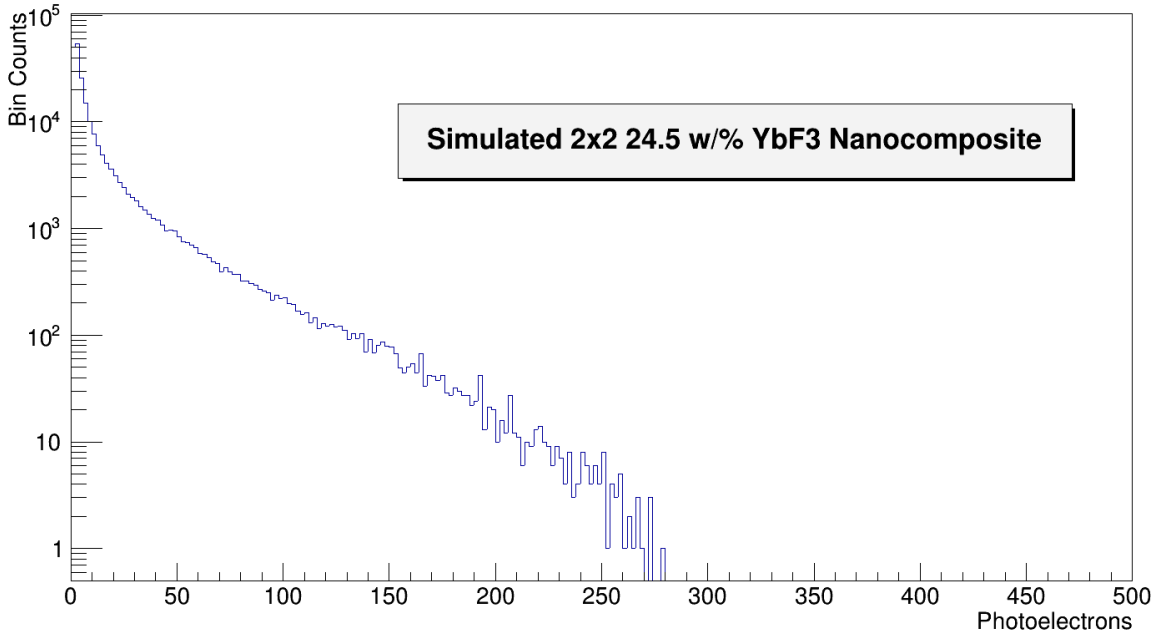


Figure 4.23: Simulated Cs-137 spectrum taken with a scaled up 24.5 wt/% YbF_3 nanocomposite. The simulated detector size was 2x2 inches.

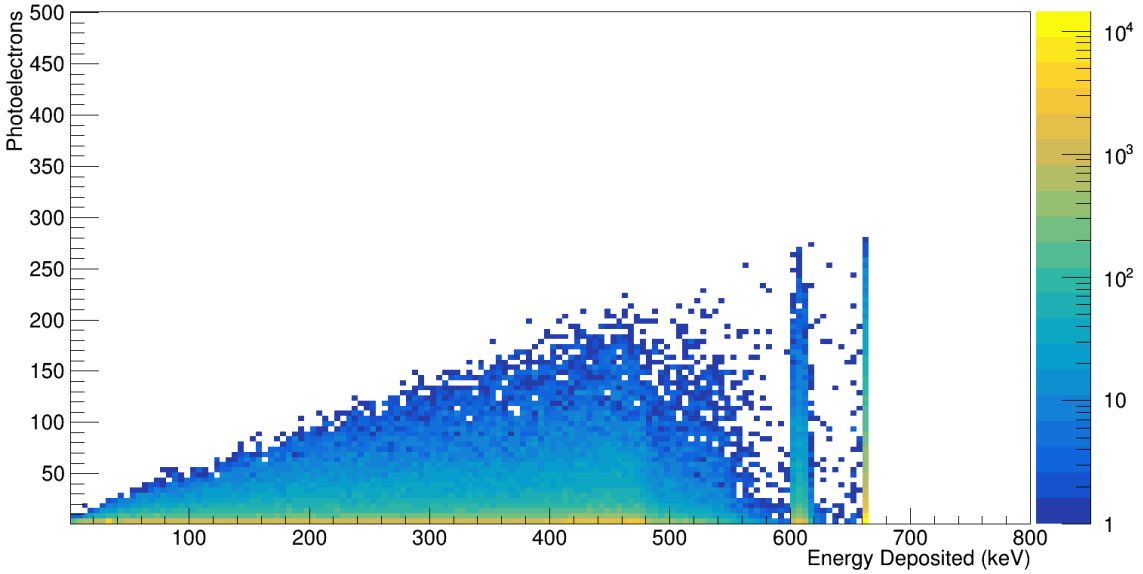


Figure 4.24: Simulated response of a scaled up 24.5 wt/% YbF_3 nanocomposite. The simulated detector size was 2x2 inches. The photopeak and escape peak are present, but not discernible in the spectrum due to the large variance in photoelectron production. Most amounts of deposited energy results in less than 50 photoelectrons. The color scale refers to the counts per pixel.

in the scintillator. This, in combination with the low light output, is responsible for washing out the photopeak.

It may not be any surprise that the simulation indicates the bulk absorption loss mechanism is responsible for absorbing 97.33% of light produced during a given scintillation event; surface absorption on the Teflon surface removes only 0.09% of the scintillation light in this particular optical system.

4.5 Conclusion

Experiments with and simulations of high-Z loaded plastic scintillators have been performed towards validating a GEANT4 workspace and the approach used to derive the data inputs. Excellent agreement across all simulated and experimental spectrophotometry experiments was observed. Validation in the absolute sense, using EJ256 5% Pb coupled to a calibrated PMT, was also achieved with bin count rates having no discernible difference in regions of interest and relative Compton edge locations differing by approximately 10%. The simulated Compton edge location came in at a lower value than the experimental location, congruent with observations in Chapter 3 when Teflon was used.

With regards to the nanocomposites, the existence and magnitude of spectral features in the simulations and the experiments were found to be in agreement. The simulations under-predicted the light output for the nanocomposite samples when compared to the non-loaded sample of the same type. This may be due to what has now been shown to be an inappropriate use of the equation typically used to describe the Rayleigh scattering probability, or it may be due to the light yields not being corrected for bulk optical attenuation. More experiments with the nanocomposite scintillators should be performed to better understand and quantify these effects. Possible experiments could focus on distinguishing between specular transmission and diffuse transmission through the samples; if diffuse transmission exists, then measurements of the light scattering profile would be immensely beneficial to these simulations. Other experiments could include using samples of different thickness, for instance 1 mm, 2 mm, and 3 mm, to verify against the trends seen in the model and perhaps be used to update the model for future simulation.

Aside from validation studies, incremental scale up of both EJ256 and the 24.5 wt/% YbF_3 nanocomposite was investigated using a simulated Cs-137 source. The results show that for longer lengths, the photopeak becomes washed out in the spectrum due to the optical absorption and the resulting high variance in photoelectron production (from light collection efficiency variances). Thicknesses of 10 mm diameter RCC geometries were recommended which sought to minimize x-ray escape and optical losses due to bulk absorption. This thickness was 6 mm for EJ256 and 3 mm for the nanocomposite. Using this thickness is expected to produce photopeaks with FWHM of 11.5% and 16.2% respectively. However, due to x-ray escape, this resolution may not be readily achievable using NIM equipment without deconvolving the peaks. This is more of a problem for Pb loaded plastics since the two escape lines are quite separated in energy.

4.6 Acknowledgments

The author would like to thank Cordell Delzer and the Scintillation Materials Research Center for the use of the spectrophotometer and data collection for measurements on the EJ256 5% Pb sample using the same.

This material is based on work supported in part by the Defense Threat Reduction Agency under grant number HDTRA 1-18-1-005 and in part by the Department of Energy National Nuclear Security Administration through the Nuclear Science and Security Consortium under Award Number(s) DE-NA0003180 and/or DE-NA0000979.

Disclaimer: "This report was prepared as an account of work sponsored by an agency of the United States Government. Neither the United States Government nor any agency thereof, nor any of their employees, makes any warranty, express or implied, or assumes any legal liability or responsibility for the accuracy, completeness, or usefulness of any information, apparatus, product, or process disclosed, or represents that its use would not infringe privately owned rights. Reference herein to any specific commercial product, process, or service by trade name, trademark, manufacturer, or otherwise does not necessarily constitute or imply its endorsement, recommendation, or favoring by the United States

Government or any agency thereof. The views and opinions of authors expressed herein do not necessarily state or reflect those of the United States Government or any agency thereof."

Chapter 5

Additional Supported Studies

5.1 Abstract

The work presented in this chapter outlines efforts by the author to assist in advancing research in the other parts of the collaboration, one at UCLA and the other at UTK-EECS. The first section outlines a method which was developed for deconvolving the x-ray fluorescence escape peak from the photopeak in spectra with poor energy resolution. The high % energy resolution results in these two features being indistinguishable from one another. The resulting method focuses on establishing a model to describe the spectral region between the Compton edge through the upper bound of the photopeak for a single medium strength gamma (where light yield is quite proportional in the scintillator but below pair production energy). Additionally the method works to remove half of the free parameters in the model by building physical interrelationships between the other parameters and using MCNP to determine three parameters. The second section describes and demonstrates a backend and an application programming interface (API) written in Python to be used for rapid simulation of a mobile detector. The program assumes non-distributed sources and detectors, though real intrinsic efficiency values may be used. The program further allows for spatially distributed gamma background and attenuation effects of barriers, such as walls, to be accounted for using data from the NIST xray coefficient library. The user may define their own attenuator materials or use some of the predefined materials. Real detector efficiency

values have been calculated for Cs-137 gammas using MCNP to model a drone arm made of EJ200.

5.2 A Method for Deconvolving the x-ray Fluorescence Escape Peak in Gamma Pulse Height Spectra

The following section generally outlines the work as it appears in the supporting information (SI) for the author's PJA [118]. Some additional discussion and figures not in the PJA SI documents are provided here.

5.2.1 Introduction

When added to organic scintillators, high-Z elements have been shown to increase the intrinsic gamma efficiency and in some cases allow photopeaks to be visible in the gamma energy spectrum. Another feature of high-Z elements is that, due to the large number of electrons and orbitals, an inner electron may be ejected during the photoelectric process. These electrons are often denoted as K-shell electrons which indicates that they are the innermost and most tightly bound electrons. Upon the ejection of a K-shell electron, electrons in higher energy states then rush to fill the gap. This deexcitation may result in the production of a fluorescence x-ray. The energy of this x-ray is specific to the element which produces it and there may be more than one energy. For example, an electron transitioning from the L-shell to the K-shell may produce K_α x-rays which are lower in energy than K_β x-rays produced from transitions from the M-shell to the K-shell. Together, these are referred to as K-series x-rays. When these x-rays are produced in small and low density scintillator samples, it is possible that they escape the material entirely removing a portion of the energy deposited during the initial photoelectric interaction. In gamma energy spectra collected with small detectors having good energy resolution, the x-ray escape peak is clearly visible. This feature is usually located many tens of keV below the photopeak centroid, depending on the material. However, if the resolution is poor, these may not be distinguishable and instead manifest as a single broad peak. This regime is where the following work is focused.

The specific goal is to determine the energy resolution from a spectrum with a latent x-ray escape peak.

5.2.2 Photopeak Deconvolution Model

Finding the energy resolution of the sample involves a multi-step process to deconvolve the photopeak from the K-series x-ray escape peak. Since the x-ray escape peak and photopeak are not easily resolved, this process is utilized in an effort to add physical meaning to the deconvolved peaks and avoid the ambiguity and non-physicality of fitting the data with non-constrained models (i.e., two Gaussian functions with unbound parameters). Indeed, the primary fit used in this deconvolution does consist of two Gaussian functions in conjunction with an exponential component to describe the decaying nature of the Compton edge. However, in contrast to a pure mathematic approach which utilizes unbound parameters to minimize the least squares regression, this approach sets bounds on key parameters; the values of which are chosen based on the physics of the system.

The parameters of interest which require these physical bounds are: the relative (1) locations, (2) standard deviations, and (3) areas of the x-ray escape peak and the photopeak. Due to the assumption of Gaussian peak shapes, these parameters may be interrelated mathematically in closed functional form. Consider that the Gaussian representing the photopeak is denoted as function f:

$$f(E) = A \exp\left[\frac{(E-\mu_f)^2}{2\sigma_f^2}\right] \tag{5.1}$$

while the Gaussian representing the K-series x-ray escape peak is denoted as function g:

$$g(E) = A \exp\left[\frac{(E-\mu_g)^2}{2\sigma_g^2}\right] \tag{5.2}$$

The location of the x-ray escape peak can be related to the photopeak location through the mean K-series fluorescence x-ray energy, E_K, as $\mu_g = \mu_f - E_K$. The standard deviation of g may also be related to f. However, since the K-series x-ray escape peak arises as the result of multiple x-ray emissions in a narrow range of energies, the function for the x-ray escape

peak may be better described as the convolution between the function describing the x-ray escape energies, k, and the function describing the detector response, r, at these energies. It will be assumed that both of these may be described by Gaussian functions. As a result of this convolution, the standard deviation of g may simply be written as $\sigma_g = \sqrt{\sigma_r^2 + \sigma_K^2}$. Since σ_r is the component of σ_g which takes the energy resolution of the detector at μ_g into account, it can be related to the photopeak resolution according to

$$\sigma_r = \sigma_f \left(\frac{\mu_f - E_K}{\mu_f} \right)^{1/2} \tag{5.3}$$

This equation is from the assumption that the detector energy resolution (%R) at μ_g and μ_f may be related by the inverse square root of the deposited energy as described in Knoll [18]. This fitting approach does also assume proportionality between these two peak locations. This is believed to be reasonable since the energy difference is between 50-60 keV and the peaks are also located in what is generally considered to be the proportional region for many scintillating materials.

The scaling factor, B, may also be written in terms of the parameters in f, E_K, and σ_K by introducing an additional parameter, P_K, which is the probability that a photoelectric event produces a secondary K-series fluorescence x-ray which then goes on to escape the detector; these are the events which contribute to the K-series escape peak. Taking into consideration the ratio of the photopeak area to the K-series escape peak area, the following relationship is established:

$$\frac{F}{G} = \frac{1 - P_K}{P_K} \tag{5.4}$$

where F is the photopeak area found by integrating f in Equation 5.1. The result of this is

$$F = A\sqrt{2\pi\sigma_f^2} \tag{5.5}$$

The quantity G, on the other hand, is found by integrating g. The result of integration and substitution yields

$$G = B\sqrt{2\pi\left(\frac{\mu_f - E_K}{\mu_f}\sigma_f^2 + \sigma_K^2\right)} \tag{5.6}$$

Substituting 5.5 and 5.6 into 5.4 and solving for B yields

$$B = A\frac{P_K}{1-P_K}\left(\frac{\sigma_f^2}{\frac{\mu_f - E_K}{\mu_f}\sigma_f^2 + \sigma_K^2}\right)^{1/2} \tag{5.7}$$

At this point, all parameters describing the x-ray escape peak have been written in terms of the parameters describing the photopeak and physical values which may be found via simulation.

The last spectrum component needing definition is the Compton edge. This is fit with a simple exponential function which is forced to start at approximately half the Compton maximum which is located in energy at, E_C. The Compton edge fit is defined by

$$h(E) = C\exp\left[-\lambda\left(E - E_C\right)\right] \tag{5.8}$$

The final fitting function is the sum of the three components:

$$fit(E) = f(E) + g(E) + h(E) \tag{5.9}$$

The redefined function $g(E)$, is shown below with all substitutions

$$g(E) = A\frac{P_K}{1-P_K}\left(\frac{\sigma_f^2}{\frac{\mu_f - E_K}{\mu_f}\sigma_f^2 + \sigma_K^2}\right)^{1/2}\exp\left[\frac{\left(E - (\mu_f - E_K)\right)^2}{2\left(\frac{\mu_f - E_K}{\mu_f}\sigma_f^2 + \sigma_K^2\right)}\right] \tag{5.10}$$

In the case that an uncalibrated detector is being used, an extra parameter may be added. This parameter, which will be denoted as α, is the expected energy per MCA channel. When multiplied by the MCA channel number, the resulting product is energy. Strictly speaking, α is energy dependent. However, for our purposes α will be reduced to a single value which best scales the data to allow fitting in the region of energy from the Compton edge to the photopeak. This does of course assume a linear zero-offset energy calibration model. The fit for the uncalibrated detector, where E is given as the MCA channel number, then, is arrived

at by simply multiplying all instances of E by α. At this point there are 10 parameters total. However, only 5 of these need to be adjusted by the equation solver in the case of uncalibrated data. If the data is already calibrated, then this is further reduced to four fitting parameters. The parameter description and their method of valuation is shown in Table 5.1.

5.2.3 Demonstration of Deconvolution Method

The demonstration of this method will be performed on data sets provided by UCLA for 40 w/% loading of HfO_2 nanoparticles in a liquid scintillator. One data set was presented in [118] while the other was measured by UCLA at a later date in a different source-detector geometry.

The final fit utilizes 10 parameters - some of which may, and should, be found through use of a metanalysis to reduce the effects of overfitting the data which may ultimately result in wrong answers. For the purposes of this metanalysis, the Monte Carlo radiation transport code, MCNP-6.1, is utilized [119]. The parameters which may be found using MCNP are indicated in Table 5.1.

The simulated detector was defined as a right-circular cylinder with a length of 20 mm and diameter of 20 mm. This detector was clad with 1 mm thick borosilicate glass. The simulation also included a 10 cm thick concrete floor placed 80 cm below the center of the detector with air filling the remainder of the simulation space. The material definitions are included in Table 5.2. Note that the photoatomic data library, MCPLIB04, was used for cross section, form factor, scattering function, and fluorescence data.

The simulated source was an isotropic gamma source with the photon energies and emission probabilities defined as those found within the NNDC database for Cs-137 [120] and included photons with energies above 30-keV and emission probability greater than 0.001 per disintegration. The source is placed on the detector axis 4.24 mm from the face of the detector cladding. Since a 15 μCi Cs-137 source emits approximately 5.1×10^5 photons per second, this number was used to normalize the MCNP tally which is given as contribution to simulated quantity per simulated source particle. The pulse height tally, F8, was used with 148 energy bins between 20 keV and 800 keV. The simulation was terminated after 2.0×10^7

Table 5.1: Description and valuation of fitting parameters.

Parameter	Description	Valuation
A:	Peaks Normalization factor	Fit
μ_f:	Photopeak energy	Known
σ_f:	Standard deviation of photopeak	Fit
P_K:	Probability of x-ray escape	Calculated w/MCNP
E_K:	Mean x-ray energy	Calculated w/MCNP
σ_K:	Standard deviation of x-ray energy	Calculated w/MCNP
C:	Compton edge normalization factor	Fit
λ:	Compton edge shape parameter	Fit
E_C:	Compton edge origin	50 % CM
α:	Energy calibration factor	Fit/known

Table 5.2: Material definitions for MCNP simulation of liquid HfO_2 nanocomposite.

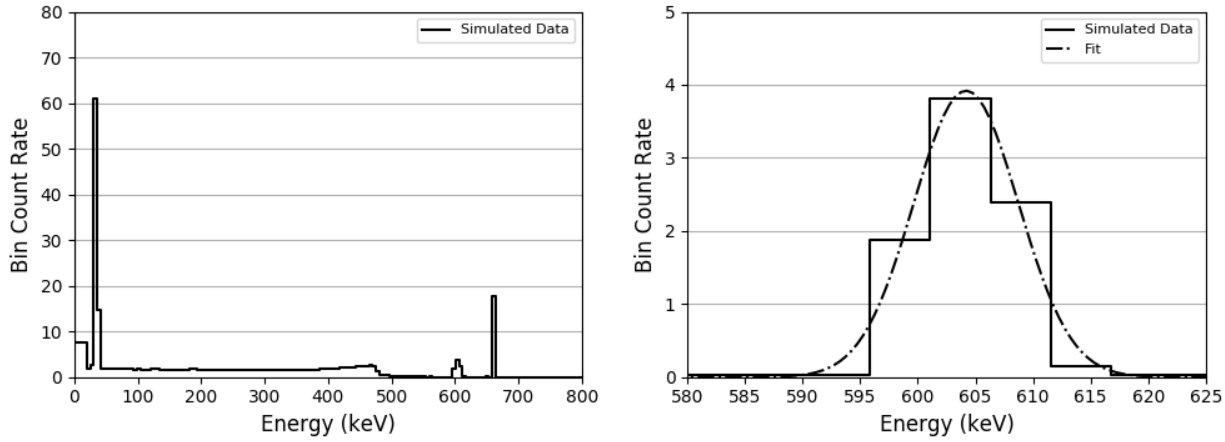
Material	Element	Atom Fraction
Liquid HfO_2 Nanocomposite $\rho = 1.36 g/cc$	H	0.5169
	C	0.4411
	N	0.002961
	O	0.02612
	Hf	0.01295
Borosilicate Glass (NIST) $\rho = 2.23 g/cc$	B	0.070452
	O	0.641094
	Na	0.023311
	Al	0.008204
	Si	0.255328
	K	0.001615
Concrete, Ordinary (NIST) $\rho = 2.3 g/cc$	H	0.304245
	C	0.00287
	O	0.498628
	Na	0.009179
	Mg	0.000717
	Al	0.010261
	Si	0.150505
	K	0.007114
	Ca	0.014882
	Fe	0.001599
Air (NIST) $\rho = 0.001205 g/cc$	C	0.000151
	N	0.784437
	O	0.21075
	Ar	0.004671

source particles were processed. A second simulation was also run with the source placed 10.56 cm from the face of the detector and ending after 1.3×10^9 source particles had been processed. This second run corresponds to the second data set received from UCLA.

The results of the pulse height tally from the second MCNP simulation are shown in Figure 5.1 alongside the fit of the K-series escape peak, which is utilized to determine E_K and σ_K. The value of P_K is found by summing the quantities in the bins which make up the K-series escape peak and dividing by the sum of the bin quantities which make up both the escape peak and the photopeak, these sums are 8.24 cps and 26.06 cps respectively. The quotient of these two values yields 0.32. This value is consistent with the value of P_K found in the first simulation when the source placement, still remaining on the detector axis, was 4.24 mm as opposed to 105.6 mm. The results from the metanalysis for parameter reduction are highlighted in Table 5.3. These data indicate that the source position, so long as it remains on axis, should not greatly affect the intensity or shape of the K-series escape peak.

Performing the fit utilizing the derived fitting function in conjunction with the reduced parameters yields the plots in Figure 5.2. The values of the fitting parameters are showcased in Table 5.4.

The results for the standard deviation of the photopeak indicate an energy resolution at 662 keV of 14.8% and 19.9% for experiments 1 and 2, respectively. Both of these results should be viewed suspiciously due to the poor quality of the fit; do note that data in Figure 5.2b was truncated at approximately 720 keV to avoid fitting the Compton background component to the significant tailing observed off of the photopeak. In addition to the poor quality of the fit, the experimental conditions were also suboptimal. In the first experiment, the source placement likely contributed to pile-up events. It is expected that the ratio of clean pulses to pulses with pileup is approximately 65:1 in experiment 1. It was believed that pileup may have been responsible for poor agreement in the photopeak tail as exhibited in Figure 5.2a and this was the impetus for performing the second experiment with the source placed further away from the detector (105.6 mm as opposed to 4.24 mm). However, by the time the second experiment was performed, the sample had undergone degradation and had become more of a gel instead of a liquid. Additionally, performance loss in regard to light output is also observed as indicated by the value of α shifting from 0.43 to 0.56

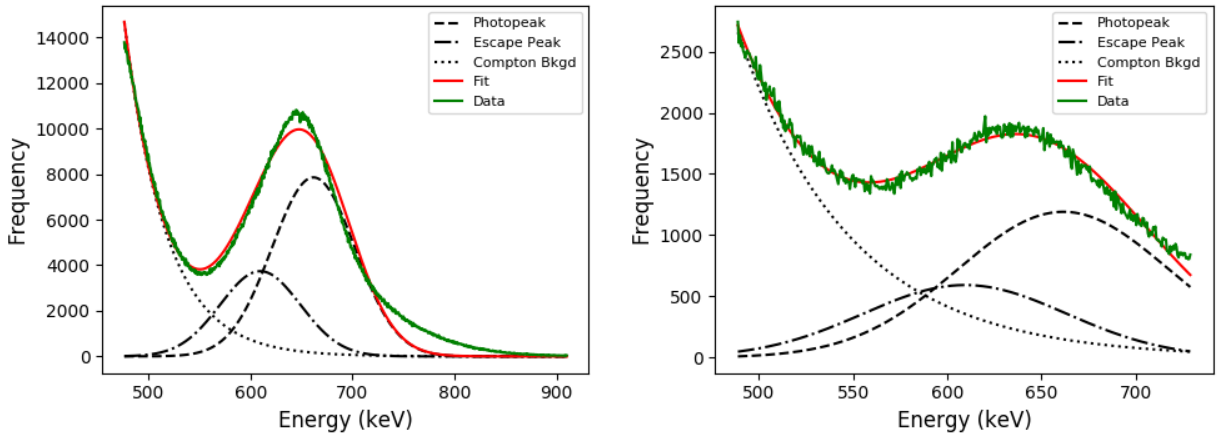


(a) **(b)**

Figure 5.1: **(a)** Simulated pulse height tally with the Cs-137 source placed 105.6 mm from the face of the detector on the detector axis. The fraction of the area of the escape peak, circa 605 keV, when compared to the area in both the photopeak and the escape peak is the parameter, P_K. **(b)** The simulated K-series escape peak is shown with the Gaussian fit overlaid. The fit is used to find the parameters E_K and σ_K.

Table 5.3: MCNP Calculated parameters for describing the K-series escape peak.

	Source Distance (mm)	P_K	E_K (keV)	σ_K (keV)
Simulation 1	4.24	0.32	52.26	4.49
Simulation 2	105.6	0.32	52.22	4.55



(a) **(b)**

Figure 5.2: Peak deconvolution results from both experiments. **(a)** Utilizes a fresh sample with the source placed 4.24 mm from the face of the detector. **(b)** The source is placed 105.6 mm from the face of the sample, which has undergone some degree of degradation.

Table 5.4: Final results from fitting algorithm.

Parameter	Experiment 1	Experiment 2
A	0.694	0.434
μ_f (keV)	661.659	661.659
σ_f (keV)	41.598	55.973
P_K	0.315	0.324
E_K (keV)	52.3	52.3
σ_K (keV)	4.49	4.49
C	1.051	1.001
λ (keV^{-1})	0.02658	0.01664
E_C (keV)	487.42	486.028
α (kev/Ch)	0.434781	0.561254

keV/Ch. Finally, it should be noted that the increased amount of photopeak tail which is observed may be from unexplored phenomena related to the consistency of the energy transfer mechanisms within the nanocomposite or perhaps it may be due to systemic variances in the light collection efficiency which may arise due to the imperfect shape of the spectrometer cell or presence and quality of a light reflector.

5.2.4 Conclusion

A method for deconvolving latent x-ray escape peaks from photopeaks has been developed. The aim of the method is twofold: 1) to have built in physical relations relating the escape peak to the photopeak, and 2) to reduce the number of fitting parameters by utilizing MCNP to calculate the parameters. The derivation and use of this method has been demonstrated with experimental spectral data taken by a liquid HfO_2 nanocomposite irradiated by Cs-137. The approach does what it is designed to do, but in some instances the energy impulse response of the detector may not be Gaussian, as was assumed in the derivation of this method. This behavior is seen in the liquid HfO_2 nanocomposite, with some strong tailing present which induces a mismatch between the model and the data on the high energy side of the photopeak. Even so, this method does provide results for the energy resolution which are very reasonable given the features visible in the spectra.

5.3 A Python Program for Rapid Simulation of Mobile Gamma/Neutron Detectors

5.3.1 Introduction

In order to develop algorithms for source mapping, search, or localization, using a UAV or other mobile platform, a testbed must be developed. A commonly used simulation toolkit for UAV applications is the Gazebo drone simulator. However, this simulator does not have the functionality to add embedded radioactive sources and emulate the corresponding drone response to these sources. The focus of this section is to define and demonstrate a small Python suite which was developed to be used with the Gazebo drone simulator. However,

the class is general enough that any mobile platform simulator can utilize this tool as long as it is able track the position of the platform and keep time within the simulation space.

5.3.2 Program Description

In general, the program is designed to compute the number of counts received by the mobile detector in a given interval of time. Typical one over r-squared behavior is modeled as are space-variable gamma backgrounds. Additionally, attenuation of gammas by barriers between the source and detector are modeled, though buildup is not accounted for. However, the energy distribution of the sources are defined within the RadSource class and are accounted for when calculating total attenuation by a barrier. Furthermore, mixed gamma/neutron sources are also able to be modeled, though the current functionality does not allow for neutron attenuation to be estimated. All of these effects are accounted for to arrive at an expected number of counts which is then used to sample from a Poisson distribution to add the effect of counting statistics.

Instantiating a source-detector object requires a source position, an isotope identifier, the source activity in Ci, and the total gamma efficiency at 1 meter.

The description of how the program works largely centers on what happens during a so-called 'interval', which is shown in Figure 5.3. Notice that the number of subintervals, N, is not the same as the number of nodes (the edge of the intervals), of which there are $N+1$. The upcoming discussion contains a few indices which are described as follows: i is associated with the nodes on the edges of the subintervals and $\exists\,[0, N]$, j is associated with the discrete gamma energies emitted by the isotope and $\exists\,[1, N_E]$, k is associated with any barriers between the source and detector and if there are any barriers then it $\exists\,[1, N_{barriers}]$, lastly l is associated with the subintervals themselves and $\exists\,[1, N]$.

The definition of the expected count rate from only the source at node i, is defined by Equation 5.11, where A_i is the gamma attenuation at node i, S_γ is the gamma count rate of the detector at 1 m separation from the source, and $\vec{r}_i$ is the 3D vector pointing from the source to the location at node i.

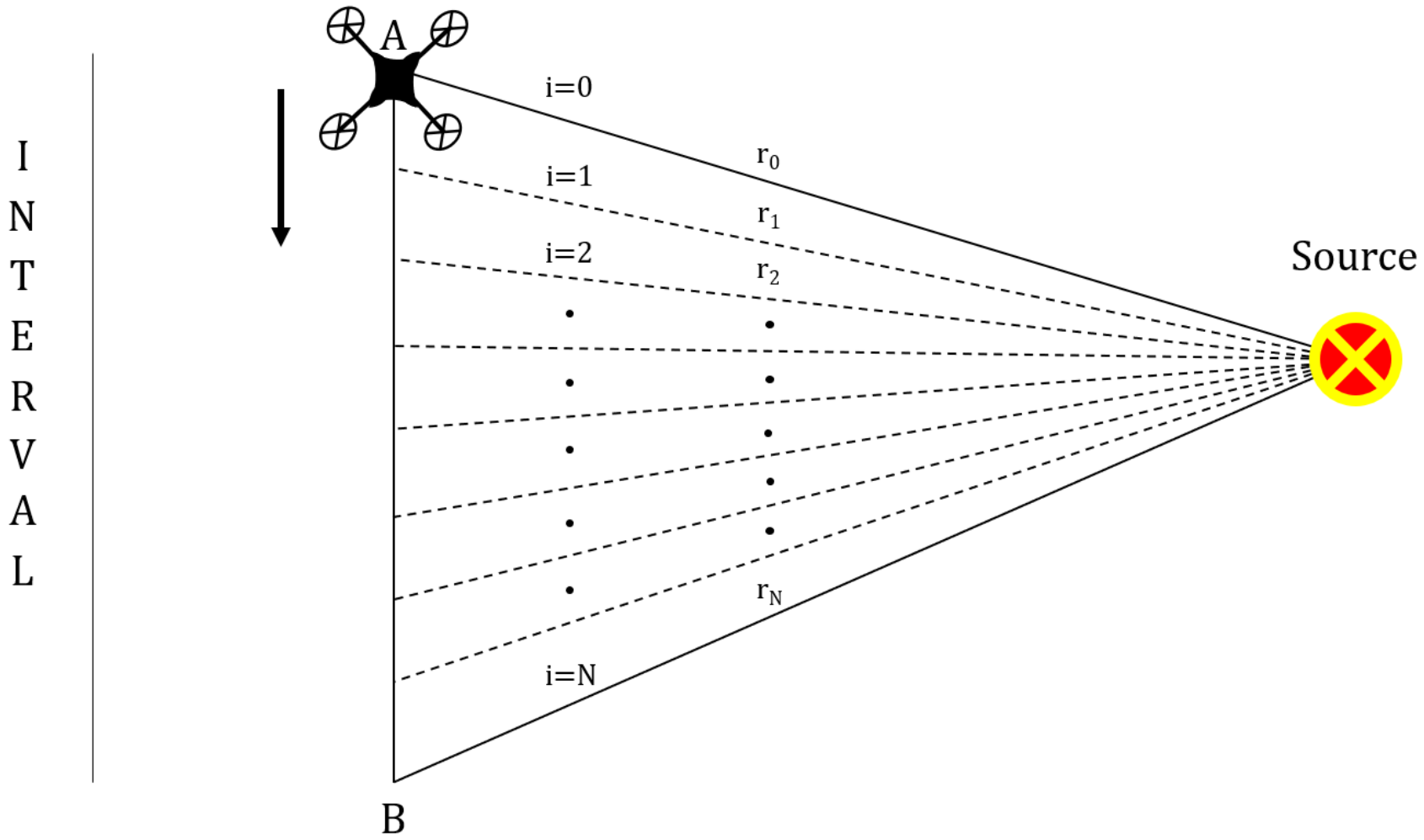


Figure 5.3: Diagram of an interval in the RadSource class paradigm. The interval between A and B may be broken up into a number of subintervals as defined by the user. The default number of subintervals is N=10. The expectation count rate is calculated separately for each subinterval and contributes to the final total number of counts in the interval.

$$C'_{\gamma,i} = A_i \frac{S_\gamma}{|\vec{r_i} \cdot \vec{r_i}|^{1/2}} \tag{5.11}$$

The definition of S_γ is provided in Equation 5.12, where A_γ is the source activity in Bq, ϵ_γ is the total detector gamma efficiency when 1 m from the source, and p_j is the discrete probability of a gamma with energy E_j being produced for a single disintegration of the radioisotope. The value of the summation refers to the expected total number of gammas emitted per disintegration.

$$S_\gamma = A_\gamma \epsilon_\gamma \sum_{j=1}^{N_E} p_j \tag{5.12}$$

The value of A_i is computed from Equation 5.13, where A_A is the attenuation factor at the start of the interval (see Figure 5.3), A_B is the attenuation factor at the end of the interval and i is the node index.

$$A_i = \frac{A_B - A_A}{N} i + A_A \tag{5.13}$$

The attenuation factor for a given location, X, is found using Equation 5.14, where k iterates over the number of barriers, $N_{barriers,X}$ is the number of barriers at location X, j iterates over the number of discrete gamma energies, w_j is the normalized weight of the gamma emission probabilities (i.e. if a gamma *is* emitted then the probability of it having energy E_j is w_j). The quantity, x_k, is the thickness of barrier k and $\mu_{j,k}$ is the attenuation coefficient of barrier k at the gamma energy indicated by j. If there are no barriers, $A_X = 1$.

$$A_X = \prod_{k=1}^{N_{barriers,X}} \sum_{j=1}^{N_E} w_j \exp\left(-x_k \mu_{j,k}\right) \tag{5.14}$$

Now it is time to refer back to Equation 5.11 and define $\vec{r_i}$ which is given by Equation 5.15, where $\vec{r}_{SB}$ is the vector from the source to location B, and $\vec{r}_{SA}$ is the vector from the source to location A.

$$\vec{r_i} = \frac{\vec{r}_{SB} - \vec{r_{SA}}}{N} i + \vec{r}_{SA} \tag{5.15}$$

That wraps up the method for calculating the expected source count rate at each node. Calculating the expected background contribution is much simpler, as illustrated by Equation 5.16, where $GBkgdRate$ is the expected background count rate provided by the user (Default: 200 cps).

$$B_{\gamma}^{'} = GBkgdRate\,(m+1) \tag{5.16}$$

By default the modifier,m, is zero, however if EnableVariableBackground() is called, the modifier is calculated according to Equation 5.17. Where $a = B_{\gamma,max}^{'}/B_{\gamma,min}^{'}$ is the ratio of the maximum expected background count rate, $B_{\gamma,max}^{'}$, to the minimum expected background count rate, $B_{\gamma,min}^{'}$. ratioMaxMin. In the program this value is denoted as ratioMaxMin and may be set by the user and has a default value of 2. The quantity, s_p, is one over the spaceParameter. The spaceParameter describes the spacial period between local maxima and minima in the variable expected background count rate. Larger values spread out the variation over a larger area. The spaceParameter default value is 20.

$$m = \frac{a-1}{3\,(a+1)}\left[\cos\left(1.2 s_p r_y\right) + \cos\left[s_p\left(3.1 r_x + 1.8 r_y\right)\right] - \sin\left[s_p\left(1.2 r_x + 2.1 r_y\right)\right]\right] \tag{5.17}$$

Now that the expected count rates at the node locations have been defined for each contribution (source+background) it is now time to define the expected number of counts in each sub interval. In order to do this , time must be considered. The time spent traversing each subinterval is given by Equation 5.18, where T_A and T_B are the simulation times when the drone is at location A and location B, respectively. This is assumed to be the same for all subintervals.

$$t_l = \frac{T_B - T_A}{N} \tag{5.18}$$

The expected number of counts in each subinterval, l, is simply defined as the average of the count rate at the bounding edge nodes of the subinterval multiplied by the time traversing

the subinterval. This is shown for the source and background contribution in Equations 5.19 and 5.20.

$$\langle C_{\gamma,l} \rangle = \frac{t_l}{2} \left(C'_{\gamma,i=l} + C'_{\gamma,i=l-1} \right) \tag{5.19}$$

$$\langle B_{\gamma,l} \rangle = \frac{t_l}{2} \left(B'_{\gamma}(r_x, r_y)_{i=l} + B'_{\gamma}(r_x, r_y)_{i=l-1} \right) \tag{5.20}$$

Using the expected number of counts, the returned number of counts is sampled from a Poisson distribution which is done separately for each subinterval and each count contributor (source+background). This is shown in the final expression, Equation 5.21. The same approach is used for mixed neutron/gamma sources, though because there is no implementation to approximate neutron attenuation, the energy structure of the neutrons is not relevant.

$$C_{\gamma,T} = \sum_{l=1}^{N} \left[\mathrm{P}(\langle C_{\gamma,l} \rangle) + \mathrm{P}(\langle B_{\gamma,l} \rangle) \right] \tag{5.21}$$

The preceding method describes the calculations which are performed in the RadSource class, but this clearly requires some information regarding the materials, drone locations, etc. This best way to describe this is through a class diagram showing the way in which the classes relate to each other and showing the public member functions of the two most relevant classes, 'RadSource' and 'Material'. This is shown in Figure 5.4.

5.3.3 Program Demonstration

Efficiency calculations for a 2x20 cm cylinder (diameter x length) of EJ200 with a Cs-137 source were performed using MCNP. In the simulation the source was placed 1 m from the center of the cylinder in a side-on irradiation configuration. The result of the simulation shows that the combined geometric and intrinsic efficiency of the single cylinder, for Cs-137 gammas, is 1.506×10^{-5}. A rough approximation for four drone arms, of the same size and material, would be to multiply by $2\sqrt{2}$ which accounts for the 4 arms and a 45 degree tilt added to the arms. This yields 6.025×10^{-5} for the gamma efficiency. This value is used

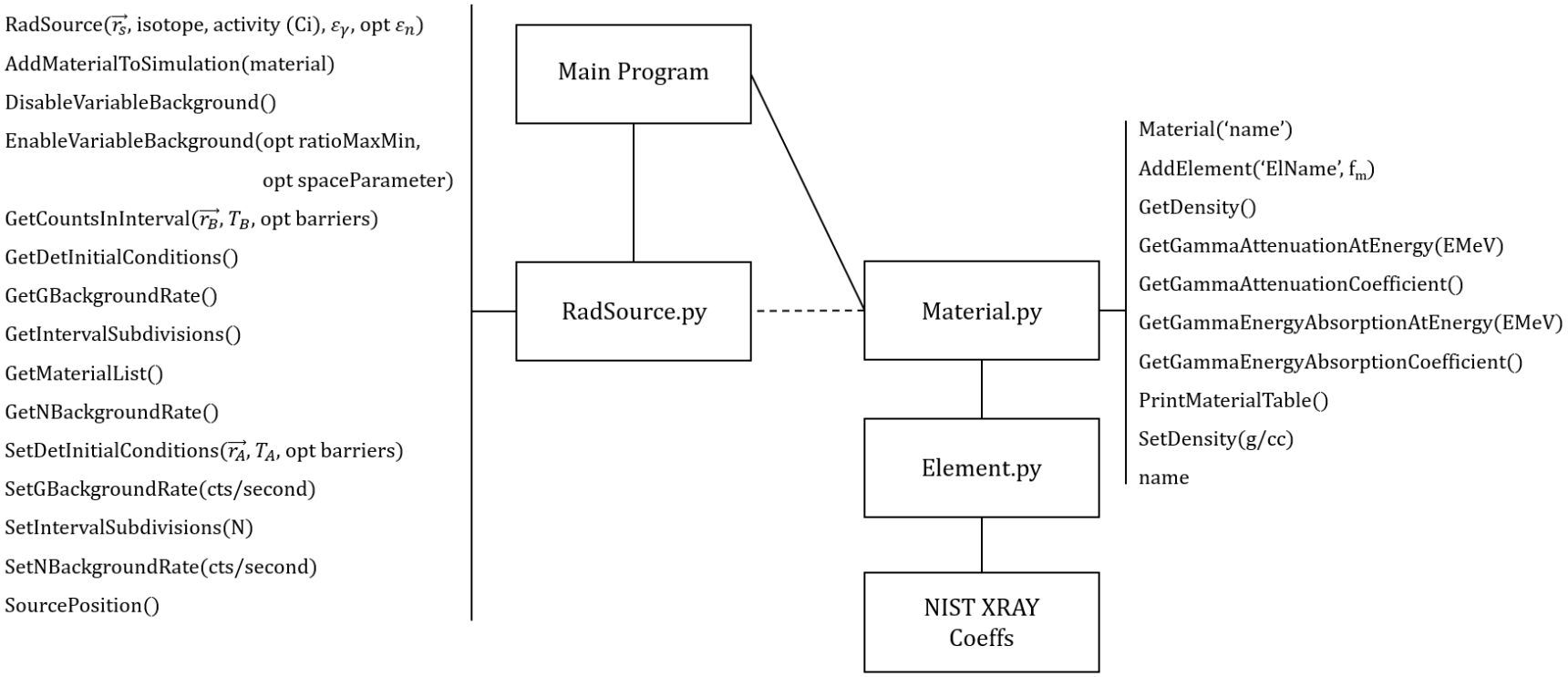
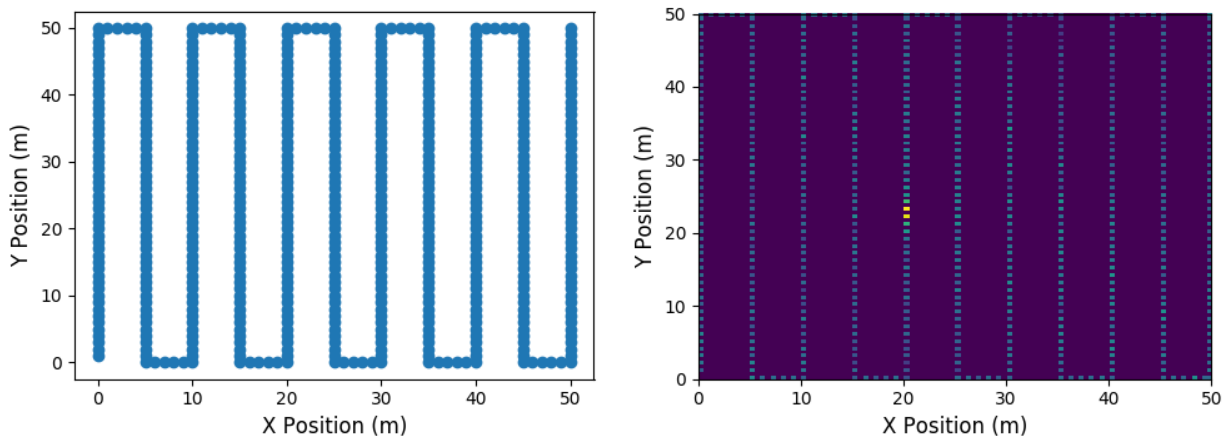


Figure 5.4: Class diagram showing the relationship of the package classes with main. The public member functions of the two most relevant classes, RadSource and Material, are also shown.

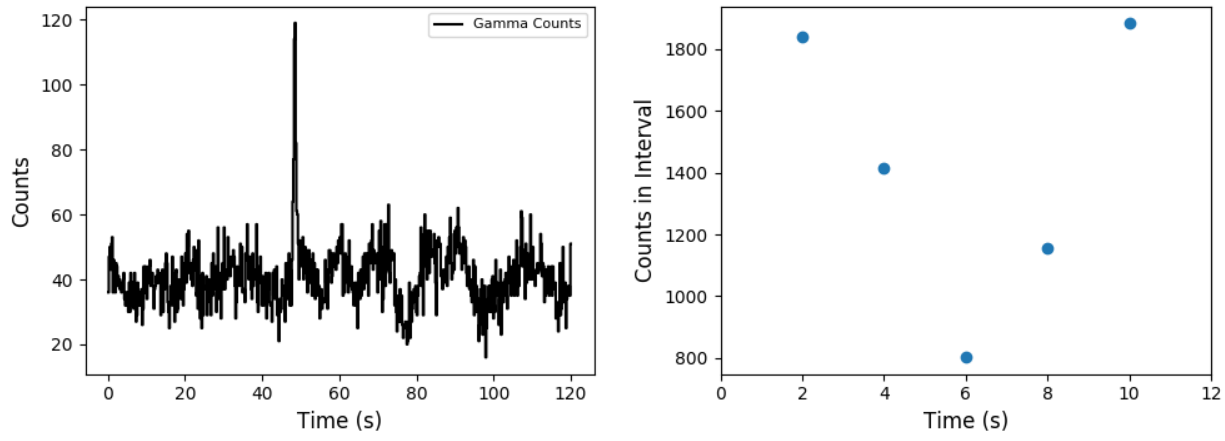
for the efficiency input, and along with a source activity of 250 μCi, which is placed at $\vec{r}_s = (20., 22., 0.)$ m in the simulation. A path is created so that the drone flies in a grid pattern 1 m above ground ($r_z = 0$). The total fight area is a 50 x 50 m square, and adjacent passes are spaced 50 m apart. The drone speed is set to 5 m/s and the sampling frequency (the frequency that the GetCountsInInterval mathod is called) is set to 5 Hz. The gamma background is set to be variable with a max/min ratio of 2 and mid value of 200 cps. A second example is completed to show the functionality of the barrier feature. In this run, the source was placed at $\vec{r}_s = (5., 5., 0.)$ m and the drone hovered at $\vec{r} = (4., 4., 1.)$ m taking readings every two seconds. In the first reading there was no barrier in place. In the second reading 10 cm of block was between the source and detector. The third reading had the most attenuating material with 10.1 cm of block, 5 cm of concrete, and 0.4 cm of water. The fourth reading has no barriers, same as the fifth reading. Results from both of these demonstrations are shown in Figures 5.5 and 5.6.

Examining Figure 5.5a, the drone measurement points appear to be spaced by 1 m, this is easy to see when looking along the x axis. The 1 m spacing is congruent with the 5 m/s drone speed coupled to the 5 Hz sampling rate. This indicates that the mechanics of generating a path and calling to the GetCountsInInterval() method are in order. Figure 5.5b shows a heatmap of the counts received when updating at the declared measurement points. The bright spot on this figure is located where the source was placed, again indicating that the mechanics of the program are working well. In Figure 5.6a, the counts in each interval are plotted. The baseline seems centered on 40 counts, when multiplied by 5 Hz this is 200 cps, as declared. This are also large swings in the baseline beyond what would be seen for a constant base line, (40 ± 6.3) at one sigma deviations. This indicates that the variable background works as it should. Lastly, Figure 5.6b shows the effect of adding and removing attenuators. At 2s, no attenuator is present. At 4s one is present but it does not manifest its full attenuation capability because of the interpolation on the attenuation factor between the starting point, A, and end point, B, of the interval. At 6s three different attenuators are added, at 8s there are no attenuators but the effect of them is still felt because of the interpolation that is performed. At 10s, there has been no attenuator for two interval



(a) **(b)**

Figure 5.5: **(a)** Drone measurement points along path and, **(b)** a 2D histogram showing the counts at those points. The higher readings at approximately (20, 22) are congruent with the source placement.



(a) **(b)**

Figure 5.6: **(a)** Gamma counts in the interval for the grid search. **(b)** Gamma counts in the interval for the attenuator demonstration.

endpoints so there is no effective attenuation. All of this indicates that the attenuation behavior is as designed.

5.3.4 Conclusion

A Python program was designed, coded, and tested to aid with source injection for an algorithm development testbed. The detector efficiency can be accounted for by providing it as an input to the program (this should be found a-priori). The program can emulate the effect of attenuators, such as walls, and can provide variable background count rates with changes in position.

5.4 Conclusion of Additional Studies

This concludes the chapter on the studies and tasks which were completed as auxiliary to the authors primary work. The first section showed a method which was developed to reveal latent x-ray escape peaks in a gamma spectrum. The results were used to make better approximations of the energy resolution at the photopeak; these approximations appear to be quite reasonable given the spectral features evident in the spectrum as a whole. The second section outlines a program which was written to aid in the development of source search, localization, and/or mapping algorithms. It is a source injection tool which has enough functionality to mirror reality but is not so precise as to need tons of computation time. Demonstrations of this were presented to show that the program functions as intended.

Chapter 6

Conclusion and Final Remarks

6.1 Dissertation Conclusion

This dissertation has outlined and described research aimed at providing a better understanding of a wide variety of plastic scintillators. The completed studies sought to examine these materials in the radiation sensing and mechanical application space. An emphasis was placed on answering basic science questions about these scintillators. Some of these answers are of value to those designing radiation detector platforms utilizing the scintillator material for mechanical purposes, while other answers apply more broadly to the radiation detector and scintillation materials development communities as a whole.

Chapter 1 addressed the 'what' and 'why' of this research while also providing a cursory introduction to the scintillator class of materials in a radiation sensing context. Attention is given to high-Z loaded plastics and to questions related to understanding Rayleigh scattering of light in plastic-inorganic nanocomposites. Additionally, an introduction to viscoelasticity was provided along with a description of some mechanical characteristics of viscoelastic materials.

The studies in Chapter 2 examined the mechanical properties and relative light output of many scintillators. Tensile and flexural testing showed that many plastic scintillators are both stronger and stiffer than average acrylonitrile butadiene styrene (ABS) plastic in both modes of deformation. When compared to the even stronger and stiffer polylactic acid (PLA) plastic, a few of the tested plastics presented with a tensile modulus which

exceeds the average PLA standard. Due to the heightened modulus being coupled to unremarkable strengths, it is reasonable to describe many plastic scintillators as brittle, with a few exceptions. This observed brittleness is more pronounced under tensile deformation and becomes obscured under flexural deformation. Further observations are made to quantify the effect of a variety of chemical modifications on the mechanical properties and light output. These modifications include the addition of crosslinking molecules, tin organometallics, lithium organometallics, or compounds meant to enhance the plastics resistance to environment-driven fogging. The observations reveal that these modifications may affect all studied aspects of the scintillator performance, either detrimentally or advantageously. However, it is possible, with the right choice of additives, to modify a select property of the scintillator without having terribly severe consequences on the desirability of the remaining scintillator features. An example of this would be the crosslinking of EJ299-33 which resulted in significantly enhanced mechanical properties while only decreasing the light output by 4.6%.

The same chapter additionally described the efforts made to understand if and how DMA moduli could be compared to moduli measured using the ASTM D790 flexural test standard. These efforts showed that these two moduli are comparable for identically sized samples of EJ200 and EJ200-PS when the DMA frequency and amplitude combine to provide an average strain rate that is comparable to the one used in the ASTM test.

Chapter 3 outlines the approach and methods used to create a radiation and optical transport model in Geant4. This work went further in that a series of completed simulations and experiments were described in order to guide the selection of an optical surface model in Geant4 for use in future simulations. In order to make comparisons on an absolute scale, something not often (if ever) done in typical related literature, the light output in terms of the number of photoelectrons is the observable quantity used for comparison. The results of this showed that the *unified* surface model was the best to use for cylindrical detectors with polished surfaces. The simulations using this model served as better predictors of the light output and boasted a quicker time-to-completion as compared to simulations utilizing the LUT-LBNL model.

Having developed a sufficiently well-designed simulation space with a heuristically-selected optical surface model, experiments with, and simulations of, high-Z loaded plastic scintillators were performed. These are documented in Chapter 4. This set of work showed validation with EJ256 5 wt/% Pb in 2x2 inch RCC geometry and with multiple wt/% loading of YbF_3 nanocomposites in 2x10 mm (thickness x diameter). The expected response from scaled up 24.5 wt/% YbF_3 is shown in a range of sizes from 1x10 mm up to 2x2 inch RCC. Due to short optical absorption lengths, leading to poor photon statistics and higher variance in the light collection efficiency, the photopeak becomes obscured with increasing sizes. This chapter additionally highlighted current issues, previously unknown (or unannounced) in this field of study, surrounding the description of Rayleigh scattering lengths in nanocomposites. The currently propagated expression for the Rayleigh scattering lengths was only ever intended to apply in situations where adjacent nanoparticles are spaced many wavelengths (of the optical photon) apart. This is not the case for most nanocomposite materials.

Chapter 5 reports on a method developed to deconvolve latent x-ray escape peaks from photopeaks. The idea for this hinged on physically grounded inter-relationships between the photopeak and x-ray escape peak. It was shown that some of the parameters describing these relationships may be bound by values calculated with Monte Carlo calculations which avoided unnecessarily overfitting the data. Additionally in Chapter 5 is the description of a toolkit written in Python for use in a testbed for developing mobile radiation detection/mapping/localization algorithms.

Lastly, Appendix C describes efforts to calculate the Cramer Rao Lower Bound on the TOF-PET timing resolution of EJ232Q. Results show that this bound is dependent on the size of the sample and source-sample geometry. The trends of the results track well with, but are less than, reported experimental timing resolution results.

6.2 Future Work

A considerable amount of work towards furthering this vein of knowledge still remains. With regards to mechanical properties, studies on the level of creep present in potential

candidate materials should be performed. This will address mostly long-term concerns related to potential permanent deformation of these materials if they are placed under a low, but constant, stress. If a set of materials is identified as containing potential candidates for a radiation sensing and mechanical application, it would be of value to perform shock testing on relevant configurations both without and with candidate light transducers. Tests performed without light readout should be aimed at determining the point at which fractures or breakage begin to occur and the point at which these make the material unusable. Tests performed with light readout should look for decoupling of the readout from the scintillator in addition to damage occurring to the readout itself. With regards to comparing DMA moduli with results from the ASTM D790 test, an experiment should be performed going to increasingly smaller sizes, but still with the proper span to depth ratio of 16:1. If the small sizes produce comparable moduli, then this may be a useful tool moving forward though many caveats will likely exist depending on the viscoelastic material constants.

With regards to surface models in Geant4, no currently available model in the Geant4 distribution is a perfect reflection of what occurs in nature. The question of whether or not to further develop this functionality, though, is largely philosophical. Because, ultimately, the models currently available are able to quickly produce answers which are 'close' without requiring tons of difficult-to-know information such as the precise location and description of all surface micro-structures, the complex refractive indices of the scintillator, gap material (if applicable), and reflector, the dependence function of the refractive indices to temperature, and the precise description of how the thickness of any gap changes with respect to the detector surface. Characterizing a single detector to this level of detail would require enormous amounts of time and effort for what many may see as a small or negligible return. It is likely that even if such a feat were demonstrated, it would not be widely adopted for reasons of efficiency.

Regarding the approach to acquiring data inputs and conducting the simulations presented in Chapters 3 and 4, it is believed some aspects may be improved upon. The first of these would be to characterize the PMT used in the validation experiments to a level that allows the photocathode reflectivity and photoelectron production term to be well understood and included in the model. It is believed that the best approach to accomplishing

this would be to determine the wavelength dependent complex refractive index of the photocathode using data from spectroscopic reflectometry and ellipsometry measurements fit to a parametric optical model (see [74, 121]). This complex refractive index may then be used in the Geant4 materials properties table belonging to the photocathode material. Geant4 already has the functionality to calculate the reflectivity at a dielectric-metal interface based on this data input. The resulting reflectivity is a function of the wavelength, incident angle, and polarization of the optical photon. Based on the Geant4 documentation, some work in the backend may need to be completed in order to additionally use this data for generating photon 'detection' or photoelectron production, though in principle this is possible. It would require an additional input, the conversion factor, which is related to the photon energy in excess of the photocathode work-function and the thickness of the photocathode; Geant4 already allows the user to input a similar parameter referred to simply as the 'efficiency'.

It would additionally be beneficial to have better measurements of the bulk optical attenuation lengths of all materials. This is particularly a concern in the EJ200 case since very clear materials present sensitivity difficulties when measuring the attenuation length through sample dimensions which are $\ll$ the optical length being measured. Typically, such an experiment is done in a dark room using very long rods of varied lengths as demonstrated in [122].

For the nanocomposites, additional studies quantifying the specular and diffuse transmission, as done in [110], would be extremely valuable in addressing the quantification of the Rayleigh scattering length in these materials. Of additional value for these materials would be direct measurements of the refractive indices, perhaps alongside comparisons predicted from various effective medium theories, usually the Maxwell-Garnett or Bruggeman models as demonstrated in [110, 123], and many others. Further experimentation could examine the light output for varied thicknesses to begin showing and quantifying the effect of bulk optical attenuation on the reported light yields, since for modeling purposes it is important this be as close to the internal absolute light yield as possible.

The nanocomposites may additionally be studied further using the finite difference time domain method for solving Maxwell's equations. This approach was developed as a subset of the field of Computational Electromagnetics/Electrodynamics. A book on the subject

may be found in [124], where Chapter 9 is quite relevant to the situation here. Additional relevant examples may be found in [125, 126]. Some pre-existing computational suites, such as JCMsuite, should be up to this task. Of course, this will also require good knowledge of the permittivity and permeability of the matrix and nanoparticles. Results of these simulations may provide information related to light scattering, effective refractive indices, and effective optical absorption lengths.

Bibliography

[1] H. Moon, J. Martinez-Carranza, T. Cieslewski, M. Faessler, D. Falanga, A. Simovic, D. Scaramuzza, S. Li, M. Ozo, C. De Wagter, et al., Intelligent Service Robotics **12**, 137 (2019), ISSN 1861-2784, URL https://doi.org/10.1007/s11370-018-00271-6. 3

[2] T. T. Mac, C. Copot, A. Hernandez, and R. De Keyser, in *2016 IEEE 14th International Symposium on Applied Machine Intelligence and Informatics (SAMI)* (IEEE, 2016), pp. 345–350. 3

[3] K. S. Lee, M. Ovinis, T. Nagarajan, R. Seulin, and O. Morel, in *2015 IEEE 15th International Conference on Environment and Electrical Engineering (EEEIC)* (IEEE, 2015), pp. 1291–1297. 3

[4] M. Saska, T. Krajnik, and L. Pfeucil, in *International Multi-Conference on Systems, Signals Devices* (IEEE, 2012), pp. 1–6. 3

[5] S. Grzonka, G. Grisetti, and W. Burgard, IEEE Transactions on Robotics **28**, 90 (2012), ISSN 1552-3098. 3

[6] F. Fraundorfer, L. Heng, D. Honegger, G. H. Lee, L. Meier, P. Tanskanen, and M. Pollefeys, in *2012 IEEE/RSJ International Conference on Intelligent Robots and Systems* (IEEE, 2012), pp. 4557–4564, ISSN 2153-0866. 3

[7] A. S. Huang, A. Bachrach, P. Henry, M. Krainin, D. Maturana, D. Fox, and N. Roy, in *Robotics Research* (Springer, 2017), pp. 235–252. 3

[8] K. Boudergui, F. Carrel, T. Domenech, N. Guenard, J.-P. Poli, A. Ravet, V. Schoepff, and R. Woo, in *2011 2nd International Conference on Advancements in Nuclear Instrumentation, Measurement Methods and Their Applications* (IEEE, 2011), pp. 1–9. 3

[9] M. Gmar, M. Agelou, F. Carrel, and V. Schoepff, Nuclear Instruments and Methods in Physics Research Section A: Accelerators, Spectrometers, Detectors and Associated Equipment **652**, 638 (2011), ISSN 0168-9002, symposium on

Radiation Measurements and Applications (SORMA) XII 2010, URL http://www.sciencedirect.com/science/article/pii/S0168900210019169. 3

[10] J. Aleotti, G. Micconi, S. Caselli, G. Benassi, N. Zambelli, D. Calestani, M. Zanichelli, M. Bettelli, and A. Zappettini, in *2015 IEEE nuclear science symposium and medical imaging conference (NSS/MIC)* (IEEE, 2015), pp. 1–5. 5

[11] P. Martin, S. Kwong, N. Smith, Y. Yamashiki, O. Payton, F. Russell-Pavier, J. Fardoulis, D. Richards, and T. Scott, International Journal of Applied Earth Observation and Geoinformation **52**, 12 (2016), ISSN 0303-2434, URL http://www.sciencedirect.com/science/article/pii/S0303243416300733.

[12] C. Cai, B. Carter, M. Srivastava, J. Tsung, J. Vahedi-Faridi, and C. Wiley, in *2016 IEEE Systems and Information Engineering Design Symposium (SIEDS)* (IEEE, 2016), pp. 165–169.

[13] P. Royo, E. Pastor, M. Macias, R. Cuadrado, C. Barrado, and A. Vargas, Remote Sensing **10** (2018), ISSN 2072-4292, URL https://www.mdpi.com/2072-4292/10/11/1712. 5

[14] J. Towler, B. Krawiec, and K. Kochersberger, Remote Sensing **4**, 1995 (2012), ISSN 2072-4292, URL https://www.mdpi.com/2072-4292/4/7/1995. 5

[15] J. Jiang, K. Shimazoe, Y. Nakamura, H. Takahashi, Y. Shikaze, Y. Nishizawa, M. Yoshida, Y. Sanada, T. Torii, M. Yoshino, et al., Journal of Nuclear Science and Technology **53**, 1067 (2016), URL https://doi.org/10.1080/00223131.2015.1089796. 5

[16] C. Redding, A. Hackett, M. Laubach, R. Feng, P. Feng, C. Hurlbut, P. Liaw, and J. P. Hayward, Nuclear Instruments and Methods in Physics Research Section A: Accelerators, Spectrometers, Detectors and Associated Equipment **954**, 161448 (2020). 4, 52

[17] Napy1kenobi (2010), URL https://commons.wikimedia.org/wiki/File:Strahlenarten_en.svg. 6

[18] G. F. Knoll, *Radiation Detection and Measurement* (John Wiley and Sons, 2000), 3rd ed. 7, 8, 161

[19] J. E. Turner, *Atoms, Radiation, and Radiation Protection* (Wiley VCH, 2007), 3rd ed., ISBN 978-3-527-40606-7. 7, 8, 11

[20] H. Bethe, Annalen der Physik **397**, 325 (1930), URL https://onlinelibrary.wiley.com/doi/abs/10.1002/andp.19303970303. 8

[21] N. Tsoulfanidis and S. Landsberger, *Measurement and Detection of Radiation* (Taylor and Francis Group, LLC, 2015), 4th ed., ISBN 978-1-4822-1549-6. 14, 15

[22] O. Klein and Y. Nishina, Zeitschrift für Physik **52**, 853 (1929), ISSN 0044-3328, URL https://doi.org/10.1007/BF01366453. 18

[23] C. Combes, P. Dorenbos, C. van Eijk, K. Krämer, and H. Güdel, Journal of Luminescence **82**, 299 (1999), ISSN 0022-2313, URL https://www.sciencedirect.com/science/article/pii/S0022231399000472. 28

[24] W. Klamra, T. Szczesniak, M. Moszynski, J. Iwanowska, L. Swiderski, A. Syntfeld-Kazuch, V. Shlegel, Y. V. Vasiliev, and E. Galashov, Journal of Instrumentation **7**, P03011 (2012). 28

[25] R. Hofstadter, Physical Review **74**, 100 (1948). 31

[26] I. Holl, E. Lorenz, and G. Mageras, IEEE Transactions on Nuclear Science **35**, 105 (1988). 31

[27] E. Sakai, IEEE Transactions on Nuclear Science **34**, 418 (1987).

[28] D. Persyk and T. Moi, IEEE Transactions on Nuclear Science **25**, 615 (1978). 31

[29] N. D'olympia, P. Chowdhury, C. Lister, J. Glodo, R. Hawrami, K. Shah, and U. Shirwadkar, Nuclear Instruments and Methods in Physics Research Section A: Accelerators, Spectrometers, Detectors and Associated Equipment **714**, 121 (2013). 32

[30] M. Smith, T. Achtzehn, H. Andrews, E. Clifford, P. Forget, J. Glodo, R. Hawrami, H. Ing, P. O'Dougherty, K. Shah, et al., Nuclear Instruments and Methods in Physics Research Section A: Accelerators, Spectrometers, Detectors and Associated Equipment **784**, 162 (2015). 32

[31] F. Brooks, Nuclear Instruments and Methods **162**, 477 (1979). 32, 36

[32] G. Wright, Proceedings of the Physical Society. Section B **69**, 358 (1956). 33

[33] R. Owen, IRE Transactions on Nuclear Science **5**, 198 (1958). 33

[34] L. J. Basile, The Journal of Chemical Physics **27**, 801 (1957), https://doi.org/10.1063/1.1743832, URL https://doi.org/10.1063/1.1743832. 36, 40

[35] J. Birks, Photochemistry and Photobiology **24**, 287 (1976).

[36] A. Hallam and J. Birks, Journal of Physics B: Atomic and Molecular Physics **11**, 3273 (1978).

[37] J. B. Birks, *The theory and practice of scintillation counting: International series of monographs in electronics and instrumentation*, vol. 27 (Elsevier, 2013).

[38] R. C. Evans, P. Douglas, and H. D. Burrow, *Applied photochemistry* (Springer, 2013). 36

[39] T. Förster, Discussions of the Faraday Society **27**, 7 (1959). 36

[40] D. L. Dexter, The journal of chemical physics **21**, 836 (1953). 36

[41] S. Moser, W. Harder, C. Hurlbut, and M. Kusner, Radiation Physics and Chemistry **41**, 31 (1993). 37

[42] W. Moses, G. Bizarri, R. T. Williams, S. Payne, A. Vasil'Ev, J. Singh, Q. Li, J. Grim, and W.-S. Choong, IEEE Transactions on Nuclear Science **59**, 2038 (2012). 39

[43] J. Allison, K. Amako, J. Apostolakis, P. Arce, M. Asai, T. Aso, E. Bagli, A. Bagulya, S. Banerjee, G. Barrand, et al., Nuclear Instruments and Methods in Physics Research

Section A: Accelerators, Spectrometers, Detectors and Associated Equipment **835**, 186 (2016), ISSN 0168-9002, URL http://www.sciencedirect.com/science/article/pii/S0168900216306957. 39, 82

[44] J. B. Birks, Proceedings of the Physical Society. Section A **64**, 874 (1951). 39

[45] R. Craun and D. Smith, Nuclear Instruments and Methods **80**, 239 (1970). 39

[46] M. Taniguchi and J. S. Lindsey, Photochemistry and photobiology **94**, 290 (2018). 38

[47] N. Zaitseva, A. Glenn, A. Mabe, M. Carman, C. Hurlbut, J. Inman, and S. Payne, Nuclear Instruments and Methods in Physics Research Section A: Accelerators, Spectrometers, Detectors and Associated Equipment **889**, 97 (2018). 39

[48] I. Campbell and B. Crone, Applied Physics Letters **90**, 012117 (2007). 40

[49] Pichat, L., Pesteil, P., and Clément, J., J. Chim. Phys. **50**, 26 (1953), URL https://doi.org/10.1051/jcp/1953500026. 40

[50] M. Hyman and J. J. Ryan, IRE Transactions on Nuclear Science **5**, 87 (1958), ISSN 2374-9814.

[51] S. Sandler and K. Tsou, The International Journal of Applied Radiation and Isotopes **15**, 419 (1964), ISSN 0020-708X, URL http://www.sciencedirect.com/science/article/pii/0020708X64901401.

[52] N. J. Cherepy, S. A. Payne, B. W. Sturm, S. P. O'Neal, Z. M. Seeley, O. B. Drury, L. K. Haselhorst, B. L. Rupert, R. D. Sanner, P. A. Thelin, et al., in *Hard X-Ray, Gamma-Ray, and Neutron Detector Physics XIII*, edited by L. A. Franks, R. B. James, and A. Burger, International Society for Optics and Photonics (SPIE, 2011), vol. 8142, pp. 215 – 222, URL https://doi.org/10.1117/12.896656.

[53] G. Bertrand, F. Sguerra, C. Dehé-Pittance, F. Carrel, R. Coulon, S. Normand, E. Barat, T. Dautremer, T. Montagu, and M. Hamel, Journal of Materials Chemistry C **2**, 7304 (2014).

[54] E. van Loef, G. Markosyan, U. Shirwadkar, M. McClish, and K. Shah, Nuclear Instruments and Methods in Physics Research Section A: Accelerators, Spectrometers, Detectors and Associated Equipment **788**, 71 (2015).

[55] P. L. Feng, W. Mengesha, M. R. Anstey, and J. G. Cordaro, IEEE Transactions on Nuclear Science **63**, 407 (2016). 40, 53

[56] B. Rupert, N. Cherepy, B. Sturm, R. Sanner, and S. Payne, EPL (Europhysics Letters) **97**, 22002 (2012). 40

[57] N. Cherepy, R. Sanner, T. Tillotson, S. Payne, P. Beck, S. Hunter, L. Ahle, and P. Thelin, in *2012 IEEE Nuclear Science Symposium and Medical Imaging Conference Record (NSS/MIC)* (IEEE, 2012), pp. 1972–1973.

[58] N. J. Cherepy, R. D. Sanner, P. R. Beck, E. L. Swanberg, T. M. Tillotson, S. A. Payne, and C. R. Hurlbut, Nuclear Instruments and Methods in Physics Research Section A: Accelerators, Spectrometers, Detectors and Associated Equipment **778**, 126 (2015), ISSN 0168-9002, URL http://www.sciencedirect.com/science/article/pii/S0168900215000261. 53

[59] N. J. Cherepy, S. Hok, S. P. O'Neal, H. P. Martinez, P. R. Beck, R. D. Sanner, O. B. Drury, E. L. Swanberg, S. A. Payne, and C. R. Hurlbut, in *Hard X-Ray, Gamma-Ray, and Neutron Detector Physics XX* (International Society for Optics and Photonics, 2018), vol. 10762, p. 107620B.

[60] S. O'Neal, N. Cherepy, S. Hok, and S. Payne, IEEE Transactions on Nuclear Science **67**, 746 (2020). 40

[61] C. Liu, T. J. Hajagos, D. Kishpaugh, Y. Jin, W. Hu, Q. Chen, and Q. Pei, Advanced Functional Materials **25**, 4607 (2015), https://onlinelibrary.wiley.com/doi/pdf/10.1002/adfm.201501439, URL https://onlinelibrary.wiley.com/doi/abs/10.1002/adfm.201501439. 40, 41, 42, 120

[62] Y. Chen, C. Liu, Y. Jin, T. J. Hajagos, D. Kishpaugh, Q. Zhuang, and Q. Pei, in *Hard X-Ray, Gamma-Ray, and Neutron Detector Physics XVIII*, edited by R. B. James,

M. Fiederle, A. Burger, and L. Franks, International Society for Optics and Photonics (SPIE, 2016), vol. 9968, pp. 82 – 93, URL https://doi.org/10.1117/12.2238336. 40, 42, 53, 122, 127, 131, 133, 134, 135, 141, 142

[63] Y. Jin, D. Kishpaugh, C. Liu, T. J. Hajagos, Q. Chen, L. Li, Y. Chen, and Q. Pei, Journal of Materials Chemistry C **4**, 3654 (2016). 40, 41, 120, 122, 143

[64] C. Liu, Z. Li, T. J. Hajagos, D. Kishpaugh, D. Y. Chen, and Q. Pei, ACS nano **11**, 6422 (2017). 41

[65] T. Crane, J. Hitchens, C. Macqueen, and N. Bazin, in *2018 IEEE Nuclear Science Symposium and Medical Imaging Conference Proceedings (NSS/MIC)* (IEEE, 2018), pp. 1–2. 41

[66] C. Lü and B. Yang, Journal of Materials Chemistry **19**, 2884 (2009). 41, 120

[67] T. J. Hajagos, C. Liu, N. J. Cherepy, and Q. Pei, Advanced Materials **30**, 1706956 (2018). 41, 120

[68] W. Caseri, Macromolecular Rapid Communications **21**, 705 (2000). 42

[69] B. M. Novak, Advanced Materials **5**, 422 (1993). 42

[70] D. W. Richerson, *Modern Ceramic Engineering* (Marcel Dekker, New York, 1982). 42

[71] W. Caseri, Materials Science and Technology **22**, 807 (2006). 42, 120

[72] R. J. Nussbaumer, Ph.D. thesis, ETH Zurich (2004). 42, 120

[73] H. P. K.K., *Photomultiplier Tubes - Basics and Applications*, fourth edition ed. (2017). 44, 45, 47

[74] D. Motta and S. Schönert, Nuclear Instruments and Methods in Physics Research Section A: Accelerators, Spectrometers, Detectors and Associated Equipment **539**, 217 (2005). 45, 100, 183

[75] J. D. Ferry, *Viscoelastic Properties of Polymers* (John Wiley & Sons, 1961). 47

[76] J. D. Ferry, *Viscoelastic Properties of Polymers* (John Wiley & Sons, 1980), 3rd ed.

[77] I. Ward, *Mechanical Properties of Solid Polymers* (John Wiley & Sons, 1983), second ed. ed., ISBN 0-471-90011-7.

[78] E. Riande, R. Díaz-Calleja, M. G. Prolongo, R. M. Masegosa, and C. Salom, *Polymer Viscoelasticity* (Marcel Dekker, 2000), ISBN 0-8247-7904-5.

[79] R. M. Christensen, *Theory of Viscoelasticity* (Academic Press, Inc., 1982), 2nd ed.

[80] V. Shah, *Handbook of Plastics Testing and Failure Analysis* (John Wiley & Sons, 2007), 3rd ed. 47

[81] N. Mohammadi, M. Mahjoob, B. Kaffashi, and S. Malakooti, Journal of Mechanical Science and Technology **24**, 1829 (2010). 49

[82] N. Zaitseva, A. Glenn, L. Carman, H. P. Martinez, R. Hatarik, H. Klapper, and S. Payne, Nuclear Instruments and Methods in Physics Research Section A: Accelerators, Spectrometers, Detectors and Associated Equipment **789**, 8 (2015). 53

[83] N. Zaitseva, B. L. Rupert, I. PaweŁczak, A. Glenn, H. P. Martinez, L. Carman, M. Faust, N. Cherepy, and S. Payne, Nuclear Instruments and Methods in Physics Research Section A: Accelerators, Spectrometers, Detectors and Associated Equipment **668**, 88 (2012).

[84] P. Zhmurin, V. Lebedev, V. Titskaya, A. Adadurov, D. Elyseev, and V. Pereymak, Nuclear Instruments and Methods in Physics Research Section A: Accelerators, Spectrometers, Detectors and Associated Equipment **761**, 92 (2014).

[85] T. J. Hajagos, D. Kishpaugh, and Q. Pei, Nuclear Instruments and Methods in Physics Research Section A: Accelerators, Spectrometers, Detectors and Associated Equipment **825**, 40 (2016). 53

[86] C. Burt and D. Ramsden, in *2008 IEEE Nuclear Science Symposium Conference Record* (IEEE, 2008), pp. 1186–1190. 53

[87] A. International, *ASTM D638-14, Standard Test Method for Tensile Properties of Plastics*, ASTM International, 100 Barr Harbor Drive, PO Box C700, West Conshohocken, PA 19428-2959. United States (2015). 55

[88] A. International, *ASTM D790-15E2, Standard Test Methods for Flexural Properties of Unreinforced and Reinforced Plastics and Electrical Insulating Materials*, ASTM International, 100 Barr Harbor Drive, PO Box C700, West Conshohocken, PA 19428-2959. United States (2016). 59, 77

[89] A. Savitzky and M. J. Golay, Analytical chemistry **36**, 1627 (1964). 61

[90] E. Technology, *Ej-200, ej-204, ej-208, ej-212 - plastic scintillators - eljen technology* (2016), URL https://eljentechnology.com/products/plastic-scintillators/ej-200-ej-204-ej-208-ej-212. 62, 99, 102, 129

[91] S. E. Zeltmann, B. B. Kumar, M. Doddamani, and N. Gupta, Polymer **101**, 1 (2016). 64

[92] M. L. Williams, R. F. Landel, and J. D. Ferry, Journal of the American Chemical Society **77**, 3701 (1955), https://doi.org/10.1021/ja01619a008, URL https://doi.org/10.1021/ja01619a008. 64

[93] J. Dealy and D. Plazek, Rheol. Bull **78**, 16 (2009). 65

[94] Matweb, *Overview of materials for acrylonitrile butadiene styrene (abs), molded* (2020), URL http://www.matweb.com/search/DataSheet.aspx?MatGUID=c8bc69525dd04bd9bca54c475f6b38c3. 65

[95] Matweb, *Overview of materials for polylactic acid (pla) biopolymer* (2020), URL http://www.matweb.com/search/DataSheet.aspx?MatGUID=ab96a4c0655c4018a8785ac4031b9278. 65

[96] M. Loyd, Ph.D. thesis, University of Tennessee, Knoxville (2019). 68

[97] E. M. Ellis, C. Hurlbut, C. Allwork, and B. Morris, in *2017 IEEE Nuclear Science Symposium and Medical Imaging Conference (NSS/MIC)* (IEEE, 2017), pp. 1–5. 72

[98] A. Levin and C. Moisan, in *1996 IEEE Nuclear Science Symposium. Conference Record* (IEEE, 1996), vol. 2, pp. 702–706. 82

[99] M. Janecek and W. W. Moses, IEEE Transactions on Nuclear Science **57**, 964 (2010). 82, 83, 100

[100] E. Roncali and S. R. Cherry, Physics in Medicine & Biology **58**, 2185 (2013). 82

[101] M. Janecek and W. W. Moses, IEEE transactions on nuclear science **55**, 2443 (2008). 83, 100

[102] M. Janecek and W. W. Moses, IEEE transactions on nuclear science **55**, 2432 (2008). 83, 100

[103] E. Bellamy, G. Bellettini, F. Gervelli, M. Incagli, D. Lucchesi, C. Pagliarone, F. Zetti, Y. Budagov, I. Chirikov-Zorin, and S. Tokar, Nuclear Instruments and Methods, Section A **339**, 468 (1994). 86, 89

[104] R. Brun and F. Rademakers, Nuclear Instruments and Methods in Physics Research Section A: Accelerators, Spectrometers, Detectors and Associated Equipment **389**, 81 (1997). 87

[105] T. Depireux, F. Dumont, and A. Watillon, Journal of colloid and interface science **118**, 314 (1987). 99

[106] F. Schneider, J. Draheim, R. Kamberger, and U. Wallrabe, Sensors and Actuators A: Physical **151**, 95 (2009). 99

[107] I. H. Malitson, Josa **55**, 1205 (1965). 99

[108] J. De Haas, P. Dorenbos, and C. Van Eijk, Nuclear Instruments and Methods in Physics Research Section A: Accelerators, Spectrometers, Detectors and Associated Equipment **537**, 97 (2005). 100

[109] C. O. Steinbach, F. Ujhelyi, and E. Lőrincz, in *2012 IEEE Nuclear Science Symposium and Medical Imaging Conference Record (NSS/MIC)* (IEEE, 2012), pp. 2555–2558. 100, 105

[110] T. Tsuzuki, Macromolecular materials and engineering **293**, 109 (2008). 120, 183

[111] B. Wang, G. Wilkes, J. Hedrick, S. Liptak, and J. McGrath, Macromolecules **24**, 3449 (1991). 120

[112] M. Kerker, *The scattering of light and other electromagnetic radiation*, vol. 1 (Academic press, 1969). 120

[113] R. M. Almeida, P. J. Morais, and H. C. Vasconcelos, in *Sol-Gel Optics IV* (International Society for Optics and Photonics, 1997), vol. 3136, pp. 296–303. 121

[114] H. C. Van de Hulst, *Light scattering by small particles* (Courier Corporation, 1981). 121, 122

[115] L. R. F.R.S., The London, Edinburgh, and Dublin Philosophical Magazine and Journal of Science **47**, 375 (1899), https://doi.org/10.1080/14786449908621276, URL https://doi.org/10.1080/14786449908621276. 122

[116] T. Amotchkina, M. Trubetskov, D. Hahner, and V. Pervak, Applied optics **59**, A40 (2020). 131

[117] P. Bansal and A. J. Ardell, Metallography **5**, 97 (1972). 143

[118] H. Zhao, H. Yu, C. Redding, Z. Li, T. Chen, Y. Meng, T. J. Hajagos, J. P. Hayward, and Q. Pei, ACS Applied Nano Materials **4**, 1220 (2021). 159, 163

[119] T. Goorley, M. James, T. Booth, F. Brown, J. Bull, L. Cox, J. Durkee, J. Elson, M. Fensin, R. Forster, et al., Nuclear Technology **180**, 298 (2012). 163

[120] E. Browne and J. Tuli, Nuclear Data Sheets **108**, 2173 (2007). 163

[121] M. Moorhead and N. Tanner, Nuclear Instruments and Methods in Physics Research Section A: Accelerators, Spectrometers, Detectors and Associated Equipment **378**, 162 (1996). 183

[122] M. Bodmer, N. Phan, M. Gold, D. Loomba, J. Matthews, and K. Rielage, Journal of Instrumentation **9**, P02002 (2014). 183

[123] M. Quinten, *Optical properties of nanoparticle systems: Mie and beyond* (John Wiley & Sons, 2010). 183

[124] A. Taflove, A. Oskooi, and S. G. Johnson, *Advances in FDTD computational electrodynamics: photonics and nanotechnology* (Artech house, 2013). 184

[125] C. Oubre and P. Nordlander, The Journal of Physical Chemistry B **108**, 17740 (2004). 184

[126] A. V. Panov, Optics letters **43**, 2515 (2018). 184

[127] X. Wen and J. P. Hayward, IEEE Transactions on Nuclear Science **67**, 2081 (2020). 211, 216, 241, 242

[128] P. Lecoq, IEEE Transactions on Radiation and Plasma Medical Sciences **1**, 473 (2017). 211

[129] S. Seifert, H. T. van Dam, and D. R. Schaart, Physics in Medicine & Biology **57**, 1797 (2012). 211, 212

[130] R. Vinke, P. D. Olcott, J. W. Cates, and C. S. Levin, Physics in Medicine & Biology **59**, 6215 (2014). 212

[131] J. W. Cates, R. Vinke, and C. S. Levin, Physics in Medicine & Biology **60**, 5141 (2015). 211

Appendices

A EJ200 Sample Preparation

This appendix outlines the methods used to prepare the EJ200 samples used in the Surface Model Selection study presented in Chapter 3.

A.1 Sample Machining

The initial bulk stock was received from Eljen in 18 inch lengths and with the following cross sectional areas: 1 inch diameter circle, 1x1 inch square, and hexagonal 1 inch across when measuring from any two parallel sides. These were milled into lengths from 2 inches to 16 inches, in 2 inch steps. A rough cut was performed initially using a General International 4 inch bandsaw. This cut was 1/8 to 1/4 inches longer than the target length. A permanent marker was used to mark a patch of ink on the sample in the vicinity of the target length; this mark served as an indicator. A digital caliper was then used to precisely measure the sample and mark a line into the patch of ink (the points on the outside jaws of the caliper were sufficiently sharp to make a scratch in the ink). The samples were individually loaded into a Kurt workholding clamp which was mounted onto the motion stage of a Birmingham knee mill. A square end milling bit with 1.5 inch length of cut and 3/4 in diameter was loaded into the mill's chuck. The setup of these components is shown in Figure A.1.

Once the work stage was set and loaded, the mill was activated and the motion stage controls were used to pass the sample by the bit so that a small amount of material, hundreds of micrometers thick, was removed from the sample. This action was repeated in a series of several passes until the indicator line was reached by the bit. Once the end milling was completed, all samples measured to be within three thousandths of an inch of their target length.

A.2 Polishing Procedure

After milling the stock to the target lengths, the samples needed to be polished. This was completed using a combination of abrasive pads/paper and a buffing wheel loaded with polishing compound. The abrasive paper was placed on a flat glass plate which had been lightly doused with water. A combination of surface tension and vacuum forces held the

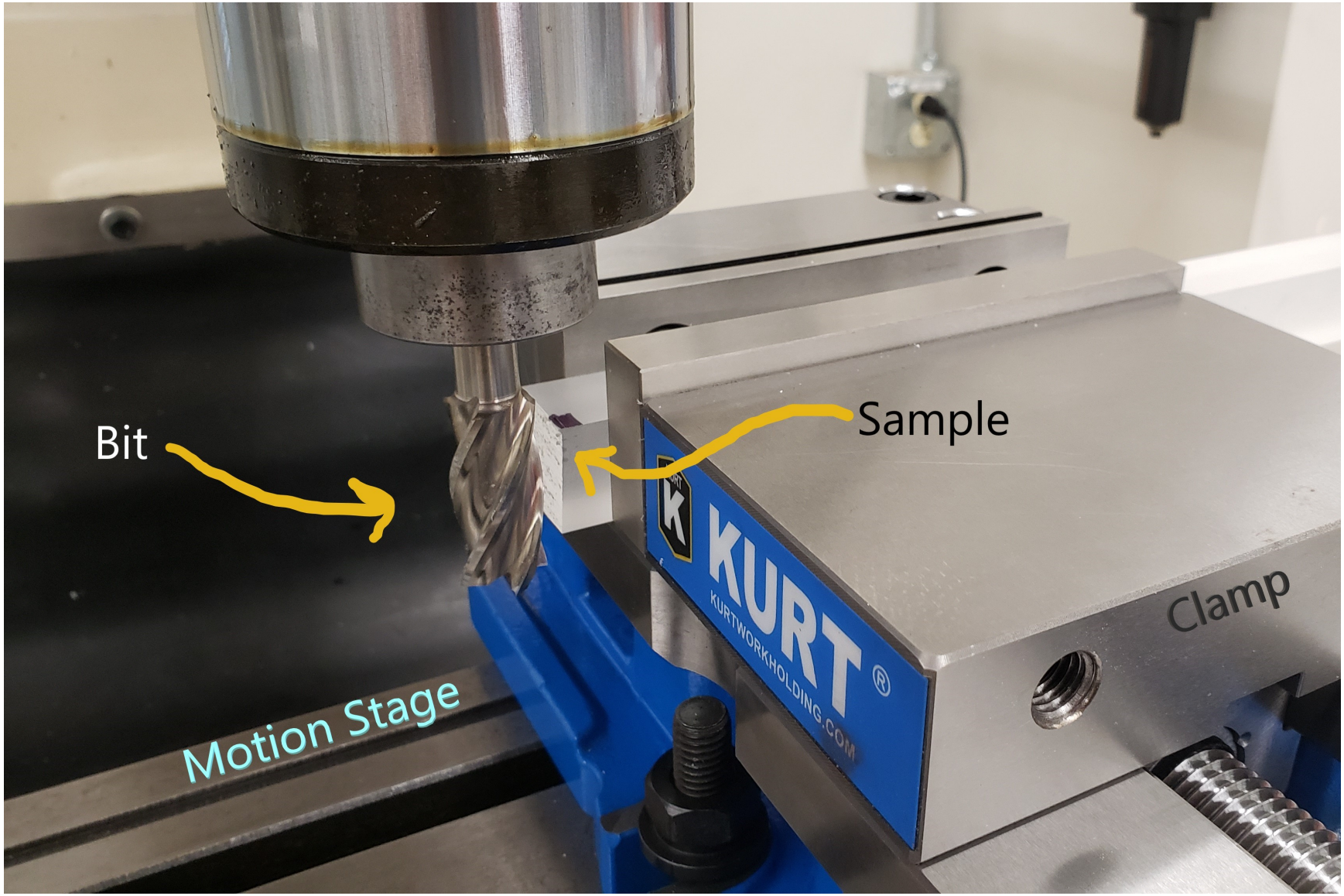


Figure A.1: End milling of the EJ200 samples. The sample material was incrementally removed until the indicator line on the patch of ink was met. The ink is easily visible on the sample; closer inspection will reveal the indicator line in this patch of ink.

paper firm to the glass plate, which also served as an excellent flat and hard substrate. The first abrasive paper used was the 3M Wet or Dry with a designation of "400". Water was used as a lapping fluid and the sample was passed over the surface of the abrasive in circular and back-and-forth motions. This was followed by repeating with the same brand of paper with designations of "800", "1500", and then finally with polishing pads from Buehler designated as P1500 and P2500. After polishing by hand, the samples were polished using a flannel wheel loaded with TC6 polishing compound and then a second flannel wheel loaded with PBC polishing compound. Care was taken so that not much pressure was applied to the wheel and that the sample was not allowed to dwell with the wheel at any location for a prolonged time. This was done because practice on throwaway samples showed that optical distortion would present if too much heat was allowed to build up on the surface.

As a note about choosing abrasives: always strive for acquiring high quality abrasive materials (such as those from Buehler). These will generally be denoted with a 'P' leading the number. Any abrasive labeled with the 'grit' designation or with no designation should be avoided as the size distribution of the abrasive particles is not guaranteed and some rogue particles may gouge the surface of the sample! Aside from using high quality abrasives, the increment in abrasive particle size should never be by more than a factor of two. Check this by using available data tables which correlate the designation on the paper with the mean abrasive particle size. Since the 3M paper was not designated with 'P' or with 'grit', a feel-test was conducted which seemed to indicate that the mean size was most closely correlated with 'P' designated abrasives and it is thought that this label was not used because large variations in the particle size would not allow it to be labeled with the 'P' standard of quality. This is mostly observational, though, because sometimes a random scratch would appear in the otherwise nicely polished surfaces.

B Experimental and Simulated Spectra With EJ200

The following pages contain an aggregate of the background subtracted spectra of Cs-137 taken with EJ200. The experiment is described in Chapter 3. Subsequently, spectra generated using Geant4 are presented. The first set of simulated spectra was generated using the *unified* optical surface model while the second set was generated using the LUT-LBNL surface model. The simulated spectra were normalized to be directly comparable to the experimental count rates. Instances in which the simulated bin count rate exceeds the experimental bin count rate at the location of a spectral feature (e.g. Compton maximum or Compton minimum) occur when those features are located at a lesser position on the photoelectron axis. This is not surprising at all since the total count rate is represented by an *area*.

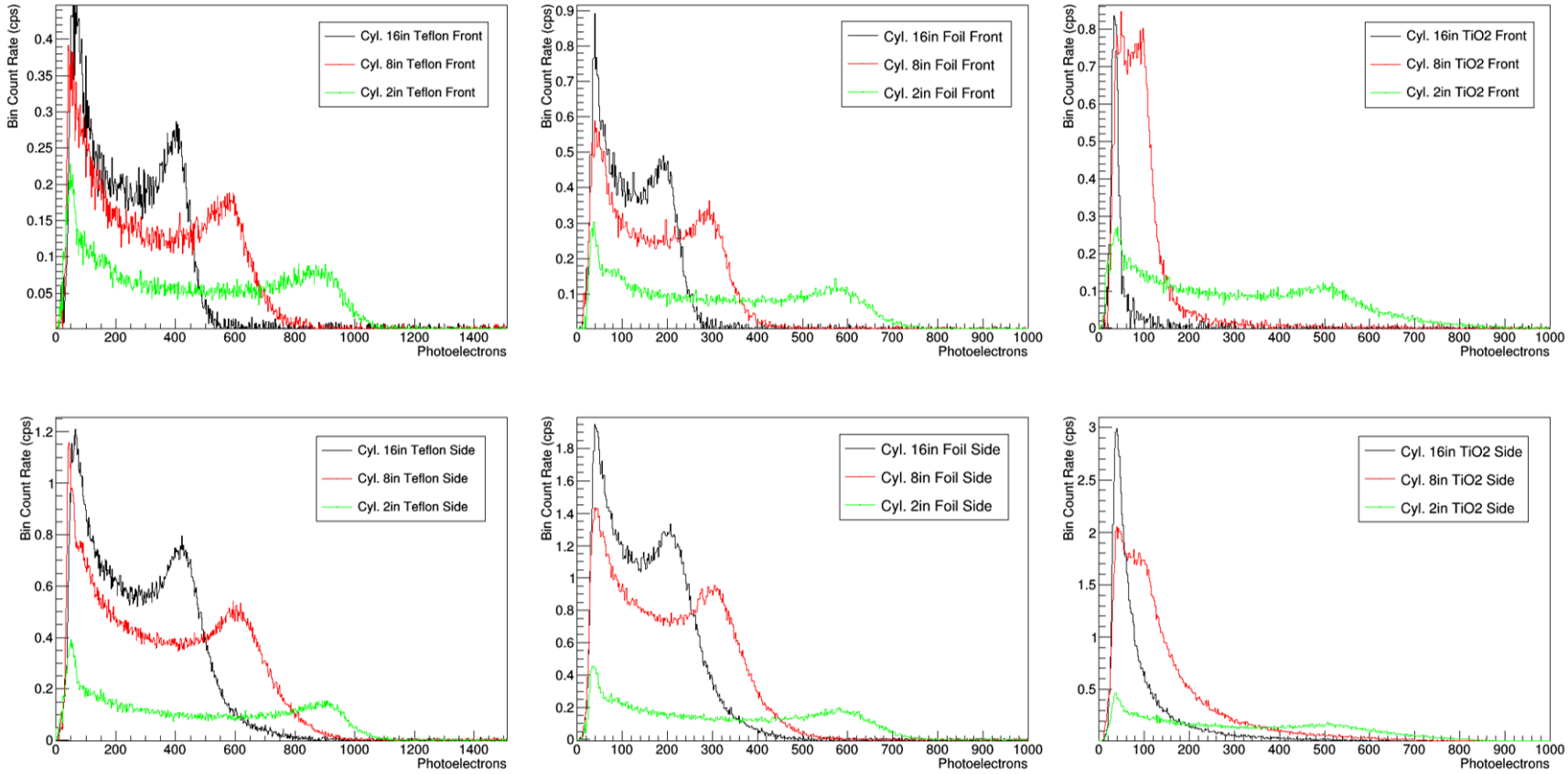


Figure B.1: Aggregation of experimental Cs-137 spectra taken with cylindrical EJ200 and varied optical reflectors. The sample was coupled to a calibrated PMT. Teflon is used in the left column, foil in the center column, and TiO_2 in the right column. Spectra in the top row are from front irradiation; the bottom row represents side irradiation.

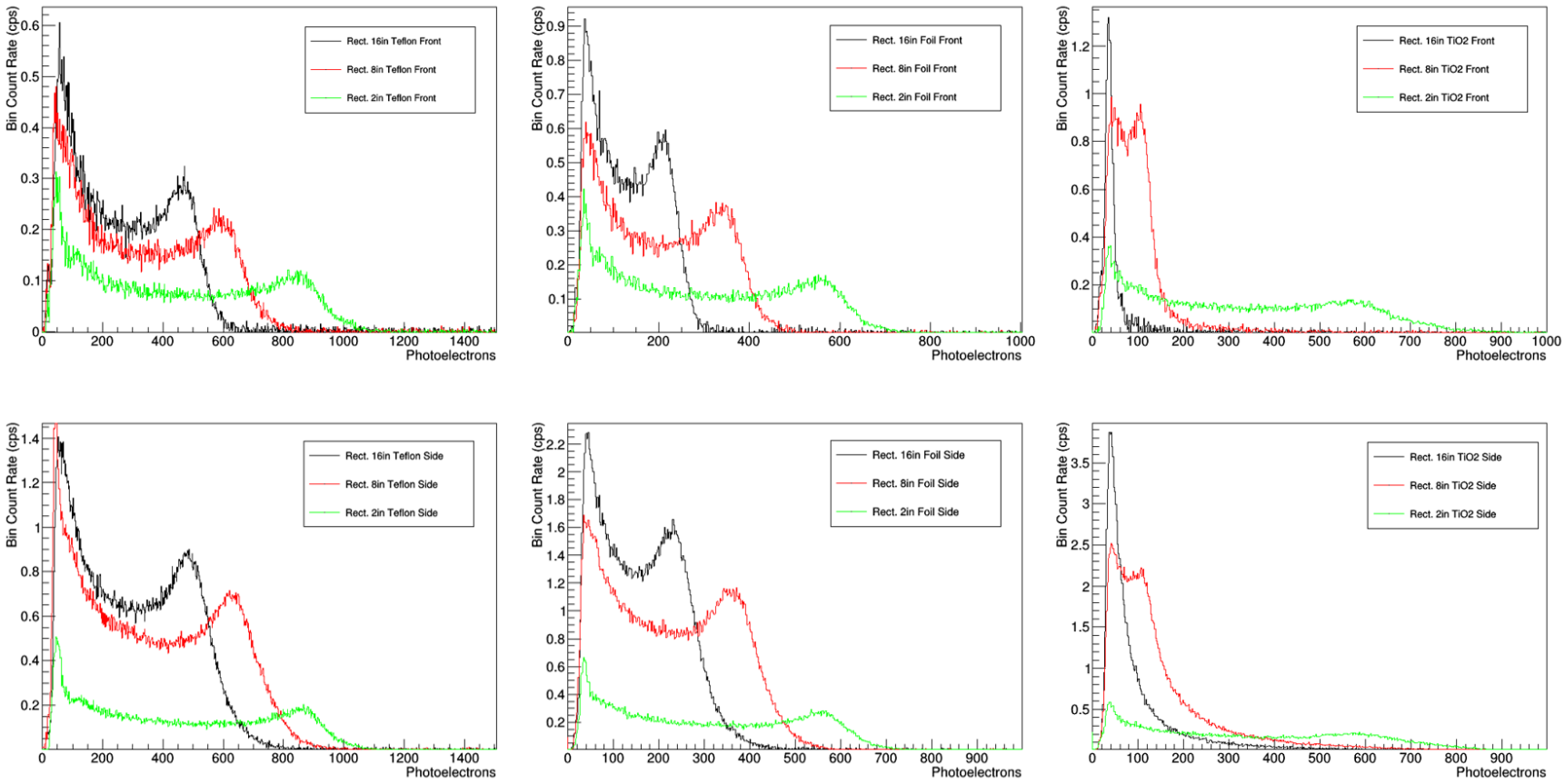


Figure B.2: Aggregation of experimental Cs-137 spectra taken with rectangular EJ200 and varied optical reflectors. The sample was coupled to a calibrated PMT. Teflon is used in the left column, foil in the center column, and TiO_2 in the right column. Spectra in the top row are from front irradiation; the bottom row represents side irradiation.

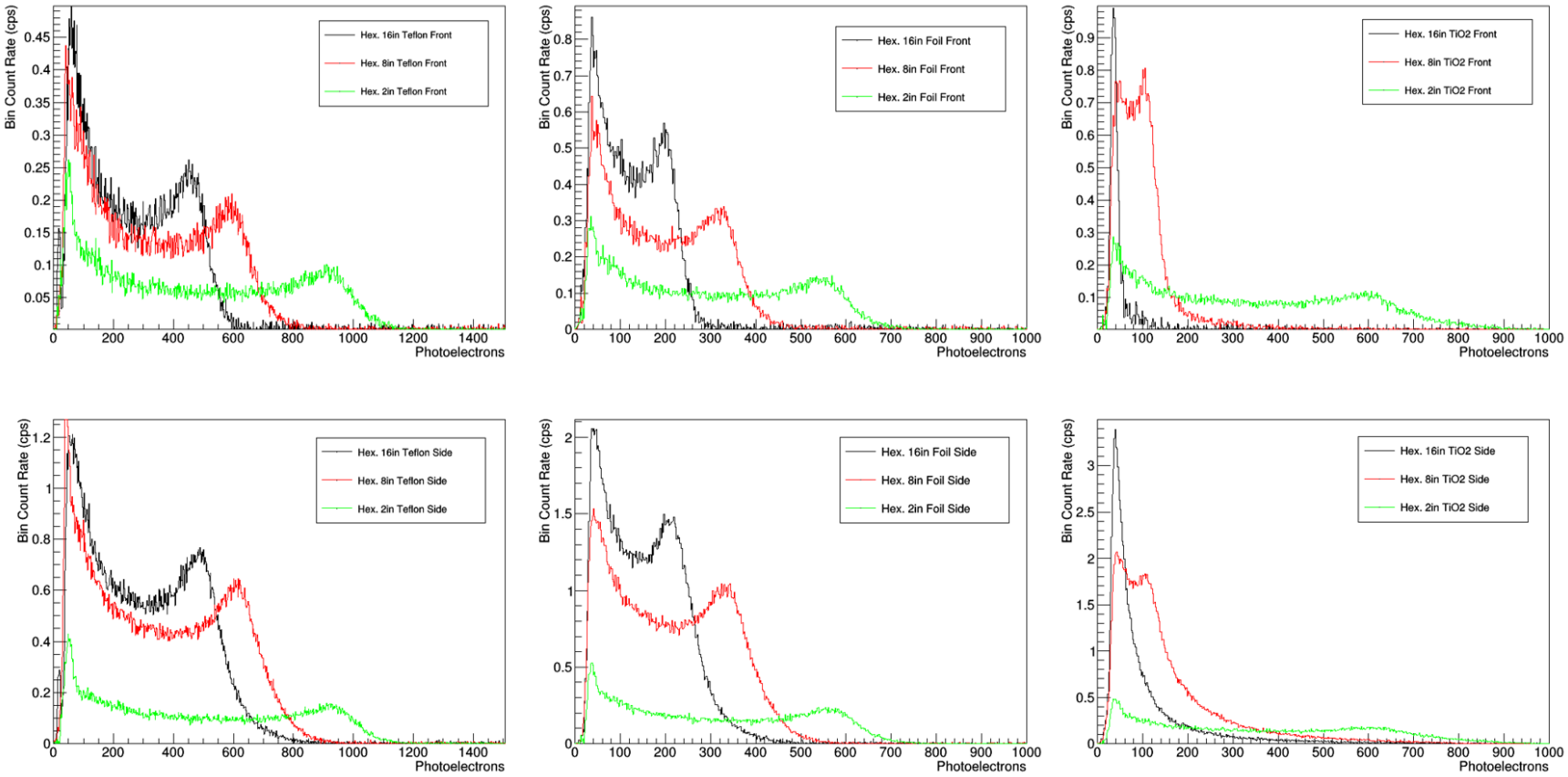


Figure B.3: Aggregation of experimental Cs-137 spectra taken with hexagonal EJ200 and varied optical reflectors. The sample was coupled to a calibrated PMT. Teflon is used in the left column, foil in the center column, and TiO_2 in the right column. Spectra in the top row are from front irradiation; the bottom row represents side irradiation.

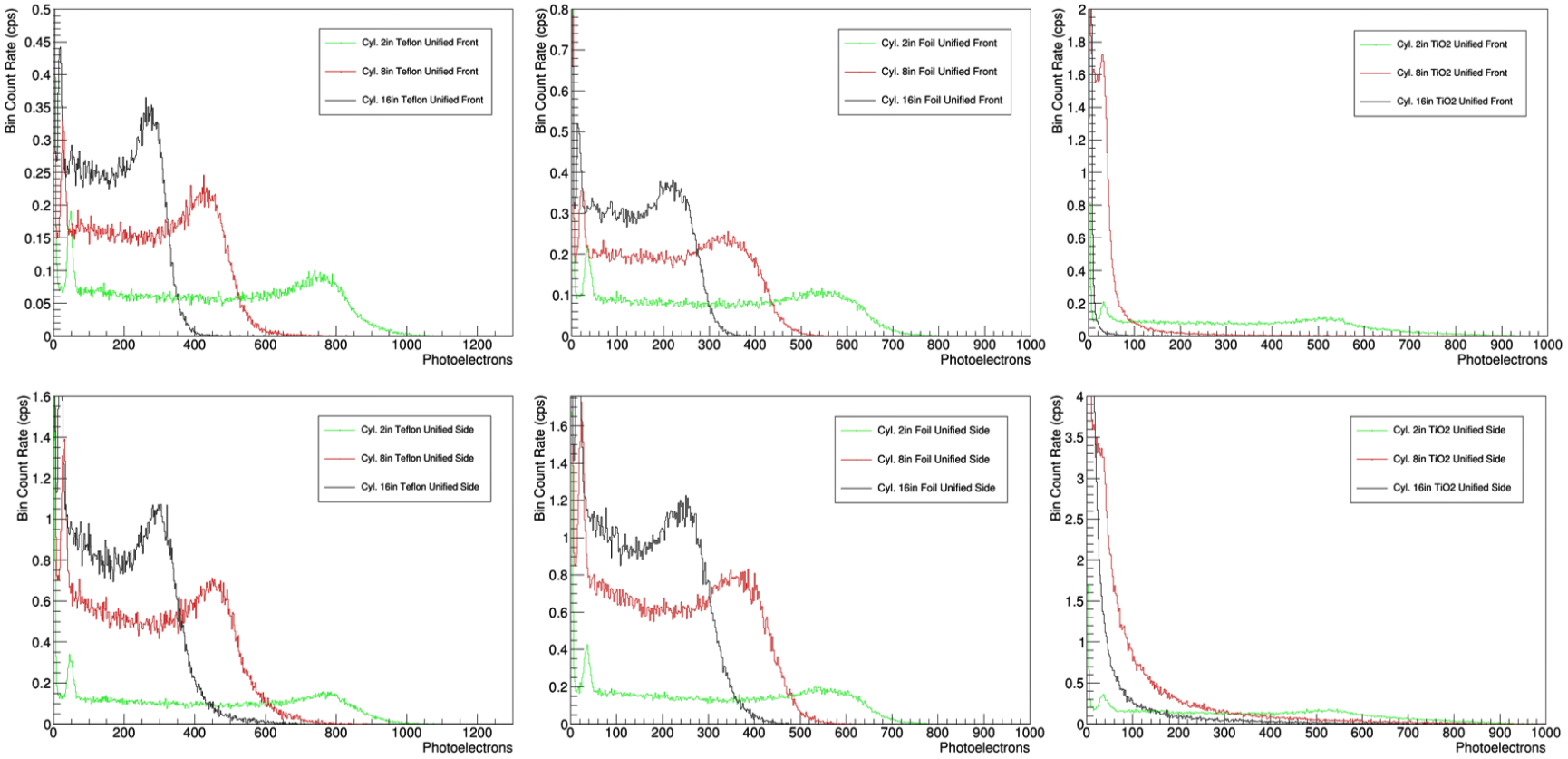


Figure B.4: Aggregation of simulated Cs-137 spectra taken with cylindrical EJ200 and varied optical reflectors using the *unified* surface model. Teflon is used in the left column, foil in the center column, and TiO_2 in the right column. Spectra in the top row are from front irradiation; the bottom row represents side irradiation.

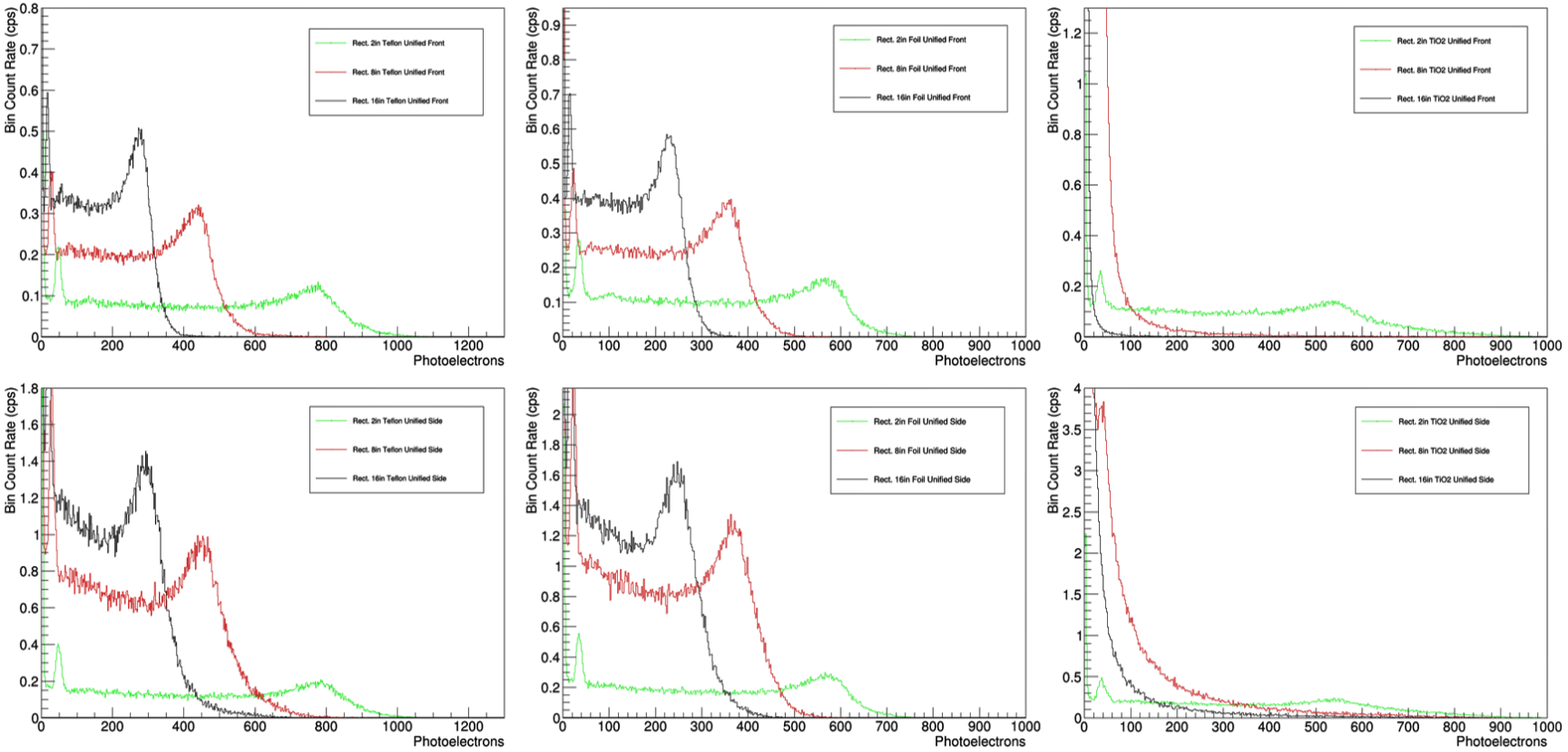


Figure B.5: Aggregation of simulated Cs-137 spectra taken with rectangular EJ200 and varied optical reflectors using the *unified* surface model. Teflon is used in the left column, foil in the center column, and TiO_2 in the right column. Spectra in the top row are from front irradiation; the bottom row represents side irradiation.

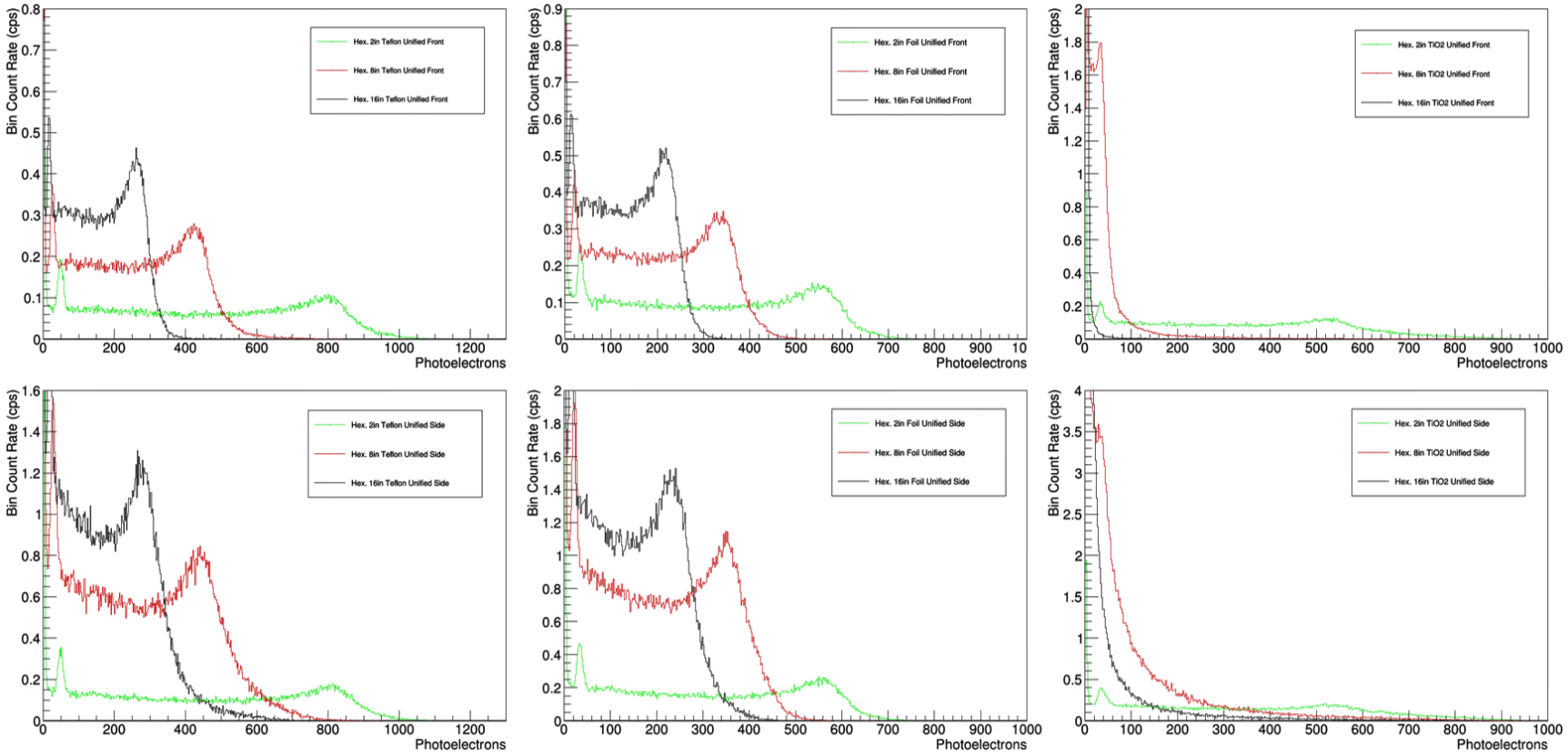


Figure B.6: Aggregation of simulated Cs-137 spectra taken with hexagonal EJ200 and varied optical reflectors using the *unified* surface model. Teflon is used in the left column, foil in the center column, and TiO_2 in the right column. Spectra in the top row are from front irradiation; the bottom row represents side irradiation.

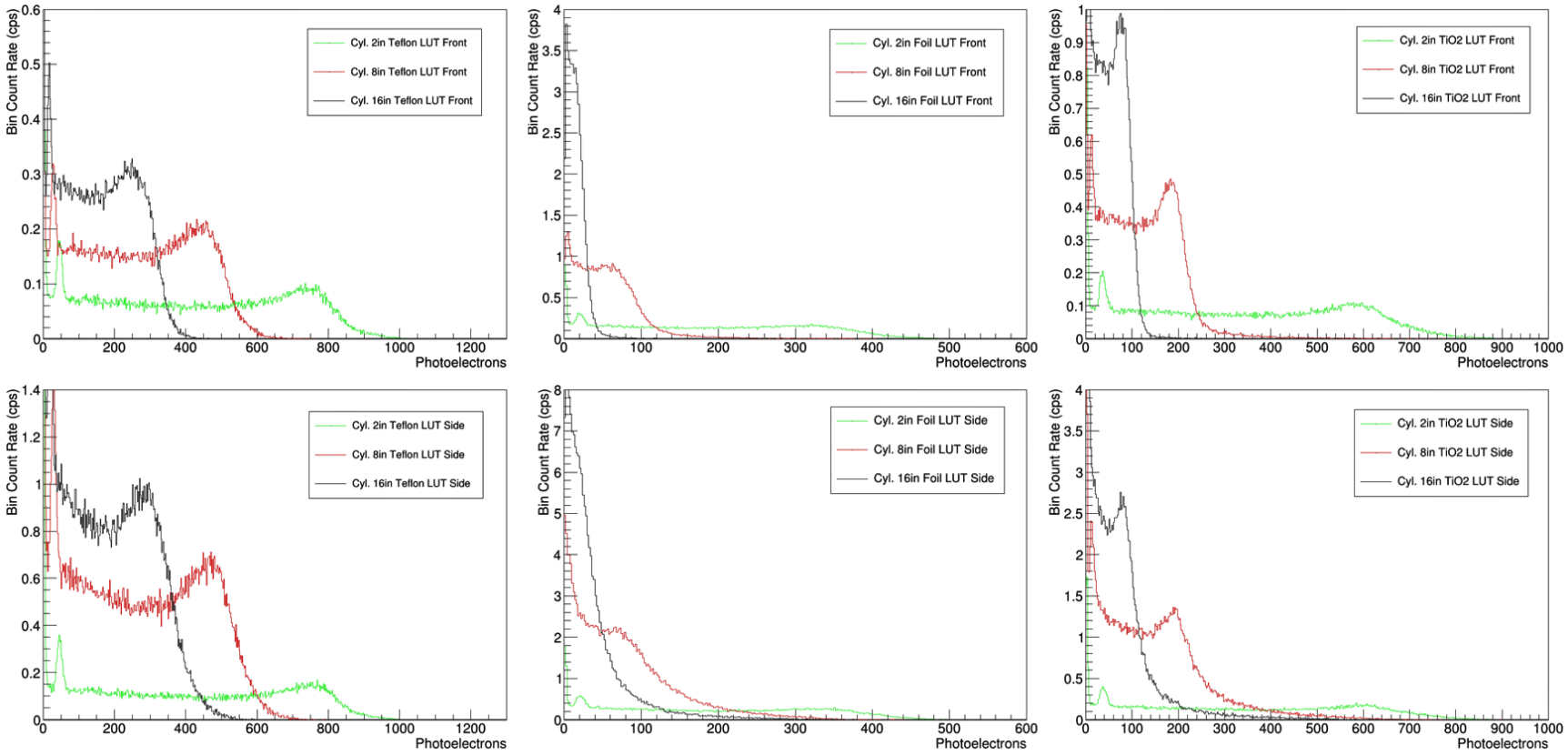


Figure B.7: Aggregation of simulated Cs-137 spectra taken with cylindrical EJ200 and varied optical reflectors using the LUT-LBNL surface model. Teflon is used in the left column, foil in the center column, and TiO_2 in the right column. Spectra in the top row are from front irradiation; the bottom row represents side irradiation.

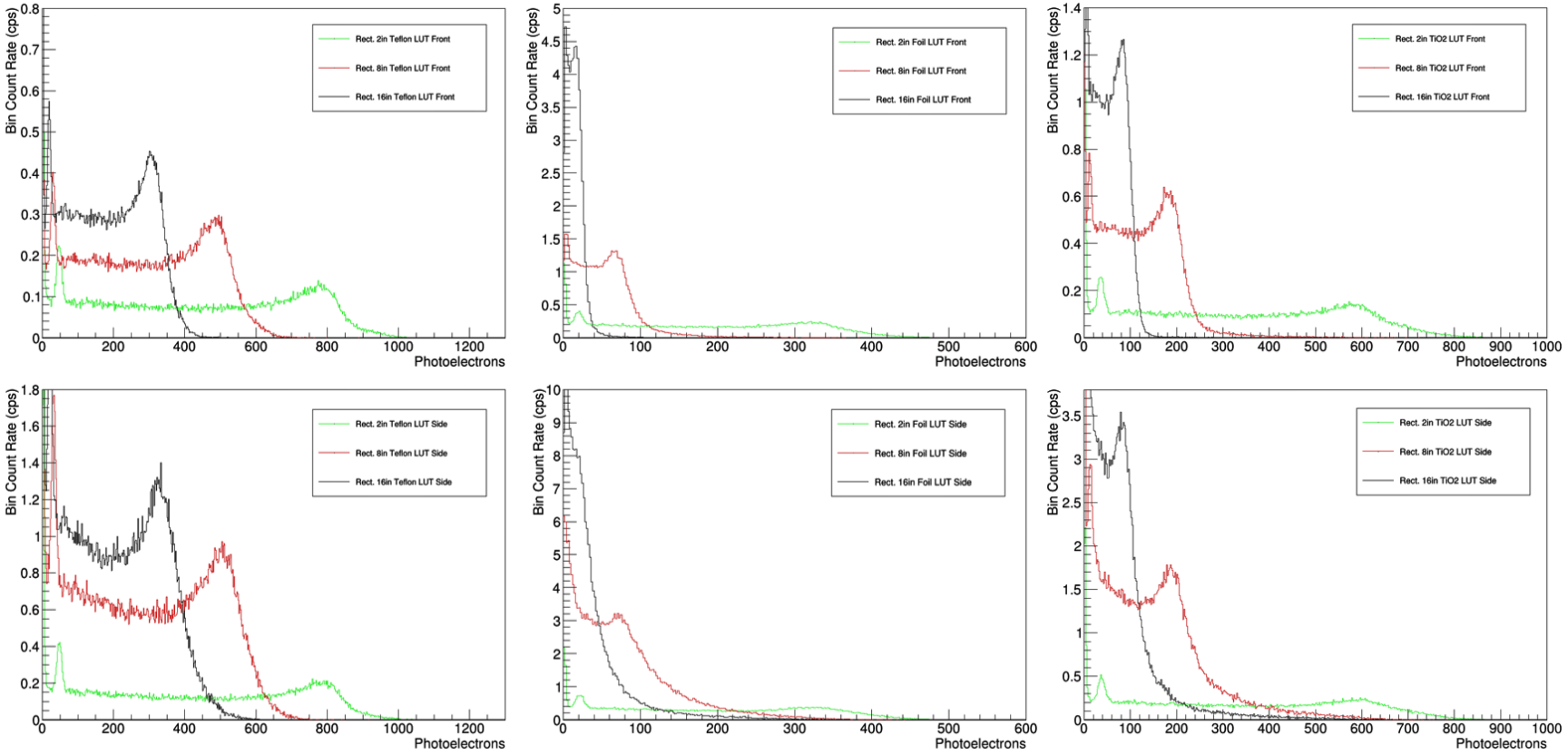


Figure B.8: Aggregation of simulated Cs-137 spectra taken with rectangular EJ200 and varied optical reflectors using the LUT-LBNL surface model. Teflon is used in the left column, foil in the center column, and TiO_2 in the right column. Spectra in the top row are from front irradiation; the bottom row represents side irradiation.

C Cramer Rao Lower Bound on the Timing Resolution of EJ232Q

The content in this appendix outlines work which was done to calculate the Cramer Rao Lower Bound (CRLB) on the timing resolution of EJ232Q with 0.5% benzophenone; a light quenching molecule which increases the time response of the material. This work has been placed in the appendix due to this topic lying somewhat outside of the scope of the dissertation. The relevance to the dissertation is that this exercise represents one of the first major banks of simulations performed using the Geant4 simulation space devised for the study of the high-Z loaded samples and was performed in the Fall of 2019. It was seen as an opportunity to: 1) compare the CRLB results with real data taken experimentally by one of the research scientists in our group, Xianfei Wen, see [127], and 2) as a chance to apply more rigorous data analysis and statistical techniques than has been needed for completion of the research contained in the body of the dissertation.

C.1 Introduction

Many fields utilize radiation detector systems to retrieve time-domain information from energetic particles of interest. Depending on the configuration, time-domain information may allow for time of flight (TOF) neutron spectroscopy, source imaging, application of Compton rejection or coincidence methods, TOF mode positron emission tomography (PET), and neutron coincidence counting (among others). Fields of application range from high energy physics and space applications to defense and medical. Of particular interest in the medical field is to develop a complete detector with a timing resolution of 10 ps, full width at half maximum (FWHM), or less [128]. In the TOF-PET application, this would result in an on-axis position resolution of approximately half a centimeter.

One particular method of evaluating the timing resolution potential of a material + photosensor system is to calculate the CRLB, often simply referred to as the lower bound, on the timing resolution [129–131]. For the sake of definition, the CRLB is simply the lower bound of the variance of an unbiased estimator used to estimate a given parameter belonging

to a defined statistical model. In the case of TOF-PET, one wishes to estimate either the interaction time of the gamma in the crystal [129] or the annihilation time of the positron, t_{annih}, [130]. There is a distinct difference between the lower bound in the variance computed with these two approaches which most readily manifests itself when using high aspect ratio crystals with the positron source on the long axis of the crystal. This results in an additional time-spreading mechanism related to the depth of interaction of the gamma in the crystal. This work focuses on scintillators over a range of aspect ratios, 1:2 to 1:20, so the estimator of interest will be for the positron annihilation time.

The general approach, which is fully outlined in [130] and references therein, is to start with the notion of a photodetector from which the arrival times of the photons generated in a scintillation event, i, are registered and then sorted into an ordered set of photon arrival times:

$$\mathbf{t} = \{t_{i,1}, t_{i,2}, t_{i,3}, \ldots, t_{i,n}\} \tag{C.1}$$

Then the annihilation time, t_{annih}, may be related to $\mathbf{t}$ and the two parameters μ, and $\mathbf{\Sigma}$ by

$$P\left(\mathbf{t} \mid t_{annih}\right) = \frac{1}{\sqrt{(2\pi)^n \left|\mathbf{\Sigma}\right|}} \exp\left[-\frac{1}{2}\left(\mathbf{t} - \mu - t_{annih}\right)^{\mathrm{T}} \mathbf{\Sigma^{-1}} \left(\mathbf{t} - \mu - t_{annih}\right)\right] \tag{C.2}$$

where $P\left(\mathbf{t} \mid t_{annih}\right)$ is the probability of observing the outcome $\mathbf{t}$ given an annihilation time of t_{annih}, μ is the expected set of the ordered photon arrival times, and $\mathbf{\Sigma}$ is the covariance matrix of the ordered sets of photon arrival times. In order to calculate the CRLB, all that is really needed is this covariance matrix which must be inverted and the elements summed in order to calculate the Fisher information as shown below:

$$I\left(t_{annih}\right) = -\mathrm{E}\left[\frac{\partial^2}{\partial t_{annih}^2} \ln P\left(\mathbf{t} \mid t_{annih}\right)\right] = \mathbf{1}^{\mathrm{T}} \mathbf{\Sigma^{-1}} \mathbf{1} = \sum_{i=1}^{n} \sum_{j=1}^{n} \left(\mathbf{\Sigma^{-1}}\right)_{i,j} \tag{C.3}$$

In the equation above, E, is an operator yielding the expected value of the quantity inside the brackets, $\mathbf{1}$ is an n dimensional vector of ones, and $\left(\mathbf{\Sigma^{-1}}\right)_{i,j}$ is the i,j^{th} element of the

inverted covariance matrix. Once the Fisher information has been obtained, the CRLB is defined as

$$\sigma_{lb}^2 = \frac{1}{I\left(t_{annih}\right)} \tag{C.4}$$

C.2 Methodology

This work aims to calculate the CRLB for EJ232Q with 0.5% benzophenone in rectangular prism shapes with a base size of 5x5 mm in lengths of 10, 25, 50, 75, and 100 mm. The CRLB was calculated for these in both front and side irradiation modalities. Geant4 was used to simulate a 511 keV gamma source which then interacted in the scintillator volume creating optical photons which were transported throughout the scintillator. Some of the photons made it to the photocathode where they may have been detected. The simulated scintillator/photodetector system was similar to the one shown in Figure 3.14 with the differences being that the window was 1 mm thick and the window material was borosilicate. The material definition for the EJ232Q sample contained hydrogen in a 1:6 ratio with carbon at a density of 1.023 g/cc. A constant refractive index of 1.58 was used as was a constant optical absorption length of 10 cm. The optical photon source term had a scintillation light yield of 2.9 photons/keV which produced photons of a wavelength according to the luminescence spectrum provided by Eljen. The scintillation rise time was set to 110 ps and the fall time was 700 ps. The RESOLUTIONSCALE parameter was chosen so that the shape of the Compton continuum best matched the real data, as shown in Figure . This value of the RESOLUTIONSCALE was 2.976. The optical surfaces between the scintillator and air were selected from the LUT-LBNL model. The surfaces on the sides of the scintillator used the polishedvm2000air reflector with reflectivity set to 0.98 and the surface on the front-facing end of the scintillator used the polishedteflonair LUT with unity reflectivity. All other optical surfaces utilized the *unified* model with dielectric_dielectric types and polished finish.

Once an optical photon reached the surface of the photocathode in the simulation, the phase space information of the photon was recorded (energy, position, time, direction), and the photon was killed. As such, reflection off of the photocathode was not accounted for but is believed to only be a small contribution to the total signal since the base of the scintillator

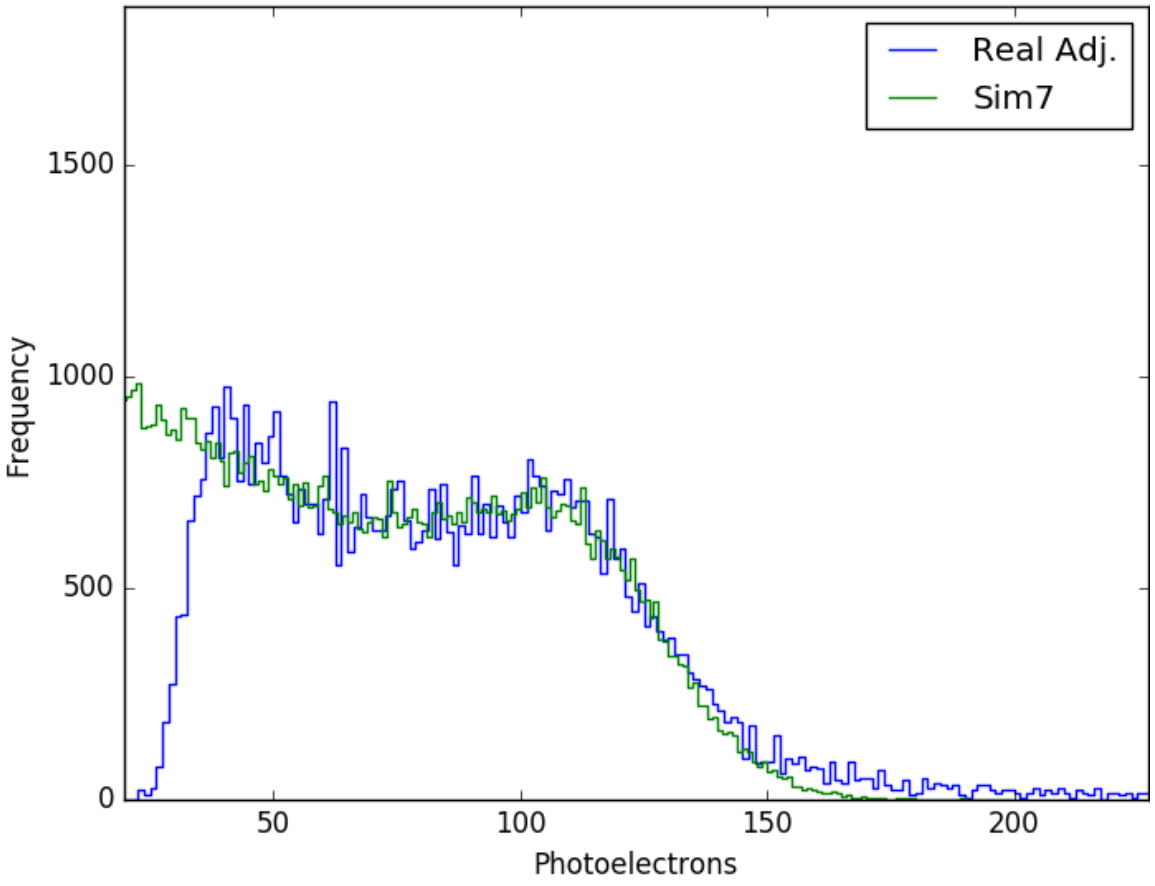


Figure C.1: Comparison of measured and simulated 511 keV gamma spectrum taken with 5x5x10 mm EJ232Q under front irradiation. RESOLUTIONSCALE was iterated over many times to arrive at the best-fit value of 2.976, shown here.

is quite small. This means a photon reflected off of the photocathode would not have been very likely to find its way back into the scintillator, and even if it did, the short absorption length in the scintillator would have likely resulted in bulk optical absorption of the photon as opposed to a reintroduction to the photocathode. The phase space information was used in post processing to: 1) calculate the CRLB and 2) to emulate a PMT pulse by convolving a model of the time-impulse response of PMT with the frequency distribution of the photon arrival times.

The first step to accomplishing both of these goals was to determine the photon arrival times. This was accomplished by looping over the recorded photons, taking a sample from a uniform distribution, and if the random sample was less than or equal to the external quantum efficiency of the PMT (400K spectral response from Hamamatsu) for the photon's wavelength, then the photon was kept, otherwise the photon was removed from the analysis. At this point, the times belonging to the remaining photons may be thought of as photoelectron generation times (referring to photoelectrons generated on the PMT photocathode). The next step took the PMT transit time spread (TTS) into consideration. This was done by taking the 'time' associated with the remaining photons and taking a sample from a Gaussian with a mean of that time and standard deviation equal to the TTS divided by 2.355 since the TTS is reported in FWHM. The TTS of the Hamamatsu H6533 PMT is 160 ps. This newly sampled photon arrival time was stored in a vector with all the other re-sampled arrival times corresponding to a single scintillation event and was then sorted (least to greatest) to form the ordered set of photon arrival times. The length of this vector was 50 for the 10, 25, and 50 mm samples, 35 for the 75 mm sample, and 26 for the 100 mm sample because of the limitations on this number set by the energy window which was used to remove events from which not much light was received.

To compute the CRLB, each of the arrival time vectors were stored in a matrix as a row, meaning each column of the matrix represented a variable (the i^{th} photon arrival time) and each row was an observation. The covariance matrix (CM) was computed using the Numpy module distributed with Python 2.7 as CM = numpy.cov(DataMatrix, rowvar=False). This CM was inverted and the sum of all the inverted matrix elements was found, yielding the Fisher information. The CRLB was computed according to Equation C.4. The reported

CRLB is given in FWHM. Furthermore, the effect on the CRLB by incrementally including the information from 1 to n photons was also examined and is shown in the results.

The second focus of this study was to emulate a PMT response in order to generate simulated time pick off data by using a constant fraction discriminator (CFD) on the emulated PMT signal and compare the FWHM of the pick off time frequency distribution to the CRLB. This was accomplished using a simple model of the PMT time impulse response shown below:

$$R(t) = \begin{cases} \exp\left(-\frac{t}{\tau_f}\right) - \exp\left(-\frac{t}{\tau_r}\right), & t \geq 0 \\ 0, & t < 0 \end{cases} \tag{C.5}$$

where τ_r is the PMT rise time which was set to 700 ps while τ_f is the PMT fall time and was set to 3X the rise time, 2.1 ns. This impulse response was convolved with the frequency distribution of the modified photon arrival times and multiplied by 1.05 in order to produce a signal of comparable height (in mV) to the PMT signal. This was verified by comparing the experimental pulse height spectrum to the emulated pulse height spectrum (literally found by histogramming the maximum of the pulses). Additionally, Gaussian noise, with a standard deviation of 0.358 mV, was added to the signal. The results from the noisy and clean signals are compared. An example of the emulated PMT signal, with and without noise, is shown in Figure C.2, while the comparison of the experimental and emulated pulse height spectra are shown in Figure C.3. A check to verify whether or not this scales with the varied lengths was not performed. However, it is not believed that this would greatly affect the performance of the CFD given that the purpose of the CFD is to consistently produce a pick off time which is invariant to the pulse height.

While only used in the setup of the simulations to verify some parameters, it is still important to note the methods by which the experimental data were taken. These methods are described for the single PMT readout setup found in [127]. The data used for comparison here are one and the same as those taken for the analysis in the aforementioned reference.

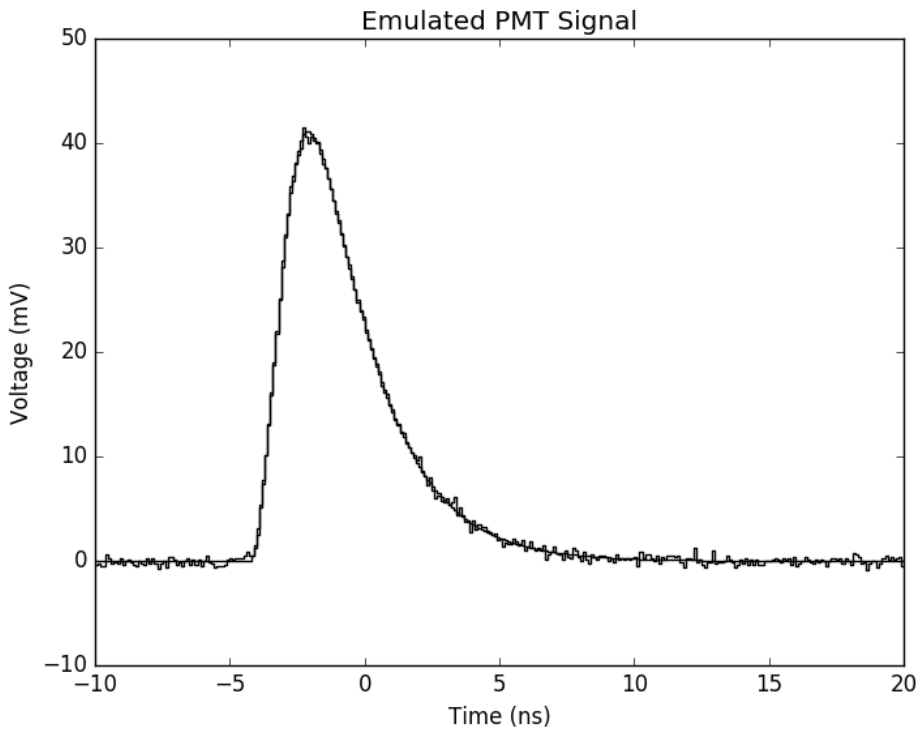


Figure C.2: The emulated PMT pulse with and without Gaussian noise.

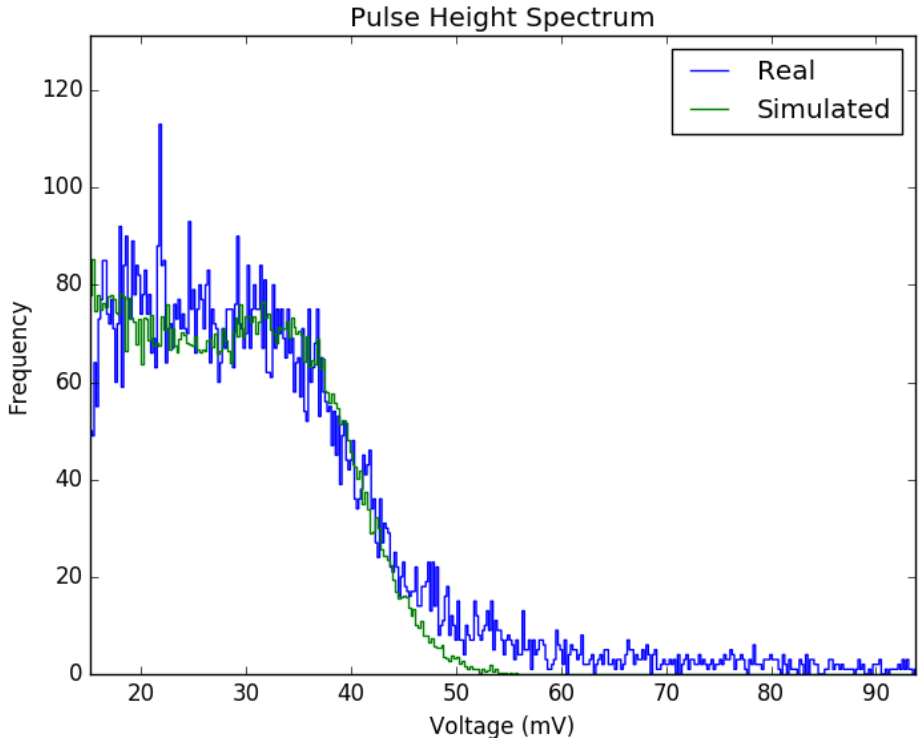


Figure C.3: Comparison of the experimental and emulated PMT pulse height spectrum. Spectra are for the 10 mm sample under front irradiation with a 511 keV gamma source.

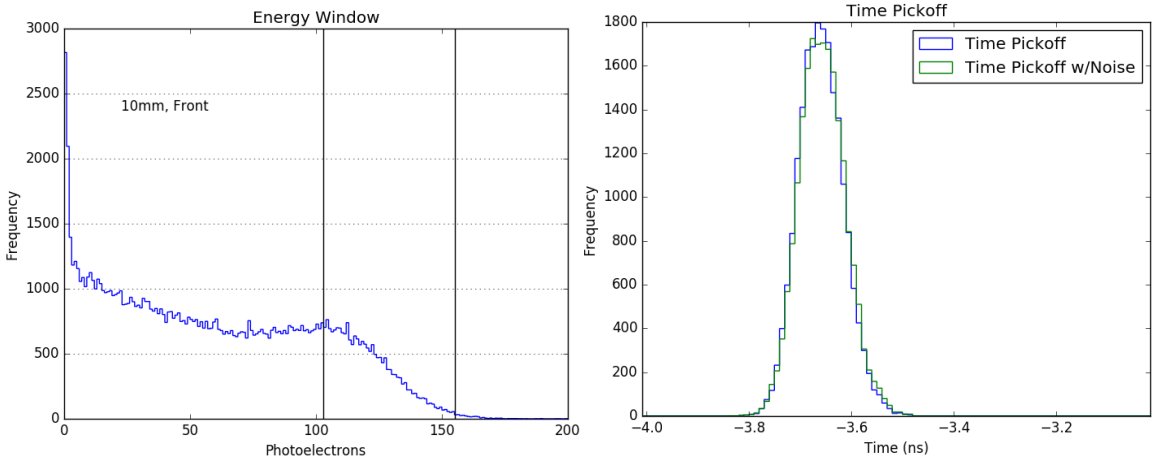
C.3 Results

The following Figures, C.4 - C.39, contain results showing the selected energy window, the time pick off frequency distributions, the Gaussian fits of those distributions, the frequency distributions of a subset of the ordered photon arrival times, the intensity map of the covariance matrix of the ordered photon arrival times, and the CRLB with respect to the number of first i photons. These are all shown for each scintillator length and each mode of irradiation (front, side). The 'punchline' results are shown in the final two Figures: C.44 and C.45. These highlight the calculated CRLB vs. lengths and the comparison to the FWHM of the frequency distribution of the pick off times using the emulated PMT pulse with a CFD fraction of 0.3.

C.4 Discussion

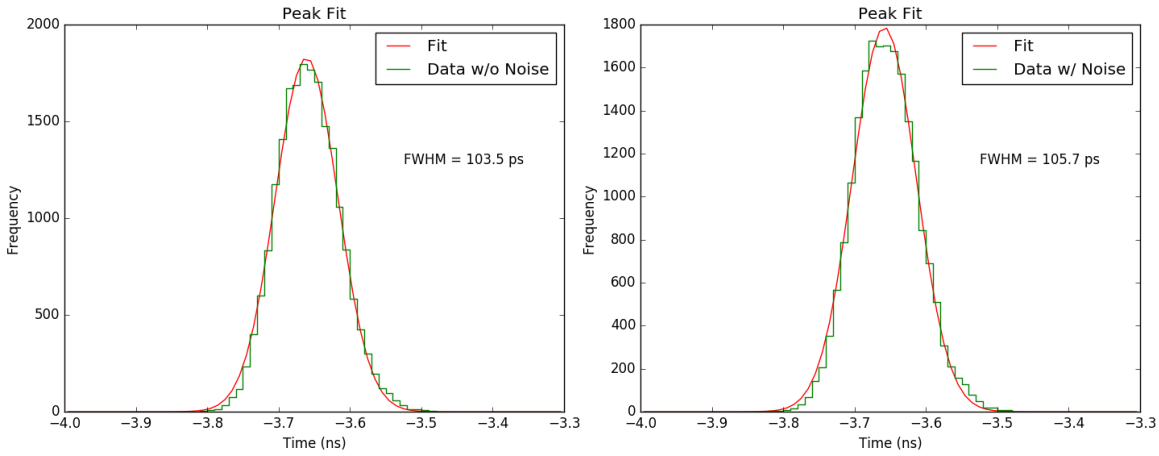
The aim of this discussion is to highlight the observed trends in the presented data with respect to the scintillator length and, if necessary, the mode of irradiation. Discussion of the trend in the final CRLB value and the FWHM of the time pick off frequency distributions will be relegated to the end since those data are presented in the last set of figures.

The first observation is the need for the position of the energy window encompassing the events used to calculated the CRLB to consistently decrease with length due to the change in the Compton edge location. For the 75 and 100 mm lengths, the lower bound of this window fell below the 50 photoelectron generation times (photon arrival times) which were used to calculate the CRLB for the 10, 25, and 50 mm samples. As a result, the upper limit on the fraction of the registration times used to calculate the CRLB relative to the total number of registration times in the pulse increases from approximately 48% in the 10 mm case to 100% in the 75 and 100 mm case. This change in the window position was necessitated, and ultimately caused by, the low simulated light output. This is in part due to the inherently low light yield of the scintillator and in part due to the short optical absorption length of 10 cm, leading to ever increasing bulk optical absorption with increasing scintillator sizes. The effect this low level of photon statistics has on the all other derivative data is quite evident due to the observed emerging shift in the features of the various distributions with



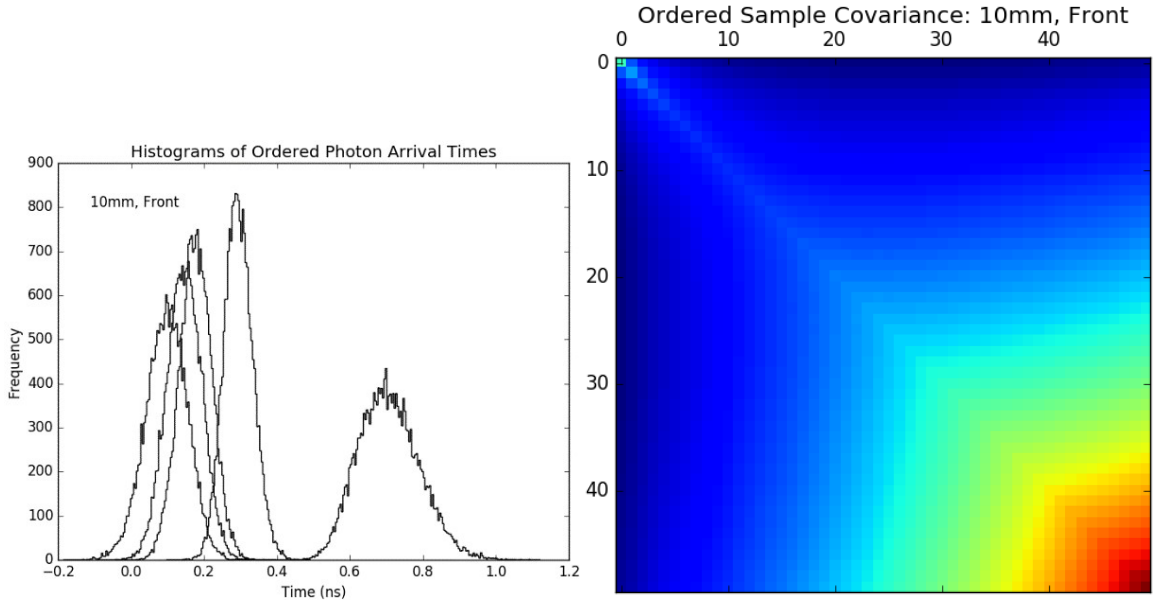
(a) **(b)**

Figure C.4: Data is for the 10mm sample under front irradiation. **(a)** The energy window for events contributing to the CRLB calculation and emulated PMT pulses. **(b)** The frequency distributions of the pick off time using the emulated PMT signal both with and without noise applied to the pulse.



(a) **(b)**

Figure C.5: Fit and FWHM of the time pick off distributions using the emulated PMT pulse both without noise **(a)** and with noise **(b)** added to the signal. Data is shown for the 10mm sample under front irradiation.



(a) **(b)**

Figure C.6: The data is for the 10mm sample under front irradiation. **(a)** Shown are the arrival time distributions for the 1^{st}, 2^{nd}, 3^{rd}, 10^{th}, and 50^{th} detected photons (left to right). **(b)** The intensity map of the covariance matrix for the ordered photon arrival times. The x and y axis values are the arrival time index: $i \exists [0, 50)$.

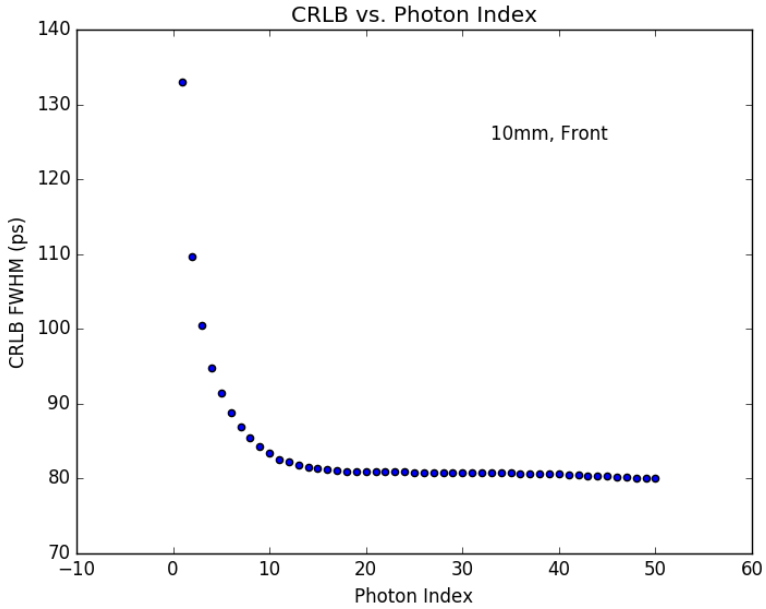
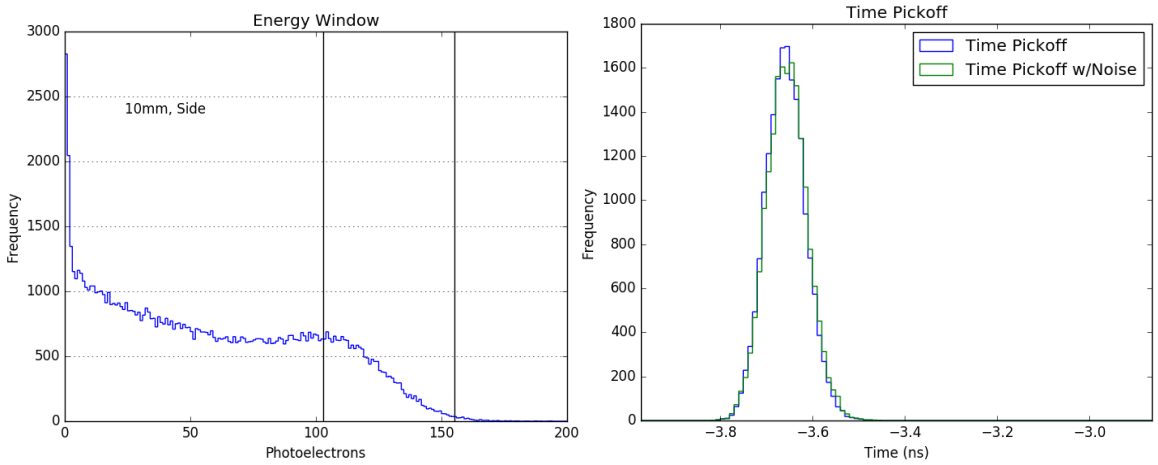
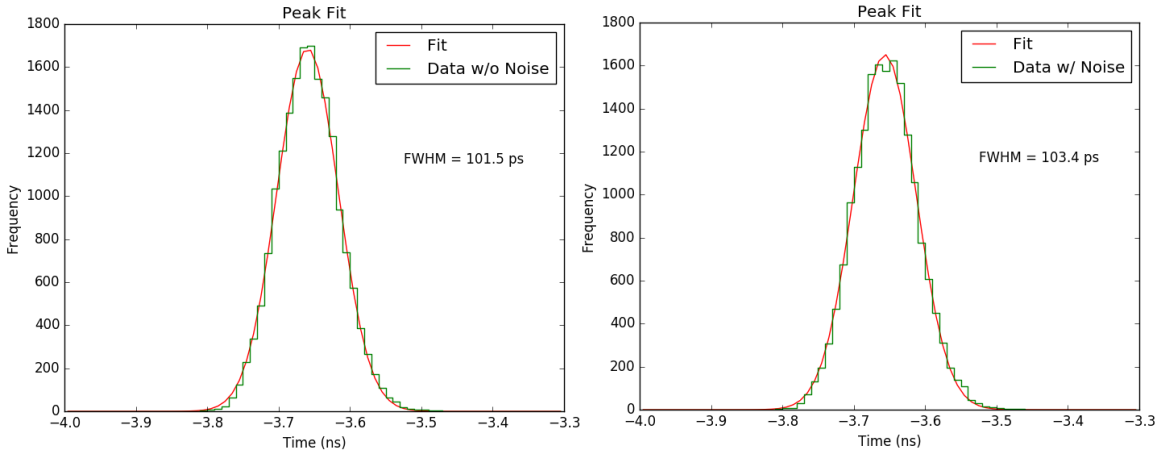


Figure C.7: The calculated CRLB vs. the number of first i arrival times used in its calculation. Data is for the 10mm sample under front irradiation.



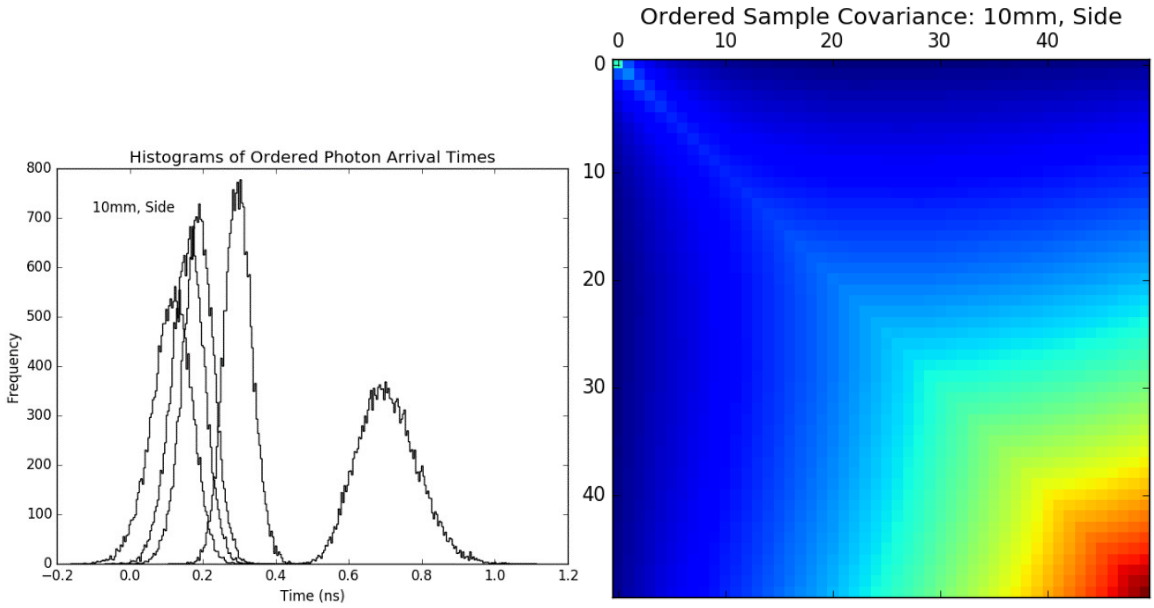
(a) **(b)**

Figure C.8: Data is for the 10mm sample under side irradiation. **(a)** The energy window for events contributing to the CRLB calculation and emulated PMT pulses. **(b)** The frequency distributions of the pick off time using the emulated PMT signal both with and without noise applied to the pulse.



(a) **(b)**

Figure C.9: Fit and FWHM of the time pick off distributions using the emulated PMT pulse both without noise **(a)** and with noise **(b)** added to the signal. Data is shown for the 10mm sample under side irradiation.



(a) **(b)**

Figure C.10: The data is for the 10mm sample under side irradiation. **(a)** Shown are the arrival time distributions for the 1^{st}, 2^{nd}, 3^{rd}, 10^{th}, and 50^{th} detected photons (left to right). **(b)** The intensity map of the covariance matrix for the ordered photon arrival times. The x and y axis values are the arrival time index: $i \exists [0, 50)$.

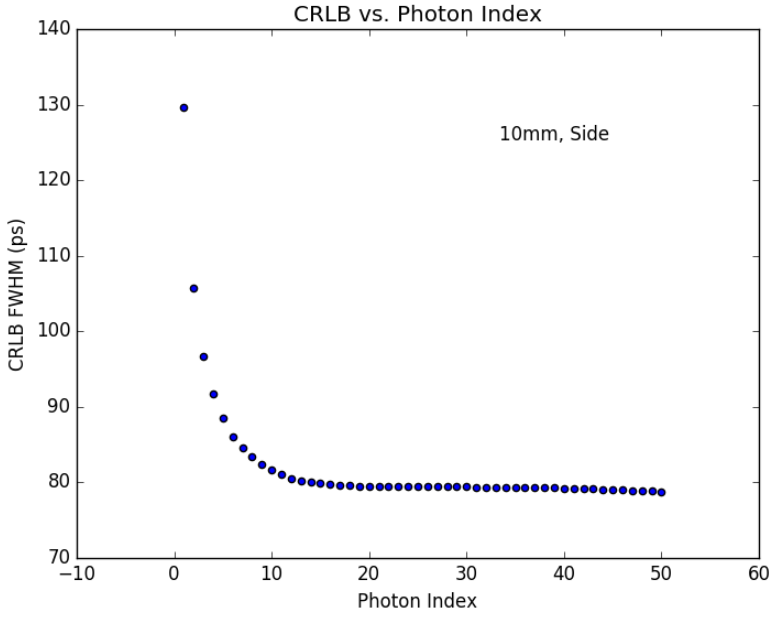
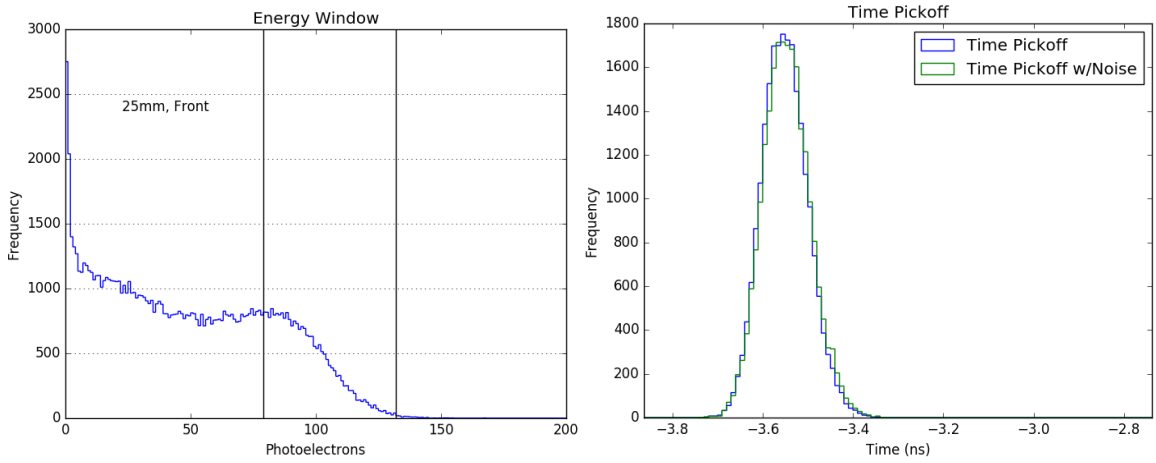
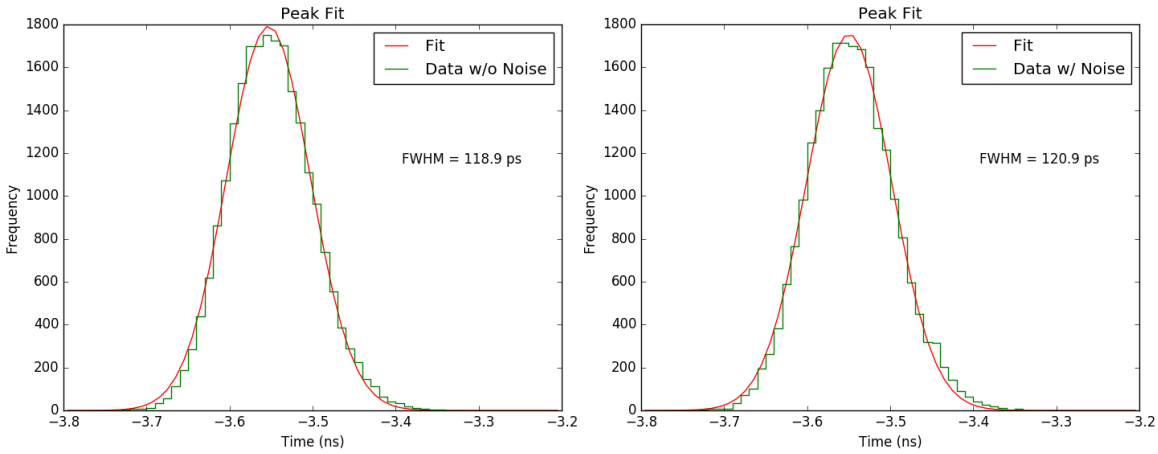


Figure C.11: The calculated CRLB vs. the number of first i arrival times used in its calculation. Data is for the 10mm sample under side irradiation.



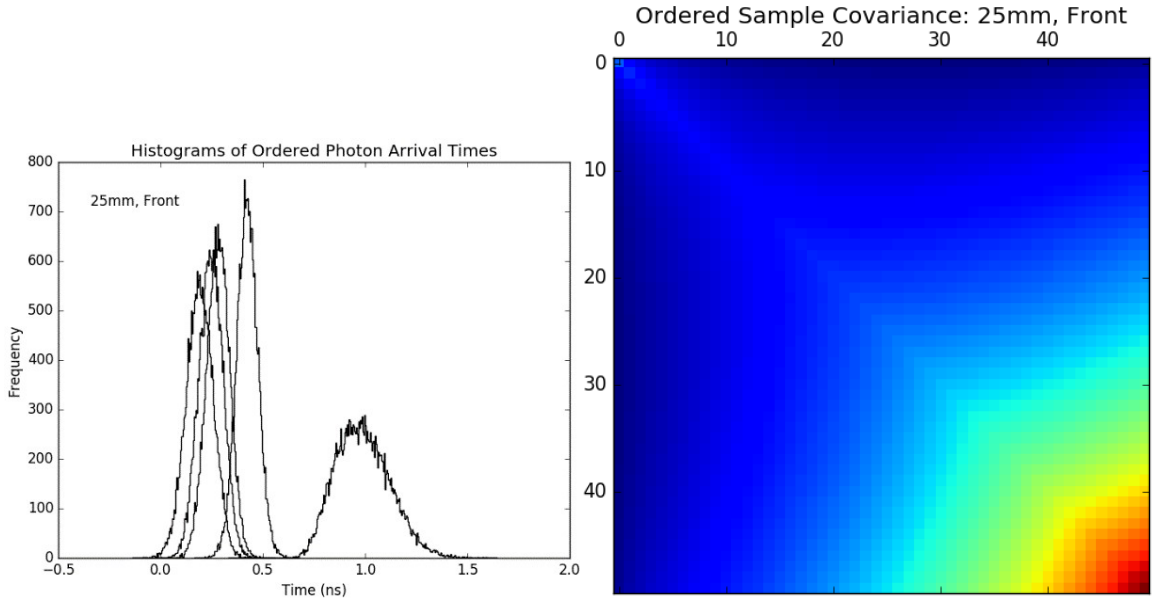
(a) **(b)**

Figure C.12: Data is for the 25mm sample under front irradiation. **(a)** The energy window for events contributing to the CRLB calculation and emulated PMT pulses. **(b)** The frequency distributions of the pick off time using the emulated PMT signal both with and without noise applied to the pulse.



(a) **(b)**

Figure C.13: Fit and FWHM of the time pick off distributions using the emulated PMT pulse both without noise **(a)** and with noise **(b)** added to the signal. Data is shown for the 25mm sample under front irradiation.



(a) **(b)**

Figure C.14: The data is for the 25mm sample under front irradiation. **(a)** Shown are the arrival time distributions for the 1^{st}, 2^{nd}, 3^{rd}, 10^{th}, and 50^{th} detected photons (left to right). **(b)** The intensity map of the covariance matrix for the ordered photon arrival times. The x and y axis values are the arrival time index: $i \exists [0, 50)$.

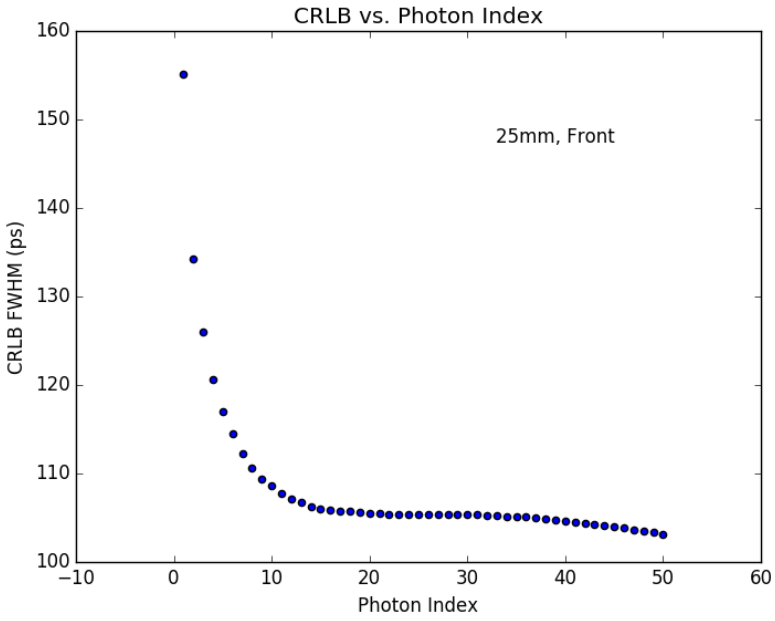
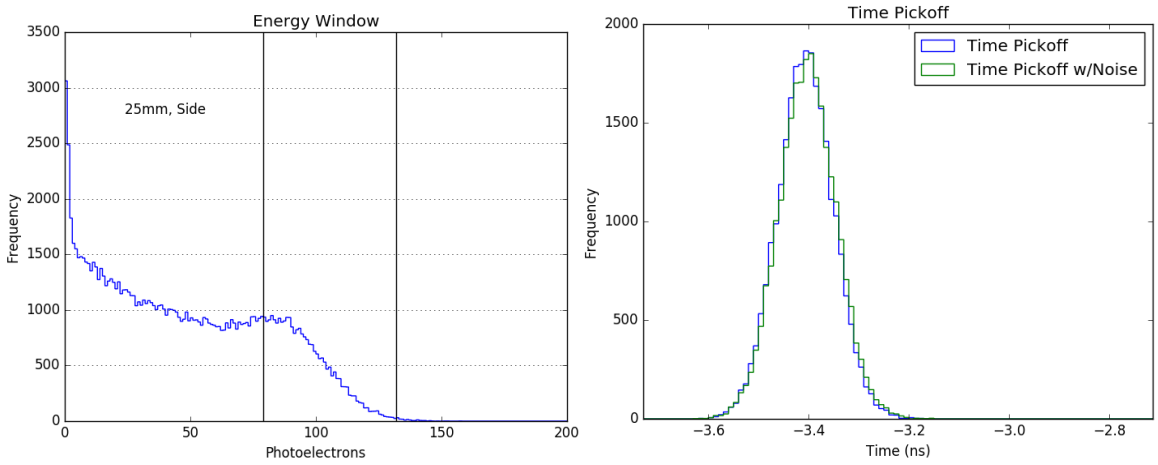
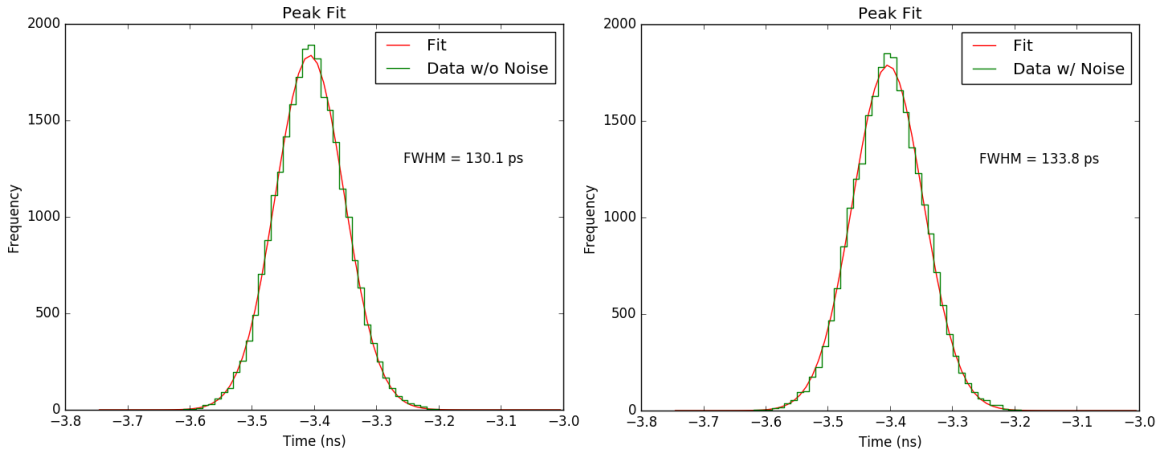


Figure C.15: The calculated CRLB vs. the number of first i arrival times used in its calculation. Data is for the 25mm sample under front irradiation.



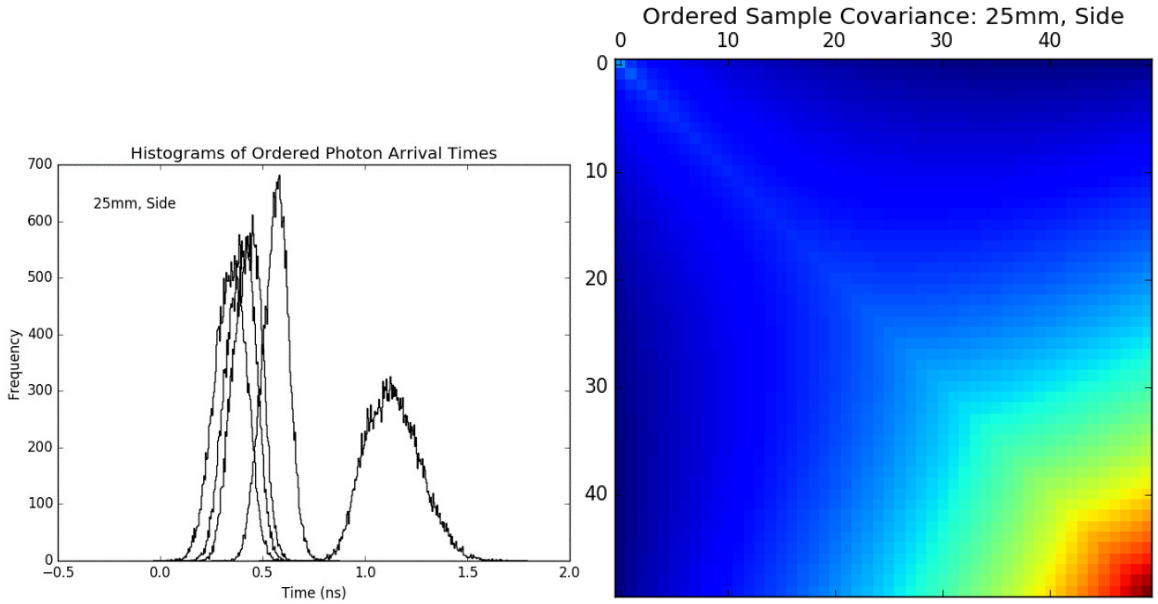
(a) **(b)**

Figure C.16: Data is for the 25mm sample under side irradiation. **(a)** The energy window for events contributing to the CRLB calculation and emulated PMT pulses. **(b)** The frequency distributions of the pick off time using the emulated PMT signal both with and without noise applied to the pulse.



(a) **(b)**

Figure C.17: Fit and FWHM of the time pick off distributions using the emulated PMT pulse both without noise **(a)** and with noise **(b)** added to the signal. Data is shown for the 25mm sample under side irradiation.



(a) **(b)**

Figure C.18: The data is for the 25mm sample under side irradiation. **(a)** Shown are the arrival time distributions for the 1^{st}, 2^{nd}, 3^{rd}, 10^{th}, and 50^{th} detected photons (left to right). **(b)** The intensity map of the covariance matrix for the ordered photon arrival times. The x and y axis values are the arrival time index: $i \exists [0, 50)$.

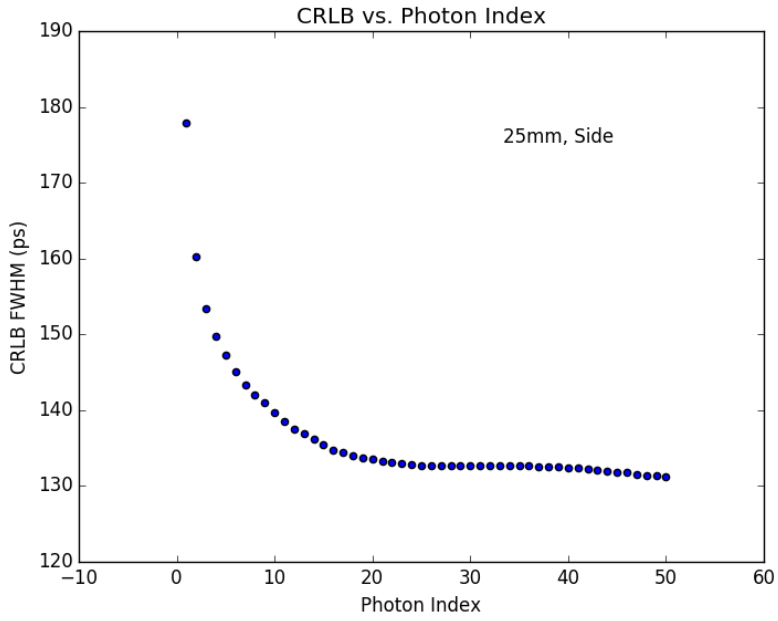
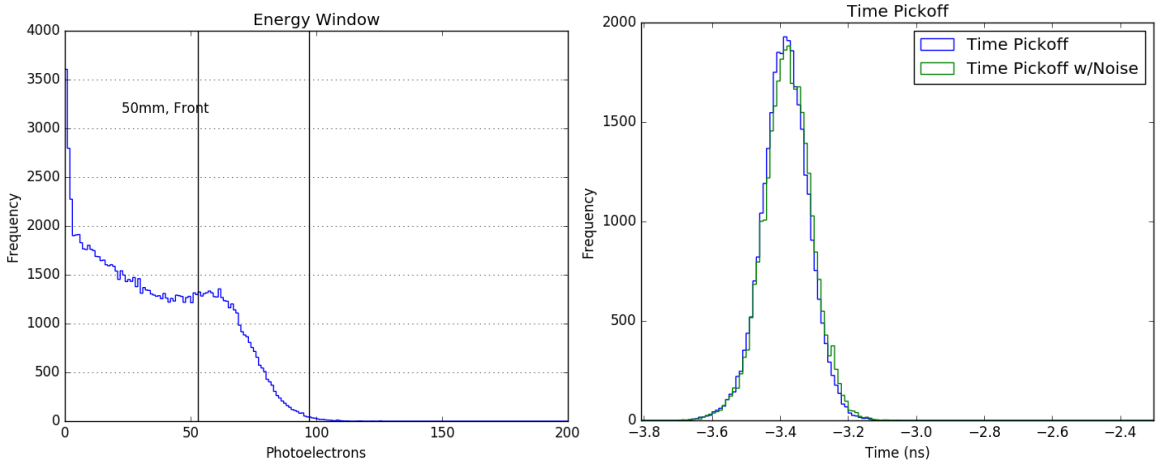
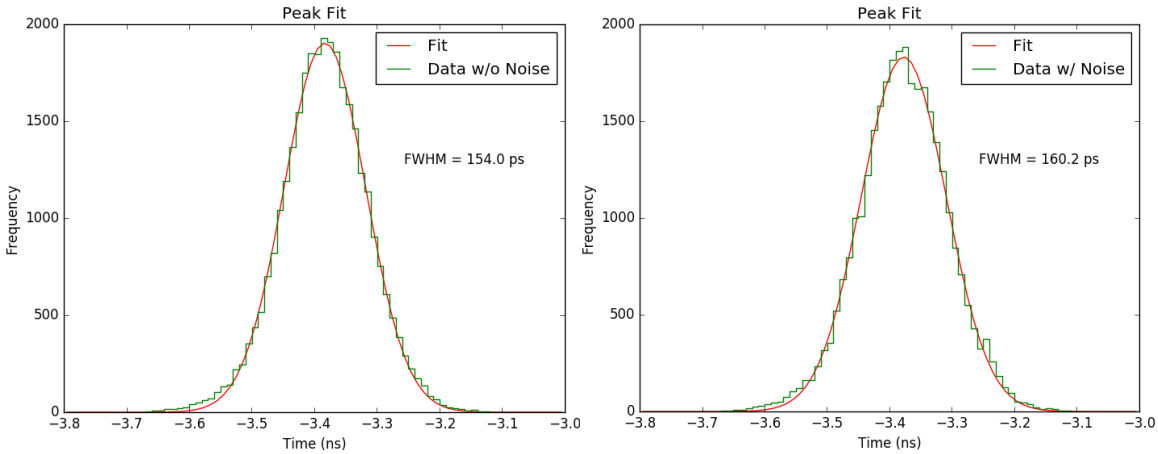


Figure C.19: The calculated CRLB vs. the number of first i arrival times used in its calculation. Data is for the 25mm sample under side irradiation.



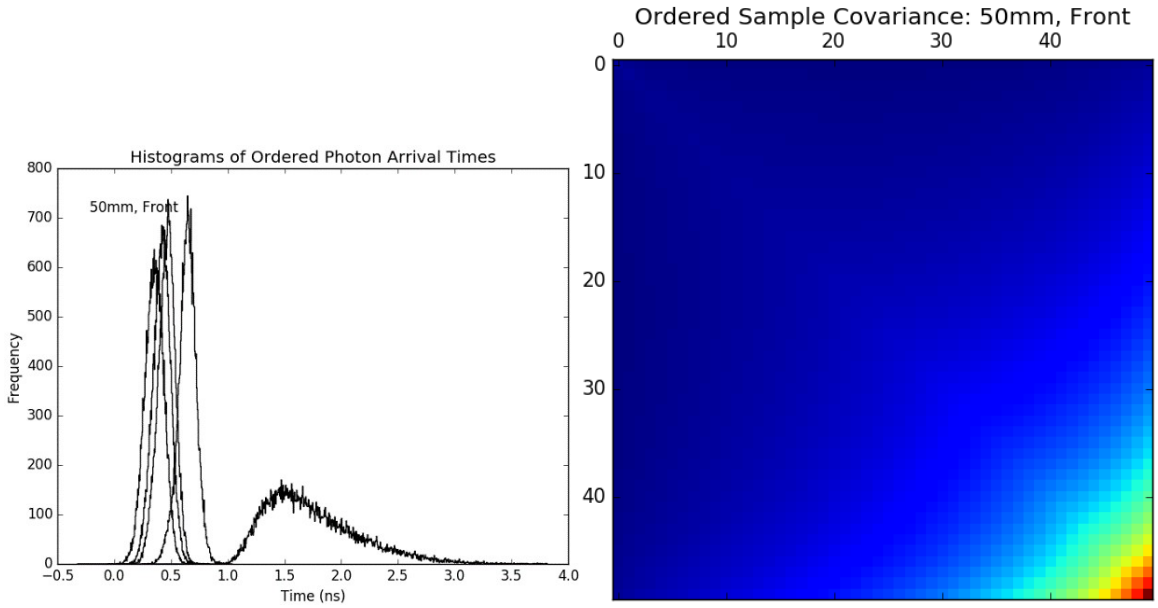
(a) **(b)**

Figure C.20: Data is for the 50mm sample under front irradiation. **(a)** The energy window for events contributing to the CRLB calculation and emulated PMT pulses. **(b)** The frequency distributions of the pick off time using the emulated PMT signal both with and without noise applied to the pulse.



(a) **(b)**

Figure C.21: Fit and FWHM of the time pick off distributions using the emulated PMT pulse both without noise **(a)** and with noise **(b)** added to the signal. Data is shown for the 50mm sample under front irradiation.



(a) **(b)**

Figure C.22: The data is for the 50mm sample under front irradiation. **(a)** Shown are the arrival time distributions for the 1^{st}, 2^{nd}, 3^{rd}, 10^{th}, and 50^{th} detected photons (left to right). **(b)** The intensity map of the covariance matrix for the ordered photon arrival times. The x and y axis values are the arrival time index: $i \exists [0, 50)$.

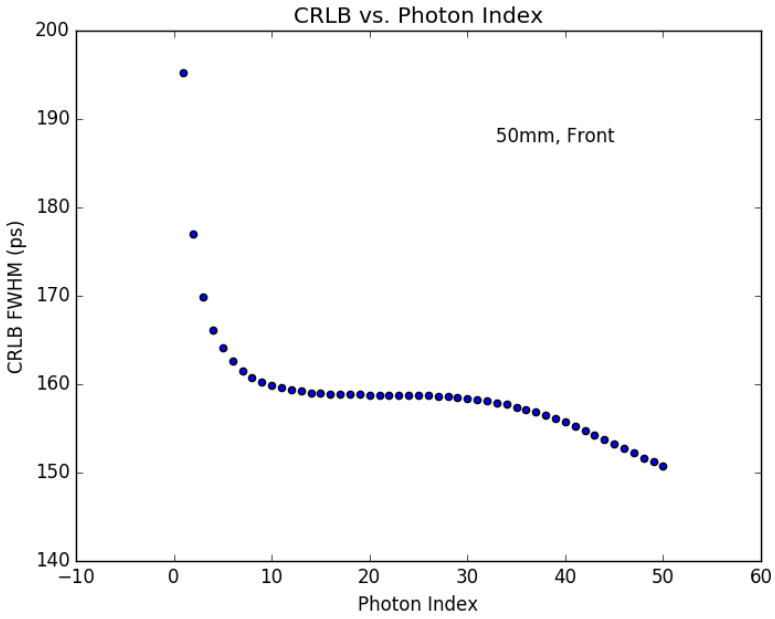
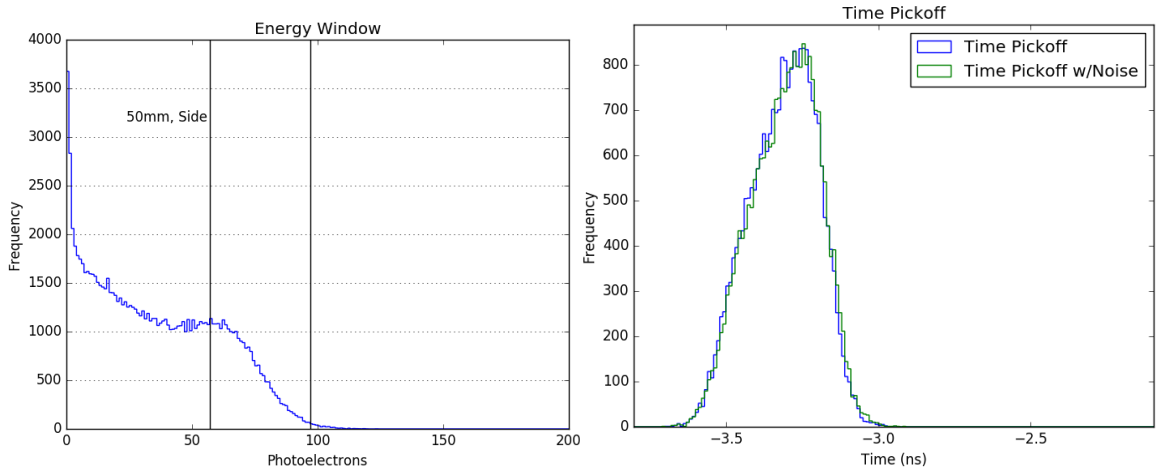
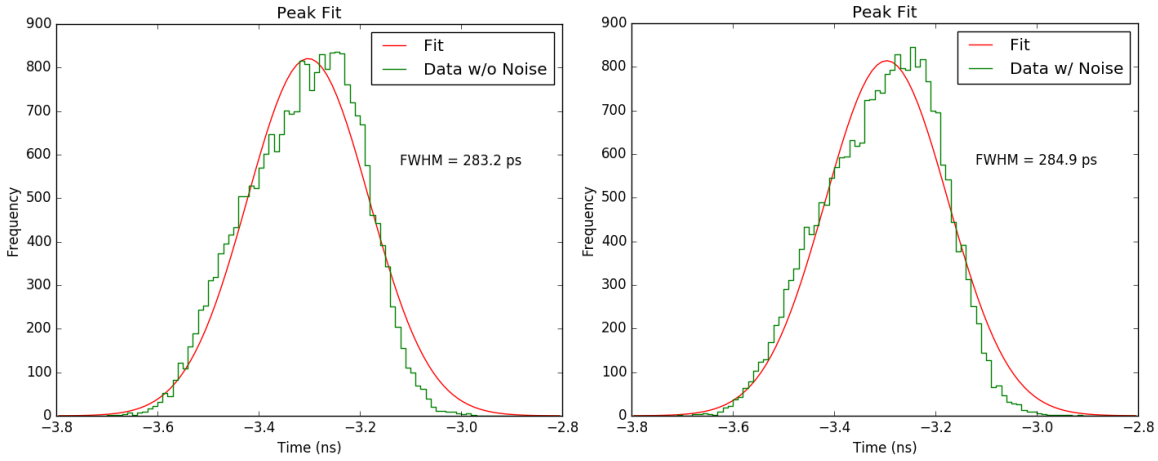


Figure C.23: The calculated CRLB vs. the number of first i arrival times used in its calculation. Data is for the 50mm sample under front irradiation.



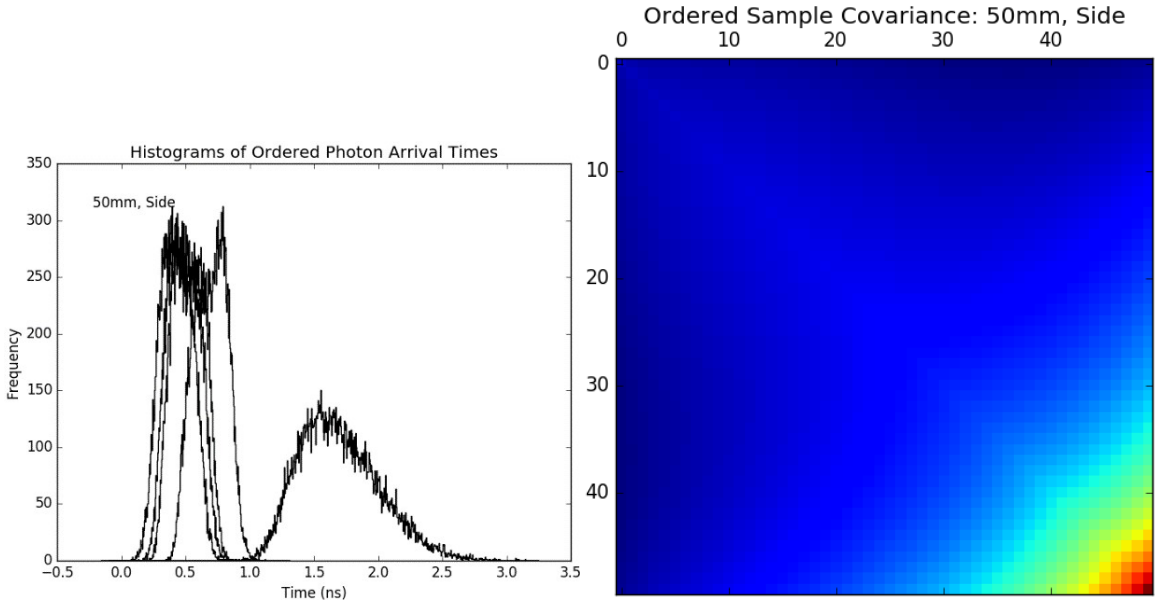
(a) **(b)**

Figure C.24: Data is for the 50mm sample under side irradiation. **(a)** The energy window for events contributing to the CRLB calculation and emulated PMT pulses. **(b)** The frequency distributions of the pick off time using the emulated PMT signal both with and without noise applied to the pulse.



(a) **(b)**

Figure C.25: Fit and FWHM of the time pick off distributions using the emulated PMT pulse both without noise **(a)** and with noise **(b)** added to the signal. Data is shown for the 50mm sample under side irradiation.



(a) **(b)**

Figure C.26: The data is for the 50mm sample under side irradiation. **(a)** Shown are the arrival time distributions for the 1^{st}, 2^{nd}, 3^{rd}, 10^{th}, and 50^{th} detected photons (left to right). **(b)** The intensity map of the covariance matrix for the ordered photon arrival times. The x and y axis values are the arrival time index: $i \exists [0, 50)$.

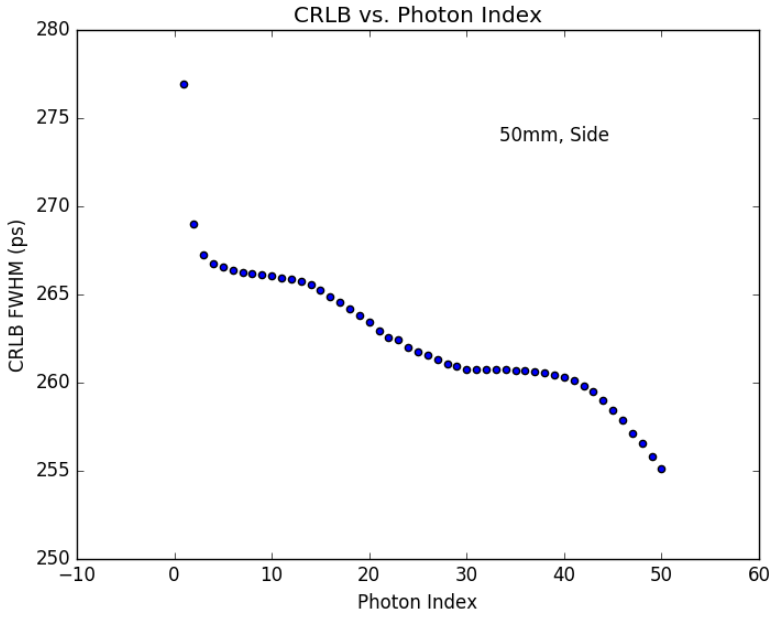
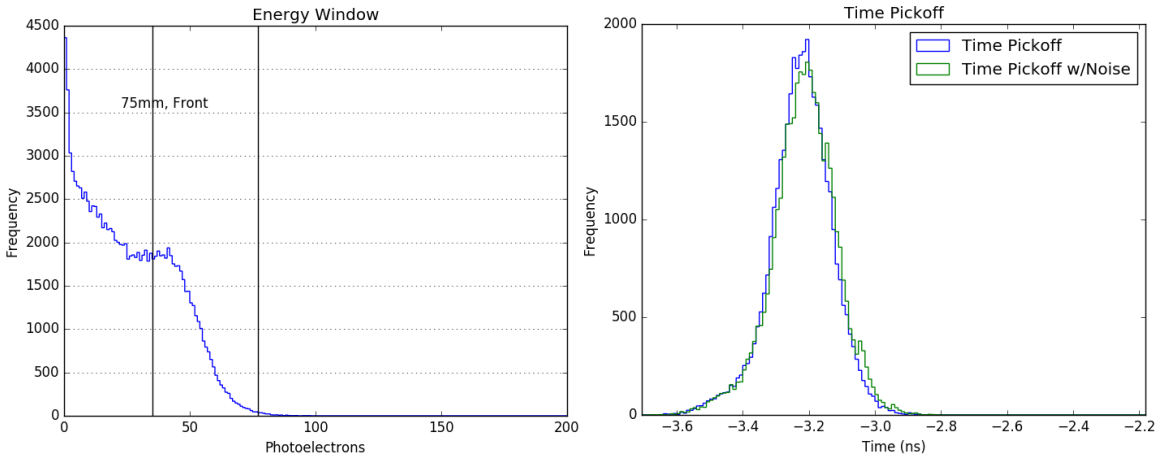
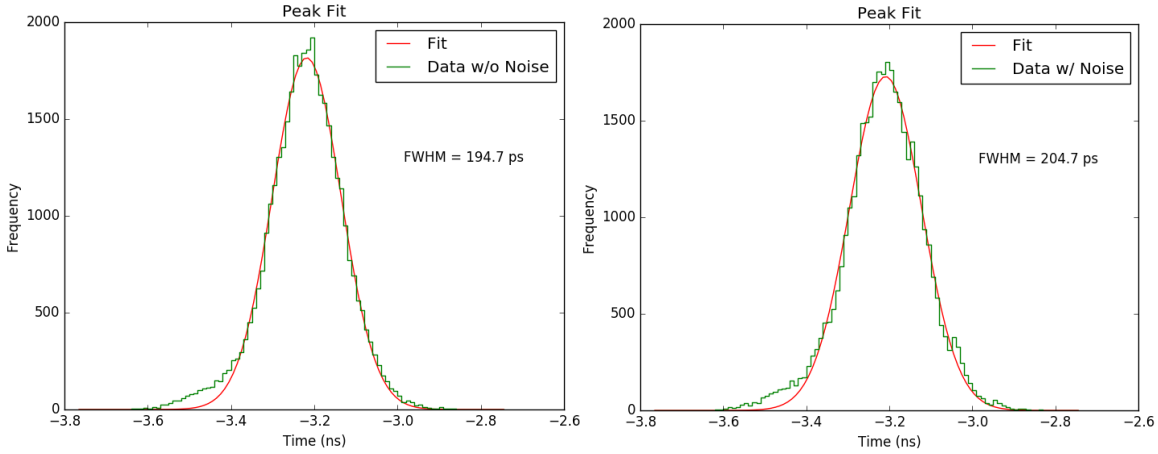


Figure C.27: The calculated CRLB vs. the number of first i arrival times used in its calculation. Data is for the 50mm sample under side irradiation.



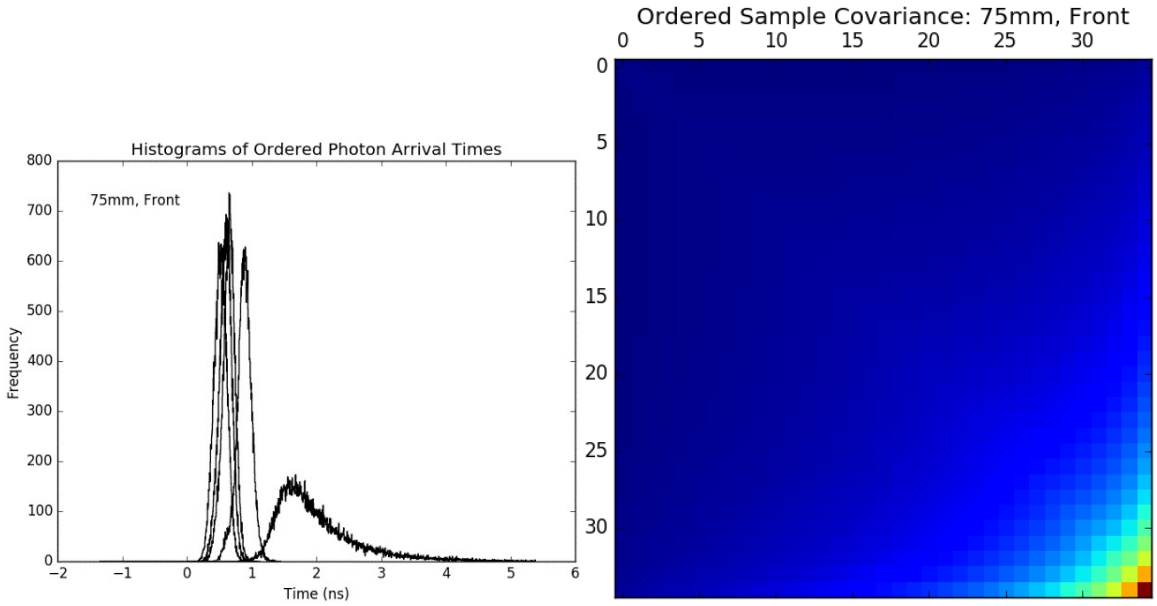
(a) **(b)**

Figure C.28: Data is for the 75mm sample under front irradiation. **(a)** The energy window for events contributing to the CRLB calculation and emulated PMT pulses. **(b)** The frequency distributions of the pick off time using the emulated PMT signal both with and without noise applied to the pulse.



(a) **(b)**

Figure C.29: Fit and FWHM of the time pick off distributions using the emulated PMT pulse both without noise **(a)** and with noise **(b)** added to the signal. Data is shown for the 75mm sample under front irradiation.



(a) **(b)**

Figure C.30: The data is for the 75mm sample under front irradiation. **(a)** Shown are the arrival time distributions for the 1^{st}, 2^{nd}, 3^{rd}, 10^{th}, and 35^{th} detected photons (left to right). **(b)** The intensity map of the covariance matrix for the ordered photon arrival times. The x and y axis values are the arrival time index: $i \exists [0, 35)$.

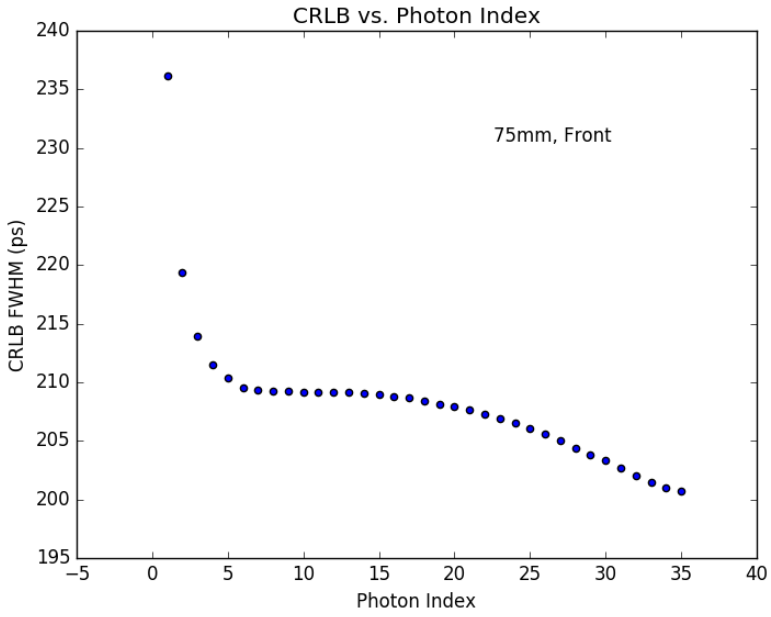
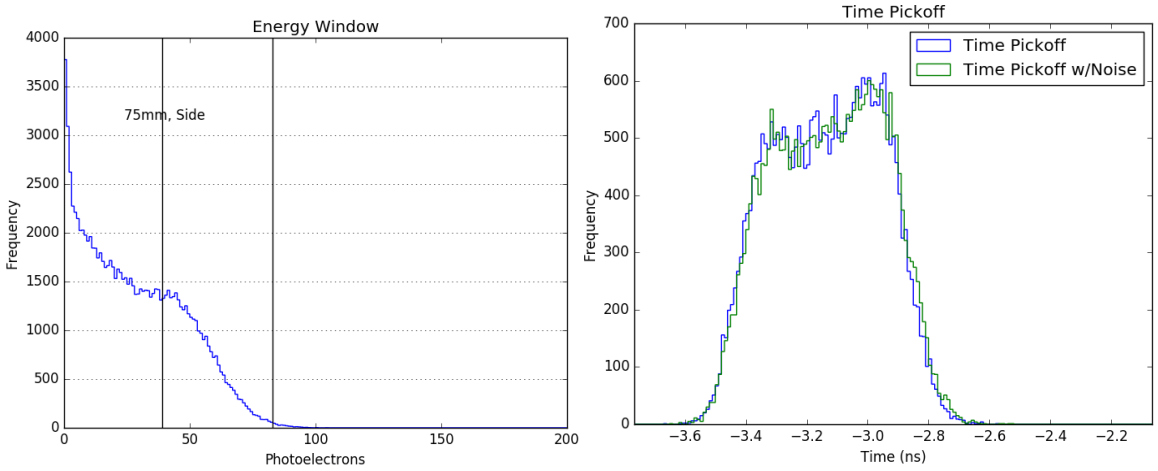
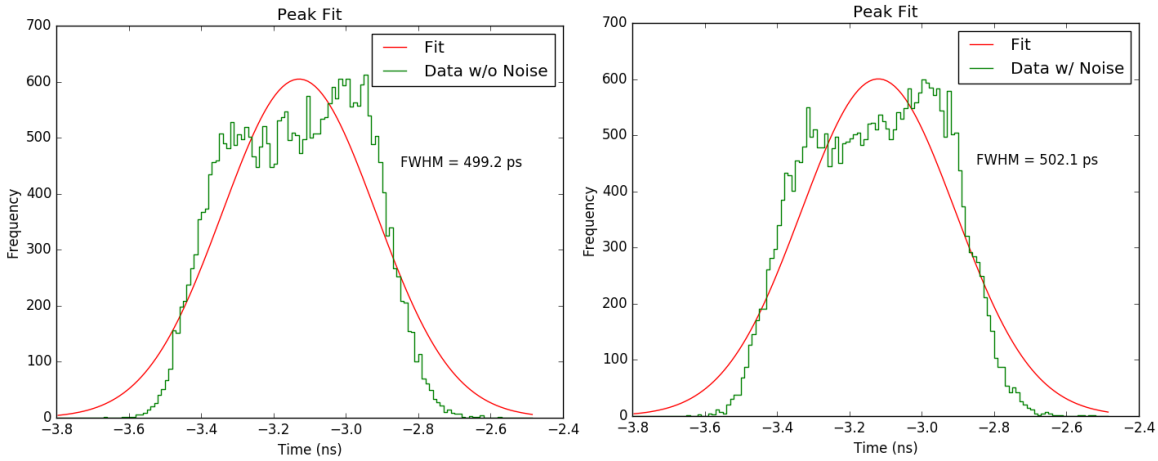


Figure C.31: The calculated CRLB vs. the number of first i arrival times used in its calculation. Data is for the 75mm sample under front irradiation.



(a) **(b)**

Figure C.32: Data is for the 75mm sample under side irradiation. **(a)** The energy window for events contributing to the CRLB calculation and emulated PMT pulses. **(b)** The frequency distributions of the pick off time using the emulated PMT signal both with and without noise applied to the pulse.



(a) **(b)**

Figure C.33: Fit and FWHM of the time pick off distributions using the emulated PMT pulse both without noise **(a)** and with noise **(b)** added to the signal. Data is shown for the 75mm sample under side irradiation.

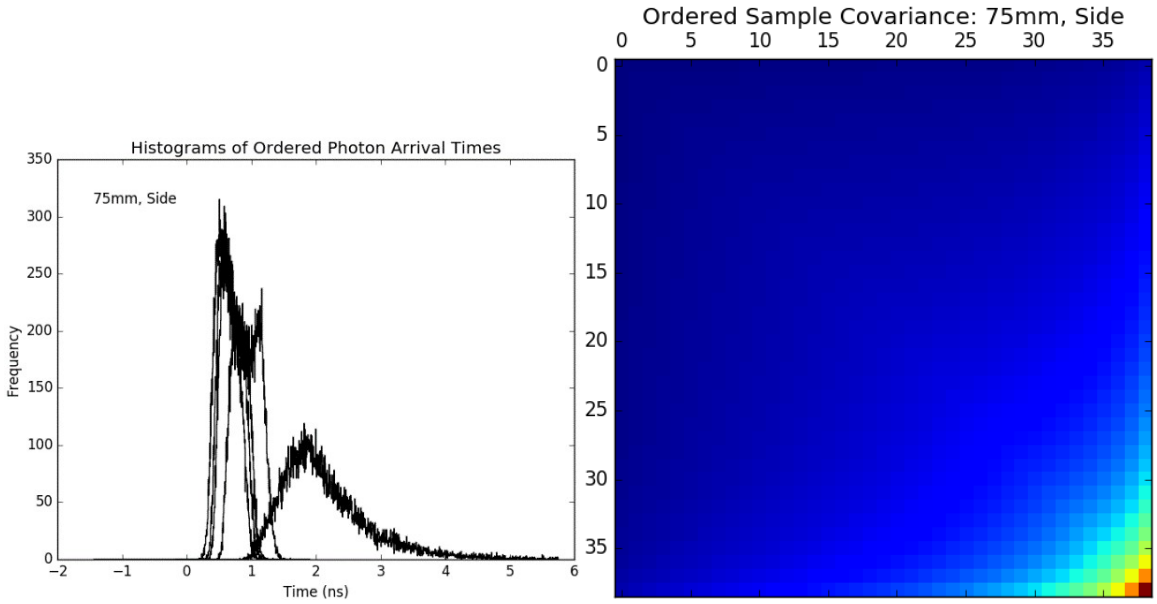


Figure C.34: The data is for the 75mm sample under side irradiation. **(a)** Shown are the arrival time distributions for the 1^{st}, 2^{nd}, 3^{rd}, 10^{th}, and 35^{th} detected photons (left to right). **(b)** The intensity map of the covariance matrix for the ordered photon arrival times. The x and y axis values are the arrival time index: $i \exists [0, 35)$.

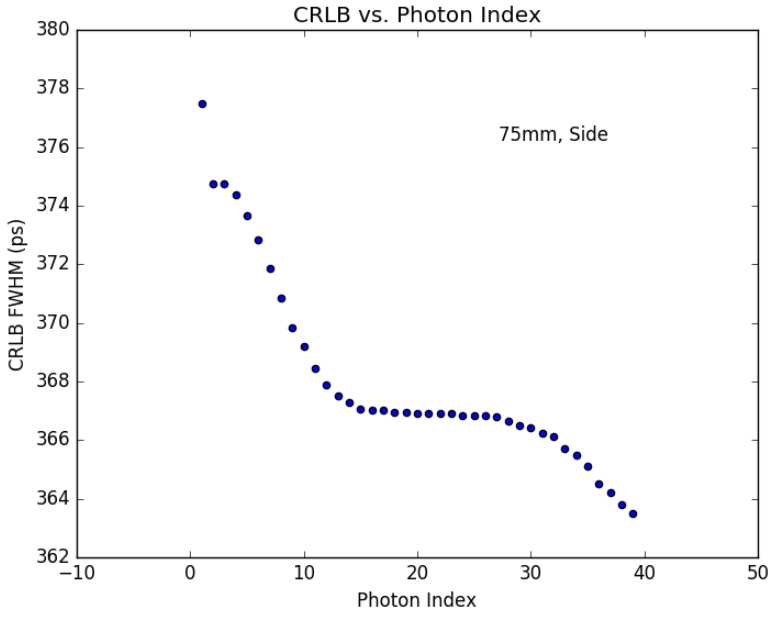
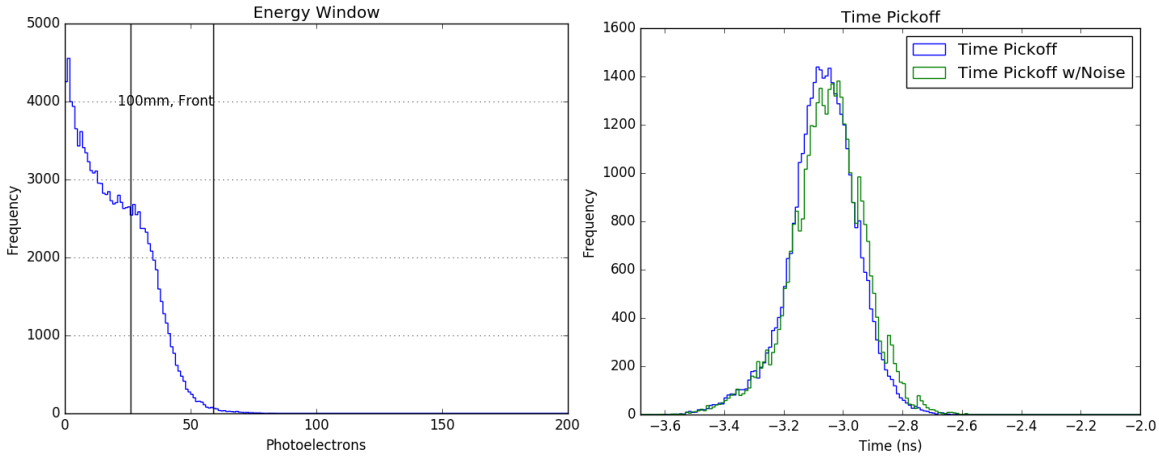
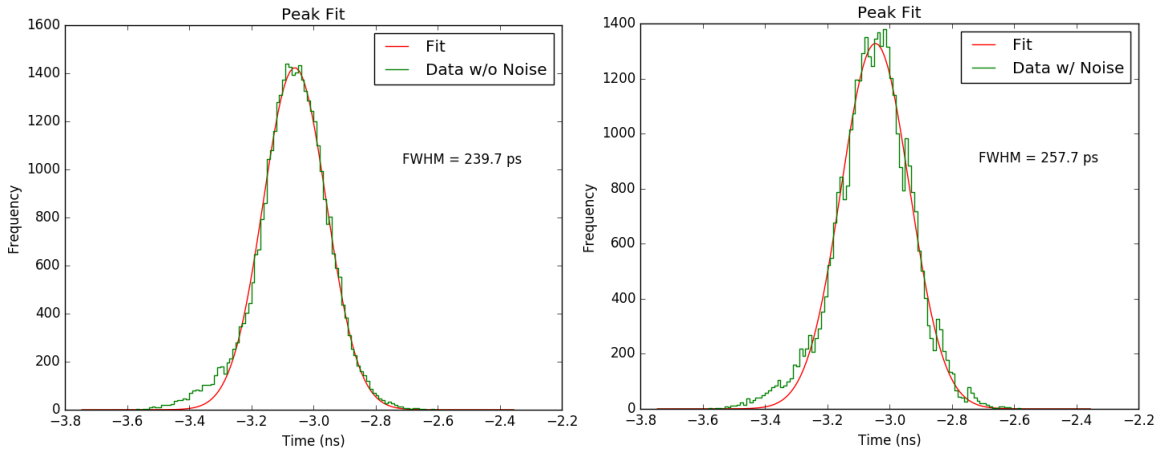


Figure C.35: The calculated CRLB vs. the number of first i arrival times used in its calculation. Data is for the 75mm sample under side irradiation.



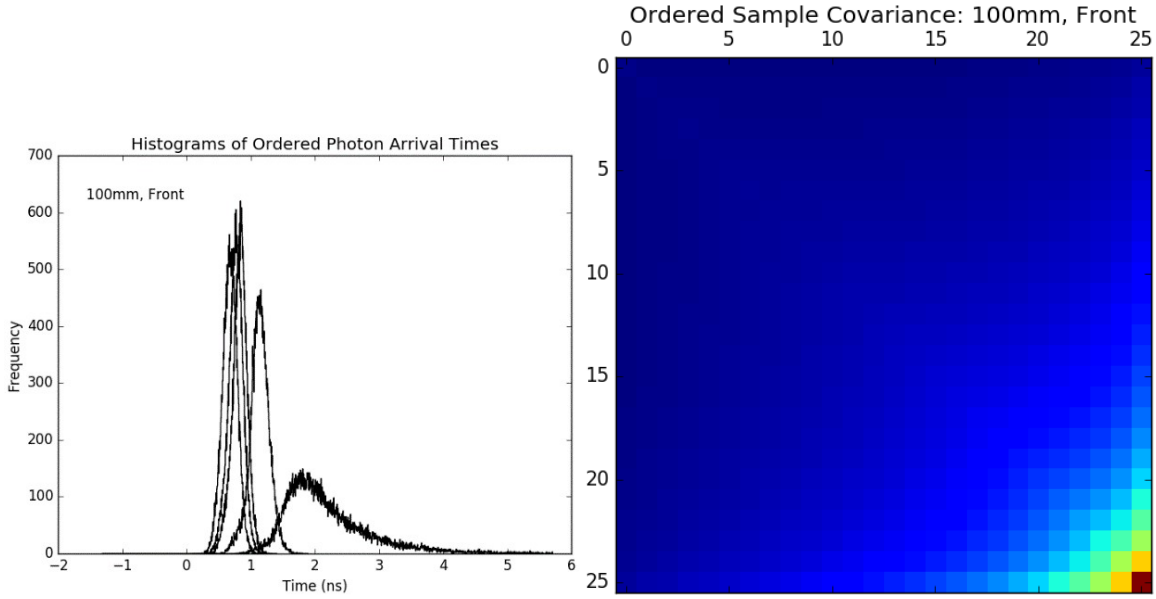
(a) **(b)**

Figure C.36: Data is for the 100mm sample under front irradiation. **(a)** The energy window for events contributing to the CRLB calculation and emulated PMT pulses. **(b)** The frequency distributions of the pick off time using the emulated PMT signal both with and without noise applied to the pulse.



(a) **(b)**

Figure C.37: Fit and FWHM of the time pick off distributions using the emulated PMT pulse both without noise **(a)** and with noise **(b)** added to the signal. Data is shown for the 100mm sample under front irradiation.



(a) **(b)**

Figure C.38: The data is for the 100mm sample under front irradiation. **(a)** Shown are the arrival time distributions for the 1^{st}, 2^{nd}, 3^{rd}, 10^{th}, and 26^{th} detected photons (left to right). **(b)** The intensity map of the covariance matrix for the ordered photon arrival times. The x and y axis values are the arrival time index: $i \exists [0, 26)$.

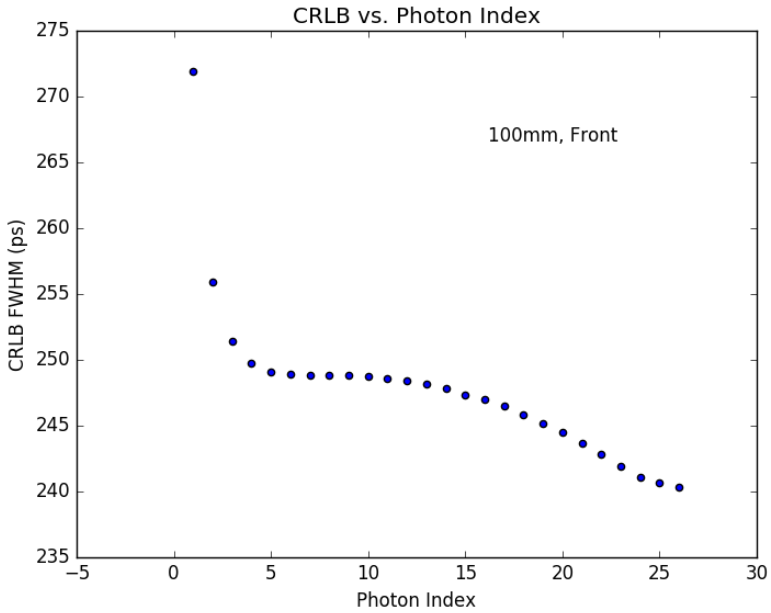
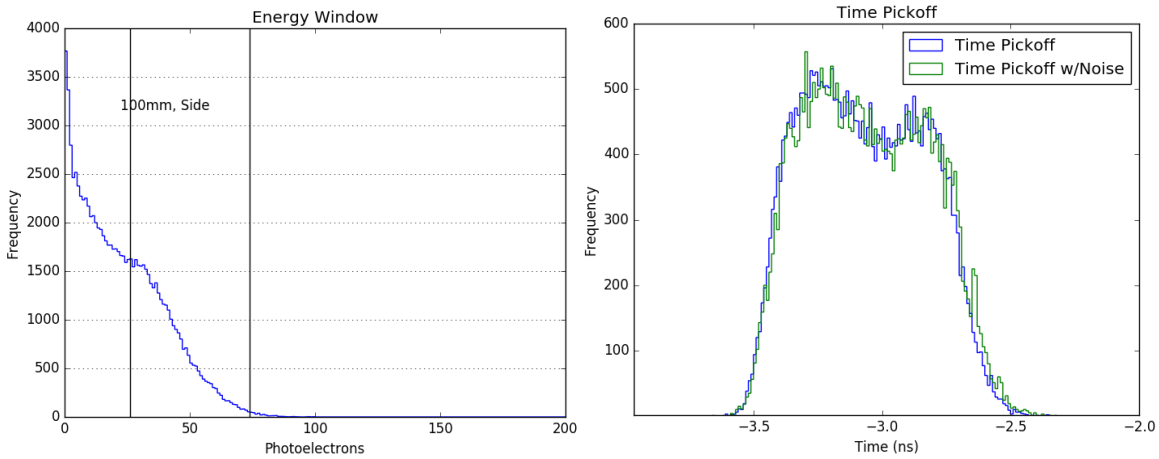
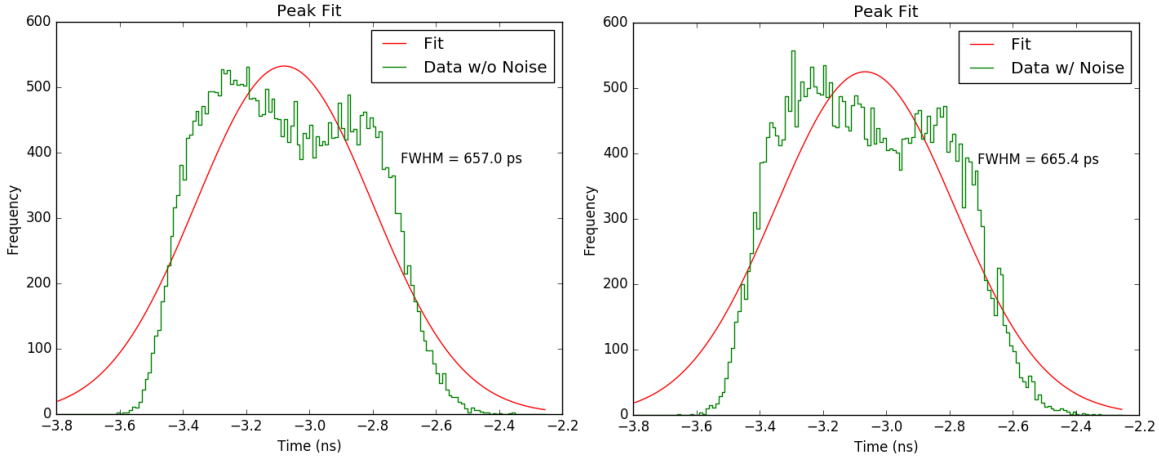


Figure C.39: The calculated CRLB vs. the number of first i arrival times used in its calculation. Data is for the 100mm sample under front irradiation.



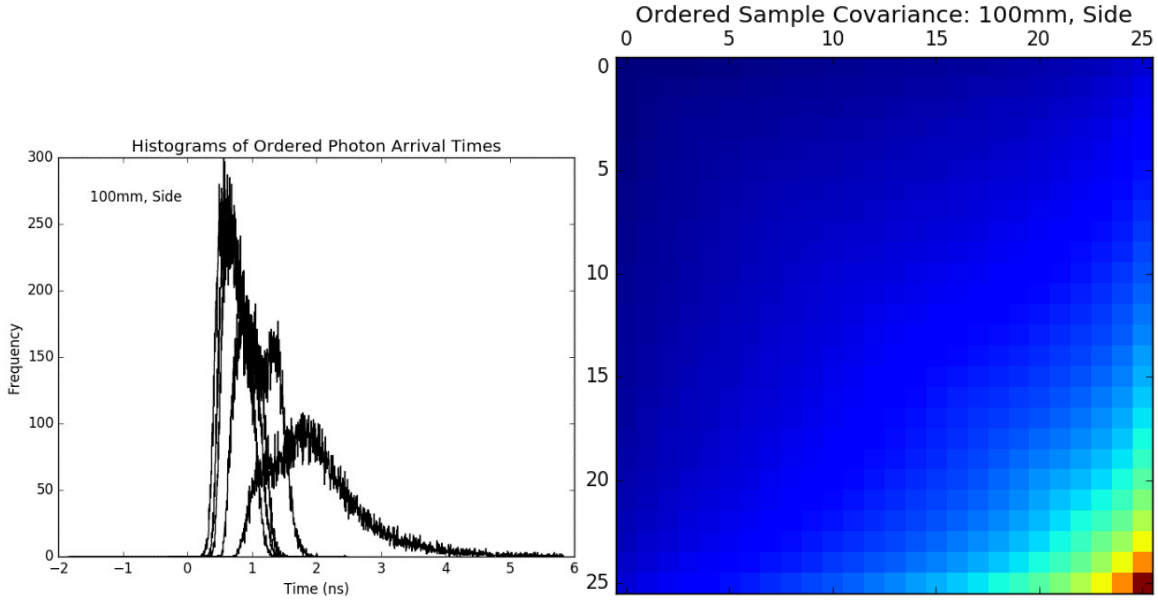
(a) **(b)**

Figure C.40: Data is for the 100mm sample under side irradiation. **(a)** The energy window for events contributing to the CRLB calculation and emulated PMT pulses. **(b)** The frequency distributions of the pick off time using the emulated PMT signal both with and without noise applied to the pulse.



(a) **(b)**

Figure C.41: Fit and FWHM of the time pick off distributions using the emulated PMT pulse both without noise **(a)** and with noise **(b)** added to the signal. Data is shown for the 100mm sample under side irradiation.



(a) **(b)**

Figure C.42: The data is for the 100mm sample under side irradiation. **(a)** Shown are the arrival time distributions for the 1^{st}, 2^{nd}, 3^{rd}, 10^{th}, and 26^{th} detected photons (left to right). **(b)** The intensity map of the covariance matrix for the ordered photon arrival times. The x and y axis values are the arrival time index: $i \exists [0, 26)$.

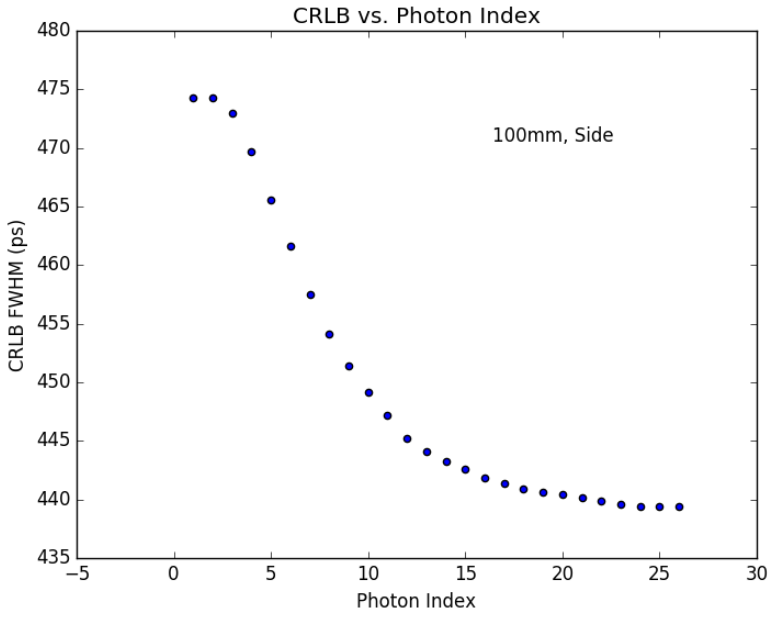


Figure C.43: The calculated CRLB vs. the number of first i arrival times used in its calculation. Data is for the 100mm sample under side irradiation.

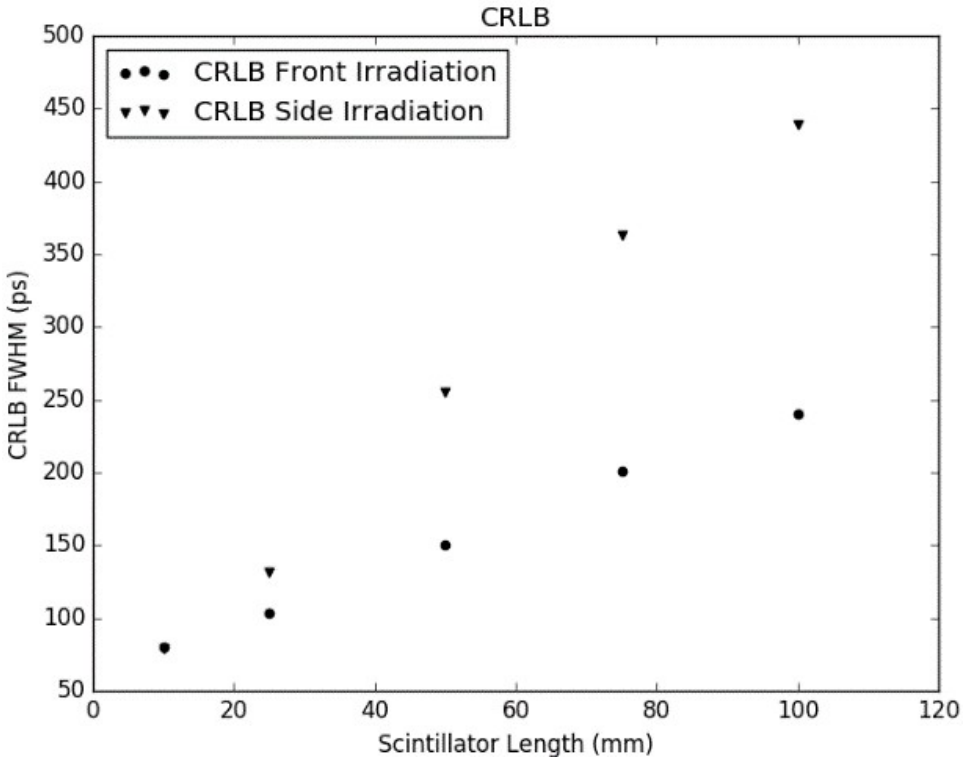
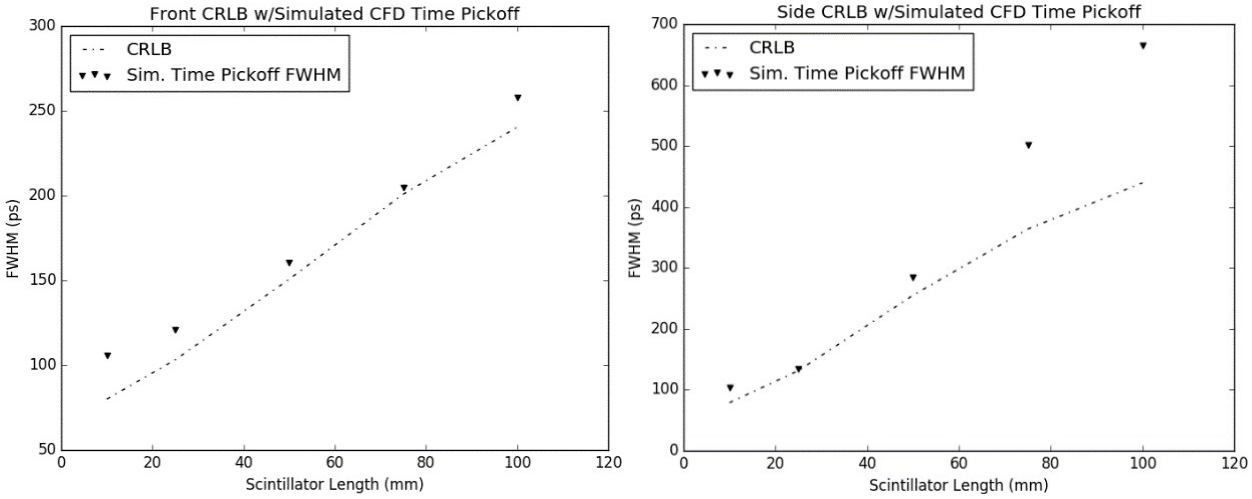


Figure C.44: The calculated CRLB vs. scintillator length for front and side modes of irradiation.



(a) **(b)**

Figure C.45: The FWHM of the frequency distribution of the pick off times using the emulated PMT pulse and CFD fraction of 0.3. **(a)** Shows the result against the CRLB for the front irradiation simulations. **(b)** Shows the result against the CRLB for the side irradiation simulations.

length and/or irradiation mode. These emerging features will be noted in the subsequent discussion.

The frequency distributions of the pick off times show little difference between those generated from the PMT signal without noise and those generated with noise. This is likely due to the simple Gaussian model of the noise being unable to capture and communicate various changes on the noise distribution tied to dynamic PMT processes. Nevertheless, the FWHM of all distributions with the added noise is larger than those without noise by an amount ranging from 2-18 ps. Observable trends in these frequency distributions show a widening of the distribution with increasing scintillator length. Using the distributions generated from the noise-added PMT pulses, these widths range from 105.7 ps and 103.4 for the 10 mm sample under front and side irradiation modes respectively to 257.7 ps and 665.4 ps for the 100 mm samples under front and side irradiation, respectively. Additional observations related to these data is the development of heavy left-ward tails for the 75 mm and 100 mm samples under front irradiation. Additionally, there is an observed potential development of multiple distribution modes for the 50 mm, 75 mm, and 100 mm samples when under side irradiation.

The frequency distributions of the i^{th} photon's arrival time show fairly Gaussian shaped distributions for the 1^{st}, 2^{nd}, 3^{rd}, 10^{th}, and 50^{th}, photons within the 10 mm and 25 mm samples. The distributions for the 50^{th}, 35^{th}, and 26^{th} photons, the last ones used in the CRLB calculation, begin to reveal heavy rightward tails in the 50 mm, 75 mm, and 100 mm samples respectively. Additionally, the distribution of the arrival time for a given photon index appears to widen as the scintillator length increases; with the width of the first photon's arrival time being about 180 ps for the 10 mm sample under front irradiation compared to approximately 650 ps for the 100 mm sample.

All data for the CRLB vs the number of first i photon arrival times included in the calculation show a general trend that as more photon arrival times are added to the calculation, the value for the CRLB tends to trend downward. In the instances where the number of photons used for the calculation is larger, by about a factor of 2 or more, than the number of photons in the pulse, the CRLB appears to stabilize after 20 photons as shown in the 10 mm and 25 mm cases, though a slight downward trend is noticeable past the index of

40 in the 25 mm sample. The longer samples under front irradiation present a CRLB which tends downward at varying rates as more photon arrival times are added to the calculation. Under side irradiation, the 50 mm and 75 mm samples present a CRLB with two plateaus having a downward transition between them.

The final reported value of the CRLB is the value calculated with 50 photon arrival times for the 10 mm, 25 mm, and 50 mm geometries while 35 and 26 photon arrival times are used for the 75 mm and 100 mm geometries, respectively. Examining Figure C.44, the CRLB for the 10 mm sample appears invariant between the front vs. side irradiation modes. For the longer geometries, the CRLB is greater under side irradiation than front irradiation. This difference becomes more pronounced as the length of the scintillator increases and may be attributed to the greater variance in the depth of interaction which presents in the side irradiation mode. It is of utmost importance to understand that this is not the same time-spreading mechanism arising from on axis DOI effects which result from a spreading of the gamma interaction time in the crystal relative to the annihilation time. Instead, this is due to the effect of optical absorption and the resulting high variance in the photon statistics which is better for events occurring near the photo sensor and poorer for events occurring near the end opposite of the sensor. This idea is supported by the dual PMT readout data in [127], see Figure 7.a in that reference. That data shows a lower timing resolution and one which increases at a considerably lower rate with respect to scintillator length when compared to the single PMT readout. This is because the variance in the photon arrival time statistics has decreased overall, regardless of the origin of the light, and is now symmetric about the center plane bisecting the scintillator between the two PMTs. This symmetry means that the variance of the photon statistics will not be higher if the light originates on one end vs. the other. However, variance in the photon statics will likely increase as the origin of light moves from the ends towards the center; though the effect of this is expected to be lower when compared to having origins of light on one end vs the other in the case of single PMT readout.

Comparing the CRLB FWHM to the FWHM of the time pick off frequency distributions using the noisy signal shows that the CRLB FWHM remains below the FWHM of the time pick off distributions, though at some lengths these are extremely close. These two

values track fairly well with each other for the varied lengths under front irradiation but experience a noted departure for the longer lengths under side irradiation. When compared to the experimental data in [127], see Figure 3 in that reference, the calculated CRLB shows similar trends to the experimentally measured timing resolution and is 1.23 to 1.57 times lower, with the greatest difference presenting in the shorter lengths.

C.5 Conclusion

The CRLB on the TOF timing resolution has been calculated for EJ232Q with 0.5% benzophenone in lengths of 10 mm , 25 mm, 50 mm, 75 mm, and 100 mm with a base of 5x5 mm. The calculation was performed for each of these samples in both front and side irradiation modes with a 511 keV gamma source. The calculations show that the CRLB increases with increasing lengths and is higher when the samples are under side irradiation. The lowest calculated CRLB was 78.8 ps for the 10 mm sample under side irradiation while the highest was 439.4 ps for the 100 mm sample under side irradiation.

Further simulation studies may be performed using wavelength dependent optical absorption and refractive index data for all optical components in addition to making the optical surfaces congruent to those used in the experiment presented in [127].

C.6 Acknowledgments

The author would like to thank Xianfei Wen for sharing the experimental data which proved useful in selecting some of the simulation parameters.

This material is based on work supported in part by the Defense Threat Reduction Agency under grant number HDTRA 1-18-1-005 and in part by the Department of Energy National Nuclear Security Administration through the Nuclear Science and Security Consortium under Award Number(s) DE-NA0003180 and/or DE-NA0000979.

Disclaimer: "This report was prepared as an account of work sponsored by an agency of the United States Government. Neither the United States Government nor any agency thereof, nor any of their employees, makes any warranty, express or implied, or assumes any legal liability or responsibility for the accuracy, completeness, or usefulness of any

information, apparatus, product, or process disclosed, or represents that its use would not infringe privately owned rights. Reference herein to any specific commercial product, process, or service by trade name, trademark, manufacturer, or otherwise does not necessarily constitute or imply its endorsement, recommendation, or favoring by the United States Government or any agency thereof. The views and opinions of authors expressed herein do not necessarily state or reflect those of the United States Government or any agency thereof."

Vita

Caleb Redding was born in Nashville, Tennessee to his parents, Hal and Diane Redding; a machinist and an educator. He was raised by his parents on a small working farm alongside his grandparents, Harold and Martha, three siblings, and all manner of livestock, fowl, and pets. It was in this environment where he was taught to be independent, self-sufficient, and hard working. If something was broken you were to fix it; if you couldn't fix it then you weren't using enough duct tape. He was homeschooled by his parents from the 4^{th} grade until graduating high school in 2007. During his secondary education, he took great interest in Physics because of how elegantly it described the natural world and decided to pursue this as a collegiate major. He first attended Volunteer State Community College, taking relevant transfer credit courses, before being accepted to the undergraduate physics program at the University of Tennessee in 2009. He graduated Summa Cum Laude in the spring of 2012 before heading to the Mississippi Delta for *Teach for America's* summer institute. Under the umbrella of *Teach for America*, he accepted a position to teach secondary science at Greensboro High School in Alabama. This was an incredibly difficult and rewarding experience, through which he met many kind and remarkable individuals.

In the spring of 2015, Caleb was accepted to the Ph.D. program in the Nuclear Engineering Department at the University of Tennessee. In 2017, he earned his M.S. under the guidance of Prof. Lawrence Townsend. This work focused on performing shielding calculations for the proposed NNBar beamline at the European Spallation Source. This proposed experiment had the aim of achieving the highest-ever sensitivity for the search of the neutron-antineutron oscillation. After completing his masters, he was offered a position with Prof. Jason Hayward to conduct the research contained in this document. He will begin the next step of his journey at Oak Ridge National Laboratory working to further develop

the capabilities and output of the Nuclear Nonproliferation Division towards enabling a safer, carbon-free, and energy independent United States.